Silvan Schmid Luis Guillermo Villanueva Michael Lee Roukes

Fundamentals of Nanomechanical Resonators



Fundamentals of Nanomechanical Resonators

Silvan Schmid • Luis Guillermo Villanueva Michael Lee Roukes

Fundamentals of Nanomechanical Resonators



Silvan Schmid Vienna University of Technology Vienna, Austria

Michael Lee Roukes California Institute of Technology Pasadena, CA, USA

Luis Guillermo Villanueva École Polytechnique Fédérale de Lausanne, Switzerland

ISBN 978-3-319-28689-1 ISBN 978-3-319-28691-4 (eBook) DOI 10.1007/978-3-319-28691-4

Library of Congress Control Number: 2016942892

© Springer International Publishing Switzerland 2016

This work is subject to copyright. All rights are reserved by the Publisher, whether the whole or part of the material is concerned, specifically the rights of translation, reprinting, reuse of illustrations, recitation, broadcasting, reproduction on microfilms or in any other physical way, and transmission or information storage and retrieval, electronic adaptation, computer software, or by similar or dissimilar methodology now known or hereafter developed.

The use of general descriptive names, registered names, trademarks, service marks, etc. in this publication does not imply, even in the absence of a specific statement, that such names are exempt from the relevant protective laws and regulations and therefore free for general use.

The publisher, the authors and the editors are safe to assume that the advice and information in this book are believed to be true and accurate at the date of publication. Neither the publisher nor the authors or the editors give a warranty, express or implied, with respect to the material contained herein or for any errors or omissions that may have been made.

Printed on acid-free paper

This Springer imprint is published by Springer Nature The registered company is Springer International Publishing AG Switzerland

Preface

Back in December 1959, future Nobel laureate Richard Feynman gave a visionary and now oft-quoted talk entitled "There's Plenty of Room at the Bottom." The occasion was an American Physical Society meeting at the California Institute of Technology. Although he did not intend it, Feynman's 7000 words were a defining moment in nanotechnology, long before anything "nano" appeared on the horizon. The breadth of Feynman's vision is staggering. In that lecture 42 years ago, he anticipated a spectrum of scientific and technical fields that are now well established, among them electron-beam and ion-beam fabrication, molecular beam epitaxy, nanoimprint lithography, atom-by-atom manipulation, quantum-effect electronics, spin electronics (also called spintronics), and microelectromechanical systems (MEMS) or, even smaller, nanoelectromechanical systems (NEMS).

It is the latter topic which has been the focus of our research careers: mechanical systems with at least one dimension below $1\,\mu m$ ($10^{-6}\,m$) where the number of atoms departs from what is usually considered *macroscale* and enters into the *mesoscale*.

NEMS have been developed for a bit more than two decades now. Fabrication technology has evolved and improved enormously for these devices which allows, for reproducibility and yield, two *sine qua non* conditions for an eventual commercialization and, with it, a direct impact on society. The two driving forces for NEMS research have been *metrology* and *fundamental science*.

Matter at this mesoscale is often awkward to explore. It contains too many atoms to be easily understood by straightforward application of quantum mechanics (although the fundamental laws still apply). Yet these systems are not so large as to be completely free of quantum effects; thus, they do not simply obey the classical physics governing the macroworld. It is precisely in this intermediate domain, the mesoworld, that unforeseen properties of collective systems might emerge. Indeed, many efforts have been invested into cooling mechanical resonators down to their *ground state*, which has been recently proven. In addition, interaction between NEMS and q-bits, operation within Coulomb blockade, etc., have been also studied over the years.

vi Preface

On the other hand, NEMS can also be used as extremely good sensors. After the first pioneering experiments on measuring the quanta of electrical conductance and the one of thermal conductance, NEMS have also been targeted to detect spins, radiation, temperature, mass, etc. The theoretical limits for the performance of NEMS-based sensors are outstanding. However, these devices have seldom made it to the market. Comparing to their *bigger brothers*, MEMS, which it took them around 35 years to start having a great impact in consumer market, we can learn several lessons to foster the applicability of NEMS:

- Standardized fabrication: Fabrication should be reproducible, with high yield and the fabrication process should be standard (or very similar) across many different foundries.
- *Education*: An educated and trained workforce is required to tackle the problems that arise within these systems. Unfortunately, almost no university in the world offers a course in these type of devices, covering both the electrical and mechanical aspects.

It is the latter point that this book aims to address: to be a textbook for a course for engineers, not going into the details of atomic-scale simulation and analysis but rather taking an approach such as "top-down," i.e., using macroscopic formulas to model the devices.

At this point, it is important to note that this book focused on NEMS, that is, electrically transduced nanomechanical resonators, in contrast to cavity optomechanics, which fully transduces and controls nanomechanical resonators by optic techniques. However, in particular, the mechanical models introduced in this book are key to the understanding and optimization of nanomechanical resonators used in optomechanics. There are also natural overlaps between the fields in hybrid devices, as it is the case, e.g., in microwave-based cavity optomechanics, which is based on electrostatic transduction but uses optomechanical techniques.

Copenhagen, Denmark Lausanne, Switzerland Pasadena, CA, USA Silvan Schmid Luis Guillermo Villanueva Michael Lee Roukes

Contents

1	Res	onance	Frequency	1
	1.1	Eigen	modes of Ideal Continuum Mechanical Structures	2
		1.1.1	One-Dimensional Bending Vibrations	6
		1.1.2	One-Dimensional Bulk Vibrations	17
		1.1.3	Two-Dimensional Bending Vibrations	20
		1.1.4	Torsional Vibration of Thin Beams	27
	1.2	Lump	ed-Element Model Resonator	29
		1.2.1	Damped Linear Resonator	29
		1.2.2	Coupled Linear Resonators	42
		1.2.3	Damped Nonlinear Resonators	45
	Refe	erences		54
2	Ona	lity Fa	ctor	57
-	2.1		ım Interaction Losses	58
	2.1	2.1.1	Liquid Damping	58
		2.1.2	Gas Damping	61
	2.2 Clamping Loss			66
		2.2.1	Cantilever Beams	67
		2.2.2	Membranes	68
	2.3			69
			Intrinsic Damping Mechanisms	69
		2.3.2	Damping Dilution in Strings and Membranes	81
	Refe	erences		88
3	Reci	noncivi	ty	91
J	3.1	•	ency Response to Mass	92
	3.1	3.1.1	Point Mass	93
		3.1.2	Distributed Mass	99
	3.2		itude and Frequency Response to Force	101
	3.4	3.2.1	Amplitude Response to a Force	101
		3.2.1	Frequency Response to a Force Gradient	101
		3.4.2	rrequeries response to a roice Gradient	102

viii Contents

	3.3			
		3.3.1	Stress Released Resonators	106
		3.3.2	Resonators Under Tensile Stress (Strings)	108
	Refe	erences		113
4	Tra	nsducti	on	115
	4.1	Electr	odynamic (Actuation and Detection)	116
		4.1.1	Lorentz Force on a Straight Wire	117
		4.1.2	Electrodynamically Induced Voltage	
			(Electromotive Force)	118
	4.2	Electr	ostatic (Actuation and Detection)	119
		4.2.1	Electrostatic Forces	120
		4.2.2	Capacitively Induced Current	126
		4.2.3	Other Capacitive Detection Schemes	131
	4.3	Thern	noelastic (Actuation)	131
	4.4	Piezo	resistive (Detection)	132
	4.5	Piezo	electric (Actuation and Detection)	134
		4.5.1	Piezoelectric Actuation	136
		4.5.2	Piezoelectric Detection	137
	4.6	Optic	(Actuation and Detection)	138
		4.6.1	Optical Forces	138
		4.6.2	Interferometric Detection	139
		4.6.3	Beam Deflection Detection	141
		4.6.4	Plasmonic Detection	142
	Refe	erences		143
5	Mea	surem	ent and Noise	149
	5.1	Ampli	itude Noise	149
		5.1.1	Fundamentals	150
		5.1.2	Thermomechanical Fluctuations	151
		5.1.3	Transduction Related Noise	155
		5.1.4	Amplifier Noise	159
	5.2	Frequ	ency Noise	163
		5.2.1	Phase-Locked Loop	163
		5.2.2	Self-Sustained Oscillator	165
		5.2.3	Allan Variance	168
	Refe	erences		170
	_			
In	dex			173

Chapter 1 Resonance Frequency

Abstract Nanomechanical resonators are continuum mechanical structures, such as beams, strings, plates, or membranes. In this chapter the eigenmodes of such ideal lossless continuum mechanical structures are estimated by simple analytical models. Specific resonance modes of a damped continuum mechanical structure are best described by an effective lumped-element model. In this chapter, the eigenmodes of the most common continuum mechanical structures used as nanomechanical resonators are derived. Then linear, coupled, and nonlinear damped and driven resonators are discussed by means of lumped-element models.

At the *eigenfrequency* of an ideal (lossless) mechanical structure, according to the equipartition theorem, the kinetic energy of a specific mechanical vibration is equal to the potential energy stored in the respective vibrational deformation of the structure. Continuum mechanical structures have many such vibrational modes, called *eigenmodes*, at which this situation occurs. At the eigenfrequency, the total energy in the mechanical system is passed back and forth endlessly between kinetic and potential energy. Thus, once energy is added, e.g. by a kick, such a system would endlessly oscillate precisely at its eigenfrequency with a constant vibrational amplitude.

In a real mechanical structure however, not the entire energy is commuting between kinetic and potential energy, but a little part of the energy is lost during every cycle of vibration. There are many different mechanisms by which energy can dissipate, as will be discussed in Chap. 2 on page 57. Hence, a real mechanical structure will oscillate only for a finite amount of time, until all the energy that was initially entered into the system, e.g. by the kick, has been lost. In real mechanical structures with inherent energy loss, the eigenmode mechanism is called *resonance*. And the predominant frequency at which the energy is commuting between kinetic and potential energy is called the *resonance frequency*. The resonance frequency is typically close (slightly lower) to the eigenfrequency of the same system assumed without losses.

The resonance frequency of a micro- or nanomechanical resonator is typically estimated from the respective eigenfrequency, which can be calculated by means of analytical continuum mechanical models, as discussed in Sect. 1.1, or finite element method (FEM) simulations. FEM tools are readily available and are the

1

most convenient way to obtain a precise estimate of the eigenmodes of specific micro- and nanomechanical resonators. On the one hand, compared to FEM, analytical models represent idealized mechanical structures and often do not reproduce specific features of the mechanical resonator to be modelled. But on the other hand, analytical models give valuable insight in the effect of geometry and material parameters on the resulting eigenmodes. Therefore, despite FEM, analytical continuum mechanical models are indispensable for the design process of micro- and nanomechanical resonators.

As analytical continuum mechanical models, for simplicity, typically do not consider energy losses, it is convenient to represent an individual eigenmode of a mechanical resonator by an equivalent lumped-element model, as discussed in Sect. 1.2 on page 29. It is straightforward to include energy losses in lumped-element models, which allows for a more accurate description of the dynamic response of an individual eigenmode of a real dissipative micro- and nanomechanical resonator.

1.1 Eigenmodes of Ideal Continuum Mechanical Structures

In this section, analytical models are introduced to describe the free and lossless (conservative) vibration of continuum mechanical structures typically used as micro- and nanomechanical resonators. Bending vibrations of "one-dimensional" resonators, such as *beams* and *strings*, are introduced in Sect. 1.1.1. A string is a special case of a doubly clamped beam that is under tensile stress, such that the effect of the tensile stress is dominating over the beam's bending stiffness (flexural rigidity). In other words, the difference between beams and strings lies in the way potential energy is stored. While in beams the potential energy is stored in the elastic bending, in strings it is stored in the work done against the strong tensile stress during deflection. In Sect. 1.1.2 "one-dimensional" bulk modes are described. Bending vibrations of "two-dimensional" plates are introduced in Sect. 1.1.3. Here the distinction is made between pure stress-free *plates* and pre-stressed *membranes*, similar to the distinction between beams and strings in the one-dimensional case. Finally, in Sect. 1.1.4 torsional vibration in slender rods are discussed.

The classical way to find the eigenmodes of a continuum mechanical structures is by deriving the differential equation of motion, which can be obtained by equalizing all the forces (inertial and elastic) acting on an infinitesimally small piece of structure (Newton's third law). In this way it is readily possible to derive exact solutions for many simple and idealized continuum mechanical structures, such as beams, strings, or membranes. But for some structures, such as plates, it can be very hard to find the solution of the resulting differential equations. In that case the eigenmodes can be approximated by methods based on energy assumptions.

Rayleigh's method is a useful tool to obtain a good approximation for the fundamental eigenfrequency of a conservative system (a system without loss of energy). The method is based on the complete commute of the energy between its

kinetic and potential state (equipartition theorem), as explained previously. Hence, we can assume that the maximal kinetic energy $(W_{\rm kin,max})$ must be equal to the maximal potential energy $(W_{\rm pot,max})$

$$W_{\rm kin,max} = W_{\rm pot,max}. \tag{1.1}$$

All the potential and kinetic energies of a few common ideal structures introduced in this chapter are listed in Table 1.1. It is obvious that in order to calculate the energies, the structure specific mode shape u(x, y, t) is required. It is possible to separate the spatial modal shape from the temporal variations. Separating the variables, the mode shape function of a specific normal mode can be written in the form

$$u(x, y, t) = U(x, y)\cos(\omega t) \tag{1.2}$$

where the spatial mode shape function U(x, y) gets modulated by the temporal sinusoidal function $\cos(\omega t)$ with the angular velocity ω .¹ The separation of variables is done likewise with polar coordinates.

Since the maximal value of the temporal function is unity $(\max\{\cos(\omega t)\} = 1)$, the potential energy maximum is readily given by

$$W_{\text{pot,max}} = \max\{W_{\text{pot}}(u(x, y, t))\} = W_{\text{pot}}(U(x, y)).$$
 (1.3)

Because for the kinetic energy it is essential that

$$W_{\rm kin} \propto \left(\frac{\partial u(x,y,t)}{\partial t}\right)^2,$$
 (1.4)

and with the Ansatz (1.2) the maximal kinetic energy readily can be written as

$$W_{\text{kin,max}} = \max\{W_{\text{kin}}(u(x, y, t))\} = \omega^2 W_{\text{kin}}(U(x, y)).$$
 (1.5)

Substituting (1.3) and (1.5) in (1.1), it is now possible to calculate the eigenfrequency Ω of a specific eigenmode

$$\Omega^2 = \omega^2 = \frac{W_{\text{pot}}(U(x, y))}{W_{\text{kin}}(U(x, y))}$$
(1.6)

for a suitable displacement function U(x, y). Rayleigh's method yields the exact eigenfrequency if the exact mode shape is known. But typically, the correct mode shape function is unknown and a suitable approximation has to be assumed that satisfies all the boundary conditions. A common approach is to use the displacement

¹For convenience, the term "frequency" is subsequently used in place for the actual correct term "angular velocity."

Table 1.1 Strain and kinetic energies of various continuum mechanical structures with E: Young's modulus, I_y : geometrical moment of inertia, h: structure thickness, w: beam width, A = hw: cross section, ρ : mass density, G shear modulus, I_p : polar moment of inertia, ν : Poisson's ratio, $D_P = Eh^3/(12(1-\nu^2))$: flexural rigidity of plate, σ : tensile stress [1–4]

Member	Potential energy (W _{pot})	Kinetic energy (W _{kin})
Beam of length L in bending vibration	$\frac{1}{2}EI_{y}\int_{0}^{L}\left(\frac{\partial^{2}u}{\partial x^{2}}\right)^{2}\mathrm{d}x$	
String of length L in bending vibration	$\frac{1}{2}\sigma A \int_0^L \left(\frac{\partial u}{\partial x}\right)^2 \mathrm{d}x$	$\int_{-\frac{1}{2}A\rho} \int_{0}^{L} \left(\frac{\partial u}{\partial t}\right)^{2} dx$
Beam or String of length L in bending vibration	Energy stored in longitudinal extension $\frac{1}{8}EA\int_0^L \left(\frac{\partial u}{\partial x}\right)^4 dx$	$\int_{0}^{2} \int J_{0} \left(\frac{\partial t}{\partial t} \right)^{-\frac{1}{2}}$
Rod of length L in longitudinal vibration	$\frac{1}{2}EA\int_0^L \left(\frac{\partial u}{\partial x}\right)^2 \mathrm{d}x$	
Rod of length L in torsional vibration	$\frac{1}{2}GI_p \int_0^L \left(\frac{\partial u}{\partial x}\right)^2 \mathrm{d}x$	$\frac{1}{2}I_p\rho\int_0^L\left(\frac{\partial u}{\partial t}\right)^2\mathrm{d}x$
Rectangular plate of size <i>S</i> in bending vibration	$\frac{D_P}{2} \iint_{S} \left\{ \left(\frac{\partial^2 u}{\partial x^2} + \frac{\partial^2 u}{\partial y^2} \right)^2 + 2(1 - \nu) \left[\left(\frac{\partial^2 u}{\partial x \partial y} \right)^2 - \frac{\partial^2 u}{\partial x^2} \frac{\partial^2 u}{\partial y^2} \right] \right\} dxdy$	$\frac{1}{2}\rho h \iint\limits_{S} \left(\frac{\partial u}{\partial t}\right)^2 \mathrm{d}x \mathrm{d}y$
Circular plate of radius <i>R</i> in center symmetrical bending vibration	$\pi D_P \int_0^R \left\{ \left(\frac{\partial^2 u}{\partial r^2} + \frac{1}{r} \frac{\partial u}{\partial r} \right)^2 -2(1-v) \frac{\partial^2 u}{\partial r^2} \frac{1}{r} \frac{\partial u}{\partial r} \right\} r dr$	$\pi \rho h \int_0^R r \left(\frac{\partial u}{\partial t}\right)^2 \mathrm{d}r$
Rectangular membrane of size <i>S</i> in bending vibration	$\frac{1}{2}\sigma h \iint_{S} \left\{ \left(\frac{\partial u}{\partial x} \right)^{2} + \left(\frac{\partial u}{\partial y} \right)^{2} \right\} dxdy$	$\frac{1}{2}\rho h \iint_{S} \left(\frac{\partial u}{\partial t}\right)^{2} dxdy$
Circular membrane of radius <i>R</i> in bending vibration	$\sigma h\pi \int_0^R \left(\frac{\partial u}{\partial r}\right)^2 r \mathrm{d}r$	$\pi \rho h \int_0^R r \left(\frac{\partial u}{\partial t}\right)^2 \mathrm{d}r$

function of the respective static deflection of the structure of interest due to a uniform load. An assumed approximate mode shape is always stiffer than the correct function and the resulting eigenfrequency obtained by Rayleigh's method is always slightly higher than the exact eigenfrequency.

Rayleigh's method gives a decent approximation for the fundamental eigenfrequency. But in order to obtain more accurate solutions, also of higher modes, Rayleigh's method is often combined with *Ritz's method*. This method is a so-called *variational method* used to approximate various mechanical boundary value problems. The Ritz method is based on minimizing the total potential energy in a mechanical system. The minimum energy is found by varying free variables of a test solution that obeys all boundary conditions. The combined method to approximate the eigenfrequencies of specific mechanical boundary value problems is often called the *Rayleigh–Ritz method*. According to the Ritz method, n free variables c_i are introduced to the spatial mode shape function U(x, y) [1]

$$U(x,y) = \sum_{i=1}^{n} c_i U_i(x,y).$$
 (1.7)

The set of variables c_i that minimize the total energy in the structure resulting in a minimum eigenfrequency can be found by minimizing the so-called *Rayleigh quotient* (1.6)

$$\frac{\partial}{\partial c_i}\omega^2 = \frac{\partial}{\partial c_i} \left\{ \frac{W_{\text{pot}}(U(x,y))}{W_{\text{kin}}(U(x,y))} \right\} = 0 \quad (i = 1, 2, 3, \dots, n)$$
 (1.8)

which by applying the quotient derivation rule and with (1.6) becomes

$$\frac{\partial}{\partial c_i} \{ W_{\text{pot}}(U(x, y)) - \omega^2 W_{\text{kin}}(U(x, y)) \} = 0 \quad (i = 1, 2, 3, \dots, n).$$
 (1.9)

Substituting (1.7) into (1.9) yields a homogeneous linear system of equations of n variables, which can be written as

$$\mathbf{M}_n(\omega)\mathbf{c}_i = 0 \tag{1.10}$$

with the square matrix $\mathbf{M}_n(\omega)$ of order n multiplied by the c_i values of the vector \mathbf{c}_i . In order to get the non-trivial solution, the determinant of this system has to be equal to zero

$$\det(\mathbf{M}_n(\omega)) = 0. \tag{1.11}$$

This results in the *frequency* or *characteristic equation* yielding the corresponding n eigenfrequencies ω_i . It is clear from (1.9) that the Rayleigh–Ritz method for n = 1 reduces to the Rayleigh method (1.6).

In this chapter, the eigenfrequencies of a few exemplary structures, such as beams, strings, and rectangular membranes are derived exactly. For all other structures, the fundamental eigenfrequency is approximated by Rayleigh's method, yielding the basic terms of the particular eigenfrequencies. Approximations for the higher modes, which typically were derived by the Rayleigh–Ritz method, are taken from mechanics textbooks.

1.1.1 One-Dimensional Bending Vibrations

One-dimensional bending vibrations of beams and strings are among the most common nanomechanical structures. By some definitions, they are the only actual nanomechanical resonators with at least 2 dimension below the size of 1 μ m. A few typical examples are shown in Fig. 1.1.

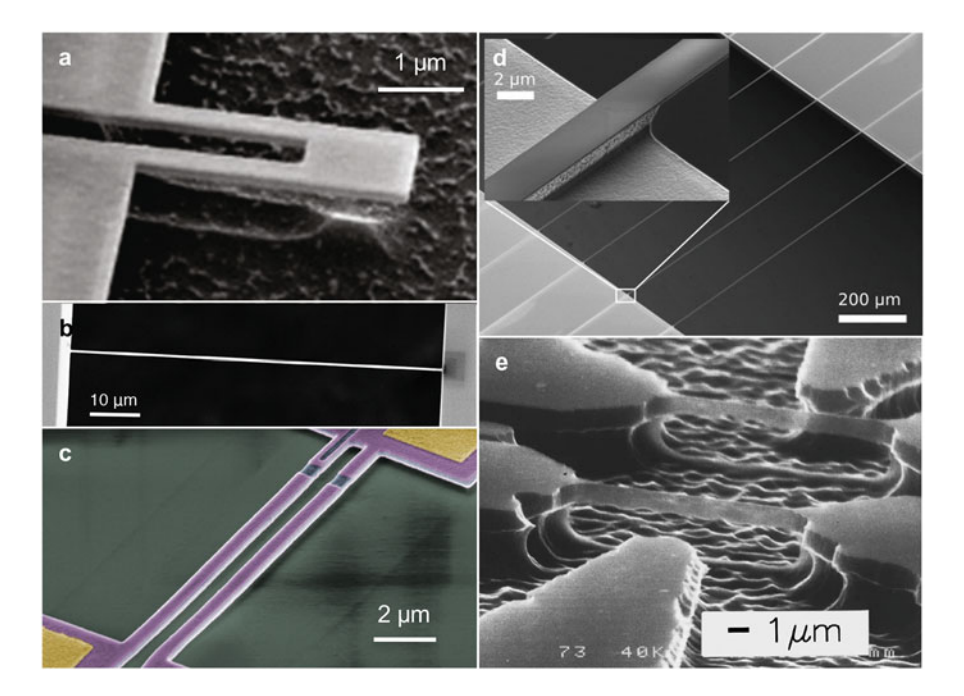


Fig. 1.1 Examples of flexural one-dimensional nanomechanical resonators. (a) Silicon nitride nanocantilever for gravimetric gas chromatography. (Reprinted with permission from [5]. Copyright 2010 American Chemical Society.) (b) Silicon nitride nanostring for airborne nanoparticle detection [6]. (c) Aluminium nitride beam resonators. (d) High-Q silicon nitride string resonators. (Reprinted with permission from [S. Schmid, K.D. Jensen, K.H. Nielsen, A. Boisen, Damping mechanisms in high-Q micro and nanomechanical string resonators. Phys. Rev. B 84(16), 165307 (2011)]. Copyright 2011 by the American Physical Society.) (e) Silicon nanobridges. (Reprinted from [10], with permission from AIP Publishing)

1.1.1.1 Free Bending Vibration of Beams

The eigenmode problem of bending beams is one of the prominent cases that can be solved exactly. The model is based on the beam bending theory finalized in the eighteenth century by the Swiss mathematicians Leonard Euler and Daniel Bernoulli, hence the name *Euler–Bernoulli beam theory*. The bending behavior of beams can be modelled under the of assumptions that the beam is slender (L/h > 10) (see Fig. 1.2), and that the rotational inertia and the shear deformation can be neglected. The equation of motion of a thin beam can be derived by means of the equilibrium of forces for an infinitesimal piece of beam. Assuming a linear elastic material and small deflections u(x, t), the equation of motion of a thin beam (Euler–Bernoulli beam) is given by [12, 13]

$$\rho A \frac{\partial^2 u(x,t)}{\partial t^2} + E I_y \frac{\partial^4 u(x,t)}{\partial x^4} = 0, \tag{1.12}$$

where ρ is the mass density, A is the cross sectional area, E is the Young's modulus, and I_y is the geometric moment of inertia. The solution to this differential equation is a superposition of normal modes that can be separated into a position dependent and a time-dependent term via a separation of variables [14]

$$u(x,t) = \sum_{n=1}^{\infty} U_n(x) \cos(\omega t), \qquad (1.13)$$

where ω is the frequency of motion and n denotes the modal number. A general solutions to the displacement function of the beam $U_n(x)$ can be written in the form

$$U_n(x) = a_n \cos \beta_n x + b_n \sin \beta_n x + c_n \cosh \beta_n x + d_n \sinh \beta_n x \tag{1.14}$$

with the *wavenumber* β_n . The first two terms with the trigonometric functions represent the standing waves in the beam center, while the last two hyperbolic terms represent the influence of the clamping. From this equation it is clear that a beam will vibrate in certain vibrational modes each with a distinct spatial shape.

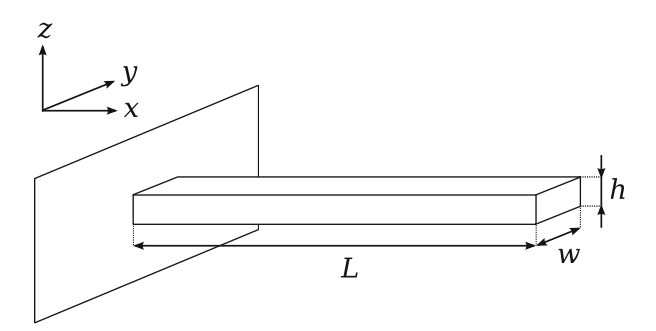


Fig. 1.2 Schematic drawing of a single-clamped beam

By insertion of Eq. (1.14) into (1.12), the differential equation can be rewritten as

$$-\rho A\omega^{2}u(x,t) + EI_{\nu}\beta_{n}^{4}u(x,t) = 0$$
 (1.15)

which results in the dispersion relationship which yields the eigenfrequency Ω as a function of the wavenumber

$$\Omega = \omega = \beta_n^2 \sqrt{\frac{EI_y}{\rho A}}.$$
 (1.16)

The dispersion relationship can be written as

$$\Omega = \beta_n^2 c_E \sqrt{\frac{I_y}{A}}.$$
 (1.17)

with the wavevelocity c_E in the elastic beam

$$c_E = \sqrt{\frac{E}{\rho}}. (1.18)$$

Assuming a rectangular cross section with beam thickness h the geometric moment of inertia is given by $I_y = \frac{Ah^2}{12}$. By defining a flexural rigidity of a square beam

$$D_E = \frac{Eh^3}{12} \tag{1.19}$$

the eigenfrequency of a beam can be written as

$$\Omega = \beta_n^2 \sqrt{\frac{D_E}{\rho h}}.$$
 (1.20)

The Euler–Bernoulli beam theory assumes a thin and long beam. If the beam width to height ratio becomes larger w/h > 5, the flexural rigidity of a Euler–Bernoulli beam has to be replaced by the flexural rigidity of a plate

$$D_P = \frac{Eh^3}{12(1-\nu^2)} \tag{1.21}$$

where ν is the Poisson's ratio to account for the suppression of the in-plane dilatation accompanying axial strain which makes a plate stiffer than a beam [1, 3].

In the next step, the wavenumber of specific eigenmodes of a beam is derived. This is done by finding the unknown coefficients a_n, b_n, c_n, d_n in (1.14) by means of the specific boundary conditions of the beam. We take into account two specific

cases: (1) singly clamped beams, also called cantilevers, and (2) doubly clamped beams, also called bridges.

Cantilevers

Cantilevers are fixed at one end, while the free end is curvature free and does not experience a momentum. The boundary conditions of a cantilever are hence described by

$$U_n(0) = \frac{\partial}{\partial x} U_n(0) = \frac{\partial^2}{\partial x^2} U_n(L) = \frac{\partial^3}{\partial x^3} U_n(L) = 0.$$
 (1.22)

These fourth boundary conditions create a system of linear equations of fourth order, which can be written as

$$\begin{bmatrix} 1 & 0 & 1 & 0 \\ 0 & 1 & 0 & 1 \\ -\cos(\beta_n L) - \sin(\beta_n L) & \cosh(\beta_n L) & \sinh(\beta_n L) \\ \sin(\beta_n L) & -\cos(\beta_n L) & \sinh(\beta_n L) & \cosh(\beta_n L) \end{bmatrix} \begin{pmatrix} a \\ b \\ c \\ d \end{pmatrix} = \begin{cases} 0 \\ 0 \\ 0 \\ 0 \end{cases}.$$
(1.23)

A non-trivial solution exists for this homogeneous system if the determinant is zero, that is

$$\cos(\beta_n L)\cosh(\beta_n L) + 1 = 0 \tag{1.24}$$

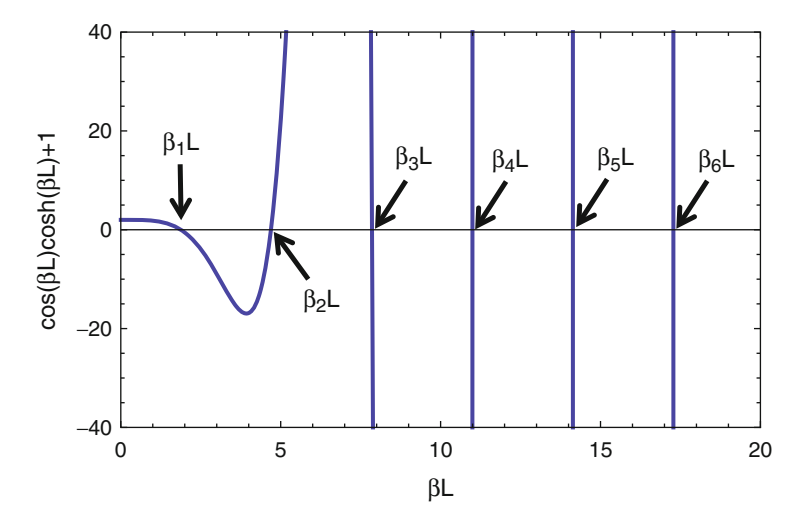


Fig. 1.3 Depiction of the roots of the frequency equation (1.24) for a cantilever

which is the frequency equation. The equation is plotted in Fig. 1.3. From this equation has discrete solutions for specific wavenumbers β_n , which correspond to the specific eigenfrequencies of the cantilever. This transcendent equation can be solved numerically for the lower order modes. The cosine is a periodic function while the hyperbolic cosine is exponentially increasing with increasing $\beta_n L$. The number of roots of (1.24) are hence corresponding to the number of periods of $\cos(\beta_n L)$. For higher eigenvalues (1.24) simplifies to

$$\cos(\beta_n L) \approx 0 \quad \forall \quad n > 3 \tag{1.25}$$

and $\beta_n L \approx (2n-1)\pi/2$. In conclusion, the roots of the frequency equation of a cantilever beam are

$$\lambda_n = \beta_n L = 1.8751, 4.6941, 7.8548, (2n-1)\pi/2.$$
 (1.26)

We can now write the eigenfrequency of a cantilever as

$$\Omega_n = \frac{\lambda_n^2}{L^2} \sqrt{\frac{EI_y}{\rho A}}.$$
(1.27)

The mode shape function $U_n(x)$ of a cantilever can be obtained from the boundary conditions (1.22). From the first two boundary conditions we obtain

$$U_n(0) = 0: a_n + c_n = 0$$
 (1.28)

$$\frac{\partial U_n(0)}{\partial x} = 0: \ b_n + d_n = 0 \tag{1.29}$$

and (1.14) reduces to

$$U_n(x) = a_n(\cos \beta_n x - \cosh \beta_n x) + b_n(\sin \beta_n x - \sinh \beta_n x). \tag{1.30}$$

With the third boundary condition we obtain the ratio of the coefficients a_n and b_n

$$\frac{\partial^2}{\partial x^2} U_n(L) = 0: \frac{b_n}{a_n} = -\frac{\cos(\beta_n L) + \cosh(\beta_n L)}{\sin(\beta_n L) + \sinh(\beta_n L)}$$
(1.31)

and (1.14) becomes

$$U_n(x) = a_n \left[\cos \beta_n x - \cosh \beta_n x - \frac{\cos(\beta_n L) + \cosh(\beta_n L)}{\sin(\beta_n L) + \sinh(\beta_n L)} (\sin \beta_n x - \sinh \beta_n x) \right].$$
(1.32)

The first four mode shapes of a cantilever are shown in Fig. 1.4. It can be seen from the figure that certain areas of the cantilever have a large vibrational amplitude whereas other areas (near the nodal points) are moving with low amplitude. The number of nodal points increases with increasing mode number.

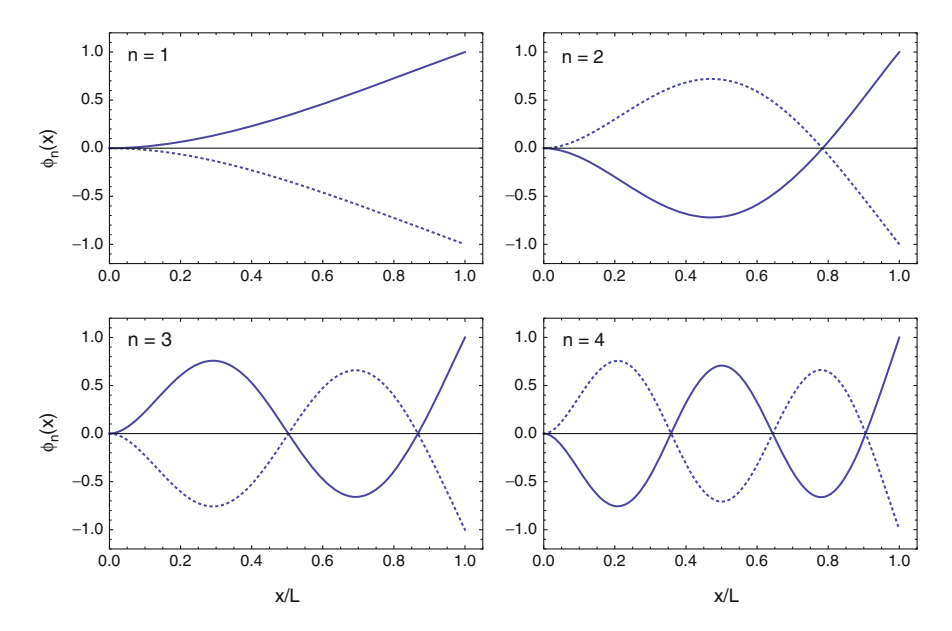


Fig. 1.4 Schematics of the first four bending modes (a)–(d) of a cantilever seen from the side. The amplitude is in units of A_n and the position is in units of the length L, where 0 indicates the base of the cantilever [15]

Typically, the mode shape function is used in a normalized form $\phi_n(x)$ with $\phi_n(L) = 1$. In a normalized form, (1.32) becomes

$$U_n(x) = U_{0n} \phi_n(x) \tag{1.33}$$

where

$$\phi_n(x) = \frac{1}{2} \left[\cos \beta_n x - \cosh \beta_n x - \frac{\cos(\beta_n L) + \cosh(\beta_n L)}{\sin(\beta_n L) + \sinh(\beta_n L)} (\sin \beta_n x - \sinh \beta_n x) \right]. \tag{1.34}$$

Bridges

Bridges are fixed at both ends, and the boundary conditions are hence described by

$$U_n(0) = U_n(L) = \frac{\partial}{\partial x} U_n(0) = \frac{\partial}{\partial x} U_n(L) = 0.$$
 (1.35)

These four boundary conditions create a system of equations of fourth order, which can be written as

$$\begin{bmatrix} 1 & 0 & 1 & 0 \\ 0 & 1 & 0 & 1 \\ \sin(\beta_n L) - \cos(\beta_n L) & \sinh(\beta_n L) & \cosh(\beta_n L) \\ \cos(\beta_n L) + \sin(\beta_n L) & \cosh(\beta_n L) & \sinh(\beta_n L) \end{bmatrix} \begin{bmatrix} a \\ b \\ c \\ d \end{bmatrix} = \begin{bmatrix} 0 \\ 0 \\ 0 \\ 0 \end{bmatrix}.$$
 (1.36)

Setting the determinant zero, we obtain the frequency equation

$$\cos(\beta_n L)\cosh(\beta_n L) - 1 = 0 \tag{1.37}$$

with the solutions for n = 1, 2, 3, n > 3 are $\lambda_n = \beta_n L = 4.7300, 7.8532, 10.9956, (2n+1)\pi/2$, respectively. The frequency equation for a bridge is plotted in Fig. 1.5.

The mode shape function of a bridge can be obtained from the boundary conditions (1.35). From the first two boundary conditions we obtain, equal to the case of cantilevers

$$U_n(0) = 0: a + c = 0 (1.38)$$

$$\frac{\partial U_n(0)}{\partial x} = 0: \ b + d = 0 \tag{1.39}$$

and (1.14) reduces to

$$U_n(x) = a_n(\cos \beta_n x - \cosh \beta_n x) + b(\sin \beta_n x - \sinh \beta_n x). \tag{1.40}$$

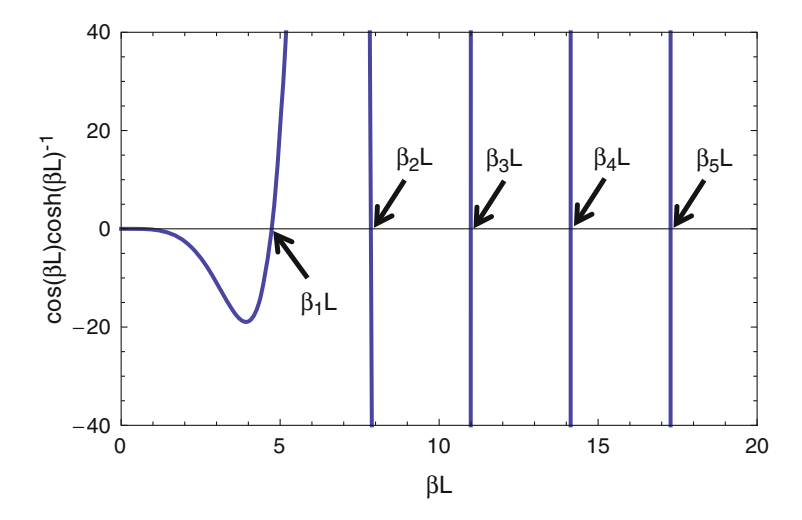


Fig. 1.5 Plot of the roots of the frequency equation (1.37) for a bridge

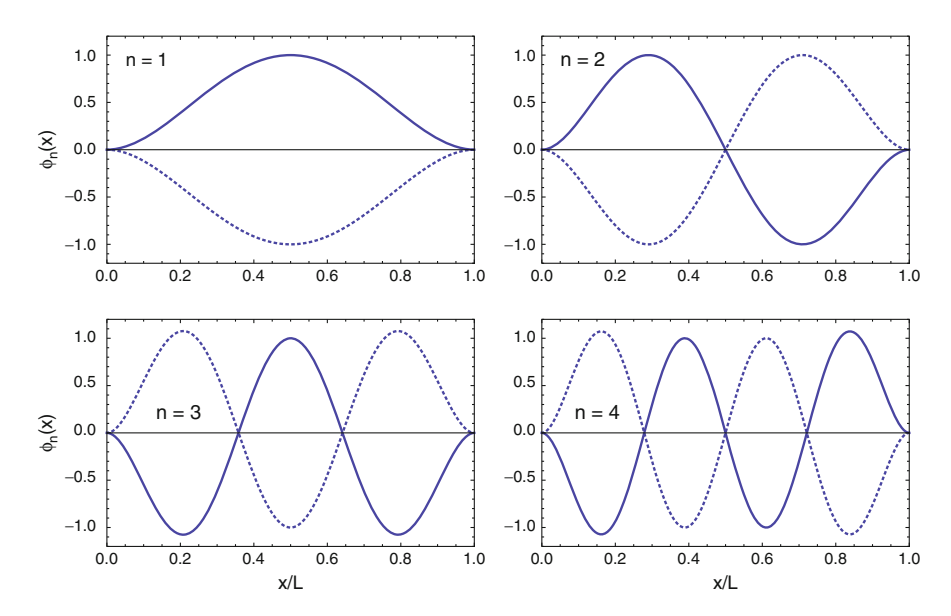


Fig. 1.6 Schematics of the first four bending modes (a)–(d) of a cantilever seen from the side. The amplitude is in units of a_n and the position is in units of the length L, where 0 indicates the base of the cantilever [15]

With the third boundary condition we obtain the ratio of the coefficients a_n and b_n

$$\frac{\partial^2}{\partial x^2} U_n(L) = 0: \frac{b_n}{a_n} = -\frac{\cos(\beta_n L) - \cosh(\beta_n L)}{\sin(\beta_n L) - \sinh(\beta_n L)}$$
(1.41)

and (1.14) becomes

$$U_n(x) = a_n \left[\cos \beta_n x - \cosh \beta_n x - \frac{\cos(\beta_n L) - \cosh(\beta_n L)}{\sin(\beta_n L) - \sinh(\beta_n L)} (\sin \beta_n x - \sinh \beta_n x) \right].$$
(1.42)

The first four mode shapes of a cantilever are shown in Fig. 1.6.

The normalized mode shape function for the edge peak of a bridge $\phi_n(x)$ is approaching

$$\phi_n(x) = \frac{1}{\sqrt{2}} \left[\cos \beta_n x - \cosh \beta_n x - \frac{\cos(\beta_n L) - \cosh(\beta_n L)}{\sin(\beta_n L) - \sinh(\beta_n L)} (\sin \beta_n x - \sinh \beta_n x) \right]$$
(1.43)

for n > 3. For lower mode numbers n = 1, 2, 3, ..., the normalization factors are 0.6297, 0.6626, 0.7112, $\approx 1/\sqrt{2}$.

1.1.1.2 Free Bending Vibration of Beams Under Tensile Stress (Strings)

Thin films typically used in microfabrication tend to have a process related tensile stress. Doubly clamped beams made of such thin films are therefore usually prestressed. A tensile stress σ increases the eigenfrequency and has to be taken into account by adding a term for the tensile force $N = \sigma A$ to (1.12). Applying Newton's third law, the free and undamped bending vibration for small amplitudes can then be described by

$$\rho A \frac{\partial^2 u(x,t)}{\partial t^2} + E I_z \frac{\partial^4 u(x,t)}{\partial x^4} - N \frac{\partial^2 u(x,t)}{\partial x^2} = 0$$
 (1.44)

This equation of motion can be solved with the Ansatz (1.13) for the case of a simply supported doubly clamped beam with the boundary conditions

$$U_n(0) = U_n(L) = \frac{\partial^2}{\partial x^2} U_n(0) = \frac{\partial^2}{\partial x^2} U_n(L) = 0$$
 (1.45)

assuming a sinusoidal mode shape with wavenumber β_n

$$U_n(x) = U_{0,n} \sin(\beta_n x).$$
 (1.46)

Substituting (1.46) in the general Ansatz (1.13), the equation of motion (1.44) readily yields the dispersion relationship which yields the eigenfrequency Ω_n as a function of β_n

$$\Omega_n = \omega = \sqrt{\frac{\sigma}{\rho}\beta_n^2 + \frac{EI_y}{\rho A}\beta_n^4}.$$
 (1.47)

This equation can be rearranged into the following form

$$\Omega_n = \beta_n^2 \sqrt{\frac{EI_y}{\rho A}} \sqrt{1 + \frac{\sigma A}{EI_y \beta_n^2}}.$$
 (1.48)

It shows that the eigenfrequency is basically the eigenfrequency of an unstressed beam (1.16) multiplied by a term which increases with stress. Choosing a wavenumber that satisfies the boundary conditions (1.45)

$$\beta_n = \frac{n\pi}{L},\tag{1.49}$$

two extreme conditions can be defined. On the one hand, if

$$\frac{\sigma A}{EI_v} \frac{L^2}{(n\pi)^2} \ll 1 \tag{1.50}$$

Eq. (1.48) reduces to (1.16) of an unstressed simply supported beam, as mentioned already. On the other hand, if

$$\frac{\sigma A}{EI_{\nu}} \frac{L^2}{(n\pi)^2} \gg 1 \tag{1.51}$$

the flexural rigidity can be neglected and (1.48) reduces to

$$\Omega_n = \frac{n\pi}{L} \sqrt{\frac{\sigma}{\rho}} \tag{1.52}$$

which is the eigenfrequency of a string, a pre-stressed thread-like elastic continuum without flexural rigidity. Compared to cantilevers or stress-free bridges, the resonance frequency of strings is not a function of the beam thickness. It is mainly defined by the length and the tensile stress. The eigenfrequency (1.52) can also be written in the following form

$$\Omega_n = \frac{n\pi}{L} c_{\sigma} \tag{1.53}$$

with the wave velocity inside a string of

$$c_{\sigma} = \sqrt{\frac{\sigma}{\rho}}. (1.54)$$

The derivations above were done for a simply supported beam. These are valid boundary conditions for an ideal string with zero flexural rigidity. But a real micro or nanomechanical string-like resonator typically is clamped at both ends and possesses a non-negligible rigidity. As long as the string condition (1.51) is fulfilled, the beam rigidity can be neglected for the calculation of the eigenfrequency (1.52). However, the finite string rigidity will influence the mode shape, particularly at the clamping sites. The full set of wavenumbers required to model a suitable mode shape function of a string, on the basis of (1.14), can be found by solving the dispersion relation of the pre-stressed beam (1.47)

$$\beta_n^4 + \frac{\sigma A}{EI_y} \beta_n^2 - \Omega^2 \frac{\rho A}{EI_y} = 0. \tag{1.55}$$

The four solutions of β_n are then

$$\beta_{n,1-4} = \pm \sqrt{\frac{1}{2} \frac{\sigma A}{EI_y}} \left[-1 \pm \sqrt{1 + 4\Omega^2 \frac{\rho}{\sigma} \frac{EI_y}{\sigma A}} \right]. \tag{1.56}$$

Inserting the string eigenfrequency (1.52) shows that the last term in (1.56), according to the string condition (1.51), is a lot smaller than unity. Hence, the inner square root can be approximated by a Taylor series and (1.56) becomes

$$\beta_{n,1-4} = \pm \sqrt{\frac{1}{2} \frac{\sigma A}{EI_y} \left[-1 \pm \left(1 + 2 \left(\frac{n\pi}{L} \right)^2 \frac{EI_y}{\sigma A} \right) \right]}.$$
 (1.57)

In this form, the two positive solutions are apparent, namely

$$\beta_{n,1} = \beta_{\sigma} = \frac{n\pi}{L},\tag{1.58}$$

which is the already known wavenumber of a perfect string, and

$$\beta_{n,2} = \beta_E = \sqrt{\frac{\sigma A}{EI_y}} \tag{1.59}$$

which is the wave number related to the flexural stiffness of the string.

The mode shape of a "realistic" string resonator can now be approximated by using the string wavenumber β_{σ} for the trigonometric terms in (1.14) which represent the standing waves in the string. For the hyperbolic terms, representing the clamping conditions, the wavenumber β_E from the flexural stiffness of the string is used instead

$$U_n(x) = a_n \cos \beta_{\sigma} x + b_n \sin \beta_{\sigma} x + c_n \cosh \beta_{E} x + d_n \sinh \beta_{E} x. \tag{1.60}$$

The first two boundary conditions for a doubly clamped beam (1.35) yield a simplified mode shape

$$U_n(x) = a_n \left(\cos \beta_{\sigma} x - \cosh \beta_E x\right) + b_n \left(\sin \beta_{\sigma} x + \frac{\beta_{\sigma}}{\beta_E} \sinh \beta_E x\right). \tag{1.61}$$

The last two conditions result in $a_n \approx -\frac{\beta_\sigma}{\beta_E} b_n$ under the valid string assumption of $\beta_E \gg 1$ and the mode shape function can be expressed as

$$U_n(x) = \begin{cases} \phi_n(x) & ,0 \le x \le L/2\\ (-1)^{n+1}\phi_n(L-x) & ,L/2 < x \le L \end{cases}$$
 (1.62)

with

$$\phi_n(x) = \left(\sin(\beta_{\sigma}x) - \frac{\beta_{\sigma}}{\beta_E} \left[\cos(\beta_{\sigma}x) - \cosh(\beta_E x) + \sinh(\beta_E x)\right]\right),\tag{1.63}$$

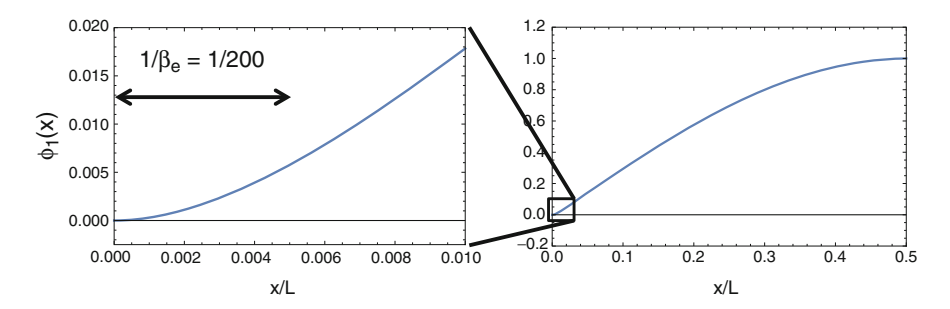


Fig. 1.7 String modeshape (1.64) for $\beta_E = 200$

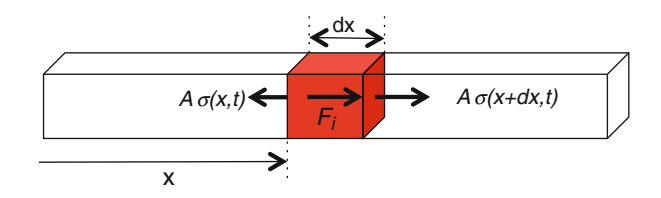


Fig. 1.8 Schematics of a thin beam under longitudinal vibration

which can be further simplified with the algebraic expressions $\sinh x = (e^x - e^{-x})/2$ and $\cosh x = (e^x + e^{-x})/2$ to the following form

$$\phi_n(x) = \left(\sin(\beta_{\sigma}x) - \frac{\beta_{\sigma}}{\beta_F} \left[\cos(\beta_{\sigma}x) - e^{-\beta_E x}\right]\right). \tag{1.64}$$

This equation shows that β_E represents the inverse of the exponential edge-correction decay length which results from the flexural rigidity of the string. The string modeshape (1.64) and the edge effect resulting from the flexural rigidity of the string is visualized in Fig. 1.7.

1.1.2 One-Dimensional Bulk Vibrations

Nanomechanical one-dimensional bulk resonators are rarer than flexural resonators, as it can be challenging to detect the small vibrational amplitudes. On the other hand, such bulk mode resonators have become the facilitating device in recent breakthrough experiments in quantum optomechanics due to their high resonance frequencies in the GHz-regime [16, 17].

In this subsection we consider longitudinal waves in a thin beam which produces the axial displacement u(x, t). Figure 1.8 shows a schematic of a thin cross section piece of a thin beam. According to Newton's third law, all forces acting on the small beam piece have to equalize. The acting force are, on the one hand, the inertial force

 F_i and, on the other hand, the forces exerted from the neighbor piece. Assuming a thin beam with cross section area A with an even axial stress distribution $\sigma(x, t)$, the force equation can be written as

$$F_i = \rho A \frac{\partial^2 u(x,t)}{\partial t^2} dx = A[\sigma(x+dx,t) - \sigma(x,t)],$$
 (1.65)

with the mass density ρ . For a short piece, the term in the square brackets can be approximated by

$$\sigma(x + dx, t) - \sigma(x, t) \approx \frac{\partial \sigma}{\partial x} dx$$
 (1.66)

and (1.65) simplifies to

$$\rho \frac{\partial^2 u(x,t)}{\partial t^2} = \frac{\partial \sigma}{\partial x}.$$
 (1.67)

Applying Hook's law of elasticity, we can express the axial stress as a function of the axial deformation

$$\sigma(x,t) = E\varepsilon(x,t) = E\frac{\partial u(x,t)}{\partial x}$$
 (1.68)

and (1.67) turns into the one-dimensional wave equation

$$\frac{\partial^2 u(x,t)}{\partial t^2} = c_E^2 \frac{\partial^2 u(x,t)}{\partial x^2} \tag{1.69}$$

with the wave velocity inside the material of

$$c_E = \sqrt{\frac{E}{\rho}}. (1.70)$$

This one-dimensional wave equation is also obtained in the case of the string resonator, as discussed in the previous Sect. 1.1.1.2, when dismissing the flexural rigidity in the respective equation of motion (1.44), with the appropriate wave velocity for a string (1.54).

The one-dimensional wave equation (1.69) can readily be solved with the common Ansatz of separating the spatial and temporal variables, which for a individual normal mode writes

$$u(x,t) = U_n(x)\cos(\omega t) = U_{0,n}\phi_n(x)\cos(\omega t)$$
 (1.71)

which yields the ordinary differential equation

$$\frac{\partial^2 \phi_n}{\partial x^2} + \beta_n^2 \phi = 0 \tag{1.72}$$

with the dispersion relationship

$$\beta_n = \frac{\omega}{c_F}.\tag{1.73}$$

The resulting differential equation (1.72) can now be solved for specific boundary conditions with the general solution

$$\phi_n(x) = a\sin(\beta_n x) + b\cos(\beta_n x). \tag{1.74}$$

In the case of both ends free condition, the stress is disappearing at the beam ends which can be expressed by

$$\frac{\partial \phi_n(0)}{\partial x} = \frac{\partial \phi_n(L)}{\partial x} = 0. \tag{1.75}$$

When applying these boundary conditions to the ordinary differential equation (1.72) results in

$$a = 0 \& \sin(\beta L) = 0.$$
 (1.76)

The latter solution is true for all wave numbers $\beta_n = n\pi/L$ with the mode numbers $n = 1, 2, 3, \dots$ From (1.73), the eigenfrequencies can be calculated

$$\Omega_n = \omega = \frac{n\pi}{L} c_E. \tag{1.77}$$

The similarity with the eigenfrequency of a string (1.53) is now obvious. The string is fixed at both ends which results in a sinusoidal mode shape. The longitudinally vibration beam on the other hand is free at both ends and the mode shape is given by

$$U_n(x) = U_{0,n}\phi_n(x) = U_{0,n}\cos\left(\frac{n\pi}{L}x\right)$$
 (1.78)

and depicted in Fig. 1.9.

In the case of the boundary condition that one end is free, the stress is disappearing at the beam ends which can be expressed by

$$\frac{\partial U_n(0)}{\partial x} = U_n(L) = 0 \tag{1.79}$$

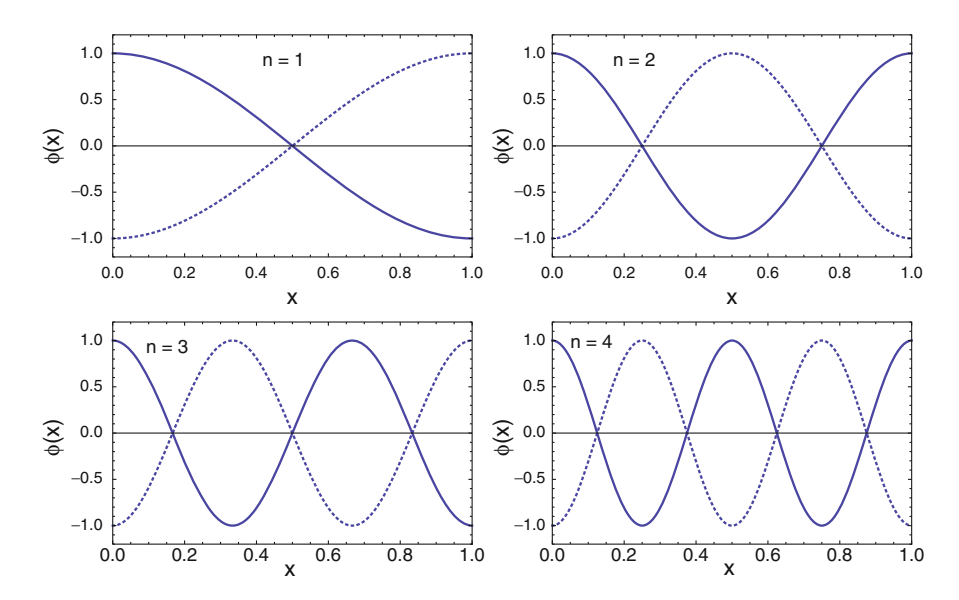


Fig. 1.9 Mode shapes $\phi_n(x)$ for a longitudinal vibration of a beam with length L=1 with two free ends

the eigenfrequency becomes

$$\Omega_n = \pi \frac{(2\pi - 1)}{2} \frac{c_E}{L}.$$
 (1.80)

1.1.3 Two-Dimensional Bending Vibrations

Two-dimensional bending resonators can be separated into *plates* and *membranes*, similar to the distinction between one-dimensional *beams* and *strings*, as introduced in Sect. 1.1.1 on page 6. The ideal case of a *plate* is reached if the mechanical behavior is dominated by the bending stiffness (flexural rigidity) of the structure. The other ideal case of a *membrane* occurs if there is a tensile stress inside the structure that is dominating its behavior, and the flexural rigidity does not have to be taken into account. They are interesting partly for two reasons. First, they can be fabricated from thin films with thicknesses reaching from a few tens of nanometers down to a few angstroms when, e.g., fabricated from single layers of graphene. Second, the large lateral dimensions allow for a strong optical or electrical interaction, which results in efficient transduction of the vibrational motion. The low mass combined with the strong external coupling is the reason that two-dimensional resonators have become key structures in many applications, most prominently in optomechanics. Typical examples of two-dimensional resonators are shown in Fig. 1.10.

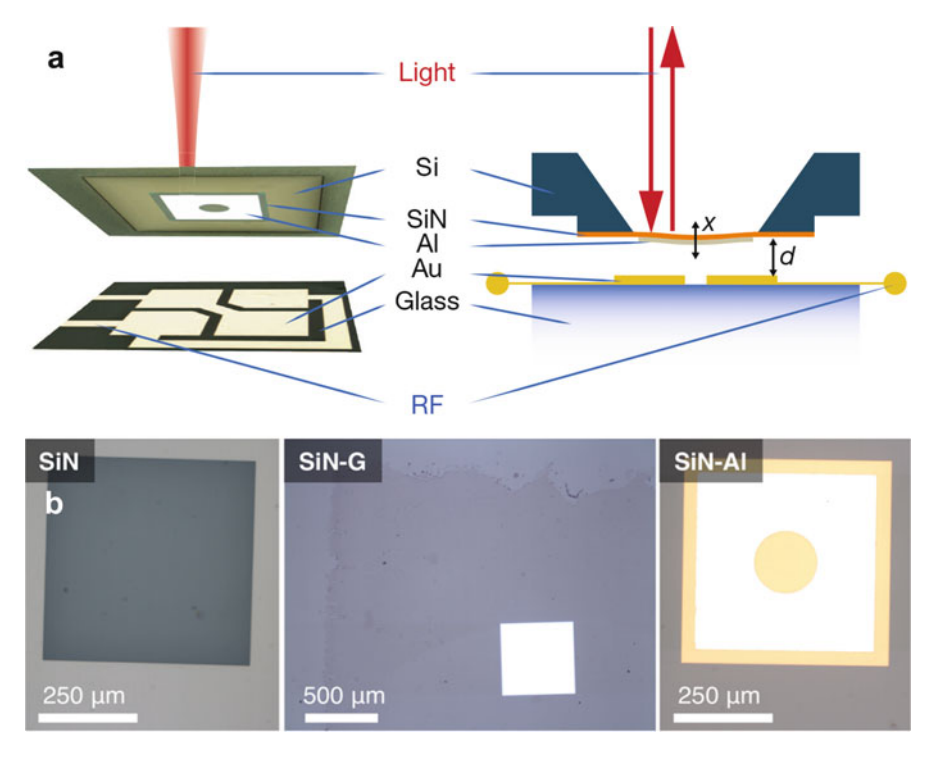


Fig. 1.10 Examples of two-dimensional flexural micromechanical resonators. (a) aluminium coated silicon nitride membrane resonator [12]. (b) SiN membranes coated with a single graphene layer (SiN-G) and aluminium (SiN-Al) for optoelectromechanical coupling. (Reprinted from [23], with permission from AIP Publishing)

All subsequently presented continuum mechanical models are based on the general assumptions of a perfectly elastic, homogeneous, and isotropic materials.

1.1.3.1 Free Bending Vibration of Plates

Rectangular Plates

The equation of motion of a *rectangular plate* with a flexural rigidity D_P [see Eq. (1.21) on page 8] is given by the two-dimensional wave equation [1, 24]

$$D_P \nabla^2 \nabla^2 u - \rho \frac{\partial^2 u}{\partial t^2} = 0 \tag{1.81}$$

which, however, can only be solved for the case that the plate is simply supported with the common Ansatz of separating the time and spatial variables

$$u(x, y, t) = U(x, y)\cos(\omega t)$$
 (1.82)

with a sinusoidal mode shape

$$U(x,y) = \sum_{n=0}^{\infty} \sum_{i=0}^{\infty} U_{0,nj} \sin\left(\frac{n\pi x}{L_x}\right) \sin\left(\frac{j\pi y}{L_y}\right)$$
(1.83)

where L_x and L_y are the side lengths in x and y direction. Inserting (1.82) into (1.81) yields the eigenfrequencies of a *simply supported* plate

$$\Omega_{n,j} = \pi^2 \sqrt{\frac{D_P}{\rho h}} \left(\frac{n^2}{L_x^2} + \frac{j^2}{L_y^2} \right)$$
 (1.84)

which in the case of a quadratic plate with $L_x = L_y = L$ reduces to

$$\Omega_{n,j} = \frac{\pi^2 (n^2 + j^2)}{L^2} \sqrt{\frac{D_P}{\rho h}}.$$
 (1.85)

As presented, the problem of simply supported plates is straightforward to solve. But simply supported plates are basically impossible to realize on the micro and nanoscale and the more likely boundary conditions are, e.g., all 4 edges clamped or free. The eigenmode problem of these boundary conditions is very hard to solve. For this case, *Rayleigh's method* is a useful tool to obtain a good approximation for the fundamental eigenfrequency. The maximal kinetic and potential energies of a plate are given by (from Table 1.1)

$$W_{\rm kin,max} = \frac{\omega^2}{2} \rho h \iint U^2 dx dy. \tag{1.86}$$

and

$$W_{\text{pot,max}} = \frac{1}{2} D_P \iint \left\{ (\nabla^2 U)^2 + 2(1 - \nu) \left[\left(\frac{\partial^2 U}{\partial x \partial y} \right)^2 - \frac{\partial^2 U}{\partial x^2} \frac{\partial^2 U}{\partial y^2} \right] \right\} dx dy.$$
(1.87)

For a rectangular plate the following displacement function describes the exact shape of the fundamental mode to a good approximation

$$U(x,y) = c(x^2 - (L_x/2)^2)^2(y^2 - (L_y/2)^2)^2$$
(1.88)

and it satisfies the clamped boundary conditions

$$\frac{\partial U}{\partial x} = 0 \bigg|_{x = \pm L_y/2} \& \frac{\partial U}{\partial y} = 0 \bigg|_{y = \pm L_y/2}.$$
 (1.89)

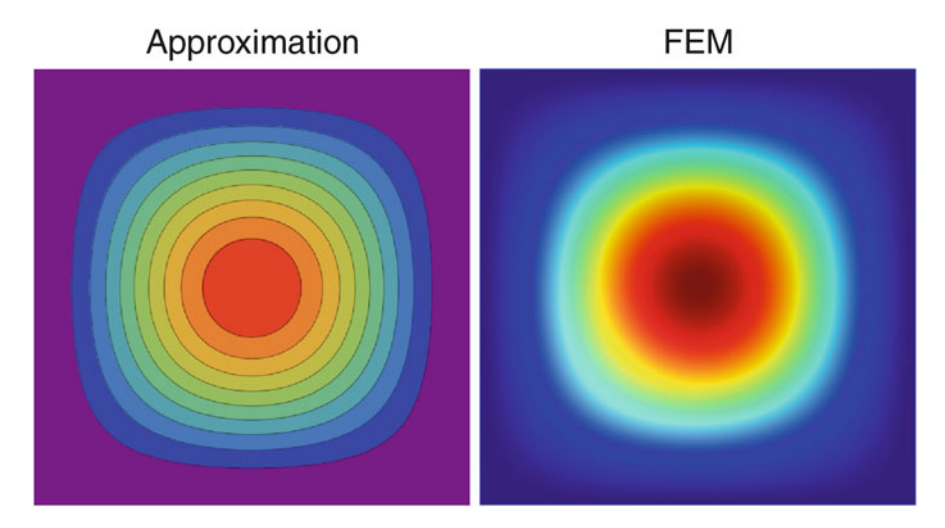


Fig. 1.11 Comparison of the plate displacement assumed for the analytical approximation and the actual displacement calculated by FEM

A comparison of this displacement function to the actual mode shape simulated by FEM is shown in Fig. 1.11. Inserting the mode shape Ansatz (1.88) into Rayleigh's equation (1.6) results in the approximate eigenfrequency solution for the fundamental mode of a *clamped plate*

$$\Omega_{1,1} = 6\sqrt{2}\sqrt{\frac{7L_x^4 + 4L_x^2L_y^2 + 7L_y^4}{L_x^4L_y^4}}\sqrt{\frac{D_P}{\rho h}}$$
(1.90)

which for a square plate $(L_x = L_y = L)$ simplifies to

$$\Omega_{1,1} = \frac{36}{L^2} \sqrt{\frac{D_P}{\rho h}}.$$
 (1.91)

This approximate result obtained via Rayleigh's method has an error smaller than $0.1\,\%$ compared to the result obtained via FEM.

The approximate solution for the fundamental eigenfrequency (1.92) is qualitatively correct. Hence, the general eigenfrequency of a bending plate can be written as

$$\Omega_{n,j} = \alpha_{n,j} \frac{1}{L^2} \sqrt{\frac{D_P}{\rho h}}.$$
(1.92)

Circular Plates

The fundamental eigenfrequency of a circular plate can readily be approximated by means of the Rayleigh method. From Table 1.1 the maximum potential and kinetic energies are given by

$$W_{\text{Pot,max}} = \pi D_P \int_0^R \left\{ \left(\frac{\partial^2 U(r)}{\partial r^2} + \frac{1}{r} \frac{\partial U(r)}{\partial r} \right)^2 - 2(1 - \nu) \frac{\partial^2 U(r)}{\partial r^2} \frac{1}{r} \frac{\partial U(r)}{\partial r} \right\} r dr$$
(1.93)

and

$$W_{\text{Kin,max}} = \pi \rho h \int_0^R (U(r))^2 r dr. \tag{1.94}$$

The approximate mode shape function for a circular plate with clamped boundaries can be approximated by [3]

$$U(r) = c \left(1 - \left(\frac{r}{R}\right)^2\right)^2 \tag{1.95}$$

Substituting the mode shape (1.95) in (1.93) and (1.94) results in $W_{\text{Pot,max}} \approx 32\pi D_p/(3R^2)$ and $W_{\text{Kin,max}} \approx \pi h R^2 \rho/10$, and the eigenfrequency can be calculated with (1.6), which yields the approximation

$$\Omega_{1.0} \approx 10.33 \frac{1}{R^2} \sqrt{\frac{D_P}{h\rho}}.$$
(1.96)

This approximation of the fundamental eigenfrequency of a circular plate clamped at the boundary shows how to express the eigenfrequency equation more generically

$$\Omega_{n,j} = \alpha_{n,j} \frac{1}{R^2} \sqrt{\frac{D_P}{h\rho}} \tag{1.97}$$

with the exact corresponding $\alpha_{n,j}$ values, derived via the *Rayleigh–Ritz method*, listed in Fig. 1.12.

Fig. 1.12 Mode shapes of a circular plate clamped at the boundary. *n* represents the circular modes and *j* the nodal diameters

Mode (n,j) (1,0) (1,1) (1,2) (2,0) (3,0)
$$\mathbf{a}_{n,j}$$
 10.21 21.22 34.84 39.78 88.90

Table 1.2 Eigenfrequency constants $\alpha_{0,j}$ for a circular plate fixed in the center for concentric modes [3]

n	j = 0	j = 1	j = 2	j = 3
1	3.75	20.91	60.68	119.7

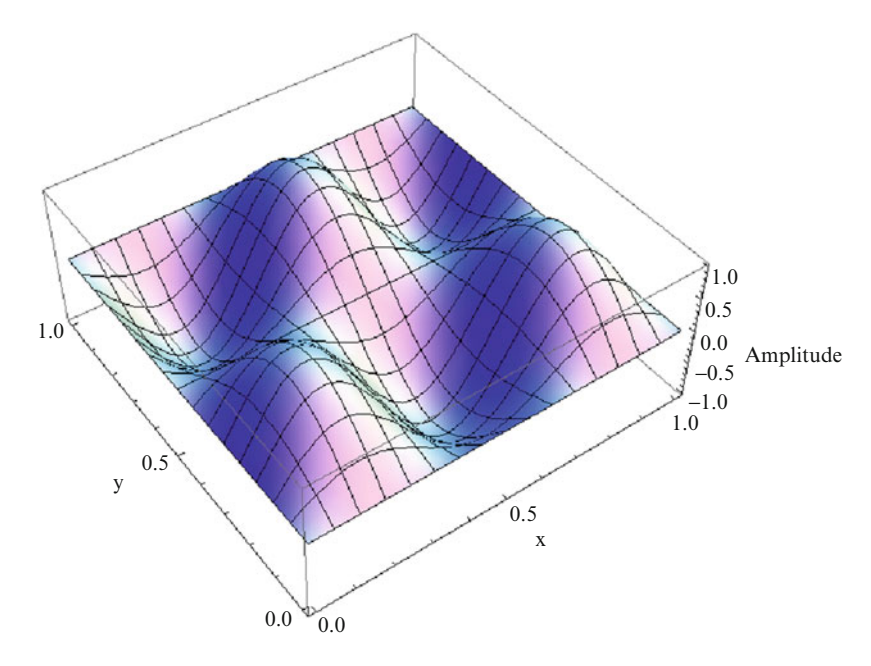


Fig. 1.13 Mode shape of a quadratic membrane for n = 2 and j = 3

A specific boundary condition typical for circular plates is the *fixed in the center* design. Corresponding $\alpha_{n,j}$ values are given in Table 1.2.

1.1.3.2 Free Bending Vibration of Plates Under Tensile Stress (Membranes)

Rectangular Membranes

The equation of motion of a *rectangular membrane* is given by the two-dimensional wave equation [24]

$$\sigma \nabla^2 u - \rho \frac{\partial^2 u}{\partial t^2} = 0 \tag{1.98}$$

and can be solved with the same Ansatz (1.82) used for plates in Sect. 1.1.3.1 on page 21 of separating the variables (Fig. 1.13).

With (1.83), Eq. (1.98) can be solved and the eigenfrequencies of a membrane becomes

$$\Omega_{n,j} = \sqrt{\frac{\sigma}{\rho}} \sqrt{\frac{n^2 \pi^2}{L_x^2} + \frac{j^2 \pi^2}{L_y^2}}$$
 (1.99)

which in the case of a quadratic membranes with $L_x = L_y = L$ reduces to

$$\Omega_{n,j} = \pi \sqrt{n^2 + j^2} \frac{1}{L} \sqrt{\frac{\sigma}{\rho}} = \pi \sqrt{n^2 + j^2} \frac{1}{L} c_{\sigma}. \tag{1.100}$$

It can be seen that the one-dimensional form of (1.100) results in the eigenfrequency of a string (1.52).

Circular Membranes

The eigenfrequency of a *circular membrane* can be readily approximated with the *Rayleigh method*, as introduced in the previous Sect. 1.1.3.1. The mode shapes of a circular membrane is best described in circular coordinates. The fundamental mode with a vibrational amplitude c in the membrane center can then be approximated by [3]

$$U(r) = c\cos\frac{\pi r}{2R} \tag{1.101}$$

with the radial coordinate r and the membrane radius R. The maximal kinetic and potential energies are given by

$$W_{\text{Kin,max}} = \frac{1}{2}\omega^2 \rho \int_0^R U(r)^2 2\pi r dr$$
 (1.102)

and

$$W_{\text{Pot,max}} = \frac{1}{2}\sigma \int_0^R \left(\frac{\partial U(r)}{r}\right)^2 2\pi r dr, \qquad (1.103)$$

respectively. An approximation for the eigenfrequency of the fundamental mode of a circular membrane can now be calculated from the Rayleigh principle (1.1), which yields

$$\Omega_{1,1} \approx \frac{\pi}{2} \sqrt{\frac{\pi^2 + 4}{\pi^2 - 4}} \frac{1}{R} \sqrt{\frac{\sigma}{\rho}} = \frac{2.415}{R} \sqrt{\frac{\sigma}{\rho}}.$$
(1.104)

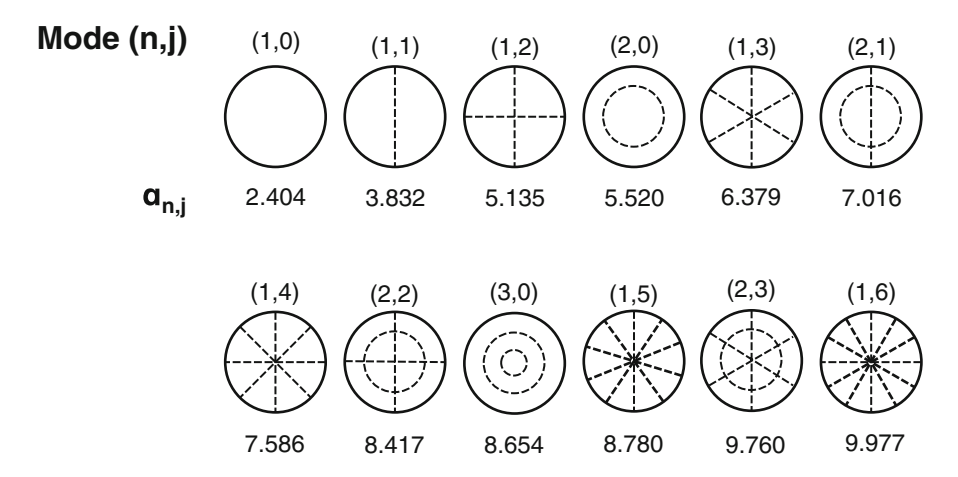


Fig. 1.14 Eigenmodes and respective $\alpha_{n,j}$ values of a circular membrane. The nodal lines (lines of zero vibration) are marked as *dashed lines*. n represents the straight nodal lines, and j concentric nodal circles

This approximation is close to the precise value of [3]

$$\frac{2.404}{R}\sqrt{\frac{\sigma}{\rho}}.\tag{1.105}$$

The term for the eigenfrequency obtained by Rayleigh's principle is qualitatively correct and the eigenfrequencies of circular membranes can generally be expressed as

$$\Omega_{n,j} = \frac{\alpha_{n,j}}{R} \sqrt{\frac{\sigma}{\rho}} = \alpha_{n,j} \frac{1}{R} c_{\sigma}$$
 (1.106)

where c_{σ} is the velocity of a bending wave on a membrane, as introduced for strings earlier in Sect. 1.1.1. Values of $\alpha_{n,j}$ for the first 12 modes are listed in Fig. 1.14.

1.1.4 Torsional Vibration of Thin Beams

Torsional vibrations of nanomechanical beams are a common resonator design. A few examples are shown in Fig. 1.15. The torsional vibration of a slender beam is very hard to electronically or optically transduce directly. Therefore, most torsional nanomechanical resonators feature a relatively large paddle, as can be seen from Fig. 1.15, which leverages the small torsional vibrations to amplitudes than can easily be actuated and detected. Typically in such torsional paddle resonators, the rotational inertia of the bars hinging the paddle can be neglected. Such resonators are best described as a lumped-element model, as discussed in Sect. 1.2.1.6 on page 40.

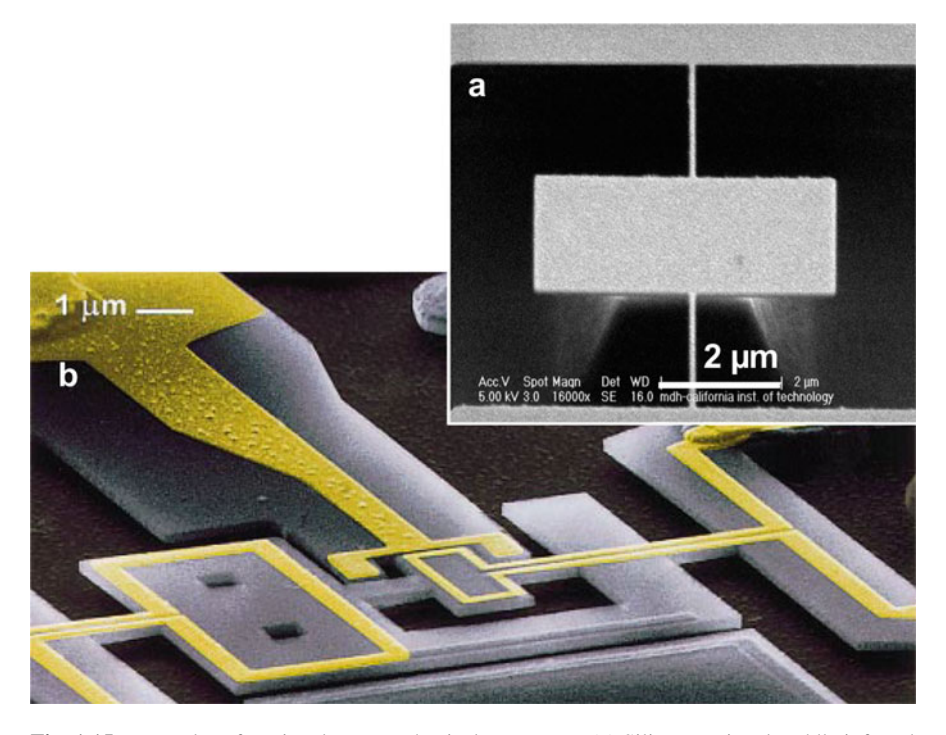


Fig. 1.15 Examples of torsional nanomechanical resonators. (a) Silicon torsional paddle infrared bolometer (Reprinted with permission from [26]. Copyright 2013, American Chemical Society.), (b) torsional nanoelectromechanical electrometer [27]

The rotational eigenfrequency of a slender bar can readily be calculated by Rayleigh's method (1.6), with the potential and kinetic energies from Table 1.1

$$W_{\text{pot,max}} = \frac{1}{2}GI_p \int_0^L \left(\frac{\partial U(x)}{\partial x}\right)^2 dx, \qquad (1.107)$$

and

$$W_{\text{kin,max}} = \frac{1}{2} I_p \rho \omega^2 \int_0^L (U(x))^2 dx.$$
 (1.108)

Assuming a sinusoidal modeshape for the case of rod clamped at both ends

$$U_n(x) = c \sin\left(\frac{n\pi}{L}x\right) \tag{1.109}$$

the eigenfrequency becomes

$$\Omega_n = \frac{n\pi}{L} \sqrt{\frac{G}{\rho}} = \frac{n\pi}{L} c_{\varphi} \tag{1.110}$$

with the shear wavevelocity

$$c_{\varphi} = \sqrt{\frac{G}{\rho}}. (1.111)$$

This eigenfrequency is apparently similar to the eigenfrequencies for strings (1.52) and one-dimensional bulk vibrations (1.77). All three structures can be fundamentally described by the one-dimensional wave equation, producing sinusoidal standing waves.

1.2 Lumped-Element Model Resonator

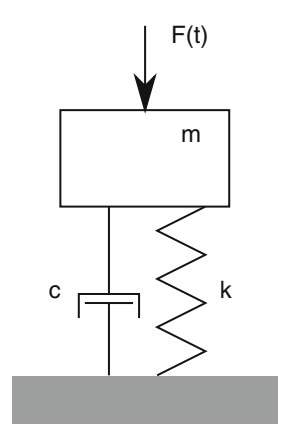
In this section the more complex behavior of mechanical resonators is discussed by means of lumped-element models, in contrast to the simple energy conservative continuum mechanical systems introduced in the pervious Sect. 1.1. In Sect. 1.2.1 behavior of non-conservative linear resonators are introduced, that is resonators that dissipate energy during vibration. Section 1.2.2 presents an analysis of linear resonators that are coupled to each other. Section 1.2.3 discussed the nonlinear behavior of resonators when driven at large amplitudes.

1.2.1 Damped Linear Resonator

Mechanical vibrations in physical systems are associated with the periodic conversion of kinetic to potential energy and vice versa. Elastic elements such as beams, strings, and plates are able to store potential energy in terms of the deformation energy. If the system comes out of its position of rest, restoring forces accelerate the mass of the system towards the rest position thereby generating kinetic energy. Due to the kinetic energy, the physical system traverses the position of rest, generating new deflection energy that is potential energy. This periodic energy conversion would continue forever if the present mechanical energy would not be resisted by dissipative forces.

For the calculation of the free vibration (eigenfrequency) of continuum mechanical resonators, as discussed in the previous chapter, dissipative forces where dismissed and the total energy remained constant at any time. In a real vibrational system energy is always dissipated by viscous damping, acoustic transmission, surface losses, internal dissipation, etc. The damping mechanisms in nanomechanical resonators are discussed in Chap. 2. Dissipative forces are approximately proportional to the velocity of the vibrational movement and are often modelled as a dashpot, as shown in Fig. 1.16.

Fig. 1.16 Damped one-dimensional oscillator with one degree of freedom



The mechanical behavior of solids is generally approximated by a linear relation between the continuum stress σ and strain ε

$$\sigma = E\varepsilon \tag{1.112}$$

with the Young's modulus E. As long as a resonator is driven in the linear regime, which is usually the case for appropriately small vibrational amplitudes, the dynamics of an individual resonance mode can be simplified with that of a linear harmonic oscillator. The forced vibration of a damped system with a single degree of freedom can hence be modelled with a one-dimensional resonator oscillator based on a linear zero mass spring, a linear damping element, and a mass, as depicted in Fig. 1.16. Assuming a periodic driving force $F(t) = F_0 \cos(\omega t)$, the second order differential equation of the system is

$$m\ddot{z} + c\dot{z} + kz = F(t),$$
 (1.113)

where m is the total mass, k is the spring constant, and c is the coefficient of damping force.

1.2.1.1 Free Undamped Vibration

In the specific case of a non-driven lumped-element resonator with zero damping c, the total energy of the system remains constant. In this case the resonator turns into an oscillator with the vibrational amplitude $z(t) = z_0 \cos(\omega t)$. During oscillation the total energy is fully swapped back and forth between kinetic (at the zero crossings) and potential (at the reversal points) energy. According to the equipartition theorem (1.1), the two energies have to be equal

$$\frac{1}{2}m\ddot{z}^2 = \frac{1}{2}kz^2\tag{1.114}$$

which yields the eigenfrequency Ω of the undamped free mechanical system, also called an "oscillator"

$$\Omega = \omega = \sqrt{\frac{k}{m}}. (1.115)$$

1.2.1.2 Free Damped Vibration

In the case of an undriven system, the equation of motion (1.113) reduces to the homogeneous differential equation

$$\ddot{z} + 2n_c \dot{z} + \Omega z = 0 \tag{1.116}$$

with the coefficient of damping

$$n_c = \frac{c}{2m} \tag{1.117}$$

Inserting a trial solution $z = z_0 e^{\gamma t}$ in (1.116) gives then solutions that satisfy

$$\gamma_{1,2} = -n_c \pm \sqrt{n_c^2 - \Omega^2}. (1.118)$$

The system performance is defined by the ratio between n_c and Ω , which is called the *damping ratio*

$$\zeta = \frac{n_c}{\Omega}.\tag{1.119}$$

If $\zeta \geq 1$, γ is real and the solution of (1.116) is an exponential decay. In this situation the system is heavily damped (over-damped case). For a slightly damped system (under-damped case) $\zeta < 1$, (1.118) becomes imaginary

$$\gamma_{1,2} = -n_c \pm i \sqrt{\Omega^2 - n_c^2}.$$
 (1.120)

Since for a linear homogeneous ordinary differential equation the linear sum of linearly independent solutions (real and imaginary) are also solutions, and by applying Euler's formula, the solution of (1.116) becomes

$$z(t) = z_0 e^{-\Omega \zeta t} \cos \left(\Omega \sqrt{1 - \zeta^2 t} \right). \tag{1.121}$$

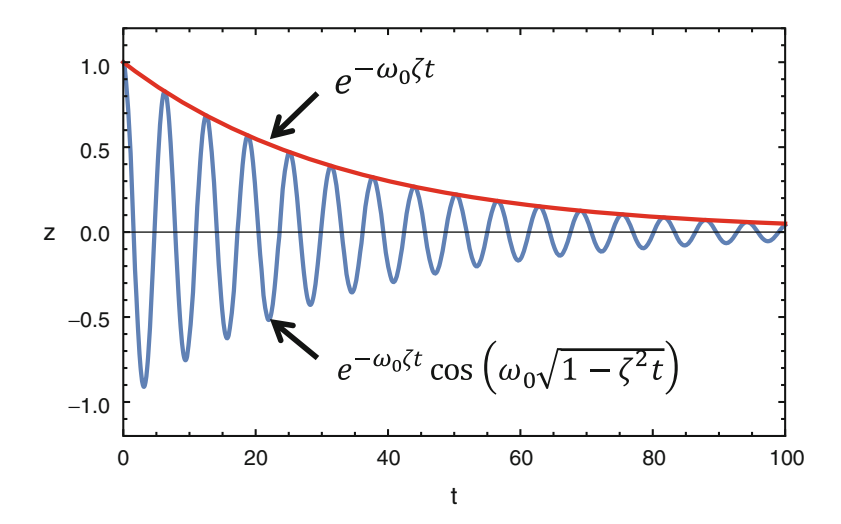


Fig. 1.17 Plot of (1.121) for $z_0 = 1$, $\Omega = 1$, and $\zeta = 0.03$

This equation indicates that the system has an exponentially decaying oscillation with a frequency $\omega_{nat} = \Omega \sqrt{1 - \zeta^2} = \sqrt{\Omega^2 - n_c^2}$, also called *natural frequency*. The solution (1.121) is depicted in Fig. 1.17.

1.2.1.3 Driven Damped Vibration

The solution of (1.113) is the sum of the transient solution of the homogeneous differential equation (1.121) and a specific steady solution that is described by

$$z(t) = z_0 e^{i\omega t}. ag{1.122}$$

where z_0 is the amplitude of the resulting vibration. Inserting (1.122) into (1.113) yields

$$z_0 = \frac{F_0/m}{(\Omega^2 - \omega^2) + 2i\zeta\Omega\omega}. (1.123)$$

This complex amplitude can be converted to the polar form, with the norm

$$|z_0| = \frac{F_0/m}{\sqrt{(\Omega^2 - \omega^2)^2 + 4\xi^2 \Omega^2 \omega^2}}$$
(1.124)

and the phase

$$arg(z_0) = \varphi = \arctan \frac{2\zeta\Omega\omega}{\omega^2 - \Omega^2},$$
 (1.125)

and the real specific solution then takes the form

$$z(t) = \frac{F_0/m}{\sqrt{(\Omega^2 - \omega^2)^2 + 4\zeta^2 \Omega^2 \omega^2}} \cos(\omega t + \varphi). \tag{1.126}$$

Both the amplitude and phase response can be written as a function of the relative frequency ω/Ω

$$|z_0| = \frac{F_0/k}{\sqrt{\left(1 - \left(\frac{\omega}{\Omega}\right)^2\right)^2 + 4\xi^2 \left(\frac{\omega}{\Omega}\right)^2}}.$$
 (1.127)

and

$$\arg(z_0) = \varphi = \arctan \frac{2\zeta\left(\frac{\omega}{\Omega}\right)}{\left(\frac{\omega}{\Omega}\right)^2 - 1}.$$
 (1.128)

The numerator in (1.127) F_0/k represents the static deflection. Hence, the relative amplitude response (also called *dynamic amplification* or *gain*) is then simply given by

$$\delta z_0 = \frac{1}{\sqrt{(1 - \left(\frac{\omega}{\Omega}\right)^2)^2 + 4\xi^2 \left(\frac{\omega}{\Omega}\right)^2}}.$$
 (1.129)

Both the amplitude and phase response of a linear resonator are plotted in Fig. 1.18a-c.

Another common way to actuate a mechanical resonator is by shaking its base by, e.g., a piezoelectric shaker. The schematic representation of this scenario is shown in Fig. 1.18d. In this case the relative amplitude and phase response become [28]

$$\delta z_0 = \frac{\left(\frac{\omega}{\Omega}\right)^2}{\sqrt{\left(1 - \left(\frac{\omega}{\Omega}\right)^2\right)^2 + 4\zeta^2 \left(\frac{\omega}{\Omega}\right)^2}}.$$
 (1.130)

and

$$\arg(z_0) = \varphi = \arctan \frac{2\zeta\left(\frac{\omega}{\Omega}\right)}{1 - \left(\frac{\omega}{\Omega}\right)^2}.$$
 (1.131)

Both functions (1.130) and (1.131) are plotted in Fig. 1.18e, f.

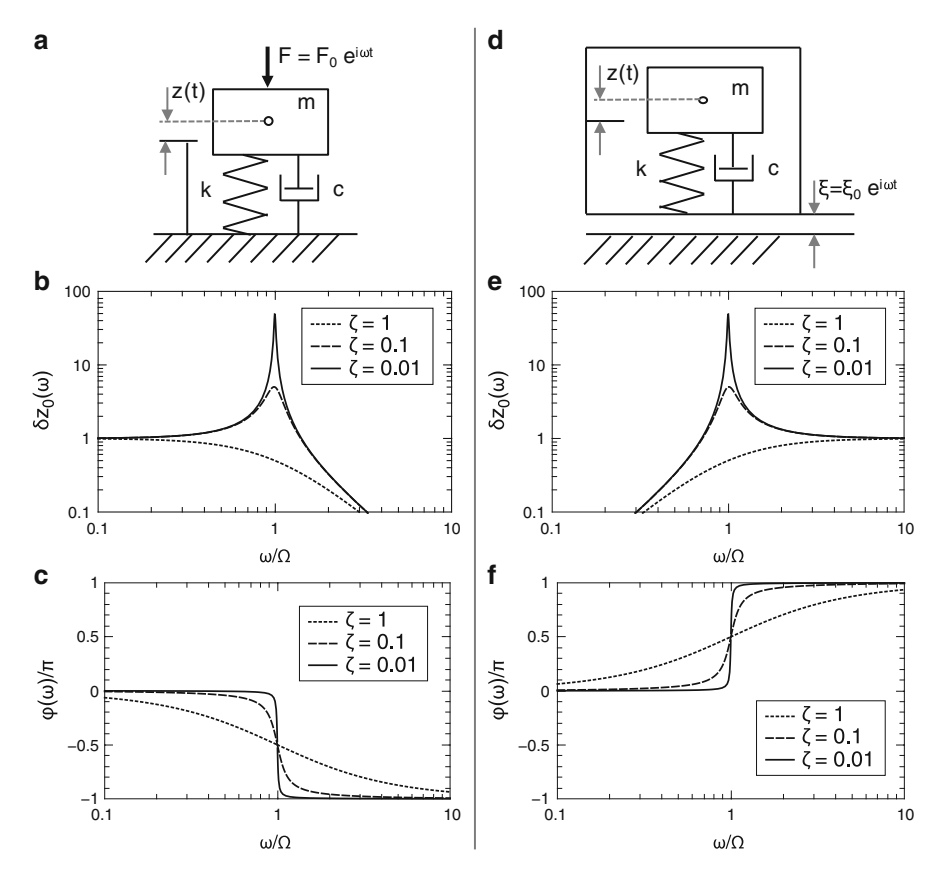


Fig. 1.18 Driven damped vibration of a lumped system. Schematic drawings of a damped resonator (**a**) driven by a force and (**d**) driven by an external vibration. (**b**) and (**c**) show the respective relative amplitude responses (1.129) and (1.130), and (**c**) and (**f**) show the respective phase responses (1.128) and (1.131)

From (1.129) it can be seen that the amplitude of a slightly damped system has a maximum near the eigenfrequency Ω , the so-called resonance peak. The frequency of the highest amplitude is called *resonance frequency* ω_r and it can be found at $\partial B/\partial \omega = 0$. The resonance frequency is given by

$$\omega_r = \Omega \sqrt{1 - 2\xi^2}.\tag{1.132}$$

For slight damping, the resonance frequency is very close to the eigenfrequency of the system $\omega_r \approx \Omega$.

When inserting ω_r into (1.128), the phase lag at resonance becomes

$$\varphi_r = \arctan \frac{\sqrt{1 - 2\zeta^2}}{\zeta}.$$
 (1.133)

For slight damping, the phase lag at resonance approaches $\varphi_r \approx \arctan 1/\zeta = \pi/2$. At resonance, the vibrational amplitude reaches a maximal value of

$$z_{0,\text{max}} = \frac{F_0}{\Omega^2 m} \, \frac{1}{2\zeta \sqrt{1 - \zeta^2}} \tag{1.134}$$

which for slight damping becomes

$$z_{0,\text{max}} = \frac{F_0}{\Omega^2 m} \, \frac{1}{2\zeta} = \frac{F_0}{k} \, Q. \tag{1.135}$$

The maximal amplitude at resonance is the static deflection times an amplification factor Q, that is called the *quality factor*, which will be discussed in the next subsection.

1.2.1.4 Quality Factor

The quality factor (Q) is a value indicating the sharpness of the resonance peak. There are several definitions of Q, all equivalent for slight damping.

The physical definition is the ratio between the energy stored and energy lost during one cycle at resonance

$$Q = 2\pi \frac{W}{\Delta W},\tag{1.136}$$

where W is the total energy stored in the system and ΔW is the energy loss during one cycle of oscillation.

With a displacement of $z = a \cos \omega_r t$ at resonance, the total energy of the system is

$$W = \max\left\{\frac{1}{2}m\dot{z}^{2}\right\} = \frac{1}{2}ma^{2}\omega_{r}^{2}.$$
 (1.137)

With the dissipative force $F_d=-c\dot{z}$, the energy lost during one cycle can be calculated as

$$\Delta W = -\int_0^{2\pi/\omega_r} F_d \dot{z} dt = \int_0^{2\pi/\omega_r} c \dot{z}^2 dt = \pi c a^2 \omega_r$$
 (1.138)

and

$$Q = 2\pi \frac{W}{\Delta W} = \frac{m\omega_r}{c} \tag{1.139}$$

With (1.117), (1.119) and (1.132) Q can be written as

$$Q = \frac{\sqrt{1 - 2\zeta^2}}{2\zeta} \tag{1.140}$$

For slight damping, the quality factor becomes $Q \approx \frac{1}{2\ell}$.

Fitting of linear oscillator model to the measured amplitude and phase lag response is a practical method to obtain Q. Therefore, the modal amplitude (1.127) and phase lag (1.128) curves can be written as

$$B = \frac{F_0/m}{\sqrt{(\Omega^2 - \omega^2)^2 + \Omega^2 \omega^2/Q^2}}$$
(1.141)

and

$$\varphi = \arctan \frac{\Omega \omega / Q}{\Omega^2 - \omega^2}.$$
 (1.142)

Instead of fitting with the oscillator model, the measured resonance curves are fitted with a *Lorentzian* function. The extraction of Q is then based on the -3 dB bandwidth method.

The -3 dB bandwidth method is based on the definition of Q in electrical resonant circuits where quality factor is given by [28]

$$Q = \frac{\omega_r}{\Delta \omega_{-3 \, dB}} = \frac{1 - 2\zeta^2}{2\zeta} \tag{1.143}$$

where $\Delta\omega_{-3\mathrm{dB}}$ is the frequency difference between the two frequencies at which the amplitude curve (1.127) has the half maximum energy $B/\sqrt{2}$ (-3 dB). For slight damping, this definition of the quality factor is equal to the physical definition. The quality factor can now be found by measuring the amplitude response around the resonance. According to (1.143) the resonance frequency divided by the -3 dB bandwidth is an approximation for Q for slight damping.

In a typical electrical measurement the power response instead of the amplitude response is measured. The power is proportional to the square of the resonator amplitude (1.127). For slightly damped systems, the resulting power response can well be approximated by the Lorentzian function f_L , which is related to the Cauchy distribution,

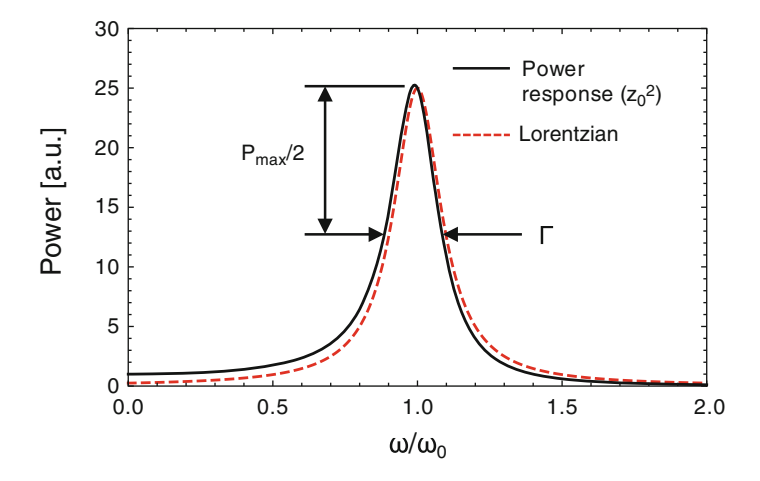


Fig. 1.19 Comparison of the power response of a linear resonator to the Lorentzian function

$$f_L(z, z_0, \Gamma, c) = c \frac{1}{4\Omega^2} \left[\frac{1}{(\Omega - \omega)^2 + (\frac{1}{2}\Gamma)^2} \right]$$
 (1.144)

where c is a fit parameter and $\Gamma = \delta \omega_{-3 \text{ dB}} \approx 2n_c$ is the *full width at half maximum* (fwhm). A comparison of the power response of a linear resonator to the corresponding *Lorentzian* (1.144) is shown in Fig. 1.19.

From the phase response the quality factor can be determined accurately. The determination of the amplitude maximum and the bandwidth can be inaccurate. In contrast, the phase response can be measured precisely. Q can be calculated from the slope of the phase response (1.128) at the resonance frequency

$$\frac{\partial \varphi}{\partial \omega}\Big|_{\omega=\Omega} = \frac{1}{n_c} \approx \frac{2Q}{\Omega}$$
 (1.145)

The ring down method makes direct use of the energy dissipation of a damped resonator. It is a particularly useful method for very high Qs where the bandwidth becomes too small and the phase angle becomes too steep to be determined precisely. The resonator is driven close to its resonance frequency. Then the actuation is stopped and the oscillation decaying, following the transient solution (1.121). The quality factor can now be found by fitting an exponential function $\exp(-t/\tau)$ to the envelope of the decaying vibrational amplitude, as shown in Fig. 1.17. With $n_c = \tau^{-1}$, Q is given by

$$Q = \frac{1}{2}\Omega\tau. \tag{1.146}$$

1.2.1.5 Effective Parameters

It is commonly used to simplify the dynamics of an individual resonance mode (normal mode) of a continuous structure with that of a harmonic oscillator

$$\Omega_n = \sqrt{\frac{k_{\text{eff},n}}{m_{\text{eff},n}}},\tag{1.147}$$

where $k_{\rm eff,n}$ and $m_{\rm eff,n}$ denote effective spring constant and effective mass of the particular normal mode. These effective parameters can readily be obtained by comparing the lumped-model potential or kinetic energies to the respective continuum mechanical energies listed in Table 1.1. It is important to note that the effective parameters depend on the chosen amplitude normalization $(U_n(x) = U_{0,n}\phi_n(x) = z_0)$. It is therefore important to mention the position x chosen for the comparison. Typically, the lateral location of the maximal displacement in the fundamental mode is chosen, which e.g. for a singly clamped beam is at the tip $(z_0 = U_n(L))$ while for a doubly clamped beam it is in the center $(z_0 = U_n(L/2))$. In the following two paragraphs, two different methods to derive the effective parameters are presented at the example of one-dimensional beams as introduced in Sect. 1.1.1.1. The methodology can directly be translated for other continuum mechanical structures. In Table 1.3 the effective mass of a few common continuum mechanical structures is listed.

Energy Approach

This approach is based on the comparison of the kinetic energy of the continuum mechanical structure to the kinetic energy of the corresponding lumped-model system. With the kinetic energy of a one-dimensional beam resonator, see Table. 1.1, the kinetic energy comparison yields

$$\frac{1}{2}A\rho \int_0^L \left(\frac{\partial}{\partial t} U_{0,n} \phi_n(x) \cos(\omega t)\right)^2 dx = \frac{1}{2} m_{\text{eff},n} \left(\frac{\partial}{\partial t} z_0 \cos(\omega t)\right)^2. \tag{1.148}$$

Setting the absolute vibrational amplitudes of the two systems equal ($U_{0,n}=z_0$), the following effective mass can be extracted

$$m_{\text{eff},n} = \rho A \int_0^L \phi_n^2(x) dx.$$
 (1.149)

Knowing the effective mass, the corresponding effective stiffness $k_{\text{eff},n}$ can readily be obtained from the eigenfrequency equation (1.115)

$$k_{\text{eff},n} = \Omega_n^2 m_{\text{eff},n} \tag{1.150}$$

Member	Effective mass $(m_{\rm eff})$	Normalization position x			
Singly clamped beam of length <i>L</i> in bending vibration	$\frac{1}{4}m_0$	At tip $(x = L)$			
Doubly clamped beam of length <i>L</i> in bending vibration	$\frac{1}{2}m_0$	Center of antinode			
String of length L in bending vibration	$\frac{1}{2}m_0$	Center of antinode			
Singly clamped rod of length <i>L</i> in longitudinal vibration	$\frac{1}{4}m_0$	At tip $(x = L)$			
Doubly clamped rod of length <i>L</i> in longitudinal vibration	$\frac{1}{2}m_0$	Center of antinode			
Rectangular plate of size <i>S</i> in bending vibration	$\frac{1}{4}m_0$	Center of antinode			
Circular plate of radius <i>R</i> in bending vibration	$\frac{1}{5}m_0$	Center of antinode			
Rectangular membrane of size <i>S</i> in bending vibration	$\frac{1}{4}m_0$	Center of antinode			

Table 1.3 Effective mass and stiffness constants of various continuum mechanical structures with total mass m_0 for various boundary conditions BC

or by comparing the potential energies of the equivalent systems, similar to the equalization of the kinetic energies for obtaining the effective mass.

Galerkin's Method

This method is a more general approach of deriving not only the effective mass but also all other effective parameters. The derivation is performed for the case of an undamped "one-dimensional" beam structure, with the differential equation of motion (1.12) extended to include an actuation force F(x, t)

$$\rho A \frac{\partial^2 u(x,t)}{\partial t^2} + E I_z \frac{\partial^4 u(x,t)}{\partial x^4} = F(x,t). \tag{1.151}$$

Assuming that the motion of the beam is only happening on one vibrational mode, i.e. $u(x,t) = u_n(t)\phi_n(x)$, multiplying by that mode shape $\phi_n(x)$ and integrating all over the length of the structure, i.e. \int_0^L , it is possible to reach the lumped- element modelling using integration by parts

$$\rho A \ddot{u}_n(t) \int_0^L \phi_n^2(x) dx + E I_z u_n(t) \int_0^L \phi_n''^2(x) dx = \int_0^L F_n(x, t) \phi_n(x) dx.$$
 (1.152)

In doing so, all other mode components disappear except the selected mode component remains. The family of normal modes ϕ_n form an orthogonal base for the Hilbert space of functions between 0 and L. The multiplication with a particular modeshape function and integrating over the resonator area is equivalent to taking the inner product between orthogonal norms.

From (1.152) it is possible to define the effective mass $m_{\text{eff},n}$ (1.149), effective stiffness $k_{\text{eff},n}$, and effective force $F_{\text{eff},n}$, so that the lumped model equation is retrieved

$$m_{\text{eff},n}\ddot{u}_n(t) + k_{\text{eff},n}u_n(t) = F_{\text{eff}}(t)$$
(1.153)

with the effective parameters

$$m_{\text{eff},n} = \rho A \int_0^L \phi_n^2(x) dx$$

$$k_{\text{eff},n} = EI_z \int_0^L \phi_n''^2(x) dx \qquad (1.154)$$

$$F_{\text{eff},n} = \int_0^L F_n(x,t) \phi_n(x) dx.$$

The presented formalism can readily be extended to different parameters (see Sect. 1.2.3) and to two-dimensional structures (see Sect. 3.2.2.1).

1.2.1.6 Torsional Paddle Resonator

The calculation of the common torsional paddle resonators as introduced in Fig. 1.20 in Sect. 1.1.4 on page 27 represents a special case of a resonator that best is modelled as a lumped-element system. The typical design of such a resonator is shown in Fig. 1.20. In this depicted case the rotational inertia is solely concentrated in the rotating paddle in the center. The hinging bars are acting as rotational springs with a negligible rotational inertia. This assumption is particularly true for paddles hinged by carbon nanotubes (see, e.g., Fig. 1.15a).

The rotational stiffness of the connecting bars can readily be derived by comparing the potential energies of the continuum mechanical bar to the corresponding lumped-element model. Assuming a rod with constant cross section, a linear modeshape function can be used

$$U(x) = U_0 \frac{x}{L} \tag{1.155}$$

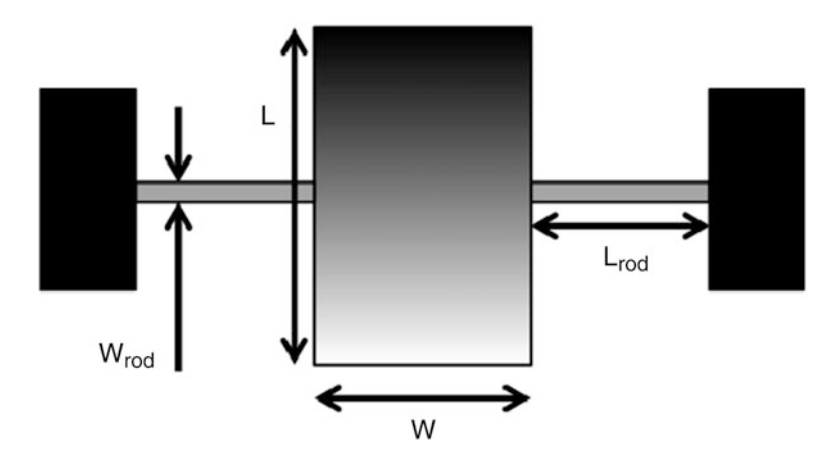


Fig. 1.20 Schematic drawing of torsional paddle resonator

and the potential energy of a rotational shaft (see Table 1.1)

$$W_{\text{pot,max}} = \frac{1}{2}GI_p \int_0^{L_{\text{rod}}} \left(\frac{\partial U(x)}{\partial x}\right)^2 dx$$
 (1.156)

becomes

$$W_{\text{pot,max}} = \frac{1}{2} U_0 \frac{GI_p}{L_{\text{rod}}}.$$
 (1.157)

This energy has to be equal to the potential energy of a lumped-element systems with $W_{\rm pot,max}=\frac{1}{2}U_0^2k_{\varphi}$, which results in the rotational stiffness of a rod of length $L_{\rm rod}$

$$k_{\varphi} = \frac{GI_p}{L_{\text{rod}}}. (1.158)$$

The polar geometrical moment of inertia I_p of a rod with rectangular cross section is given by

$$I_p = h^3 w_{\text{rod}} k_c. ag{1.159}$$

with the factor k_c , which for a square rod ($h = w_{\text{rod}}$) becomes $k_c = 0.141$, and for a thin rectangular rod ($h \ll w_{\text{rod}}$) becomes $k_c = 1/3$.

The rotational inertia of the paddle with thickness h can be calculated by Bao [28]

$$I_{\varphi} = \int_{-L/2}^{L/2} \rho w h x^2 dx = \frac{1}{12} \rho w h L^3.$$
 (1.160)

The eigenfrequency of such a rotational paddle resonator is now given by

$$\Omega = \sqrt{\frac{k_{\varphi}}{I_{\varphi}}}. (1.161)$$

1.2.2 Coupled Linear Resonators

Coupled mechanical resonators are typically studied for the modelling of mechanical waves in crystalline materials, where the individual atoms are represented by lumped masses that are coupled with each other via linear springs. Besides this more theoretical application, the rich dynamics of mutually coupled micro and nanomechanical resonators have been explored for various applications. Mechanically coupled resonators have, e.g., been used for mass sensing with micromechanical resonator pairs [29] or arrays [30]. The coupling can also happen via electrostatic forces [31], which allow the design of bandpass filters with variable filter properties [32]. Recently, in optomechanics, mechanical resonators have been coupled to electromagnetic resonators [34]. In this section, a simple case of mutually coupled mechanical resonators with equal mass and spring constant is presented. A real-world application of such a coupled micromechanical resonator pair is shown in Fig. 1.21. In this example, the two cantilevers which vibrate out of plane are coupled via a shared overhang between the structures. Such a system with two identical resonators that are mechanically coupled is schematically depicted in Fig. 1.22.

To calculate the eigenfrequencies of the coupled resonators (Fig. 1.22), the homogenous undamped system is first studied. Newton's second law readily yields the equations of motion

$$m\ddot{z_1} + kz_1 + k_c(z_1 - z_2) = 0$$

 $m\ddot{z_2} + kz_2 - k_c(z_1 - z_2) = 0.$ (1.162)

symmetric mode antisymmetric mode

Fig. 1.21 Schematic visualization of the symmetric and antisymmetric mode of vibration of two mechanically coupled cantilevers

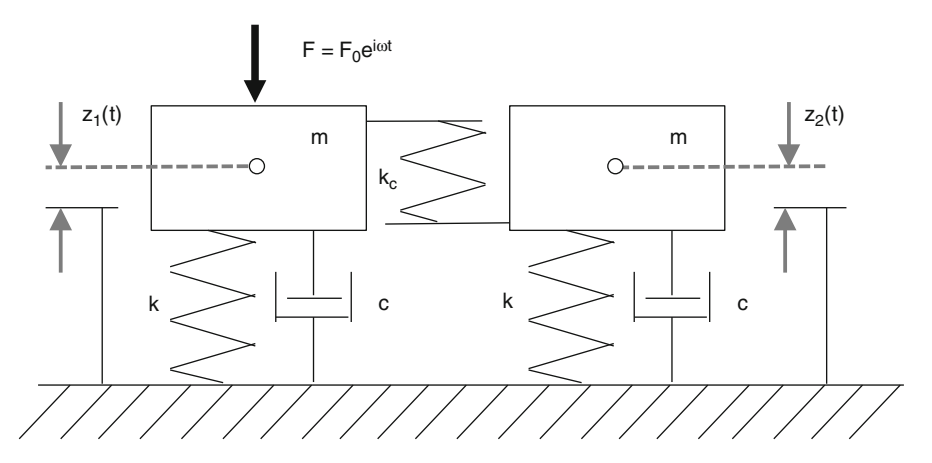


Fig. 1.22 Schematic drawing of two coupled linear damped resonators

This linear system of equations can be solved by plugging in the standard ansatz

$$\begin{pmatrix} z_1(t) \\ z_2(t) \end{pmatrix} = \begin{pmatrix} A_1 \\ A_2 \end{pmatrix} e^{i\omega t},$$
 (1.163)

which yields the linear system of equations

$$\begin{pmatrix} -\omega^2 m + k + k_c & -k_c \\ -k_c & -\omega^2 m + k + k_c \end{pmatrix} \begin{pmatrix} A_1 \\ A_2 \end{pmatrix} = \begin{pmatrix} 0 \\ 0 \end{pmatrix}. \tag{1.164}$$

The non-trivial solutions can be found when the determinant of the system is zero

$$(-\omega^2 m + k + k_c)^2 - k_c^2 = 0, (1.165)$$

which yields two positive eigenfrequencies

$$\omega_1 = \Omega_s = \sqrt{\frac{k}{m}}$$
 $\omega_2 = \Omega_a = \sqrt{\frac{k + 2k_c}{m}}.$ (1.166)

Plugging in these eigenfrequencies in (1.164) gives $A_1 = A_2$ for Ω_s and $A_1 = -A_2$ for Ω_a .

At the symmetric mode at the eigenfrequency Ω_s both vibrational amplitudes of both resonators are equal. The normal mode eigenfrequency is equal to the eigenfrequency of a single uncoupled resonator. Since both resonators are vibrating in phase, the coupling spring k_c remains unstretched. Such a symmetric mode of coupled cantilevers is shown in Fig. 1.21. For the asymmetric mode at with the eigenfrequency Ω_a the two vibrational amplitudes are moving in opposite

direction and the coupling spring is under a lot of strain, which increases the normal mode eigenfrequency. An asymmetric mode of coupled cantilevers can be seen in Fig. 1.21.

The response of a damped and driven system, as depicted in Fig. 1.22, can be calculated from the corresponding system of equations

$$m\ddot{z}_1 + c\dot{z}_1 + kz_1 + k_c(z_1 - z_2) = F_0 e^{i\omega t}$$

$$m\ddot{z}_2 + c\dot{z}_2 + kz_2 - k_c(z_1 - z_2) = 0.$$
(1.167)

This system of equation can readily be solved by adding and subtracting the two equations, which results in two new equations.

Adding the equations gives

$$m(\ddot{z_1} + \ddot{z_2}) + c(\dot{z_1} + \dot{z_2}) + k(z_1 + k_2) = F_0 e^{i\omega t}$$

$$m\ddot{q_s} + c\dot{q_s} + kq_s = F_0 e^{i\omega t},$$
(1.168)

with $q_s = z_1 + z_2$. This is of course the equation of motion (1.113) of a damped and driven linear resonator, as discussed previously in Sect. 1.2.1. In the coupled case, the *x* coordinate is replaced by the *normal coordinate* q_s . The steady state solution of a slightly damped system is then given by according to (1.126)

$$q_s = z_1 + z_2 = A_s \cos(\omega t + \varphi_s)$$
 (1.169)

with the amplitude (1.124)

$$A_{s} = \frac{F_{0}/m}{\sqrt{(\Omega_{s}^{2} - \omega^{2})^{2} + \Gamma^{2}\omega^{2}}}$$
(1.170)

and the phase (1.125)

$$\varphi_s = \arctan \frac{2\zeta \Omega_s \omega}{\omega^2 - \Omega_s^2} \tag{1.171}$$

of a single damped linear resonator of eigenfrequency Ω_s .

Similarly, subtracting the two equation of the general solution (1.167) gives

$$m(\ddot{z_1} - \ddot{z_2}) + c(\dot{z_1} - \dot{z_2}) + k(z_1 - z_2) = F_0 e^{i\omega t}$$

 $m\ddot{q}_a + c\dot{q}_a + kq_a = F_0 e^{i\omega t},$ (1.172)

with the asymmetric normal coordinate $q_a = z_1 - z_2$. The solution for a slightly damped system is now the response of a damped linear resonator with the eigenfrequency Ω_a with the steady state solution

$$q_a = z_1 - z_2 = A_a \cos(\omega t + \varphi_a)$$
 (1.173)

with the amplitude

$$A_a = \frac{F_0/m}{\sqrt{(\Omega_a^2 - \omega^2)^2 + \Gamma^2 \omega^2}}$$
 (1.174)

and the phase

$$\varphi_a = \arctan \frac{2\zeta \Omega_a \omega}{\omega^2 - \Omega_a^2}.$$
 (1.175)

The solution for $z_1(t)$ and $z_2(t)$ can be obtained by adding and subtracting (1.173) and (1.169), which gives

$$z_1(t) = \frac{1}{2} A_s \cos(\omega t + \varphi_s) + \frac{1}{2} A_a \cos(\omega t + \varphi_a)$$

$$z_2(t) = \frac{1}{2} A_s \cos(\omega t + \varphi_s) - \frac{1}{2} A_a \cos(\omega t + \varphi_a).$$
(1.176)

It shows that the general solution of the resonator system is the superposition of the symmetric and the asymmetric mode, called the *normal modes*. Examples of the average displacement $\langle z_1 \rangle$ of the driven mass m_1 is shown in Fig. 1.23. It can be seen that a so-called *normal mode splitting* occurs for a strong enough coupling. The coupling strength is typically represented by the splitting frequency

$$\Delta\omega_{\rm s} = \Omega_{\rm g} - \Omega_{\rm s},\tag{1.177}$$

which, under the assumption $k_c/k \ll 1$, is given by

$$\Delta\omega_s = \frac{k_c}{\iota}\Omega_s. \tag{1.178}$$

From Fig. 1.23 it can be seen that the normal mode splitting becomes observable for $\Delta \omega_s \ge \Gamma$. This regime is also called the *strong coupling* regime.

1.2.3 Damped Nonlinear Resonators

In previous sections, the behavior of mechanical resonators and their dumpedelement models has been analyzed within what is typically called the linear regime. This stands for the regime where the amplitude of the resonator enters linearly in the equation of motion or, in other words, that the relation between the applied force and the response of the resonator (at a given frequency) does not change when the amplitude of motion becomes larger.

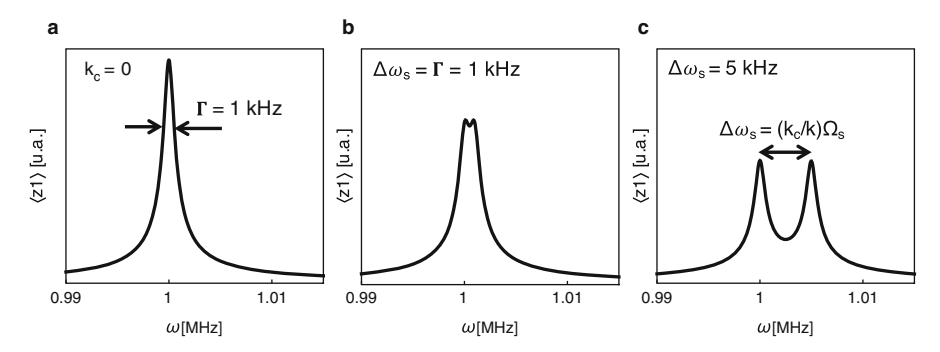


Fig. 1.23 Plot of the average displacement $\langle z_1 \rangle$ with $\Omega_s = 1$ MHz and $\Gamma = 1$ kHz for varying coupling strengths (**a**) $\Delta \omega_s = 0$ Hz, (**b**) $\Delta \omega_s = 1$ kHz, and (**c**) $\Delta \omega_s = 5$ kHz

Unfortunately, reality is far away from this simplistic point of view and nonlinearities are often encountered in most physical systems [35, 36]. The aim of this section is to briefly introduce the different sources of nonlinearity and to show how to solve the resulting equation of motion.

1.2.3.1 Sources of Nonlinearity

Material Nonlinearity

The most straightforward source of nonlinearity is the so-called material nonlinearity and happens when the relation between strain and stress is not linear anymore. Continuum solid mechanics dictates that for small deformations stress and strain are related through the Young's modulus. However, when strain becomes larger, this ratio is modified and plasticity occurs [37]. This can be written in a nonlinear version of the Hooke's law (1.112), as follows

$$\sigma = E_0 \varepsilon + E_1 \varepsilon^2 + E_2 \varepsilon^3 + \cdots \tag{1.179}$$

When translated to macroscopic deformation, (1.179) implies that the stiffness of the beam will depend on the deformation, thus the equation of motion will not be linear anymore. This source of nonlinearity can appear at any type of resonator, as it is directly linked to the material properties. However, it is typically only visible in either carefully engineered or very stiff structures [38, 39] where the rest of nonlinearities are suppressed.

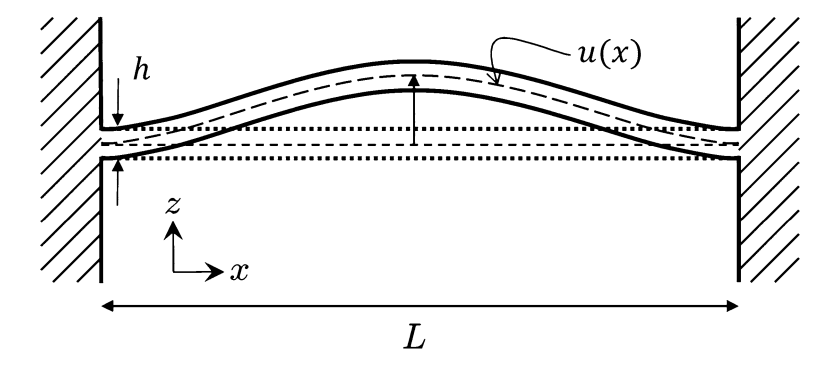


Fig. 1.24 Schematic showing the cross section of a clamped-clamped beam and how deflection induces additional strain and stress in the longitudinal axis of the beam

Geometric Nonlinearity

The second most common type of nonlinearity is that associated with the geometry and boundary conditions of the resonator itself. This type of nonlinearity is mostly seen in flexural (bending) modes [40–43]. A typical example can be found in Fig. 1.24, where a clamped-clamped beam is shown and it is evidenced that a deflection different from zero implies an effective elongation of the beam. That elongation can only be achieved by means of developing a longitudinal stress within the beam, which in turn causes the frequency to change, as it was shown in Sect. 1.1.1.2. As this developed tension is proportional to the amplitude of vibration, that is the origin of the nonlinearity.

The total tension in the structure of Fig. 1.24, with a Young's modulus E and a cross section area A, is the sum of an existing tensile force $N_0 = \sigma A$ and a tension coming from the longitudinal strain ε of the beam during vibration

$$N(u(x,t)) = N_0 + EA\varepsilon$$

$$= \sigma A + EA \frac{1}{2L} \int_0^L \left(\frac{\partial u(x,t)}{\partial x}\right)^2 dx$$
(1.180)

which can be then inserted in (1.44), together with a damping c and driving force term F to obtain

$$\rho A \frac{\partial^{2} u(x,t)}{\partial t^{2}} + c \frac{\partial u(x,t)}{\partial t} + E I_{z} \frac{\partial^{4} u(x,t)}{\partial x^{4}} - \left[\sigma A + \frac{EA}{2L} \int_{0}^{L} \left(\frac{\partial u(x,t)}{\partial x} \right)^{2} dx \right] \frac{\partial^{2} u(x,t)}{\partial x^{2}} = F(x,t)$$
(1.181)

where the nonlinear term, the second one inside the square bracket, starts to be apparent, as it can be seen that the differential equation is not a linear function of u(x, t) anymore. Applying Galerkin's method as introduced in Sect. 1.2.1.5 on page 39 leads to

$$\rho A \ddot{u}_n(t) \int_0^L \phi_n^2(x) dx + c \dot{u}_n(t) \int_0^L \phi_n^2(x) dx + E I_z u_n(t) \int_0^L \phi_n''^2(x) dx + F_0 u_n(t) \int_0^L \phi_n'^2(x) dx + \frac{EA}{2L} u_n^3(t) \left(\int_0^L \phi_n'^2(x) dx \right)^2 = F_n(t).$$
(1.182)

From (1.182) it can be defined now the effective mass $m_{\text{eff},n}$ (1.149), effective stiffness $k_{\text{eff},n}$, effective damping rate $\Gamma_{\text{eff},n}$, and nonlinear stiffness $\alpha_{\text{eff},n}$ so that the lumped model equation is retrieved

$$m_{\text{eff},n}\ddot{u}_n(t) + \Gamma_{\text{eff},n}\dot{u}_n(t) + k_{\text{eff},n}u_n(t) + \alpha_{\text{eff},n}u_n^3(t) = F_n(t)$$
 (1.183)

where the intrinsic tensile stress σaA is taken to be 0 for simplicity. Equation (1.183) can be also written as

$$\ddot{u}_n(t) + \frac{\Gamma_{\text{eff},n}}{m_{\text{eff},n}} \dot{u}_n(t) + \frac{k_{\text{eff},n}}{m_{\text{eff},n}} u_n(t) + \frac{\alpha_{\text{eff},n}}{m_{\text{eff},n}} u_n^3(t) = \frac{F_n(t)}{m_{\text{eff},n}}$$
(1.184)

which is analogous to (1.116) that is analyzed in its linear form in Sect. 1.2.1.

This derivation of the nonlinear lumped-element model can be applied to any other type of nonlinearity and not only the geometric nonlinearity. It is good to remember that the derivation has been done here for only one particular type of geometric nonlinearity, which is a nonlinearity of the effective stiffness of the mode, caused by an increase in the longitudinal tension due to motion. In other type of flexural devices, e.g. clamped-free beams or cantilevers, it can be seen that there are also inertial nonlinear terms that affect the effective mass [42–46]. Therefore, for each particular type of geometry a slightly different analysis must be made. To conclude this paragraph, it is also important to note that the lumped-model parameters are determined through the modal shapes which, as discussed at the beginning of the chapter, are in general not trivial to calculate and one might need the help of Finite Element Modelling (FEM) to determine them.

Actuation Nonlinearity

The next source of nonlinearity to be analyzed here is the one emerging from a nonlinear dependence on the displacement of the actuation force [40, 41, 47, 48]. It is possible to understand it from the point of view of an actuation force that modifies the potential well of the harmonic oscillator. This example is found quite commonly in MEMS/NEMS resonators as it is inherent to electrostatic actuation, one of the

most used actuation techniques for MEMS/NEMS. In that case, the driving force term that is included in (1.181) takes the form:

$$F(x,t) = \frac{1}{2}\varepsilon_0 \frac{bV(t)^2}{(g_0 - u(x,t))^2}.$$
 (1.185)

Equation (1.185) depends on the dynamic gap between the resonator and the driving electrode, $g_0 - u(x, t)$, and the voltage applied between them, V(t). It is possible to perform a Taylor expansion of (1.185) around g_0 :

$$F(x,t) = \frac{1}{2}\varepsilon_0 \frac{bV(t)^2}{g_0^2}$$

$$\left[1 + 2\frac{u(x,t)}{g_0} + 3\left(\frac{u(x,t)}{g_0}\right)^2 + 4\left(\frac{u(x,t)}{g_0}\right)^3 + \mathcal{O}\left(\frac{u(x,t)}{g_0}\right) \right]$$
(1.186)

where the nonlinear terms start to become apparent. The first term in the square bracket gives rise to the actual actuation force. The second term is a tunability term that affects directly the measured resonance frequency, even at small amplitudes, i.e. it does not induce nonlinearity. The third and the fourth term can be treated in a similar way to the nonlinear terms for the case of geometrical nonlinearity, yielding an equation of motion similar to (1.184), but that in this case has an additional term proportional to the displacement to the square:

$$\ddot{u}_n(t) + \frac{\Gamma_{\text{eff},n}}{m_{\text{eff},n}} \dot{u}_n(t) + \frac{k_{\text{eff},n}}{m_{\text{eff},n}} u_n(t) + \frac{\beta_{\text{eff},n}}{m_{\text{eff},n}} u_n^2(t) + \frac{\alpha_{\text{eff},n}}{m_{\text{eff},n}} u_n^3(t) = \frac{F_n(t)}{m_{\text{eff},n}}$$
(1.187)

Detection Nonlinearity

After considering the nonlinearity in the actuation, it is only logical to follow by considering the nonlinearity in the detection. This is a very typical case of nonlinearity, present in the majority of experiments performed in MEMS/NEMS resonators. However, this does not affect the dynamics of the mechanical resonators, just the conversion between the *actual displacement* and the *measured voltage* in the macroscopic laboratory equipment. This type of nonlinearity becomes very important to determine the actual nonlinear parameters of the system [39, 43].

Nonlinear Damping

The final source of nonlinearity to be considered here is the one that affects the dissipation in the mechanical structure [35, 40, 49]. This is typically considered linear, i.e. constant no matter the displacement, but in reality there is no theoretical

deterrent for the damping not to be nonlinear. In fact, in some extreme cases this nonlinearity in the damping can be observed and it can even dominate over the linear damping [33]. The origins of this nonlinear damping are still unclear and remain as an interesting field of fundamental research. In this case, the equation of motion (1.187) must be modified including terms of the type: $\eta_{\text{eff},n}u_n(t)^2\dot{u}_n(t)$ or $\mu_{\text{eff},n}u_n(t)\dot{u}_n(t)$.

1.2.3.2 Solving the Nonlinear Equation of Motion

Solving a differential equation like (1.113) is relatively easy, as one can use the Fourier transform to convert the differential equation into an algebraic one. On the contrary, when nonlinear terms are part of the equation the solution becomes less trivial. In this section, the approach taken by Cross and Lifshitz [35] to solve the nonlinear equation will be followed, and it is based on assuming that the nonlinearity is a small perturbation to the linear case. This implies that the response of the system to a harmonic external drive will be given by a fast harmonic response modulated, due to the nonlinear terms, at a much slower pace. This approximation is valid only if the quality factor of the resonator Q is large enough. Indeed, one can consider the inverse of the quality factor as the small number for which the solution is expanded around the linear case.

In order to simplify the analysis, let us start by taking (1.184) using that $k_{\text{eff},n} = m_{\text{eff},n}\omega_n^2$ and that $Q_n^{-1} = \frac{\Gamma_{\text{eff},n}}{m_{\text{eff},n}\omega_n}$:

$$\ddot{u}_n(t) + \frac{\omega_n}{Q_n} \dot{u}_n(t) + \omega_n^2 u_n(t) + \frac{\alpha_{\text{eff},n}}{m_{\text{eff},n}} u_n^3(t) = \frac{F_n(t)}{m_{\text{eff},n}}.$$
(1.188)

For this study only one vibrational mode is considered, which means that it is possible to drop the subindexes n. In addition, it is typically a good idea to work with dimensionless magnitudes. This way, the results hold validity in a universal reference frame that can be translated to actual units for each resonator independently. A normalization that is typically used consists of two steps, the first one reads as follows:

$$\hat{t} = \omega_n t; \quad \hat{x} = u_n \sqrt{\frac{\alpha_{\text{eff}}}{m_{\text{eff}}\omega_n}}; \quad \hat{F} = F_n \sqrt{\frac{\alpha_{\text{eff}}}{m_{\text{eff}}^3\omega_n^6}}; \quad \hat{\omega} = \frac{\omega}{\omega_n};$$
 (1.189)

and this converts (1.184) into (1.190) noting that now $\dot{\hat{x}} = \frac{d\hat{x}}{d\hat{t}}$:

$$\ddot{\hat{x}} + \frac{\dot{\hat{x}}}{Q} + \hat{x} + \hat{x}^3 = \hat{F}\cos\left(\hat{\omega}\hat{t}\right). \tag{1.190}$$

The second step in the normalization is based on the fact that the quality factor of our resonator is going to be $Q \gg 1$ and also using that the system will mostly behave

linearly or, in other words, that the nonlinearity is going to be weak. This latter condition is imposed by forcing the cubic term in (1.190) to be a factor proportional to Q smaller than the linear term(s). From this, it follows automatically that the driving term has to be of the order of $Q^{-3/2}$. Finally, it is possible to see that the dynamics of the mode are going to be limited to a range of frequencies around the resonance frequency, which allows the definition of the *slow* timescale and frequency. Overall:

$$T = \frac{\hat{t}}{O} = \frac{\omega_n t}{O}; \quad \Omega = 1 + \frac{\hat{\omega}}{O} = 1 + \frac{\omega}{O\omega_n}; \quad g = \frac{\hat{G}}{O^{3/2}}; \tag{1.191}$$

and the amplitude will take the form:

$$x = \frac{1}{2Q^{1/2}} \left(A(T)e^{i\hat{t}} + c.c. \right) + \frac{x_1(t)}{Q^{3/2}} + \cdots$$

$$\dot{\hat{x}} = \frac{d\hat{x}}{d\hat{t}} = \frac{1}{2Q^{1/2}} \left(\left[iA + \frac{1}{Q} \frac{dA}{dT} \right] e^{i\hat{t}} + c.c. \right) + \frac{\dot{x}_1(t)}{Q^{3/2}} + \cdots;$$

$$\ddot{\hat{x}} = \frac{d^2\hat{x}}{d\hat{t}^2} = \frac{1}{2Q^{1/2}} \left(\left[-A + \frac{2i}{Q} \frac{dA}{dT} + \frac{1}{Q^2} \frac{d^2A}{dT^2} \right] e^{i\hat{t}} + c.c. \right) + \frac{\ddot{x}_1(t)}{Q^{3/2}} + \cdots;$$
(1.192)

where c.c. stands for complex conjugate, in order to simplify the formulas. Due to the slow time scales, it can be seen that Eq. (1.192) has some terms scaled by different powers of the *small parameter*. By plugging (1.192) into (1.190) and picking all the terms proportional to $Q^{-3/2}$ we finally obtain an equation for the slow-varying amplitude A:

$$\frac{dA}{dT} = -\frac{1}{2}A + i\frac{3}{8}|A|^2A - i\frac{g}{2}e^{i\Omega T}.$$
(1.193)

The implications and fields of application of this very general equation reach far beyond the scope of this book. The amplitude A is a complex magnitude that takes the shape: $A(T) = |A|e^{i\phi}e^{i\Omega T}$ which is a dimensionless representation of: $u_n(t) = \frac{1}{2Q}\sqrt{\frac{m_{\rm eff}\omega_n}{\alpha_{\rm eff}}}|A|\left(e^{i\phi}e^{i\Omega T}e^{i\omega_n t}+c.c.\right)$. By plugging the shape of the amplitude into the amplitude equation, (1.193), it is possible to reach:

$$|A|^{2} = \frac{g^{2}}{\left(2\Omega - \frac{3}{4}|A|^{2}\right)^{2} + \frac{1}{4Q^{2}}};$$

$$\tan \phi = \left(2\Omega - \frac{3}{4}|A|^{2}\right)^{-1};$$
(1.194)

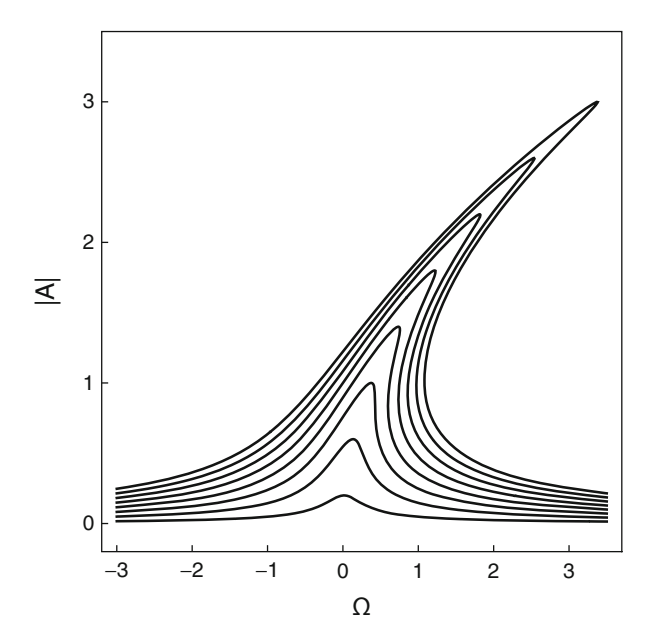


Fig. 1.25 Scaled amplitude of motion of a nonlinear resonator versus the scaled frequency for different driving forces

Figure 1.25 shows the results of Eq. (1.194), scaled amplitude of vibration (A) as a function of the scaled driving frequency (Ω) for different magnitudes of the driving force (g). It is possible to see how for small driving forces a Lorentzian curve is recovered, but as soon as the amplitude and drive increase, the curves stop being symmetrical with respect to the resonant frequency, tilting to the right showing the typical behavior of a so-called *Duffing resonator*. Indeed, it can also be seen how after a certain drive, critical drive g_c , there are frequencies for which three amplitudes hold Eq. (1.194) true. Out of these three solutions, one can perform a stability analysis and see that one of them is unstable, whereas the other two solutions are stable. This bi-stability is also typical from *Duffing* resonators and it also causes hysteresis in the resonator response when performing a frequency sweep, as depending whether you come from left to right or vice versa the final response is different, as can be seen in Fig. 1.26.

By deriving the first equation in (1.194) one can locate the frequencies for which the amplitude of response will be maximum, by imposing $\frac{d|A|^2}{d\Omega}=0$:

$$\Omega_{\text{max}} = \frac{3}{8} |A|_{\text{max}}^2; \quad \leftrightarrow \quad \omega_{\text{max},n} = \omega_n + \frac{3}{8} \frac{\alpha_{\text{eff}}}{m_{\text{eff}} \omega_n} |u_n|_{\text{max}}^2; \tag{1.195}$$

which delineates one of the most used methods to determine the nonlinear coefficient, α_{eff} , i.e. fitting the location in frequency of the maximum amplitude point

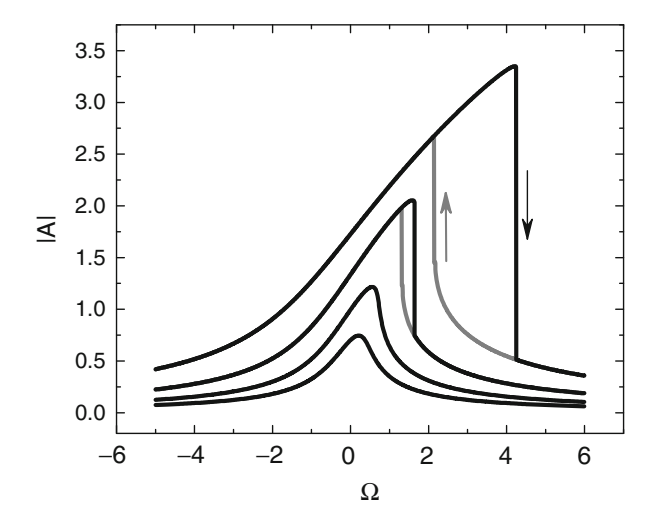


Fig. 1.26 Scaled amplitude of motion of a nonlinear resonator versus the scaled frequency for different driving forces. In this case it is shown the typical responses found experimentally, with the different result for the sweep of the frequency in the up (*darker grey*) or down (*lighter grey*) direction

for many actuation levels. In this case, of course, a very careful calibration of the displacement needs to be done prior to drawing any meaningful conclusion.

It is also possible to calculate the different *saddle-nodes* of the resonator response, or those points at which the behavior is supposed to transition from a stable solution to an unstable one, and that in reality correspond to the vertical jumps in the amplitude response that can be seen in Fig. 1.26. Those points can be calculated by imposing $\frac{d\Omega}{d|A|^2} = 0$, which results in two families of points, one family for the transitions when the sweep is performed left-to-right, and another family for the transitions when the sweep is performed right-to-left. The most interesting of all those *saddle-nodes* is the one that appears the first, when both families intersect. For that point, it is also true that $\frac{d^2\Omega}{(d|A|^2)^2} = 0$ and it determines a parameter that is known as *critical amplitude*, a_c , typically considered as the threshold at which the resonator behavior starts being nonlinear:

$$a_c = \sqrt{\frac{8}{3\sqrt{3}}} \quad \Leftrightarrow \quad u_c = \sqrt{\frac{8}{3\sqrt{3}}} \frac{1}{\sqrt{Q}} \sqrt{\frac{m_{\text{eff}}\omega_n^2}{\alpha_{\text{eff}}}}.$$
 (1.196)

In order to avoid seeing any nonlinear effects, it is necessary to ensure that the amplitude of motion of the resonator stays well below the critical amplitude. However in practice, and for simplicity, it is considered that whenever the resonator amplitude is below a_c , linear equations can be considered. The question then is how much is this critical amplitude for a given structure. Evidently, this primarily depends on the source of nonlinearity that is limiting the device under study. In the

Type of mode	Type of NL	Direction of NL	u_c
Cantilever beam—1st mode	Geometric	Stiffening	$\approx 6.3 \frac{L}{\sqrt{Q}}$
Cantilever beam—2nd mode	Geometric	Softening	$\approx 0.345 \frac{L}{\sqrt{Q}}$
Clamped-Clamped beam—1st mode	Geometric	Stiffening	$\approx 1.46 \frac{t}{\sqrt{Q}}$
Clamped-Clamped beam—2nd mode	Geometric	Stiffening	$\approx 1.024 \frac{t}{\sqrt{Q}}$
String	Geometric	Stiffening	$\approx 0.56 \frac{L}{\sqrt{Q}} \sqrt{\frac{\sigma}{E}}$

Table 1.4 Critical amplitudes at which the regime of geometrical nonlinearity is entered

case of geometric nonlinearity, different values of the critical amplitude are shown in Table 1.4. According to these values, this provides an idea of the magnitude of the motion amplitude that is required to enter the nonlinear regime or, rather, how small the amplitude should be in order to keep the behavior linear.

Other Types of Nonlinearity

To finalize this section, it is important to remember that only a simplified case with one type of nonlinearity has been analyzed in detail. In reality there might be many nonlinear terms affecting the resonator dynamics, and thus more complicated analysis needs to be done. However, it can be shown that all the nonlinear effects can be analyzed in the first order using the nonlinear stiffness that has been shown here $\alpha_{\rm eff}$ and the nonlinear damping $\eta_{\rm eff}$. As stated before, for a more detailed analysis the reader is invited to visit [35].

References

- 1. E. Ventsel, T. Krauthammer, *Thin Plates and Shells: Theory, Analysis, and Applications* (Marcel Dekker, New York, 2001)
- 2. W.F. Stokey, Vibration of systems having distributed mass and elasticity, in *Harris' Shock and Vibration Handbook* (McGraw-Hill Education, New York, 2002), pp. 7.1–7.50
- W. Weaver, S.P. Timoshenko, D.H. Young, Vibration Problems in Engineering (Wiley Interscience, New York, 1990)
- S. Schmid, Electrostatically Actuated All-Polymer Microbeam Resonators Characterization and Application. Scientific Reports on Micro and Nanosystems, vol. 6 (Der Andere Verlag, Tönning, 2009)
- M. Li, E.B Myers, H.X. Tang, S.J. Aldridge, H.C. McCaig, J.J. Whiting, R.J. Simonson, N.S. Lewis, M.L. Roukes, Nanoelectromechanical resonator arrays for ultrafast, gas-phase chromatographic chemical analysis. Nano Lett. 10(10), 3899–3903 (2010)
- S. Schmid, M. Kurek, A. Boisen, Towards airborne nanoparticle mass spectrometry with nanomechanical string resonators. SPIE Def. Secur. Sens. 8725, 872525–872528 (2013)

References 55

 A.M. Van Der Zande, R.A Barton, J.S. Alden, C.S. Ruiz-Vargas, W.S. Whitney, P.H.Q. Pham, J. Park, J.M. Parpia, H.G. Craighead, P.L. McEuen, Large-scale arrays of single-layer graphene resonators. Nano Lett. 10, 4869–4873 (2010)

- E. Gil-Santos, D. Ramos, J. Martínez, M. Fernández-Regúlez, R. García, A. San Paulo, M. Calleja, J. Tamayo. Nanomechanical mass sensing and stiffness spectrometry based on two-dimensional vibrations of resonant nanowires. Nat. Nanotechnol. 5(9), 641–645 (2010)
- S.S. Verbridge, J.M. Parpia, R.B. Reichenbach, L.M. Bellan, H.G. Craighead, High quality factor resonance at room temperature with nanostrings under high tensile stress. J. Appl. Phys. 99, 124304 (2006)
- A.N. Cleland, M.L. Roukes, Fabrication of high frequency nanometer scale mechanical resonators from bulk Si crystals. Appl. Phys. Lett. 69, 2653 (1996)
- 11. H.B. Peng, C.W. Chang, S. Aloni, T.D. Yuzvinsky, A. Zettl, Ultrahigh frequency nanotube resonators. Phys. Rev. Lett. **97**(8), 2–5 (2006)
- T. Bagci, A. Simonsen, S. Schmid, L.G. Villanueva, E. Zeuthen, J. Appel, J.M. Taylor, A. Sørensen, K. Usami, A. Schliesser, E.S. Polzik. Optical detection of radio waves through a nanomechanical transducer. Nature 507(7490), 81–85 (2014)
- 13. M.B. Sayir, S. Kaufmann, *Ingenieurmechanik 3: Dynamik* (Vieweg+Teubner, Wiesbaden, 2005)
- L. Aigouy, P. Lalanne, H. Liu, G. Julié, V. Mathet, M. Mortier, Near-field scattered by a single nanoslit in a metal film. Appl. Opt. 46(36), 8573–8577 (2007)
- A. Boisen, S. Dohn, S.S. Keller, S. Schmid, M. Tenje, Cantilever-like micromechanical sensors. Rep. Prog. Phys. 74(3), 036101 (2011)
- J. Bochmann, A. Vainsencher, D.D. Awschalom, A.N. Cleland, Nanomechanical coupling between microwave and optical photons. Nat. Phys. 9(9), 1–5 (2013)
- A.D. O'Connell, M. Hofheinz, M. Ansmann, R.C. Bialczak, M. Lenander, E. Lucero, M. Neeley, D. Sank, H. Wang, M. Weides, Others, A.D. O'Connell, J. Wenner, J.M. Martinis, A.N. Cleland, Quantum ground state and single-phonon control of a mechanical resonator. Nature 464(7289), 697–703 (2010)
- J.H. Hales, J. Teva, A. Boisen, Z.J. Davis, Longitudinal bulk acoustic mass sensor, in *International Solid-State Sensors, Actuators and Microsystems Conference*, 2009. TRANSDUCERS 2009 (IEEE, New York, 2009), pp. 311–314
- J.D. Thompson, B.M. Zwickl, A.M. Jayich, F. Marquardt, S.M. Girvin, J.G.E. Harris, Strong dispersive coupling of a high-finesse cavity to a micromechanical membrane. Nature 452(7183), 72–75 (2008)
- J.D. Teufel, T. Donner, D. Li, J.W. Harlow, M.S. Allman, K. Cicak, A.J. Sirois, J.D. Whittaker, K.W. Lehnert, R.W. Simmonds, Sideband cooling of micromechanical motion to the quantum ground state. Nature 475(7356), 359–363 (2011)
- 21. J. Lee, Z. Wang, K. He, J. Shan, P.X.-L. Feng, High frequency MoS2 nanomechanical resonators. ACS Nano 7(7), 6086–6091 (2013)
- B.M. Zwickl, W.E. Shanks, A.M. Jayich, C. Yang, B. Jayich, J.D. Thompson, J.G.E. Harris, High quality mechanical and optical properties of commercial silicon nitride membranes. Appl. Phys. Lett. 92(10), 103125 (2008)
- S. Schmid, T. Bagci, E. Zeuthen, J.M. Taylor, P.K. Herring, M.C. Cassidy, C.M. Marcus, L. Guillermo Villanueva, B. Amato, A. Boisen, Y. Cheol Shin, J. Kong, A.S. Sørensen, K. Usami, E.S. Polzik, Single-layer graphene on silicon nitride micromembrane resonators. J. Appl. Phys. 115(5), 054513 (2014)
- S.P. Timoshenko, S. Woinowsky-Krieger, W. -Krieger, Theory of Plates and Shells, 2nd edn. (McGraw-Hill, New York, 1959)
- S.J. Papadakis, A.R. Hall, P.A. Williams, L. Vicci, M.R. Falvo, R. Superfine, S. Washburn, Resonant oscillators with carbon-nanotube torsion springs. Phys. Rev. Lett. 93(14), 1–4 (2004)
- X.C. Zhang, E.B. Myers, J.E. Sader, M.L. Roukes, Nanomechanical torsional resonators for frequency-shift infrared thermal sensing. Nano Lett. 13(4), 1528–1534 (2013)
- A.N. Cleland, M.L. Roukes, A nanometre-scale mechanical electrometer. Nature, 392, 160–162 (1998)

- 28. M Bao, Analysis and Design Principles of MEMS Devices (Elsevier, Amsterdam, 2005)
- E. Gil-Santos, D. Ramos, A. Jana, M. Calleja, A. Raman, J. Tamayo, Mass sensing based on deterministic and stochastic responses of elastically coupled nanocantilevers. Nano Lett. 9(12), 4122–4127 (2009)
- M. Spletzer, A. Raman, H. Sumali, J.P. Sullivan, Highly sensitive mass detection and identification using vibration localization in coupled microcantilever arrays. Appl. Phys. Lett. 92(11), 2006–2009 (2008)
- P. Thiruvenkatanathan, J. Yan, J. Woodhouse, A.A. Seshia, Enhancing parametric sensitivity in electrically coupled MEMS resonators. J. Microelectromech. Syst. 18(5), 1077–1086 (2009)
- 32. S. Pourkamali, F. Ayazi, Electrically coupled MEMS bandpass filters: Part I: with coupling element. Sensors Actuators A Phys. **122**(2), 307–316 (2005)
- 33. V. Singh, S.J. Bosman, B.H. Schneider, Y.M. Blanter, a Castellanos-Gomez, G. a Steele, Optomechanical coupling between a multilayer graphene mechanical resonator and a superconducting microwave cavity., Nat. Nanotechnol., 9(10), 820–824 (2014)
- M. Aspelmeyer, T.J. Kippenberg, F. Marquard, Cavity optomechanics. Rev. Mod. Phys. 86(4), 1391–1452 (2014)
- 35. R. Lifshitz, M.C. Cross, *Nonlinear Dynamics of Nanomechanical and Micromechanical Resonators*, vol. 1, book section 1 (Wiley-VCH, Weinheim, 2008)
- A.H. Nayfeh, D.T. Mook, Nonlinear Oscillations. Pure and Applied Mathematics (Wiley, New York, 1979)
- J.M. Gere, B.J. Goodno, Mechanics of Materials, 8th edn. (Cengage Learning, Stamford, CT, 2013)
- V. Kaajakari, T. Mattila, A. Oja, H. Seppa. Nonlinear limits for single-crystal silicon microresonators. J. Microelectromech. Syst. 13(5), 715–724 (2004)
- M.H. Matheny, L.G. Villanueva, R.B. Karabalin, J.E. Sader, M.L. Roukes, Nonlinear modecoupling in nanomechanical systems. Nano Lett. 13(4), 1622–1626 (2013)
- I. Kozinsky, H.W.C. Postma, I. Bargatin, M.L. Roukes, Tuning nonlinearity, dynamic range, and frequency of nanomechanical resonators. Appl. Phys. Lett. 88(25), 253101 (2006)
- N. Kacem, S. Hentz, D. Pinto, B. Reig, V. Nguyen, Nonlinear dynamics of nanomechanical beam resonators: improving the performance of NEMS-based sensors. Nanotechnology 20(27), 275501 (2009)
- N. Kacem, J. Arcamone, F. Perez-Murano, S. Hentz, Dynamic range enhancement of nonlinear nanomechanical resonant cantilevers for highly sensitive NEMS gas/mass sensor applications. J. Micromech. Microeng. 20(4), 45023 (2010)
- 43. L.G. Villanueva, R.B. Karabalin, M.H. Matheny, D. Chi, J.E. Sader, M.L. Roukes, Nonlinearity in nanomechanical cantilevers. Phys. Rev. B **87**(2), 24304 (2013)
- 44. M.R.M.C. Dasilva. Non-linear flexural flexural torsional extensional dynamics of beams 2. Response analysis. Int. J. Solids Struct. **24**(12), 1235–1242 (1988)
- 45. M.R.M. Crespodasilva, C.C. Glynn, Out-of-plane vibrations of a beam including nonlinear inertia and nonlinear curvature effects. Int. J. Non Linear Mech. 13(5–6), 261–271 (1978)
- 46. S. Perisanu, T. Barois, A. Ayari, P. Poncharal, M. Choueib, S.T. Purcell, P. Vincent, Beyond the linear and Duffing regimes in nanomechanics: circularly polarized mechanical resonances of nanocantilevers. Phys. Rev. B **81**(16), 165440 (2010)
- A. San Paulo, R. Garcia, Tip-surface forces, amplitude, and energy dissipation in amplitudemodulation (tapping mode) force microscopy. Phys. Rev. B 64(19), 193411 (2001)
- J.F. Rhoads, S.W. Shaw, K.L. Turner, Nonlinear dynamics and its applications in micro- and nanoresonators. J. Dyn. Syst. Meas. Control Trans. ASME 132(3), 34001 (2010)
- S. Zaitsev, O. Shtempluck, E. Buks, O. Gottlieb, Nonlinear damping in a micromechanical oscillator. Nonlinear Dyn. 67(1), 859–883 (2012)

Chapter 2 **Quality Factor**

Abstract The quality factor defines the rate with which a nanomechanical resonator dissipates energy. Low energy loss, i.e. a high quality factor, is desirable for most applications of nanomechanical resonators. In this chapter, the three main sources of energy loss in nanomechanical resonators are presented. Energy can be lost (1) to the surrounding medium, which can be a liquid or a gas, (2) through the clamping to the substrate via elastic waves, or (3) through dissipation mechanisms that are intrinsic to the resonator. Medium interaction losses can readily be circumvented by operation in vacuum, and clamping losses can be minimized by an optimized resonator design. This typically leaves intrinsic losses as the limiting mechanism defining the maximal obtainable quality factor. Intrinsic losses consist of material friction and fundamental loss mechanisms such as thermoelastic loss and phonon—phonon interaction loss. Generally, intrinsic losses can be reduced by decreasing the temperature. Damping dilution reduces the effect of intrinsic loss in resonators under tensile stress, resulting in quality factors up to several million even at room temperature.

The quality factor (Q) of a mechanical resonator is defined as the ratio of stored energy versus lost energy during one cycle of vibration. A high quality factor enhances the vibrational amplitude at resonance and reduces the resonance peak width. Both effects are, as will be seen in Chap. 5 on page 149, related to the precision with which the resonance frequency of a nanomechanical resonator can be detected. The smallest detectable frequency change is directly determining the sensitivity of a resonant nanomechanical sensor. A high Q is desired for applications of micro and nanomechanical resonators, e.g., as mass sensors, frequency references, or filters for signal processing. The total quality factor of a resonator is the sum of dissipation mechanisms.

$$\frac{1}{Q} = \frac{1}{Q_{\text{medium}}} + \frac{1}{Q_{\text{clamping}}} + \frac{1}{Q_{\text{intrinsic}}} + \frac{1}{Q_{\text{other}}},$$
(2.1)

where $Q_{\rm medium}$ stands for all losses due to the interaction of the mechanical structure with a fluidic or ballistic medium, $Q_{\rm clamping}$ are losses from energy radiating into the environment over the physical clamping sites of the resonator, and $Q_{\rm intrinsic}$

58 2 Quality Factor

summarized all dissipation mechanisms happening within the resonator, in the bulk and on the surface. Medium losses, clamping losses, and intrinsic losses are discussed in the chapter.

 Q_{other} sums up all loss mechanisms that are not covered by the first three. This, e.g., includes *electrical charge damping* caused by charges trapped on the resonator. Such charges induce image charges on a nearby surface. The resulting electrostatic forces are a source of energy dissipation [1]. Another mechanism under this category is *magnetomotive damping*, which results from electrical dissipation in resistive elements due to Eddy currents induced by an external magnetic field [2, 3]. This form of damping has to be considered particularly in nanomechanical resonators that are transduced with magnetic transduction techniques, as discussed in Sect. 4.1 on page 116.

2.1 Medium Interaction Losses

There are roughly three different media types by which a nanomechanical resonator can be surrounded by and which cause a energy loss. Namely, a medium can be a viscous liquid, a viscous fluidic or a rarefied ballistic gas. In this section, the loss mechanisms of the three particular medium types are explained and the latest damping models are listed.

2.1.1 Liquid Damping

2.1.1.1 Resonator Immersed in Liquid

The immersion of nanomechanical resonators in viscous liquids causes substantial energy loss. In the worst case scenario, a liquid medium can overdamp the nanomechanical structure thereby ceasing the resonance phenomenon. The effect of a viscous liquid on the quality factor of resonating cantilever beams has been theoretically modelled for bending modes [4, 5], torsional modes [6], and for bending modes of beams in close proximity to a solid surface [7]. These models were developed with respect to the application in atomic force microscopy, where the vibrating microcantilever probes often are immersed in water. The models consist of numerical approximations and are not available in a short form. The behavior of a mechanical resonator in water is therefore illustrated by means of actual experimental data taken from literature, see Fig. 2.1. It can be seen that Q at the fundamental mode is of the order of unity, hence the system is close to being overdamped. The quality factor increases steadily with increasing flexural mode. The observed trend and order of magnitude of the observed values is well predicted by the theoretical model. However, the typically very low Qs obtained in liquid are a major hindrance for applications of nanomechanical resonators directly in liquid.

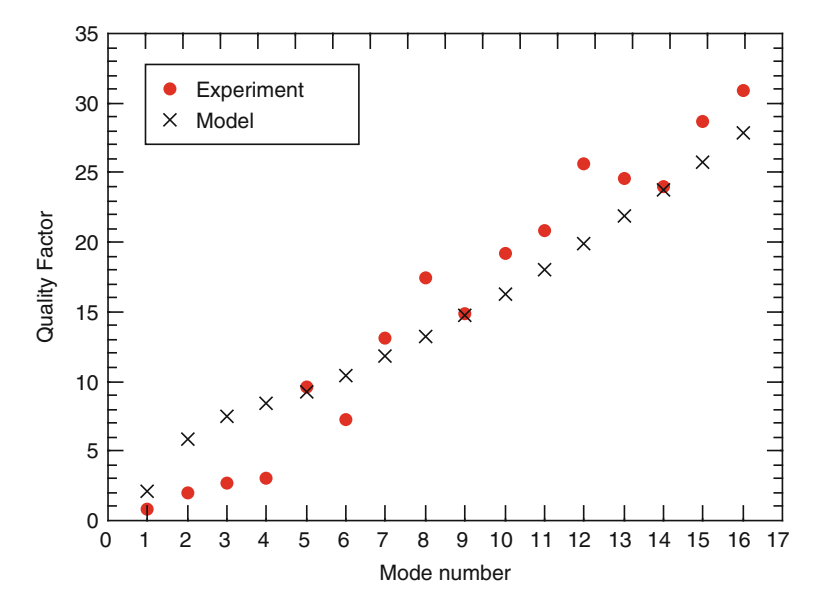


Fig. 2.1 Quality factor plotted against mode number of a cantilever ($500 \,\mu m$ long, $100 \,\mu m$ wide and $1 \,\mu m$ thick) immersed in water. The experimental data (extracted from [8]) is compared to the theoretical model by Sader [4]

Additionally to the low quality factors another challenge arises from the additional mass coming from the boundary liquid which is moved with the beam vibration. For example, the relative mass loading δm of a rectangular cantilever beam in the fundamental bending mode, whose length exceeds its width, immersed in a liquid is given to a good approximation by [4, 9, 10]

$$\delta m = \frac{\pi}{4} \frac{\rho_{\text{liquid}}}{\rho} \frac{w}{h} \tag{2.2}$$

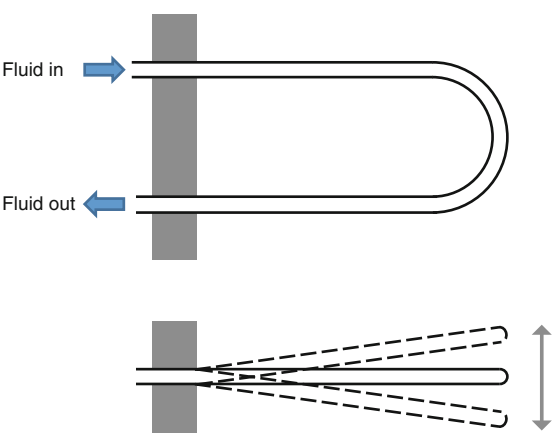
for a beam with width w, height h, and mass density ρ immersed in a liquid with mass density ρ_{liquid} . For a typical nanomechanical beam immersed in water, this results roughly in a mass load of 100 %. This additional mass strongly deteriorates the mass responsivity (see Sect. 3.1 on page 92 for more details on nanomechanical mass sensing).

2.1.1.2 Liquid Inside the Resonator

The low mass responsivity together with the low quality factor results in a low sensitivity of nanomechanical resonators when immersed in a viscous liquid. A solution to this problem is to flow the liquid through the mechanical resonator instead of immersing the resonator in the liquid, as schematically depicted in Fig. 2.2. In this

60 2 Quality Factor

Fig. 2.2 Schematic depiction of a U-tube resonator vibrating in vacuum and being filled with a viscous fluid



Transversal bending mode vibration

configuration, the resonator can be operated in vacuum, which results in almost identical quality factors for an empty or filled resonator [12]. This concept has been used for years in macroscopic U-tube density meters. More recently, micro and nanomechanical *U-tube resonators*, also called *suspended microchannel resonators*, have been successfully used for weighing of biomolecules [12] and nanoparticles [13], and for density [11, 14, 15] and viscosity [16] measurements. The viscosity detection is non-trivial because the quality factor has been shown to be a non-monotonic function of the liquids viscosity [17, 18].

For the special case of a cantilever beam (with mass density ρ , a lot longer than thick $L\gg h$, and wider than thick $w\gg h$) comprising a fluidic channel (with mass density ρ_{liquid} , length L_{liquid} , width w_{liquid} , and height h_{liquid}), whose midplane lies on the neutral axis of the cantilever has been theoretically modelled by Sader et al. [18]. In this case, the quality factor of the fundamental bending mode resulting from the flow of an incompressible viscous liquid inside the channel is given by

$$Q_{\text{liquid}} = F(\beta_{Re}) \left(\frac{\rho}{\rho_{\text{liquid}}}\right) \left(\frac{h}{h_{\text{liquid}}}\right) \left(\frac{w}{w_{\text{liquid}}}\right) \left(\frac{L}{h_{\text{liquid}}}\right)^2$$
(2.3)

with the functional

$$F(\beta_{Re}) \approx \underbrace{\frac{38.73}{\beta_{Re}}}_{\text{Small }\beta_{Re} \text{ limit}} + \underbrace{0.1521\sqrt{\beta_{Re}}}_{\text{Large }\beta_{Re} \text{ limit}}$$
(2.4)

which is a function of the Reynold's number

$$\beta_{Re} = \frac{\rho_{\text{liquid}} h_{\text{liquid}}^2}{\mu} \omega, \tag{2.5}$$

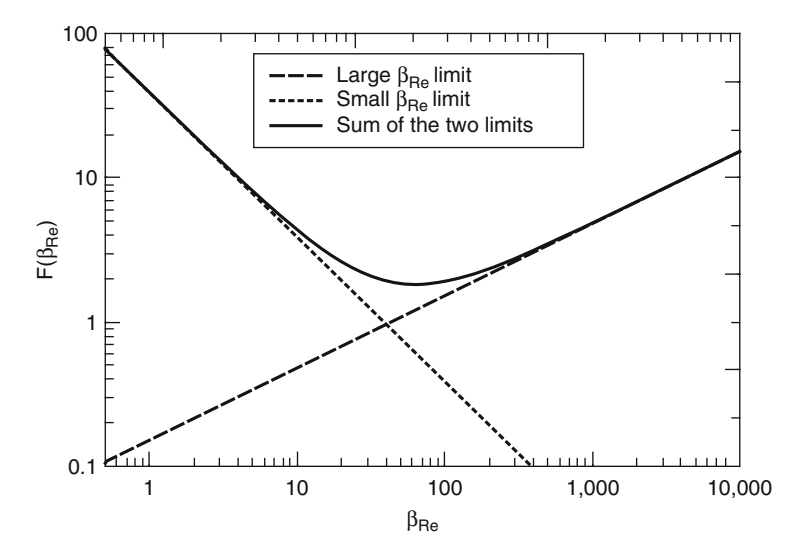


Fig. 2.3 Plot of the normalized quality factor (2.4) of a cantilever comprising an on-axis fluidic channel vs Reynold's number β_{Re}

where ω is the angular velocity of the cantilever vibration and μ is the viscosity of the fluid. The functional (2.4) is the normalized quality factor, it is plotted in Fig. 2.3. It can be approximated by the sum of two extreme solutions (1) for the small $\beta_{Re} \ll 1$ limit and (2) the large $\beta_{Re} \gg 1$ limit. From Fig. 2.3 it is obvious that the quality factor is not a monotonic function of the Reynold's number, and hence, for a fixed geometry, of the fluid viscosity.

The more intuitive behavior happens in the large Reynold's number regime, where the fluidic behavior is dominated by its inertia inside the vibrating cantilever. This inertial flow generates viscous boundary layers, which are sources of energy dissipation. As a result, an increasing fluid viscosity (decreasing β_{Re}) results in a decreasing quality factor. In contrast, the behavior in the small Reynold's number regime is a bit counter-intuitive. Here, the effect of fluid inertia disappears, and the fluid behaves like a rigid-body, that is there is no generation of lossy viscous boundary layers. Hence, an increasing fluid viscosity results in an increasing quality factor. The low Reynold's number regime can be entered by reducing the fluid channel height $h_{\rm fluid}$. It is thus possible to obtain highly sensitive suspended nanochannel resonators with high quality factors, which results in a high sensitivity for detecting small density changes, e.g. caused by biomolecules, cells, or nanoparticles.

2.1.2 Gas Damping

Damping of a system caused by the surrounding gas is related to the surface area of the moving parts. In nanomechanical systems, the ratio of surface area to volume becomes large and air damping can become the main source of energy

62 2 Quality Factor

dissipation. The pressure range can be divided into two regions where different damping mechanisms are dominant, namely the fluidic and ballistic region. The transition between ballistic and fluidic regime is described by the *Knudsen number* (Kn), which is given by the ratio of the *mean free path length* of the gas (λ_f) to the representative physical length scale of the nanomechanical structure (L_r)

$$Kn = \frac{\lambda_f}{L_r} \tag{2.6}$$

with

$$\lambda_f = \frac{k_B T}{\sqrt{2}\pi d_{gas}^2} \frac{1}{p} \tag{2.7}$$

where k_B is the Boltzmann constant, T is temperature, $d_{\rm gas}$ is the diameter of the gas particles, and p is the gas pressure. For air at atmospheric pressure, the mean free path is approximately 70 nm. The system is in the fluidic regime if the mean free path length of the gas is shorter than the representative length scale $\lambda_f < L_r$, that is to say Kn < 1. In this case, from the structures perspective, the gas is seen as a continuum, and the interaction is best described by the fluid dynamic framework. Here, the energy dissipation results from the viscous flow of the gas around the vibrating nanomechanical structure. In contrast, the system is in the ballistic regime if the mean free path length of the gas is larger than the representative length scale $\lambda_f > L_r$, that is to say Kn > 1. In this case, the gas cannot be treated as a continuous fluid. Instead, the dissipation is caused by the impact of noninteracting gas molecules.

The ballistic regime is typically reached by reducing the gas pressure. However, for small nanomechanical resonators with a representative length scale below 70 nm, the ballistic regime can even be entered at atmospheric pressure. The measured quality factor of a micromechanical string resonators as a function of air pressure is shown in Fig. 2.4. In this example, the representative length scale is the width $w = 14 \,\mu\text{m}$ of the resonating string. The pressure representing Kn = 1 is indicated by the dashed vertical line. It can be seen that the quality factor is increasing steadily with decreasing air pressure. Until at a pressure of roughly 10 Pa, the quality factor approaches a plateau which is given by the intrinsic losses of the polymer resonator.

In the following subsections, theoretical models for the quality factor of vibrating beam structures in the two regimes are presented. For simplicity, only the two most common damping scenarios to be expected in nanomechanical resonators, namely *squeeze-film damping* and *drag-force damping* are covered. Nanomechanical structures fabricated by surface micromachining techniques typically are in close proximity to an underlying substrate. The gas molecules which are trapped between the substrate and the nanomechanical structure are responsible for the main gas damping, the so-called squeeze-film damping. If the vibrating beam is far away from a surface, the gas molecules are colliding with the moving surfaces of the beam which is called drag-force damping.

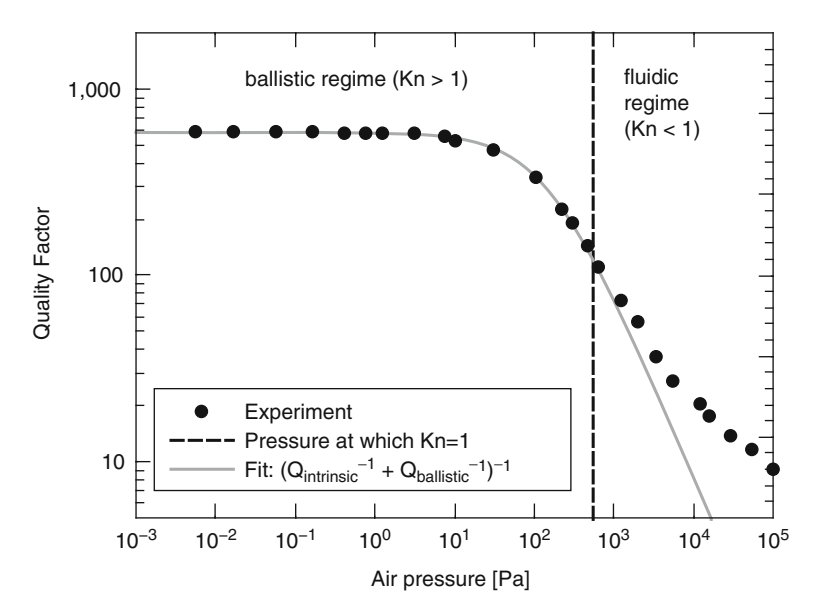


Fig. 2.4 Measured quality factors plotted against air pressure, for a 14 μ m wide SU-8 microstring. The *dashed line* shows the pressure $p = 550 \,\text{Pa}$ at which Kn = 1, which represents the transition pressure between the fluidic and the ballistic regime. (Data extracted from [19])

2.1.2.1 Fluidic Regime (Kn < 1)

In the fluidic regime the dimension of the resonators is larger than the mean free path length of the gas molecules. In this case, the air can be modelled as a viscous fluid. In case the acoustic wavelength in the fluid medium (phase velocity over vibrational frequency) is larger than the representative hydrodynamic length scale of the flow (for a vibrating beam structure this typically is the width), the models for an incompressible fluid can be applied (see Sect. 2.1.1.1 on page 58). However, for higher vibrational modes the length scale of spatial vibration of a beam can become larger than the acoustic wavelength in the fluid. In this situation, the gas medium has to be modelled as a compressible fluid [20]. In a compressible gas, significant energy is lost via acoustic radiation, where energy is carried away in the form of sound waves.

Here, simple models based on an incompressible fluid for the squeeze-film and drag-force damping of beams are presented. These models yield simple approximations for the quality factor in a viscous gas. The quality factor due to squeeze-film (sf) damping of a long beam (width w, thickness h, mass density ρ) with a gap between the beam and the substrate of d_0 is given by [21]

$$Q_{f-\mathrm{sf}} = \frac{\rho h d_0^3}{\mu w^2} \omega \tag{2.8}$$

where μ is the coefficient of viscosity of the fluid at a given temperature.

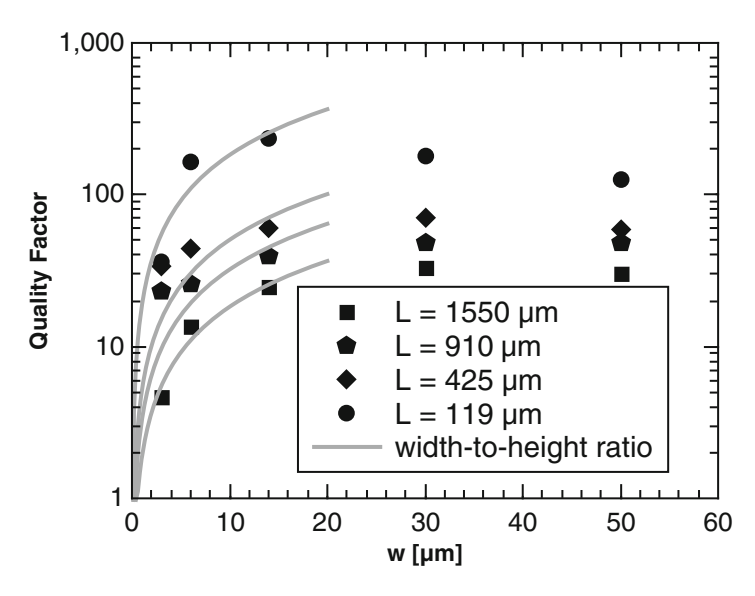


Fig. 2.5 Quality factor of silicon nitride strings as a function of the string width w measured at atmospheric pressure [23]

The drag-force damping can be approximated by a dish-string model. The drag force of a disk can be analytically modelled. The simplified dish-string model replaces the beam with a string of dishes with the diameter equal to the beam width. The quality factor due to viscous drag forces (df) is then given by [21]

$$Q_{f-\mathrm{df}} = \frac{\rho w h}{8\mu} \omega. \tag{2.9}$$

As a main rule, the quality factor due to viscous damping increases linearly with the vibrational frequency. This effect can be observed, e.g. in the measured quality factors of silicon nitride string resonators with different resonance frequencies as shown in Fig. 2.5. When comparing (2.8) and (2.9)

$$\frac{Q_{f-\text{sf}}}{Q_{f-\text{df}}} = 8\left(\frac{d_0}{w}\right)^3 \tag{2.10}$$

it becomes obvious that squeeze-film damping drastically exceeding the effect of drag-force damping if the gap distance is smaller than the beam width $(d_0 < w)$.

For both nano [22] and micro resonators [23] the influence of geometry has shown to be more complex than depicted by these simplified models for viscous damping. It seems that there is an optimal beam width at which air damping is minimal (see Fig. 2.5). Such effects come from the compressibility of the gas.

2.1.2.2 Ballistic Regime (Kn > 1)

Gas damping in the ballistic regime is based on momentum transfer from the resonator to colliding gas molecules. The energy transfer models are based on rigid oscillating plates, as schematically depicted in Fig. 2.6. The conservation of momentum and kinetic energy during a collision for a forward movement of the plate leads to a system of equations

$$m_1 v_1 - m_2 v_2 = m_1 v_1' + m_2 v_2'$$

$$\frac{1}{2} m_1 v_1^2 + \frac{1}{2} m_2 v_2^2 = \frac{1}{2} m_1 v_1'^2 + \frac{1}{2} m_2 v_2'^2.$$
(2.11)

Solving for the velocity of the gas molecule after the collision under the assumption that $m_1 \gg m_2$ gives

$$v_2' = v_2 + 2v_1. (2.12)$$

So, the gas molecule is faster and hence has gained energy after the collision. However, if the plate would move backward, in direction of the molecule, the velocity of the gas molecule after the collision would be

$$v_2' = v_2 - 2v_1, (2.13)$$

and hence the molecule would have transferred energy to the plate. At first sight it seems that the total energy of the plate remains constant during vibration, as the energy transfer with the colliding gas molecules seems balanced. However, the net energy loss comes from the fact that the number of collisions at the front side is larger than the number of collisions on the back side. In other words, the "pressure" on the front side is larger than on the back side. Based on a statistical analysis of the number collisions with gas molecules, the following formula has been derived for the drag-force damping of an oscillating plate in the ballistic regime [24, 25]

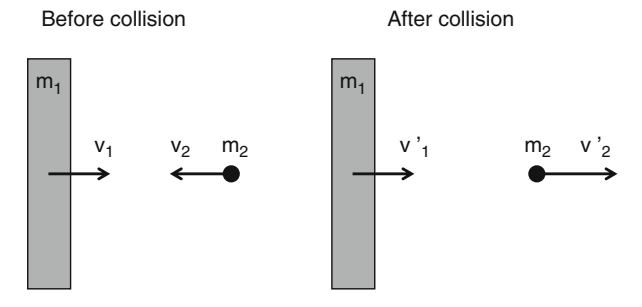


Fig. 2.6 Schematic drawing of a moving plate in rarefied gas before and after the collision with a gas molecule

$$Q_{b-\mathrm{df}}(p) = \frac{\rho h \omega}{4} \sqrt{\frac{\pi}{2}} \sqrt{\frac{R_{\mathrm{gas}} T}{M_m}} \frac{1}{p}$$
 (2.14)

where ω , T, M_m , and $R_{\rm gas}$ are the angular velocity of the oscillation, temperature, molar mass of the gas and the universal molar gas constant, respectively. This air damping model for an isolated plate has been shown to also be valid for flexible beams [26]. Dry air has an average molar mass of 28.97 g/mol.

A model for the squeeze-film damping in the ballistic regime has been obtained based on similar considerations. For a beam with a peripheral length L_p , thickness h and a distance d_0 to the substrate and a mass density ρ , the quality factor for squeeze-film damping in the ballistic regime becomes [24]

$$Q_{b-\rm sf}(p) = (2\pi)^{\frac{3}{2}} \rho h \omega \frac{d_0}{L_p} \sqrt{\frac{R_{\rm gas}T}{M_m}} \frac{1}{p}. \tag{2.15}$$

Both the drag-force damping and the squeeze-film damping in the ballistic regime are linear functions of the gas pressure. This linear behavior is visible in Fig. 2.4, until the measured quality factor reaches the intrinsic plateau. The quality factor as a function of gas pressure can thus be represented by the following function, which is plotted as a grey line in Fig. 2.4

$$Q^{-1} = Q_{\text{intrinsic}}^{-1} + c_1 p \tag{2.16}$$

with the fit parameter c_1 . It further can be observed that the experimental data starts to deviate from the fit exactly at the critical pressure (dashed line) when entering the fluidic regime, where the ballistic model ceases to be correct.

2.2 Clamping Loss

Clamping losses are caused by radiation of vibrational energy through the anchor of a micro or nanomechanical resonator. The energy loss over the clamping is strongly dependent on the detailed anchor geometry. Even though there are multiple analytical models taking account for different anchor geometries, practically, the anchor geometry of a real nanomechanical oscillator differs slightly of the theoretical scenarios. Nevertheless, the qualitative understanding based on analytical clamping loss models helps in designing of nanomechanical resonators with minimal clamping losses. Here, specific clamping loss models for cantilever beams and membrane resonators are briefly introduced.

2.2 Clamping Loss 67

2.2.1 Cantilever Beams

Clamping loss of singly clamped cantilever beams of the geometry shown in Fig. 2.7 has been analytically modelled by Photiadis et al. [27]. In the case that the supporting substrate thickness is thinner than the propagating elastic waves, and further assuming that the material properties of the base and cantilever are the same and taking $\nu = 0.3$, clamping losses for the fundamental mode can be estimated by the following expression

$$Q_{\text{clamping}}^{-1} \approx 0.95 \frac{w}{L} \frac{h^2}{h_L^2}$$
 (2.17)

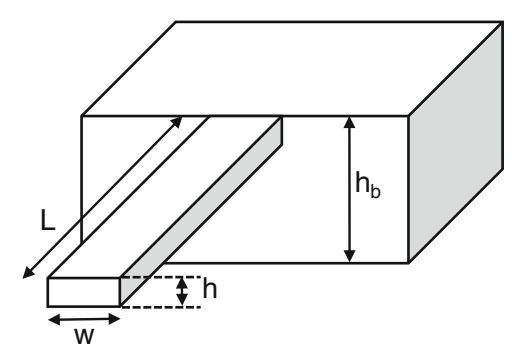
where w the width and h_b is the thickness of the supporting substrate. The $Q \propto L/w$ proportionality has also been derived for doubly clamped beams ending into a wide plate of the same thickness $(h_s = h)$ by Cross and Lifshitz [28].

In the case that the supporting structure is sufficiently thick relative to the wavelength of propagating waves, the base may be approximated as a semi-infinite elastic medium. Again, assuming that the material properties of the base and cantilever are the same and taking $\nu = 0.3$, the clamping loss expression changes to

$$Q_{\text{clamping}}^{-1} \approx 0.31 \frac{w}{L} \left(\frac{h}{L}\right)^4.$$
 (2.18)

As can be seen from (2.17) and (2.18), slight changes in the boundary conditions result in big changes in the geometrical dependence of clamping loss. From these two specific cases it is possible to derive a few general rules in order to minimize clamping losses, also for doubly clamped beams. The comparison of (2.17) and (2.18) makes it clear that clamping losses are significantly reduced with a thick body chip which mechanically behaves like a semi-infinite substrate. But in both cases (plate substrate and semi-infinite substrate), clamping losses are reduced for long and slender beams. In this case the mechanical coupling into the substrate of the vibrational energy is minimized.

Fig. 2.7 Schematic representation of the clamping area of a nanobeam resonator



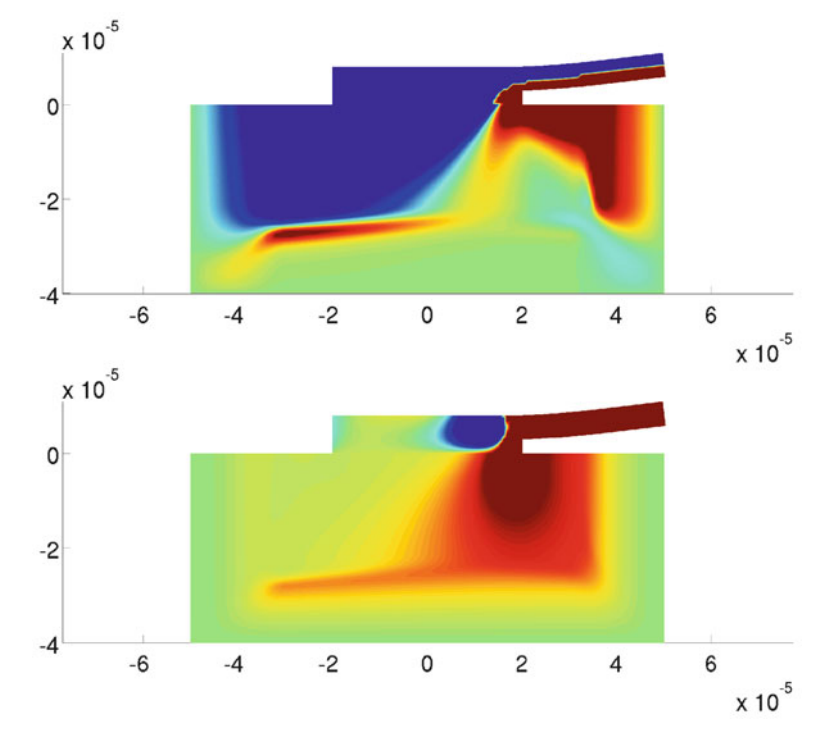


Fig. 2.8 Displacement field in *x* (*top*) and *y* (*bottom*) direction of a cantilever simulated with HiQLab. The anchor is modelled as a semi-infinite domain by terminating it with a perfectly matched layer (PML). *Red* areas experience a positive displacement *blue* areas a negative displacement [29]

Clamping losses can also be determined by means of the finite element method (FEM). The computed energy that is lost over the anchors is compared to the energy stored in the system. In order to lose energy in a FEM simulation it is assumed that all elastic waves radiating into the substrate would not be reflected and thus would be lost. Therefore, the substrate needs to be modelled as a semi-infinite domain which requires the so-called perfectly matched layer (PML) at the boundaries. A proper PML absorbs all incoming waves, regardless of the incident angle. Figure 2.8 shows the simulated displacement field of a micro cantilever with an anchor terminated with a PML which absorbs all incoming elastic waves.

2.2.2 Membranes

Another resonator design for which a clamping loss model has been derived are membranes. An analytical model based on the coupling of membrane modes to free modes of a semi-infinite substrate has been fully developed [30, 31]. The asymptotic limit for a square membrane is given by

$$Q_{\text{clamping}} \approx 1.5 \frac{\rho_s}{\rho_r} \eta^3 \frac{n^2 m^2}{(n^2 + m^2)^{3/2}} \frac{L}{h}$$
 (2.19)

with the "acoustic mismatch" (phase velocity ratio) between a semi-infinite substrate and the resonator

$$\eta \approx \sqrt{\frac{E_s \, \rho_r}{\rho_s \, \sigma}} \tag{2.20}$$

with the mass densities ρ_s and ρ_r of the substrate and resonator, respectively, and the Young's modulus of the substrate E_s . Equation (2.19) is valid under the condition $n, m \gg \sqrt{n^2 + m^2}/\eta$. Typically, $\eta \gg 1$ for, e.g., silicon nitride membranes and thus the radiation loss model is valid for all $n \sim m$. Destructive interference of the waves radiating into the substrate can lead to a suppression of the acoustic radiation loss for increasing harmonic modes (n = m) [30]. From (2.19) it can be seen that acoustic radiation loss is minimal for harmonic modes n = m and the envelope of maximal values is increasing linearly with the mode numbers $Q_{\text{clamping}} \propto n$.

It has repeatedly been shown that especially lower mode Qs are sensitive to the chip mounting conditions and that these Qs can be increased by minimizing the contact between chip and support [32–35]. A successful way of suppressing radiation losses is to locate the mechanical structure within a well-designed phononic bandgap structure. This removes the free frame modes around the membrane and suppresses the probability of phonon tunnelling, i.e. radiation loss [36, 37].

2.3 Intrinsic Damping

Under *intrinsic damping* all energy loss mechanisms that take place within, that is on the surface or in the bulk of the material of the resonating structure, are summarized. In the following Sect. 2.3.1 various intrinsic damping mechanisms are introduced. All of the presented mechanisms are valid for unstressed resonators, such as beams and plates. In Sect. 2.3.2 on page 81, the damping dilution effect in resonators under tensile stress is introduced. The magnitude of the dilution is given by the *damping dilution factor*. The resulting quality factor under tensile stress can be estimated by multiplying a particular intrinsic quality factor listed in Sect. 2.3.1 by the particular damping dilution factor derived in Sect. 2.3.2.

2.3.1 Intrinsic Damping Mechanisms

In this subsection, the most common damping mechanisms occurring in nanomechanical resonators are introduced. All the mentioned models apply for unstressed flexural beam resonators. The damping mechanisms can be divided into two

categories: friction losses and fundamental losses. The first category is based on the friction coming from material imperfections that happen in the bulk and on the surface of a resonator. The latter category are damping mechanisms constituting the fundamental loss limits present even in an ideal frictionless material. These fundamental loss mechanisms are based on interactions between the strain field inside the resonator during vibration and phonons and electrons.

2.3.1.1 Friction Losses

Friction losses origin from irreversible motion of atoms during vibration. This atomic motion can be caused by, e.g., defect dislocations in crystalline materials, grain boundary slipping in metals, phase boundary slipping in bilayer structures, or molecular chain movement in amorphous materials. Friction loss mechanisms are a ubiquitous phenomenon and are best described by the anelasticity framework.

Materials which exhibit both elastic and viscous, due to friction losses, behavior are called *viscoelastic*. A special type of viscoelastic materials that do not show any lasting deformation are called *anelastic*. There are various models to describe the anelastic response. These models are often represented by "spring-dashpot" combinations which help model materials with multiple friction loss mechanisms. The *standard linear solid* model (SLS) (see Fig. 2.9a), also called *Zener model*, is often used to describe a material with a single frequency dependent friction loss mechanism (or relaxation mechanisms). Figure 2.9b shows the response of an anelastic material, represented by the SLS model, to a constant stress σ_0 . From the response it can be seen that the induced strain ε is lagging behind the applied stress. From an immediate unrelaxed strain response ε_u , the material creeps exponentially with the relaxation time τ_{σ} until it reaches the relaxed strain ε_r .

From Fig. 2.9b it is obvious that an oscillatory displacement-induced stress $\sigma(t)$ and the accompanying oscillating strain $\varepsilon(t)$ are not perfectly in phase. If the strain lags behind the stress by a phase δ for an oscillatory stress, we write

$$\varepsilon(\omega) = \varepsilon_0 \sin(\omega t)$$

$$\sigma(\omega) = \sigma_0 \sin(\omega t + \delta).$$
(2.21)

Using the appropriate trigonometric identity, the stress can be expanded to

$$\sigma(\omega) = \sigma_0 \sin \omega t \cos \delta + \sigma_0 \cos \omega t \sin \delta. \tag{2.22}$$

It can be seen that the stress consists of two components: one of magnitude $(\sigma_0 \cos \delta)$, in phase with the strain, and the other of magnitude $(\sigma_0 \sin \delta)$, $\pi/2$ out of phase with the strain.

The stress–strain relationship can therefore be defined by a quantity E' in phase with the strain and by a quantity E'', $\pi/2$ out of phase with the strain.

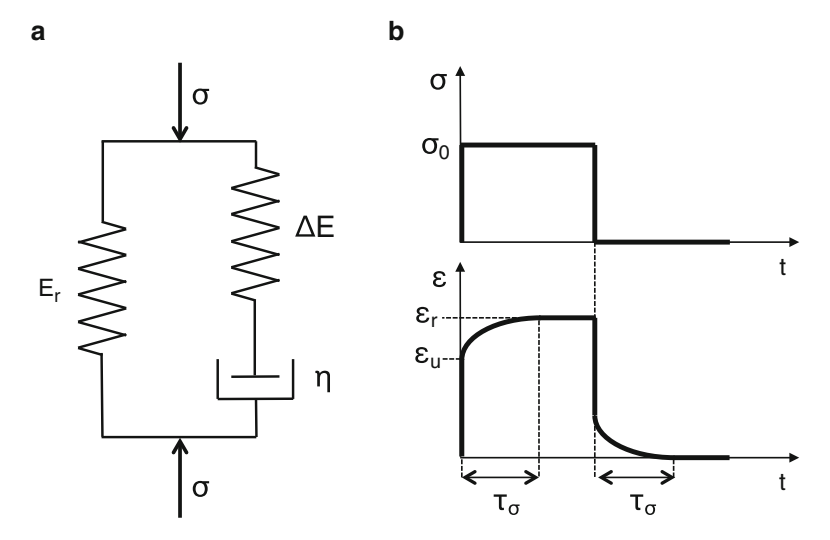


Fig. 2.9 (a) Spring-dashpot model of standard linear solid (SLS), also known as Zener model. (b) Time response of SLS to constant stress

$$\sigma = \varepsilon_0 E' \sin \omega t + \varepsilon_0 E'' \cos \omega t \tag{2.23}$$

where

$$E' = \frac{\sigma_0}{\varepsilon_0} \cos \delta \ , \ E'' = \frac{\sigma_0}{\varepsilon_0} \sin \delta \tag{2.24}$$

E' and E'' are the real and an imaginary part of the complex Young's modulus $E^*(\omega) = E'(\omega) + iE''(\omega)$, respectively. E' is called *storage Young's modulus* and defines the energy stored in the specimen due to the applied strain. E'' is the *loss Young's modulus* and represents the dissipation of energy.

Since the damping of a linear resonator typically is measured via the quality factor Q (see Sect. 1.2.1) it is of interest to express the relationship between the intrinsic material damping to Q. According to the definition (1.136), Q is the ratio of the total stored energy over the energy lost during one cycle of oscillation.

The energy (ΔW) dissipated per cycle in a volume unit of material can be calculated by

$$\Delta W = \oint \sigma d\varepsilon = \int_0^{2\pi/\omega} \sigma \frac{d\varepsilon}{dt} dt. \tag{2.25}$$

Substituting for σ and ε , this term becomes

$$\Delta W = \omega \varepsilon_0^2 \int_0^{2\pi/\omega} (E' \sin(\omega t) \cos(\omega t) + E'' \cos^2(\omega t)) dt.$$
 (2.26)

The integral is solved by using the trigonometric identities $\sin \omega t \cos \omega t = \frac{1}{2} \sin 2\omega t$ and $\cos^2 \omega t = \frac{1}{2} (1 + \cos 2\omega t)$, which results in

$$\Delta W = \pi E'' \varepsilon_0^2. \tag{2.27}$$

The maximum energy stored in a unit volume of material can be calculated by integrating the first term in (2.26) only over a quarter-cycle rather than over the complete period

$$W = E'\omega\varepsilon_0^2 \int_0^{\pi/(2\omega)} \sin(\omega t) \cos(\omega t) dt$$
 (2.28)

which evaluated as before gives

$$W = \frac{1}{2}E'\varepsilon_0^2. \tag{2.29}$$

Substituting (2.27) and (2.29) in the definition of Q (1.136) yields

$$Q_{\text{friction}} = 2\pi \frac{W}{\Delta W} = \frac{E'}{E''}.$$
 (2.30)

This equation can further be extended by the definitions for E' and E'' (2.24) which gives the definition of $\tan \delta$ also called the *loss tangent*

$$Q_{\text{friction}} = \frac{E'}{E''} = (\tan \delta)^{-1}. \tag{2.31}$$

Solid materials typically exhibit relatively low intrinsic damping Q>100 or $\tan\delta<0.01\approx\delta$. Hence, the dynamic mechanical characteristic can be defined in terms of the Young's modulus $\|E^*\|\approx E'=E$ and the quality factor due to intrinsic material damping Q_{intr} . Figure 2.10 shows the loss tangent as a function of the Young's modulus for a variety of different materials. It can clearly be seen that the materials typically used in micro and nanofabrication show a combination of high Young's modulus and low damping.

Anelastic materials can exhibit a strongly frequency dependent behavior. Furthermore, materials can have multiple relaxation mechanisms at different frequencies. The dynamic behavior of the standard linear solid, representing a single relaxation mechanism, can be calculated and the dynamic modulus is given by [39]

$$E'(\omega) = E_r + \Delta E \frac{\omega^2 \tau_{\varepsilon}^2}{1 + \omega^2 \tau_{\varepsilon}^2}$$

$$E''(\omega) = \Delta E \frac{\omega \tau_{\varepsilon}}{1 + \omega^2 \tau_{\varepsilon}^2}$$
(2.32)

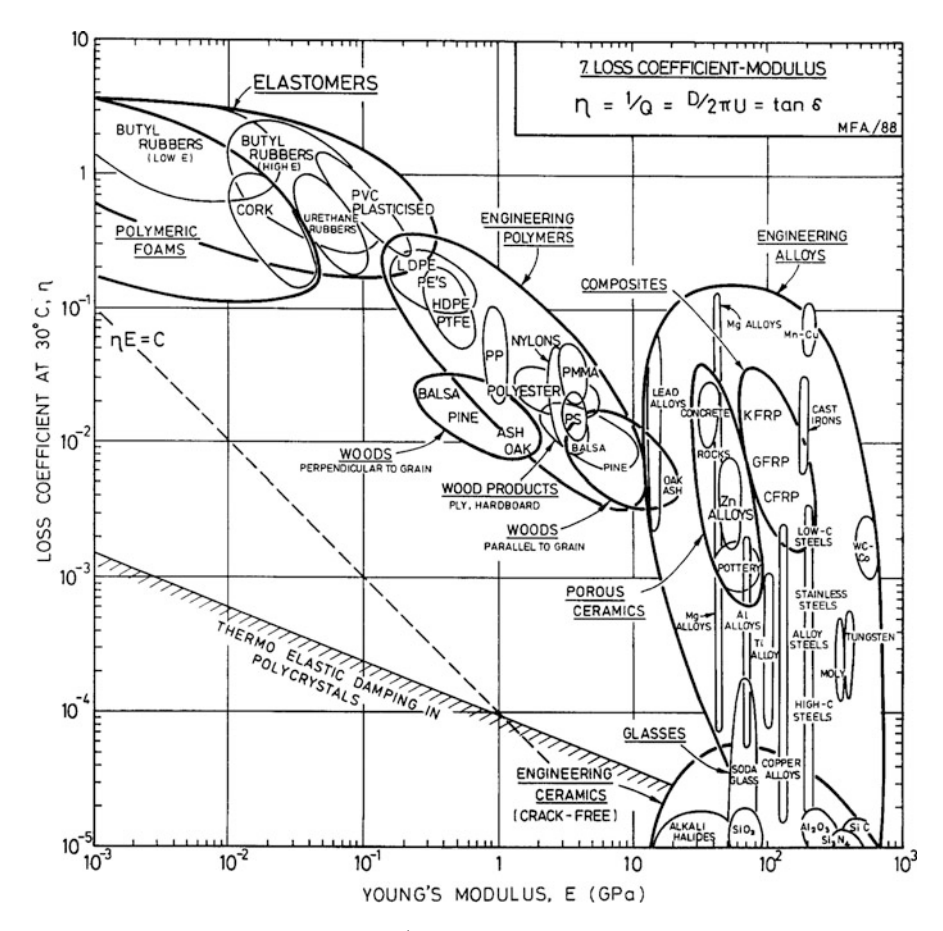


Fig. 2.10 Loss factor $(\eta' \approx \tan \delta \approx Q_{\rm friction}^{-1})$ of various common materials (Reprinted from [38], with permission from Elsevier)

with

$$\tau_{\varepsilon} = \frac{\eta}{\Delta E} \tag{2.33}$$

being the relaxation time at constant strain with the damping constant η (see dashpot in Fig. 2.9a). In contrast, the relaxation time at constant stress, as shown in Fig. 2.9b is given by

$$\tau_{\sigma} = \tau_{\varepsilon} \frac{E_r + \Delta E}{E_r}.$$
 (2.34)

These equations are called the *Debye equations* (they were first derived by Debye for the dielectric relaxation phenomena). The qualitative behavior of E' and E'' as

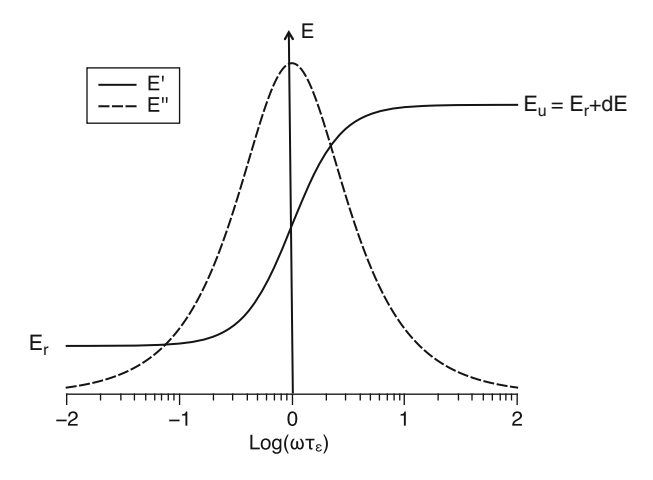


Fig. 2.11 Variation of dynamic modulus versus $\omega \tau_{\varepsilon}$

functions of $\omega \tau_{\varepsilon}$ is shown in Fig. 2.11. E' is undergoing the transition from the unrelaxed Young's modulus $E_u = E_r + \Delta E$ at $(\omega \tau_{\varepsilon} \gg 1)$ to the relaxed Young's modulus E_r at $(\omega \tau_{\varepsilon} \ll 1)$. Hence the term relaxation mechanism is often used here equivalently to loss mechanism. The curve E'' has a maximum for $\omega \tau_{\varepsilon} = 1$ at which $E''_{\max} = \frac{1}{2} \Delta E$. The shape of E'' is referred as a Debye peak.

The internal friction $\tan \delta$ can be obtained using (2.31)

$$\tan \delta(\omega) = \frac{E''}{E'} = \Delta E \frac{\omega \tau_{\varepsilon}}{E_r + E_u \omega^2 \tau_{\varepsilon}^2}.$$
 (2.35)

The internal friction varies as a Debye peak. Since E_r and E_u are of the same order of magnitude and a lot larger than ΔE , (2.35) can be written as

$$Q_{\text{friction}}^{-1} = \tan \delta(\omega) = \Delta \frac{\omega \overline{\tau}}{1 + \omega^2 \overline{\tau}^2}$$
 (2.36)

with the so-called relaxation strength

$$\Delta = \frac{\Delta E}{\sqrt{E_r E_u}},\tag{2.37}$$

where τ_{ε} was replaced by the geometrical average of the strain at constant strain and stress $\overline{\tau} = \sqrt{\tau_{\sigma}\tau_{\varepsilon}}$ for generalization purposes. The internal friction has a maximum at $\omega \overline{\tau} = 1$ and the peak height is related to the relaxation strength Δ

$$Q_{\min}^{-1} = [\tan \delta(\omega)]_{\max} = \frac{1}{2}\Delta \tag{2.38}$$

Dissipation peaks of this form (Debye peaks) are quite ubiquitous. They occur for many different relaxation mechanisms but also for phonon–phonon interaction and thermoelastic relaxation, as discussed in the next subsection.

In many of these examples there is not just one single relaxation time $\overline{\tau}$, and therefore one sees multiple or broadened Debye peaks. One can understand qualitatively why there is a peak in dissipation when $\omega \overline{\tau} = 1$ in the following way: If the ω is much smaller than the effective relaxation rate ($\omega \ll 1/\overline{\tau}$) of the solid, then the system remains essentially in equilibrium and very little energy is dissipated. This regime comparable to an isothermal process in thermodynamics. If the vibration frequency is much larger than the effective relaxation rate ($\omega \gg 1/\overline{\tau}$), the system has no time to relax and again very little energy is dissipated. This regime corresponds to an "adiabatic" process. It is only when the vibration frequency is on the order of the system's effective relaxation rate that appreciable dissipation occurs (2.38). The full picture may be more complicated.

Time-Temperature Equivalence

Besides being frequency-dependent, as shown in this section, relaxation mechanisms are also dependent on temperature. The principle of time-temperature equivalence implies that a specific relaxation mechanism in the material can equally be crossed by either changing the frequency or temperature. The damping behavior at one temperature can be related to that at another temperature by changing the time-scale, that is the frequency, as illustrated in Fig. 2.12. The two temperature responses are connected via the *shift factor* a_T .

During a material relaxation the storage modulus, as depicted in Fig. 2.11, is crossing between two energy levels E_r and E_u . Hence, such a transition can be modelled as a *two level system*, in analogy to the two energy levels, e.g., of a chemical reaction. The jump between the levels requires the activation energy ΔH . Such a transition with a constant activation energy can then be described by *Arrhenius' law* [40]

$$\omega = \omega' \, e^{-\frac{\Delta H}{k_B T}}. \tag{2.39}$$

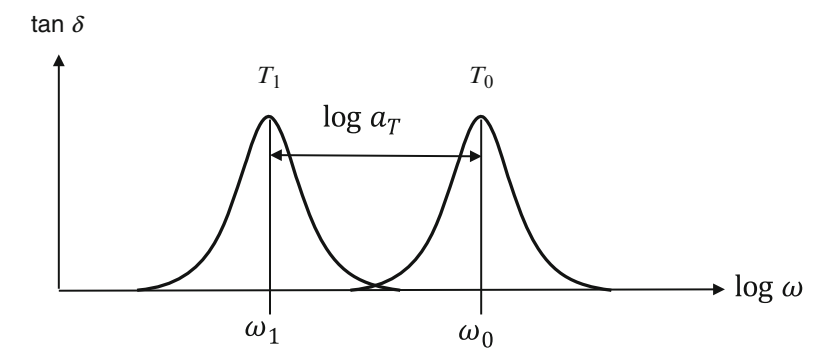


Fig. 2.12 Schematic illustration of the time-temperature equivalence

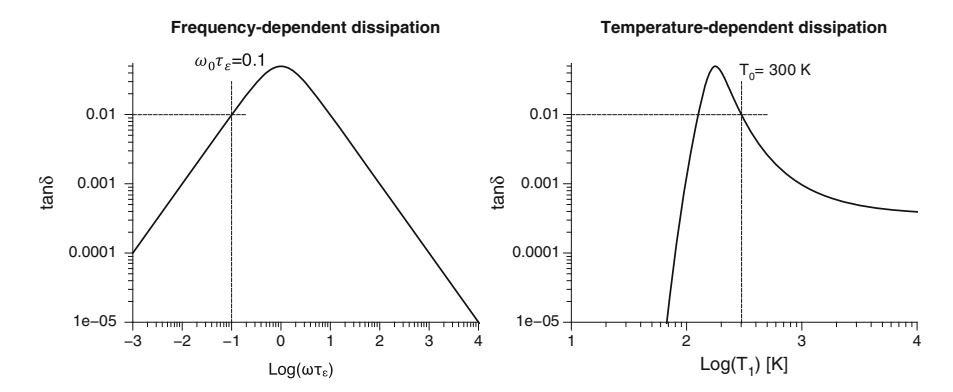


Fig. 2.13 Schematic illustration of a Debye peak in the frequency and the temperature domain, for a reference temperature $T_0 = 300 \, \text{K}$ at $\omega_0 \tau_\varepsilon = 0.1$, damping strength $\Delta E/E = 0.1$, and activation energy $\Delta H = 1000 k_B$

With (2.39), the shift factor a_T , introduced in Fig. 2.12, can now readily be calculated

$$\log a_T = \frac{\log \omega_0}{\log \omega_1}$$

$$= \frac{\Delta H}{k_B} \left(\frac{1}{T_1} - \frac{1}{T_0} \right). \tag{2.40}$$

With the shift factor it is possible to describe the Debye peak (2.36) as a function of temperature

$$Q_{\text{friction}}^{-1}(T_1) = \tan \delta = \frac{\Delta E}{E} \frac{\omega_0 \tau_{\varepsilon} \exp\left\{\frac{\Delta H}{k_B} \left(\frac{1}{T_1} - \frac{1}{T_0}\right)\right\}}{1 + \omega_0^2 \tau_{\varepsilon}^2 \exp\left\{2\frac{\Delta H}{k_B} \left(\frac{1}{T_1} - \frac{1}{T_0}\right)\right\}}$$
(2.41)

A transition through a Debye peak in the frequency and the temperature domain is visualized in Fig. 2.13. This shows that a material relaxation mechanism can be crossed either by varying the frequency or the temperature. In the example the frequency was fixed below the peak maximum. The transition can then be crossed by lowering the temperature. For relatively large activation energies small changes in temperature (within one order of magnitude) have the same effect as large changes of frequency (over four orders of magnitude). Hence, to measure material transitions it is a common technique to fix the oscillation frequency and ramp the temperature.

From Fig. 2.13 it becomes further evident that specific damping mechanisms can be frozen out. Width decreasing temperature, after the Debye peak transition, the loss tangent diminishes quickly.

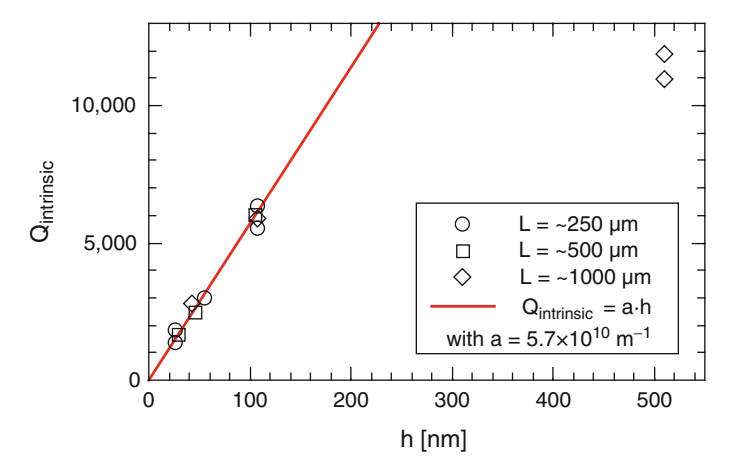


Fig. 2.14 Intrinsic quality factors of silicon-rich silicon nitride membranes as a function of membrane thickness. Data taken from [43]

Surface Friction

Surface friction loss can be the dominant source of damping in submicrometer thick beams when the surface-to-volume ratio increases. Surface loss is assumed to be caused by adsorbates on the surface [41], surface roughness [42], or surface impurities, e.g., as a result from fabrication processing [43]. Surface loss has, e.g., been found to be the dominating damping mechanism in nanomechanical silicon nitride cantilevers [44], and strings and membranes [43]. An estimate of surface loss is given by [41, 44]

$$Q_{\text{surface}} = \frac{wh}{2\delta_S(3w+h)} \frac{E}{E_S''}$$
 (2.42)

where δ_S and E_S'' are the thickness and the loss Young's modulus of the lossy surface layer and w is the beam width. For a wide beam $(w \gg h)$, surface damping becomes proportional to the inverse of the beam thickness

$$Q_{\text{surface}} = \frac{1}{6\delta_S} \frac{E}{E_S''} \cdot h. \tag{2.43}$$

This linear proportionality with the resonator thickness has, e.g., been observed with silicon nitride membranes of various thickness, as shown in Fig. 2.14.

2.3.1.2 Fundamental Losses

In this subsection, two particular fundamental loss mechanisms are introduced, namely thermoelastic loss and phonon-phonon interaction loss (also called

Akhiezer damping). Both mechanisms are coming from non-reversible heat flow inside a solid under period deformation. The heat flow (thermal relaxation) generated entropy which causes loss of energy. In thermoelastic damping the thermal relaxation happens between strain-induced temperature differences in different spatial areas in the solid. In contrast, in Akhiezer damping the thermal relaxation happens between strain-induced temperature difference in normal modes of the atomic lattice.

Similar to the description of friction losses discussed in the previous subsection, the two particular fundamental losses discussed in this subsection can be modelled with Zener's approach as Debye peaks [see (2.36)]

$$Q^{-1}(\omega) = \Delta \frac{\omega \tau}{1 + (\omega \tau)^2}$$
 (2.44)

with the particular relaxation strength Δ and relaxation time τ . The maximal loss of $\frac{1}{2}\Delta$ is reached when $\omega\tau=1$. In contrast to friction losses, the relaxation strength and relaxation time for the fundamental losses can be modelled precisely. Also, where the temperature dependence of friction loss mechanisms is described by a chemical approach, by means of Arrhenius' law, fundamental losses have a known linear temperature dependence. Both mechanisms discussed subsequently linearly decrease with temperature.

Additionally to the two loss mechanisms discussed in the subsection, there are other fundamental mechanisms. For example in materials with free electrons, such as metals and semiconductors, elastic waves can also interact with the electron-cloud. Acoustic waves can induce forces on electrons. Energy is dissipated by Joule heating from the resistive electron-movement. This so-called phonon–electron interaction loss in conductor will not be discussed here. More details can be found elsewhere [45].

Thermoelastic Damping

Strain due to the mechanical motion generates differences in the temperature at different locations in the resonator. The strain field is coupled to the temperature field by the material's thermal-expansion coefficient α_{th} of the resonator material. The locally generated heat flow between points of different temperatures is irreversible, that is it creates entropy, which results in energy dissipation. This intrinsic damping mechanism is called thermoelastic damping, and was measured in micromechanical silicon resonators for the first time by Roszhart in 1990 [46].

During transverse flexural vibration of an unstressed beam, one side is under compression while the other side is under tension. The side under compression becomes warmer while the side with tension becomes colder. This temperature gradient across the beam thickness causes the energy loss. The thermoelastic loss for a beam under transverse flexural vibration has been solved by Zener in the 1940s [47] and is approximately given by

$$\Delta_{\text{TED}} = \frac{E\alpha_{\text{th}}^2 T_0}{\rho c_p} \tag{2.45}$$

and the relaxation time

$$\tau_{\text{TED}} = \frac{h^2}{\pi^2 \gamma} \tag{2.46}$$

where $\chi = \kappa/(\rho c_p)$ is the thermal diffusivity of the material. κ and c_p are the thermal conductivity and the specific heat capacity, respectively. τ_{TED} is the characteristic time required for the heat to diffuse across the beam thickness. The maximum energy in an oscillation cycle is lost if the cycle time of the resonating beam is similar to τ_{TED} which is the time the heat needs to relax over the beam thickness. For lower vibration frequencies, the system stays more or less in equilibrium (isothermal state) and only little energy is lost. If the frequency of vibration is higher than the relaxation rate of the heat flow, the heat has no time to relax (adiabatic state) and again very little energy is lost.

The exact expression for thermoelastic damping in vibrating thin beams was obtained by Lifshitz and Roukes in 2000 [48], which has shown that Zener's model is an accurate approximation. Thermoelastic damping has also been modelled for bilayered beams [49].

Phonon-Phonon Interaction Loss (Akhiezer Damping)

Phonon–phonon interaction loss is a fundamental source of dissipation in crystalline material. The loss comes from the *Akhiezer effect*, which is the interaction of an oscillating low-frequency strain field with the existing high-frequency atomic thermal motion in a crystal lattice. The oscillating deformation periodically dilates the atomic crystal. The dilatation changes the elastic constant in the crystal, which changes the normal mode frequencies of the atoms. The effect of the dilatation on the normal mode frequencies is described by the Grüneisen constant γ_G . A positive dilatation (stretching) causes a frequency decrease (reduction of the temperature), and a negative dilatation (compression) causes a frequency increase (increase in temperature). However, the oscillating strain does not act on all normal modes equally. Hence, a deformation results in a temperature difference between different normal modes. During a periodic low-frequency deformation, the modes with different temperatures relax toward the mean temperature value. In this way, energy is lost by an increase of entropy from the heat flow between phonon modes with different temperatures.

Under the assumption that the strain field frequency ω is lower than the thermal phonon frequency (higher THz-regime), Akhiezer damping can be modelled by Zener's approach with a Debye peak with the relaxation strength [45]

$$\Delta_{\text{Akhiezer}} = \frac{c_p \rho T_0 \gamma^2}{F} \tag{2.47}$$

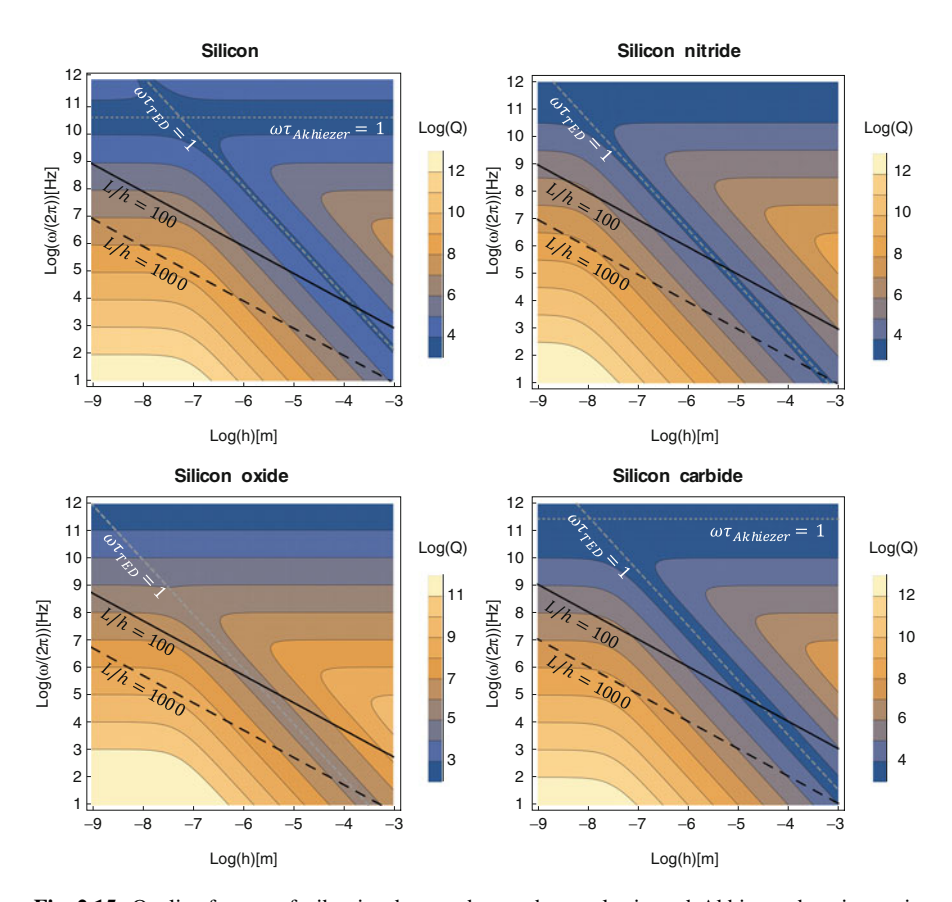


Fig. 2.15 Quality factors of vibrating beams due to thermoelastic and Akhiezer damping estimated for four typical nanomechanical materials as a function of beam thickness h and flexural frequency $\omega/(2\pi)$. The gray dashed and dotted lines represent the loss maxima for thermoelastic and Akhiezer losses. The black lines show the fundamental resonance frequencies of a doubly clamped beam resonator (bridge) of the specific material for two different ratios of length L to thickness h. The plots are based on the specific material properties listed in Table 4 in [50]

and the thermal relaxation time

$$\tau_{\text{Akhiezer}} = \frac{3\kappa}{c_p E}.\tag{2.48}$$

The intra-mode relaxation happens on a very short time-scale, typically in pico-seconds. Hence, the effect of Akhiezer damping first becomes important at frequencies in the higher GHz-regime.

In Fig. 2.15 the combined quality factor expected for thermoelastic and Akhiezer damping $(Q^{-1} = Q_{\text{TED}}^{-1} + Q_{\text{Akhiezer}}^{-1})$ of flexural beams of various materials is plotted as a function of the beam thickness h and vibrational frequency $\omega/(2\pi)$. It can be

seen that the two fundamental loss mechanisms are strongly material dependent. On the one hand, thermoelastic damping in a typical nanomechanical beam ($10 < h < 1000\,\mathrm{nm}$ and L/h > 100) allows for very high quality factors of the fundamental mode of more than a million for silicon. For thick silicon nitride beams, on the other hand, thermoelastic damping can become the limiting loss mechanism, an effect that has been observed with singly clamped cantilevers [44]. As a general rule, the effect of thermoelastic damping can be circumvented by designing thin beams (absolute: $h < 1\,\mu\mathrm{m}$, and relative: L/h > 100). Phonon–phonon interaction loss (Akhiezer effect) first starts to play a role at rather high frequencies in the GHz-regime, which can be reached with very thin ($h < 10\,\mathrm{nm}$) and short (L/h < 100) beams. Higher order flexural modes increase the vibrational frequency which generally increases the effect of thermoelastic and Akhiezer damping.

2.3.2 Damping Dilution in Strings and Membranes

In the search for high-Q mechanical resonators, in 2006 Verbridge et al. [51] have found that highly stressed silicon nitride nanostrings have extraordinarily high quality factors compared to corresponding cantilever beams in the same frequency range. They showed that Q is increasing for long strings and has obtained maximal Q values of over a million for 325 μ m long nanostrings [52]. A similar finding was made with silicon nitride membranes which showed quality factors of over one million at room temperature [53]. The observed increase in Q is coming from a stress-induced damping dilution [54, 55], as will be discussed here.

As per the definition, Q is the ratio of stored versus lost energy over one cycle of oscillation. In the case of, e.g., a cantilever, the energy is stored and lost by its bending. In contrast, strings and membranes can additionally store and dissipate energy in the lateral elongation during vibration. But most importantly, string and membranes build up a lot of potential energy when the vibrational deflection has to work against the high lateral tensile stress. According to (1.136), the quality factor of a string or a membrane can be described by [19, 35]

$$Q = 2\pi \frac{W_{\text{tensile}} + W_{\text{elongation}} + W_{\text{bending}}}{\Delta W_{\text{elongation}} + \Delta W_{\text{bending}}}$$
(2.49)

where $W_{\rm tension}$ is the stored elastic energy required to deflect the string against the tensile force. $\Delta W_{\rm elongation}$ and $\Delta W_{\rm bending}$, and $W_{\rm elongation}$ and $W_{\rm bending}$ are the lost and stored energy due to elongation and bending, respectively.

Assuming that the magnitude of the tensile pre-stress is dominating the mechanical behavior in strings and membranes, and by defining the intrinsic damping, as introduced in Sect. 2.3, to be equal for elongation and bending $Q_{\rm intrinsic} = Q_{\rm elongation} = \left(2\pi \frac{W_{\rm elongation}}{\Delta W_{\rm elongation}}\right) = Q_{\rm bending} = \left(2\pi \frac{W_{\rm bending}}{\Delta W_{\rm bending}}\right)$, (2.49) can then be simplified to

$$Q \approx \alpha_{\rm dd} \cdot Q_{\rm intrinsic}$$
 (2.50)

with the damping dilution factor

$$\alpha_{dd} = \left[\frac{W_{\text{bending}}}{W_{\text{tensile}}} + \frac{W_{\text{elongation}}}{W_{\text{tensile}}} \right]^{-1}.$$
 (2.51)

Since, by definition, in a string or membrane W_{tensile} is a lot larger than the energies stored in bending and elongation, the damping dilution factor becomes larger than unity. This means that large potential energy from by the tensile stress is "diluting" the intrinsic losses and Q gets enhanced.

The effect of the additional energy stored in the tension described in (2.49) can also be looked at from a different angle. According to (1.143), the quality factor is the resonance frequency f_r divided by the peak width Δf .

$$Q = \frac{f_r}{\Delta f} = 2\pi \frac{W}{\Delta W} \tag{2.52}$$

Thus, the tensile tension increases the resonance frequency (which is equal to the stored energy) while the peak width (which is equal to the damping or energy lost) remains constant. Assuming that an added tensile stress does not alter the intrinsic losses ($\Delta f = \text{constant}$), the tensile stress increases the frequency and hence the quality factor.

2.3.2.1 Damping Dilution in Strings

The damping dilution in strings can readily be obtained from (2.51) based on the respective energies and the respective string modeshape given by (1.64)

$$U(x) = U_0 \phi_n(x) \tag{2.53}$$

with the normalized modeshape

$$\phi_n(x) = \underbrace{\sin(\beta_{\sigma}x)}_{\text{sine shape}} + \underbrace{\frac{\beta_{\sigma}}{\beta_E} \left[e^{-\beta_E x} - \cos(\beta_{\sigma}x) \right]}_{\text{edge shape}}$$
(2.54)

and the wavenumbers related to the tensile stress $\beta_{\sigma} = \frac{n\pi}{L}$ and flexural rigidity of a membrane $\beta_{E} = \sqrt{\frac{\sigma A}{EL}}$, respectively.

The energy stored in the work against the tensile stress can be calculated from (see Table 1.1)

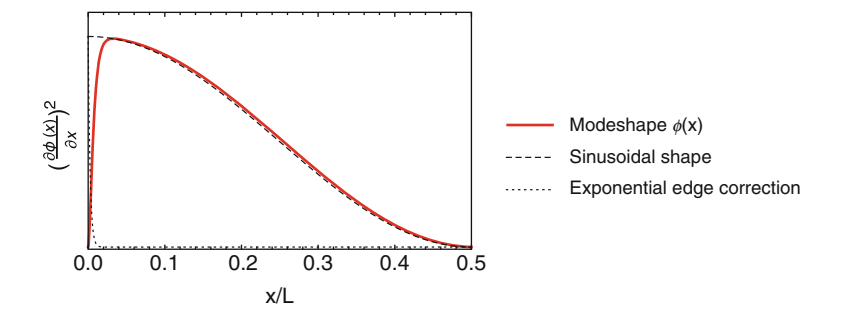


Fig. 2.16 Qualitative illustration of the tensile energy density in a string of length L

$$W_{\text{tension}} = \frac{1}{2}\sigma A \int_0^L \left(\frac{\partial u}{\partial x}\right)^2 dx$$
$$\approx \frac{1}{4}U_0^2 \sigma A L \beta_\sigma^2. \tag{2.55}$$

Apparently, the tensile stored energy can be approximated by a single term coming from the bending of the sinusoidal modeshape. The effect of the exponential edge term in (2.53) is relatively small and can be dismissed for the calculation of the total tensile energy, as can be seen from the tensile energy density plotted in Fig. 2.16.

Similarly, the energy stored due to the string bending can be calculated (from Table 1.1)

$$W_{\text{bending}} = \frac{1}{2} E I_y \int_0^L \left(\frac{\partial^2 u}{\partial x^2}\right)^2 dx$$

$$\approx \underbrace{\frac{1}{4} U_0^2 E I_y \beta_\sigma^4 L}_{\text{sine shape}} + \underbrace{\frac{1}{2} U_0^2 E I_y \beta_\sigma^2 \beta_E}_{\text{edge shape}},$$
(2.56)

which results in two terms: one coming from the anti-nodal bending of the sine modeshape, and a second coming from the bending at the edge where the string is clamped. The bending energy density is illustrated in Fig. 2.17. From this plot it can be seen that the highest bending energy density is located near the edge of the string.

Equally, the energy stored in the elongation of the string is (from Table 1.1)

$$W_{\text{elongation}} = \frac{1}{8} EA \int_0^L \left(\frac{\partial u}{\partial x}\right)^4 dx$$
$$\approx \frac{3}{64} U_0^4 EAL \beta_\sigma^4. \tag{2.57}$$

Similar to the tensile energy, the elongational energy can be approximated by a single term coming from the sine modeshape. The effect of the exponential edge correction can be dismissed.

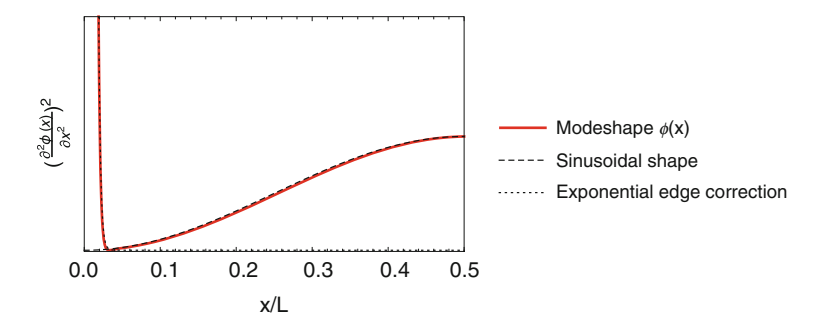


Fig. 2.17 Qualitative illustration of the bending energy density of a string of length L

With (2.62), (2.56), and (2.57) the damping dilution factor (2.51) for the "one-dimensional case" of a string can now readily be calculated

$$\alpha_{\rm dd,1D} = \left[\underbrace{\left(\frac{\beta_{\sigma}}{\beta_{E}} \right)^{2} + \frac{2}{\beta_{E}L}}_{\frac{W_{\rm bending}}{W_{\rm tensile}}} + \underbrace{\frac{9}{4} \left(\frac{U_{0}}{h} \right)^{2} \left(\frac{\beta_{\sigma}}{\beta_{E}} \right)^{2}}_{\frac{W_{\rm elongation}}{W_{\rm tensile}}} \right]^{-1}.$$
 (2.58)

The first two terms coming from the bending energy are independent of the vibrational amplitude U_0 . In contrast, the last term coming from the energy stored in the string elongation is a function of the amplitude squared. At large amplitudes, the elongational energy is accruing and the measured quality factor becomes a function of $Q \propto U_0^{-2}$. Such a measured effect could be interpreted as nonlinear damping as introduced in Sect. 1.2.3, but in reality it simply is an effect coming from the amplitude dependency of the damping dilution. Such an effect could readily happen when, e.g., measuring on ultrathin graphene resonators (h = 0.35 nm). In most cases, the amplitudes are a lot smaller than the resonator thickness and the damping dilution factor (2.58) can be reduced to the influence of the bending energy only

$$\alpha_{\rm dd,1D} \approx \left[\underbrace{\left(\frac{\beta_{\sigma}}{\beta_{E}} \right)^{2}}_{\text{sine shape}} + \underbrace{\frac{2}{\beta_{E}L}}_{\text{edge shape}} \right]^{-1},$$
(2.59)

which for a string with rectangular cross section with $I_y = \frac{wh^3}{12}$ becomes

$$\alpha_{\rm dd,1D} = \left[\underbrace{\frac{(n\pi)^2 E}{12 \sigma} \left(\frac{h}{L}\right)^2}_{\text{sine shape}} + \underbrace{\frac{1}{\sqrt{3}} \sqrt{\frac{E}{\sigma}} \left(\frac{h}{L}\right)}_{\text{edge shape}} \right]^{-1}.$$
 (2.60)

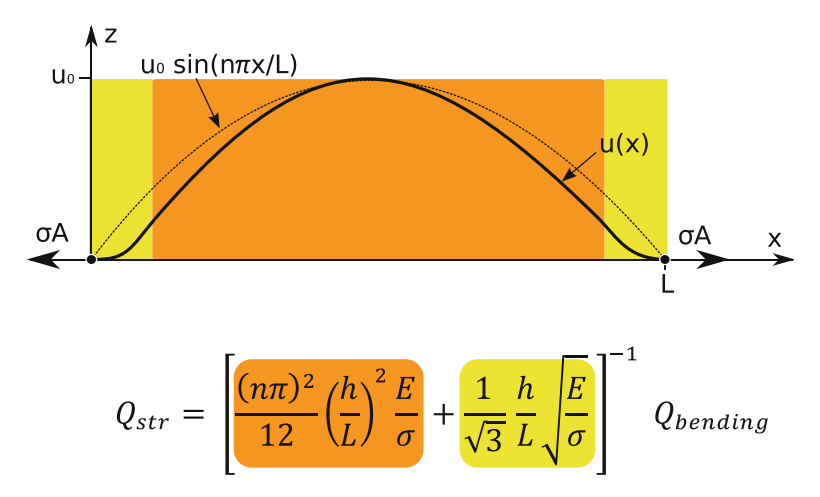


Fig. 2.18 Schematic drawing explaining the damping dilution in strings (2.59) for generic bending related damping mechanisms $Q_{\text{intr}} = Q_{\text{bending}}$. The first term comes from the damping due to the sinusoidal string bending. The second term comes from the local bending near the clamping

This form of the damping dilution factor had first been derived in 1994 for the case of a loaded wire [54]. It had been confirmed in 2012 by Yu et al. for Qs in micro and nanomechanical silicon nitride resonators [56]. Since $h \ll L$, it becomes obvious that the right term in (2.59), representing the effect of the edge bending, is a lot larger than the left term, representing the effect of the anti-nodal sine bending of the string. This means that energy loss near the edges is dominantly defining the quality factor in strings [35, 56]. The contribution of the energy loss due to the sinusoidal bending of the string (left term in brackets) becomes only important for short strings at higher mode numbers. A schematic explanation of the equation is shown in Fig. 2.18. And in Fig. 2.19 the damping dilution model is compared to measured Q values of nanomechanical silicon nitride string resonators. It shows how the quality factor decreases for increasing mode numbers and decreasing string length. The resulting intrinsic quality factor $Q_{\text{intrinsic}}$ from the comparison has been proposed to be due to surface losses as discussed in Sect. 2.3.1.1 on page 76 [43].

2.3.2.2 Damping Dilution in Membranes

The damping dilution factor for a rectangular membrane with lateral dimensions L_x and L_y can readily be calculated from (2.51) with the membrane modeshape function

$$u(x, y) = U_0 \phi_n(x) \phi_i(y) \tag{2.61}$$

with the normalized modeshape functions (2.54) in x and y direction.

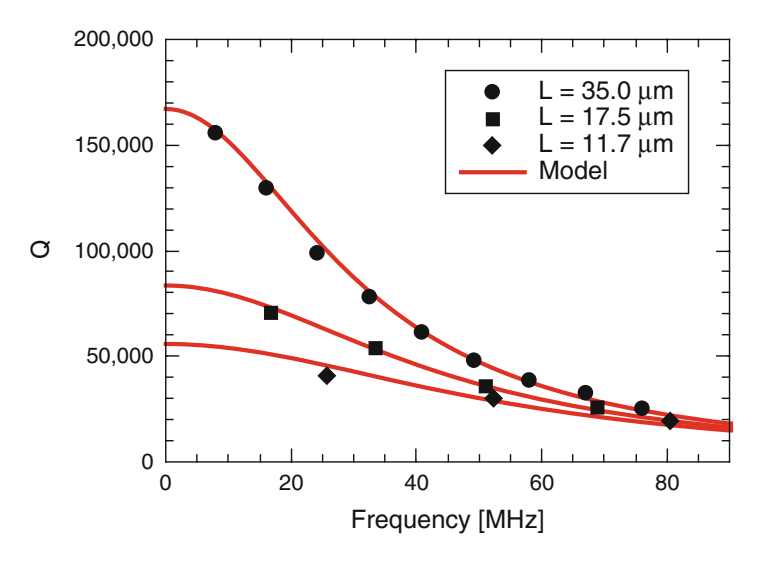


Fig. 2.19 Q values for increasing flexural modes of nanomechanical stoichiometric SiN strings with varying lengths ($\sigma = 942$ MPa, h = 100 nm) (data taken from [57]). All quality factors for the strings with different length are fitted with (2.60) with a single $Q_{\text{intrinsic}} = 4400$

The energy stored in the work against the tensile stress can be calculated from (see Table 1.1)

$$W_{\text{tension}} = \frac{1}{2} \sigma h \int_{0}^{L_{x}} \int_{0}^{L_{y}} \left\{ \left(\frac{\partial u(x, y)}{\partial x} \right)^{2} + \left(\frac{\partial u(x, y)}{\partial y} \right)^{2} \right\} dxdy$$

$$\approx \frac{1}{8} U_{0}^{2} \sigma h L_{x} L_{y} \left(\beta_{\sigma, x}^{2} + \beta_{\sigma, y}^{2} \right)$$
(2.62)

with the membrane wavenumbers $\beta_{\sigma,x} = \frac{n\pi}{L_x}$ and $\beta_{\sigma,y} = \frac{j\pi}{L_y}$. The energy stored due to the string bending can be calculated with (from Table 1.1)

$$W_{\text{bending}} = \frac{D_P}{2} \int_0^{L_x} \int_0^{L_y} \left\{ \left(\frac{\partial^2 u(x, y)}{\partial x^2} + \frac{\partial^2 u(x, y)}{\partial y^2} \right)^2 + 2(1 - \nu) \left[\left(\frac{\partial^2 u(x, y)}{\partial x \partial y} \right)^2 - \frac{\partial^2 u(x, y)}{\partial x^2} \frac{\partial^2 u(x, y)}{\partial y^2} \right] \right\} dxdy \quad (2.63)$$

with the flexural rigidity $D_P = Eh^3/(12(1-v^2))$. For a homogeneous membrane with constant thickness clamped at all four boundaries, the second term in (2.63) becomes zero according to Green's theorem [56]. The bending energy can thus be calculated by the simplified form

$$W_{\text{bending}} = \frac{D_P}{2} \int_0^{L_x} \int_0^{L_y} \left\{ \left(\frac{\partial^2 u(x, y)}{\partial x^2} + \frac{\partial^2 u(x, y)}{\partial y^2} \right)^2 \right\} dxdy$$

$$\approx \underbrace{\frac{1}{8} u_0^2 D_P L_x L_y \left(\beta_{\sigma, x}^2 + \beta_{\sigma, y} \right)^2}_{\text{sine shape}} + \underbrace{\frac{1}{4} u_0^2 D_P \beta_E \left(L_x \beta_{\sigma, y}^2 + L_y \beta_{\sigma, x}^2 \right)}_{\text{edge shape}}, \tag{2.64}$$

with the flexural wavenumber $\beta_E = \sqrt{\frac{\sigma h}{D_P}}$. The bending energy in a membrane, similar to the string case presented in the previous subsection, results in two terms: one coming from the anti-nodal bending of the sine modeshape, and a second coming from the bending at the edge where the membrane is clamped.

For small vibrational amplitudes, the "two-dimensional" damping dilution factor for a rectangular membrane then becomes

$$\alpha_{\rm dd,2D} \approx \left[\underbrace{\frac{\left(\beta_{\sigma,x}^{2} + \beta_{\sigma,y}^{2}\right)}{\beta_{E}^{2}}}_{\text{sine shape}} + \underbrace{\frac{2}{\beta_{E}} \frac{\left(L_{x} \beta_{\sigma,y}^{2} + L_{y} \beta_{\sigma,x}^{2}\right)}{L_{x} L_{y} \left(\beta_{\sigma,x}^{2} + \beta_{\sigma,y}^{2}\right)}}_{\text{edge shape}} \right]^{-1}$$

$$\approx \left[\frac{D_{P}}{\sigma h} \pi^{2} \left(\left(\frac{n}{L_{x}}\right)^{2} + \left(\frac{j}{L_{y}}\right)^{2}\right) + 2\sqrt{\frac{D_{P}}{\sigma h}} \frac{L_{y} \left(\frac{n}{L_{x}}\right)^{2} + L_{x} \left(\frac{j}{L_{y}}\right)^{2}}{L_{x} L_{y} \left(\left(\frac{n}{L_{x}}\right)^{2} + \left(\frac{j}{L_{y}}\right)^{2}\right)} \right]^{-1}$$

$$(2.65)$$

which can further be simplified for a square membrane ($L_x = L_y = L$) and assuming zero transversal strain ($\nu = 0$)

$$\alpha_{\rm dd,2D} \approx \left[\underbrace{\frac{\pi^2 (n^2 + j^2)}{12} \frac{E}{\sigma} \left(\frac{h}{L}\right)^2}_{\text{sine shape}} + \underbrace{\frac{1}{\sqrt{3}} \sqrt{\frac{E}{\sigma}} \left(\frac{h}{L}\right)}_{\text{edge shape}} \right]^{-1}.$$
 (2.66)

The resulting damping dilution factor for a square membrane is very similar to the factor for a string with rectangular cross section (2.60).

References

 B.C. Stipe, H.J. Mamin, T.D. Stowe, T.W. Kenny, D. Rugar, Noncontact friction and force fluctuations between closely spaced bodies. Phys. Rev. Lett. 87(9), 096801 (2001)

- A.N. Cleland, M.L. Roukes, External control of dissipation in a nanometer-scale radiofrequency mechanical resonator. Sens. Actuators A Phys. 72(3), 256–261 (1999)
- 3. K. Schwab, Spring constant and damping constant tuning of nanomechanical resonators using a single-electron transistor. Appl. Phys. Lett. **80**(7), 1276–1278 (2002)
- J.E. Sader, Frequency response of cantilever beams immersed in viscous fluids with applications to the atomic force microscope. J. Appl. Phys. 84(1), 64 (1998)
- C.A. Van Eysden, J.E. Sader, Frequency response of cantilever beams immersed in viscous fluids with applications to the atomic force microscope: arbitrary mode order. J. Appl. Phys. 101(4), 044908 (2007)
- C.P. Green, J.E. Sader, Torsional frequency response of cantilever beams immersed in viscous fluids with applications to the atomic force microscope. J. Appl. Phys. 92(10), 6262 (2002)
- C.P. Green, J.E. Sader, Frequency response of cantilever beams immersed in viscous fluids near a solid surface with applications to the atomic force microscope. J. Appl. Phys. 98(11), 114913 (2005)
- M.K. Ghatkesar, T. Braun, V. Barwich, J.-P. Ramseyer, C. Gerber, M. Hegner, H.P. Lang, Resonating modes of vibrating microcantilevers in liquid. Appl. Phys. Lett. 92(4), 043106 (2008)
- J.W.M. Chon, P. Mulvaney, J.E. Sader, Experimental validation of theoretical models for the frequency response of atomic force microscope cantilever beams immersed in fluids. J. Appl. Phys. 87(8), 3978 (2000)
- C.A. Van Eysden, J.E. Sader, Resonant frequencies of a rectangular cantilever beam immersed in a fluid. J. Appl. Phys. 100(11), 114916 (2006)
- 11. P. Enoksson, G. Stemme, E. Stemme, Fluid density sensor based on resonance vibration. Sens. Actuators A Phys. **47**, 327–331 (1995)
- T.P. Burg, M. Godin, S.M. Knudsen, W. Shen, G. Carlson, J.S. Foster, K. Babcock, S.R. Manalis, Weighing of biomolecules, single cells and single nanoparticles in fluid. Nature 446(7139), 1066–1069 (2007)
- 13. J. Lee, W. Shen, K. Payer, T.P Burg, S.R. Manalis, Toward attogram mass measurements in solution with suspended nanochannel resonators. Nano Lett. **10**(7), 2537–2542 (2010)
- D. Sparks, R. Schneider, R. Smith, A. Chimbayo, M. Straayer, J. Cripe, N. Najafi, S. Anasari, Measurement of density and chemical concentration using a microfluidic chip. Lab Chip 3(1), 19–21 (2003)
- D. Westberg, O. Paul, G.I. Andersson, H. Baltes, A CMOS-compatible device for fluid density measurements fabricated by sacrificial aluminium etching. Sens. Actuators A Phys. 73(3), 243–251 (1999)
- M.F. Khan, S. Schmid, P.E. Larsen, Z.J. Davis, W. Yan, E.H. Stenby, A. Boisen, Online measurement of mass density and viscosity of pL fluid samples with suspended microchannel resonator. Sens. Actuators B Chem. 185, 456–461 (2013)
- T. Burg, J. Sader, S. Manalis, Nonmonotonic energy dissipation in microfluidic resonators. Phys. Rev. Lett. 102(22), 1–4 (2009)
- J.E. Sader, T.P. Burg, S.R. Manalis, Energy Dissipation in Microfluidic Beam Resonators. J. Fluid Mech. 650, 215–250 (2010)
- S. Schmid, C. Hierold, Damping mechanisms of single-clamped and prestressed doubleclamped resonant polymer microbeams. J. Appl. Phys. 104(9), 093516 (2008)
- C.A. Van Eysden, J.E. Sader, Frequency response of cantilever beams immersed in compressible fluids with applications to the atomic force microscope. J. Appl. Phys. 106(9), 094904 (2009)
- M. Bao, Analysis and Design Principles of MEMS Devices (Amsterdam, The Netherlands, 2005)

References 89

 S.S. Verbridge, R. Ilic, H.G. Craighead, J.M. Parpia, Size and frequency dependent gas damping of nanomechanical resonators. Appl. Phys. Lett. 93(1), 13101 (2008)

- S. Schmid, B. Malm, A. Boisen, Quality factor improvement of silicon nitride micro string resonators, in 24th International Conference on Micro Electro Mechanical Systems (MEMS) (New Jersey, USA, 2011), pp. 481–484
- M. Bao, H. Yang, H. Yin, Y. Sun, Energy transfer model for squeeze-film air damping in low vacuum. J. Micromech. Microeng. 12, 341–346 (2002)
- 25. R.G. Christian, The theory of oscillating-vane vacuum gauges. Vacuum 16, 175–178 (1966)
- P. Li, R. Hu, On the air damping of flexible microbeam in free space at the free-molecule regime. Microfluid. Nanofluid. 3, 715–721 (2007)
- D.M. Photiadis, J.A. Judge, Attachment losses of high Q oscillators. Appl. Phys. Lett. 85(3), 482–484 (2004)
- M.C. Cross, R. Lifshitz, Elastic wave transmission at an abrupt junction in a thin plate with application to heat transport and vibrations in mesoscopic systems. Phys. Rev. B 64(8), 85324 (2001)
- S. Schmid, S. Kühne, C. Hierold, Influence of air humidity on polymeric microresonators. J. Micromech. Microeng. 19(6), 065018 (2009)
- I. Wilson-Rae, Intrinsic dissipation in nanomechanical resonators due to phonon tunneling. Phys. Rev. B 77(24), 245418 (2008)
- I. Wilson-Rae, R.A. Barton, S.S. Verbridge, D.R. Southworth, B. Ilic, H.G. Craighead, J.M. Parpia, High-Q nanomechanics via destructive interference of elastic waves. Phys. Rev. Lett. 106(4), 47205 (2011)
- D.J. Wilson, C.A. Regal, S.B. Papp, H.J. Kimble, Cavity optomechanics with stoichiometric SiN films. Phys. Rev. Lett. 103(20), 207204 (2009)
- D.J. Wilson, Cavity optomechanics with high-stress silicon nitride films, Ph.D. thesis, California Institute of Technology, 2012
- S. Chakram, Y.S. Patil, L. Chang, M. Vengalattore, Dissipation in ultrahigh quality factor SiN membrane resonators. Phys. Rev. Lett. 112(12), 127201 (2014)
- S. Schmid, K.D. Jensen, K.H. Nielsen, A. Boisen, Damping mechanisms in high-Q micro and nanomechanical string resonators. Phys. Rev. B 84(16), 165307 (2011)
- 36. Y. Tsaturyan, A. Barg, A. Simonsen, L.G. Villanueva, S. Schmid, A. Schliesser, E.S. Polzik, Demonstration of suppressed phonon tunneling losses in phononic bandgap shielded membrane resonators for high-Q optomechanics. Opt. Express 22(6), 6810 (2014)
- P.-L. Yu, K. Cicak, N.S. Kampel, Y. Tsaturyan, T.P. Purdy, R.W. Simmonds, C.A. Regal, A phononic bandgap shield for high-Q membrane microresonators. Appl. Phys. Lett. 104(2), 023510 (2014)
- 38. M.F. Ashby, F. Ashby, Overview No. 80: on the engineering properties of materials. Acta Metallur. 37(5), 1273–1293 (1989)
- 39. G. Fantozzi, 1.1 phenomenology and definitions. Mater. Sci. Forum **366–368**, 3–31 (2001)
- 40. I.M. Ward, J. Sweeney, An Introduction to the Mechanical Properties of Solid Polymers, 2nd edn. (Wiley, London, 2004)
- J. Yang, T. Ono, M. Esashi, Energy dissipation in submicrometer thick single-crystal cantilevers. J. Microelectromech. Syst. 11(6), 775–783 (2002)
- P. Mohanty, D.A. Harrington, K.L. Ekinci, Y.T. Yang, M.J. Murphy, M.L. Roukes, Intrinsic dissipation in high-frequency micromechanical resonators. Phys. Rev. B 66(8), 85416 (2002)
- L.G. Villanueva, S. Schmid, Evidence of surface loss as ubiquitous limiting damping mechanism in SiN micro- and nanomechanical resonators. Phys. Rev. Lett. 113(227201), 1–6 (2014)
- 44. K.Y. Yasumura, T.D. Stowe, E.M. Chow, T. Pfafman, T.W. Kenny, B.C. Stipe, D. Rugar, Quality factors in micron- and submicron-thick cantilevers. J. Microelectromech. Syst. 9(1), 117–125 (2000)
- 45. A.N. Cleland, Foundations of Nanomechanics (Springer, New York, 2003)

46. T.V. Roszhart, The effect of thermoelastic internal friction on the Q of micromachined silicon resonators, in *Solid-State Sensor and Actuator Workshop, 1990.* 4th Technical Digest (New Jersey, USA, 1990), pp. 13–16

- C. Zener. Internal friction in solids I. Theory of internal friction in reeds. Phys. Rev. 52, 230–235 (1937)
- 48. R. Lifshitz, M.L. Roukes, Thermoelastic damping in micro- and nanomechanical systems. Phys. Rev. B **61**(8), 5600–5609 (2000)
- 49. S. Prabhakar, S. Vengallatore, Thermoelastic damping in bilayered micromechanical beam resonators. J. Micromech. Microeng. 17(3), 532–538 (2007)
- 50. S. Joshi, S. Hung, S. Vengallatore, Design strategies for controlling damping in micromechanical and nanomechanical resonators. EPJ Tech. Instrum. 1(1), 1–14 (2014)
- S.S. Verbridge, J.M. Parpia, R.B. Reichenbach, L.M. Bellan, H.G. Craighead, High quality factor resonance at room temperature with nanostrings under high tensile stress. J. Appl. Phys. 99, 124304 (2006)
- 52. S.S. Verbridge, H.G. Craighead, J.M. Parpia, A megahertz nanomechanical resonator with room temperature quality factor over a million. Appl. Phys. Lett. **92**(1), 013112 (2008)
- B.M. Zwickl, W.E. Shanks, A.M. Jayich, C. Yang, B. Jayich, J.D. Thompson, J.G.E. Harris, High quality mechanical and optical properties of commercial silicon nitride membranes. Appl. Phys. Lett. 92(10), 103125 (2008)
- 54. G.I. Gonzfilez, P.R. Saulson, Brownian motion of a mass suspended by an anelastic wire. J. Acoust. Soc. Am. **96**(1), 207–212 (1994)
- G. Cagnoli, J. Hough, D. Debra, M.M. Fejer, E. Gustafson, S. Rowan, V. Mitrofanov, Damping dilution factor for a pendulum in an interferometric gravitational waves detector. Phys. Lett. A 272, 39–45 (2000)
- P.-L. Yu, T. Purdy, C.A. Regal. Control of material damping in high-Q membrane microresonators. Phys. Rev. Lett. 108(8), 083603 (2012)
- Q.P. Unterreithmeier, T. Faust, J.P. Kotthaus, Damping of nanomechanical resonators. Phys. Rev. Lett. 105(2), 27205 (2010)

Chapter 3 Responsivity

Abstract A change of mass or temperature, or an applied force causes a response of a mechanical resonator. The response can, e.g., be a change in frequency or vibrational amplitude. The responsivity of a mechanical resonator is the linear slope of the response to a particular stimulant. In case of a sensor application, the responsivity to the input parameter to be measured should be maximal. However, the responsivity to other inputs, such as a change in ambient temperature, should be minimal in order not to cause an unwanted cross-response. In this chapter, the responsivities of micro and nanomechanical resonators to mass (distributed and point masses), forces, and temperature are discussed.

The rational to develop nanomechanical resonators is to achieve unique sensors with exceptional sensitivities. In this chapter the response of nanomechanical resonators to various physical parameters such as mass, temperature, or force are discussed. The terminology used with regard to sensors and detectors differs from field to field. Therefore the main terminology used in this book is now quickly introduced.

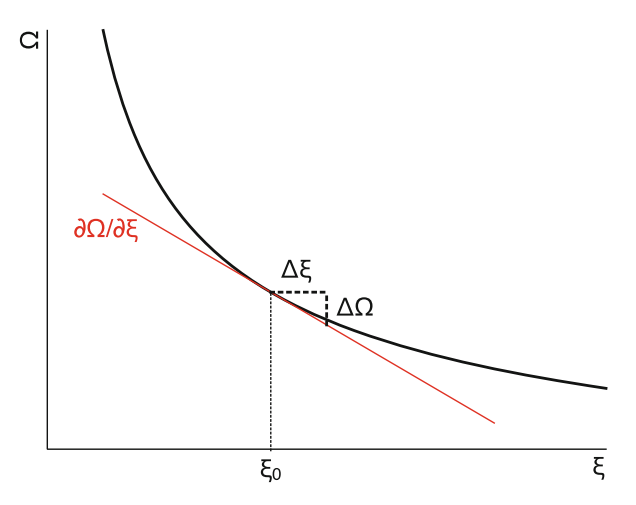
- Responsivity (R) is the slope of the sensor output as a function of the input parameter to be measured. The responsivity is constant over the linear range of the sensor.
- *Sensitivity* is the smallest detectable change of the input signal with a specified signal-to-noise ratio.
- *Response time* is the time it takes by a sensor to approach its true output when subjected to a step change of the input parameter.

With a few exceptions, the responsivity of micro- and nanomechanical resonators is the change of a resonance frequency as a function of a specific parameter ξ , which can be, e.g., mass, force, or temperature. Additionally, the resonators are assumed to be only slightly damped, such that the resonance frequency can be approximated by the eigenfrequency Ω (1.132). In that case, the responsivity at a reference parameter value ξ_0 is given by

$$\mathscr{R} = \frac{\partial \Omega}{\partial \xi} \bigg|_{\xi = \xi_0}.$$
 (3.1)

92 3 Responsivity

Fig. 3.1 Eigenfrequency Ω of a linear resonator as a function of an arbitrary input parameter ξ . The *red line* represents the slope at ξ_0 , which is the responsivity \mathcal{R}



Assuming that the change of the parameter to be measured $\Delta \xi$ is small, the resulting response can be linearized, as schematically depicted in Fig. 3.1

$$\mathcal{R} \approx \frac{\Delta\Omega}{\Delta\xi} \tag{3.2}$$

and the sensitivity, that is the smallest detectable value of the parameter $\Delta \xi_{\min}$, is approximately given by

$$\Delta \xi_{\min} \approx \mathcal{R}^{-1} \Delta \Omega_{\min},$$
 (3.3)

where $\Delta\Omega_{\rm min}$ the minimum detectable resonance frequency change. The frequency resolution and thereby $\Delta\Omega_{\rm min}$ is determined by the noise of the system originating from both the read-out circuitry and the resonator itself, as discussed in Chap. 5 on page 149.

Often, the frequency resolution relative to the resonance frequency $\delta\Omega_{\min} = \Delta\Omega_{\min}/\Omega(\xi_0)$ is given, typically in parts per million (ppm) or billion (ppb). In that case it is more useful to work with the *relative responsivity* $\delta \mathcal{R} = \mathcal{R}/\Omega(\xi_0)$ and the sensitivity is then given by

$$\Delta \xi_{\min} = \delta \mathscr{R}^{-1} \delta \Omega_{\min}. \tag{3.4}$$

3.1 Frequency Response to Mass

The probably most prominent sensor application for nanomechanical resonators is the detection of small masses. From Eq. (1.147) it is clear that the resonant frequency depends on the vibrating mass. According to the definition in the

introduction, the responsivity \mathcal{R} for a resonant mass sensor is defined by the change of resonance frequency due to a change in mass. For slightly damped resonators, the responsivity of a linear lumped-element oscillator, as shown in Fig. 1.16, is thus given by

$$\mathcal{R} = \frac{\partial \Omega(m_{\text{eff}})}{\partial m_{\text{eff}}} = -\frac{1}{2m_{\text{eff}}} \Omega(m_{\text{eff}})$$
 (3.5)

and the relative responsivity is

$$\delta \mathcal{R} = -\frac{1}{2m_{\text{eff}}}. (3.6)$$

Thus, in order to obtain a high responsivity the resonator must have a low effective mass m_{eff} . This is one of the main rational behind the development of nanomechanical resonators which have a mass typically below 1 ng.

The mass loading can happen in many ways. Here two common scenarios are discussed, namely point mass loading and distributed mass loading.

3.1.1 Point Mass

In the previous section the mass of adsorbed molecules is assumed to be distributed uniformly over the resonator surface. This approach is not viable if single molecules or particles are to be measured, since the change in frequency is dependent not only on the mass of the attached particle but also on the landing position on the resonator [1]. This is due to the shape of the vibrational modes. The areas of the beam with a large vibrational amplitude are areas where an added mass will gain a high kinetic energy and thereby change the resonant frequency considerably compared with the nodal points where a point mass remains unmoved.

Considering a cantilever with the mass m_0 loaded with a point mass Δm positioned at $x_{\Delta m}$, as schematically depicted in Fig. 3.2. If the mass load is much smaller than the resonator mass, $\Delta m \ll m_0$, the cantilever mode-shape will not change significantly, and the resonant frequency of such a system can be accurately estimated using an energy approach. According to Rayleigh's method (1.1), the time average kinetic energy, $W_{\rm kin}$, equals the time average strain energy, $W_{\rm strain}$, at resonance. In the case of a resonator with an additional point mass with the kinetic energy $W_{\rm kin}, \Delta m$, the total energy balance becomes [2]

$$W_{\text{strain}} = W_{\text{kin}} + W_{\text{kin}, \Delta m}. \tag{3.7}$$

94 3 Responsivity

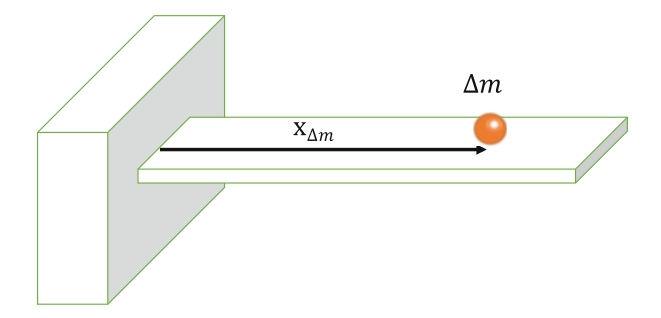


Fig. 3.2 Schematic of a cantilever with a single bead, having the mass Δm , positioned at $z_{\Delta m}$

The kinetic energy of the cantilever is

$$\begin{split} W_{\text{kin}} &= \int_{V} \frac{1}{2} \rho \Omega_{n,\Delta m}^{2} a_{n}^{2} \phi_{n}^{2}(x) dV \\ &= \frac{1}{2} A \rho \Omega_{n,\Delta m}^{2} u_{n}^{2} \int_{0}^{L} \phi_{n}^{2}(x) dx = \frac{1}{2} a_{n}^{2} \Omega_{n,\Delta m}^{2} m_{\text{eff}}, \end{split} \tag{3.8}$$

where $\Omega_{n,\Delta m}$ is the frequency of motion with the additional mass, $\phi_n(x)$ is the normalized mode-shape function of the *n*'s mode, and a_n is the modal amplitude of each mode, and the effective mass (1.149)

$$m_{\text{eff}} = \rho A \int_0^L \phi_n^2(x) dx = m_0 \frac{1}{L} \int_0^L \phi_n^2(x) dx.$$
 (3.9)

The kinetic energy of the added point mass Δm at $x_{\Delta m}$ is

$$W_{\mathrm{kin},\Delta m} = \frac{1}{2} \Delta m \Omega_{n,\Delta m}^2 a_n^2 \phi_n^2(x_{\Delta m}). \tag{3.10}$$

Assuming that neither the mode-shape nor the moment of inertial will change significantly due to the added mass, the strain energy in the cantilever is approximately equal to the kinetic energy of the cantilever without the added mass:

$$W_{\rm strain} \approx \frac{1}{2} m_{\rm eff} \omega_n^2.$$
 (3.11)

With (3.7), the eigenfrequency of the cantilever with the added mass then becomes

$$\Omega_{n,\Delta m}^2 = \Omega_n^2 \left(1 + \frac{\Delta m}{m_{\text{eff}}} \phi_n^2(x_{\Delta m}) \right)^{-1}. \tag{3.12}$$

Since the additional mass is assumed to be a lot smaller than the cantilever mass, (3.12) can be simplified by a Taylor series approximation

$$\Omega_{n,\Delta m} \approx \Omega_n \left(1 - \frac{1}{2} \frac{\Delta m}{m_{\text{eff}}} \phi_n^2(x_{\Delta m}) \right).$$
(3.13)

The point mass responsivity according to (3.5) then becomes [2-4]

$$\mathcal{R}_n = \frac{\Delta \Omega_n}{\Delta m} = -\frac{\Omega_n}{2m_{\text{eff}}} \phi_n^2(x_{\Delta m}) \tag{3.14}$$

and the respective relative responsivity is

$$\delta \mathcal{R} = -\frac{1}{2m_{\text{eff}}} \phi_n^2(x_{\Delta m}) \tag{3.15}$$

with the frequency shift $\Delta\Omega_n = \Omega_{n,\Delta m} - \Omega_n$. From (3.14) it is obvious that the position of the mass has to be known prior to the calculation of the mass itself. Hence, there are two unknowns, namely the position $x_{\Delta m}$ and the mass Δm . Both unknowns can be obtained by creating a system of equations with (3.14) based on at least two vibrational modes n.

3.1.1.1 Strings

The single mass detection with strings is discussed first. The sinusoidal mode-shape function allows for a simple analysis [5]. With the mode shape function of a string (1.46) with length L

$$\phi_n(x) = \sin\left(\frac{n\pi x}{L}\right),\tag{3.16}$$

where *n* is the mode number, and the effective mass (see Table 1.3) $m_{\text{eff}} = \frac{1}{2}m_0$, with the total string mass $m_0 = \rho AL$, the point mass Δm positioned at $x_{\Delta m}$ can readily be found from the responsivity (3.14)

$$\Delta m = -m_0 \frac{\Delta \Omega_n}{\Omega_n} \sin^{-2} \left(\frac{n\pi}{L} x_{\Delta m} \right). \tag{3.17}$$

The point mass Δm and its position $x_{\Delta m}$ are the unknowns of a defined second order system of equations based on (3.17) for the first two bending modes. For the first bending mode (n = 1), (3.17) can be solved for the position

$$x_{\Delta m} = \frac{L}{\pi} \arcsin \sqrt{-\frac{m_0}{\Delta m} \frac{\Delta \Omega_1}{\Omega_1}}.$$
 (3.18)

96 3 Responsivity

The absolute string displacement is symmetrical and it does not make a difference on which half side a point mass is added to the string. The resulting frequency shift is the same. Therefore, the positions resulting from (3.18) have only values from 0 to L/2.

The mass ratio of the point mass versus string mass can now be obtained by substituting (3.18) in (3.17) for the second mode (n = 2). By using the identity ($\sin(2\arcsin y) = 2y\sqrt{1-y^2}$), a simple term for the relative point mass can be calculated

$$\frac{\Delta m}{m_0} = \frac{4\left(\frac{\Delta\Omega_1}{\Omega_1}\right)^2}{\frac{\Delta\Omega_2}{\Omega_2} - 4\frac{\Delta\Omega_1}{\Omega_1}}.$$
(3.19)

The used identity holds only if |y| < 1. It can easily be shown that this condition is fulfilled if $x_{\Delta m} < L/2$ which is in agreement with the before mentioned symmetry of the string vibration.

With (3.19), the relative particle position (3.18) can be readily calculated

$$\frac{x_{\Delta m}}{L} = \frac{1}{\pi} \arcsin \sqrt{1 - \frac{1}{4} \frac{\Delta \Omega_2}{\Omega_2} \frac{\Omega_1}{\Delta \Omega_1}}.$$
 (3.20)

Both the relative position (3.20) and the relative mass change (3.19) are plotted in Fig. 3.3 as a function of the relative frequency shifts for the first and second mode. It can be seen that the resulting masses are collapsing for particle positions close

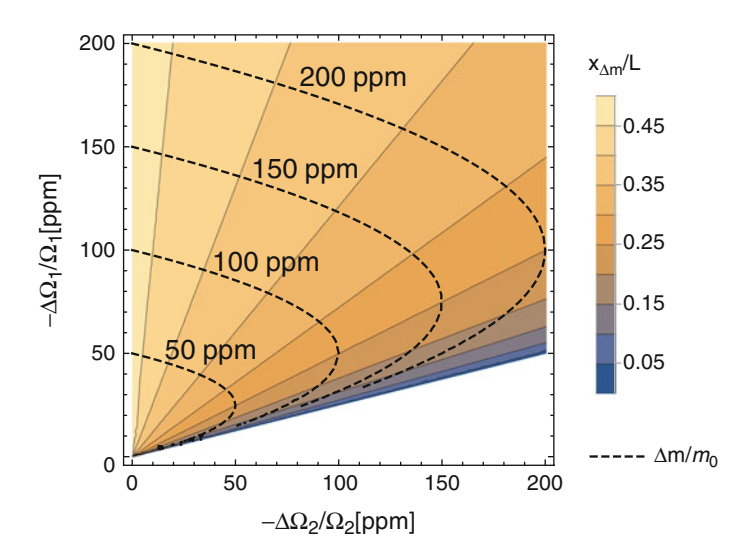


Fig. 3.3 Visualization of the particle location (3.20) and corresponding particle mass (3.19) as a function of the relative frequency shifts of the first and second bending mode

to the clamping site. The real measured relative frequency changes have a certain imprecision, as discussed in detail in Chap. 5.2 on page 163. Hence, masses that land close to the clamping, where the dashed mass lines collapse, will produce a highly imprecise mass response.

Assuming a single uncertainty for the relative frequency shift of both modes σ_{Ω} , the uncertainty of the relative mass change (3.19) is given by the Gaussian error propagation for uncorrelated variables

$$\sigma_m = \sigma_{\Omega} \sqrt{\left(\frac{\partial \frac{\Delta m}{m_0}}{\partial \frac{\Delta \Omega_1}{\Omega_1}}\right)^2 + \left(\frac{\partial \frac{\Delta m}{m_0}}{\partial \frac{\Delta \Omega_2}{\Omega_2}}\right)^2}.$$
 (3.21)

With (3.19) and (3.20) the mass uncertainty (3.21) can be transformed into a function of the mass position $x_{\Delta m}$

$$\frac{\sigma_m}{\sigma_{\Omega}} = \frac{1}{4} \sqrt{9 + 8 \frac{\cos\left(4\pi \frac{x_{\Delta m}}{L}\right)}{\left(\sin\left(\pi \frac{x_{\Delta m}}{L}\right)\right)^8}},\tag{3.22}$$

which is plotted in Fig. 3.4a. It shows that there are two regimes. For a position in the string center (0.25 $< x_{\Delta m}/L < 0.75$) an error in the frequency measurement translates directly into an error in the calculated mass with a factor of unity. For a position close to the clamping sites (0 $< x_{\Delta m}/L < 0.25$ and 0.75 $< x_{\Delta m}/L < 1$) an error in the frequency measurement is amplifying the mass uncertainty. Therefore, in single mass detection, masses that land at the ends of the resonator are typically dismissed and only masses that land in the center (0.25 $< x_{\Delta m}/L < 0.75$) are considered for the measurement, that is only 50% of the sensor surface are used [3, 5], as depicted in Fig. 3.4b.

3.1.1.2 Beams

The more complex modeshape function of beams (cantilevers and bridges) is more complicated and does not allow the derivation of a closed-form solution, as done for strings in the previous section. The point mass responsivity according to (3.14) of cantilevers and bridges can be calculated by means of the respective normalized mode shape functions (1.34) and (1.43) as derived in Sect. 1.1.1, and the respective effective masses (see Table 1.3 on page 39) $m_{\rm eff} = \frac{1}{4} m_0$ and $m_{\rm eff} \approx \frac{1}{2} m_0$, respectively.

If a single point mass is adhering to the cantilever, and the change in resonant frequency of several modes is measured, both position and mass can be calculated. For this purpose, based on the resonant frequency changes two column vectors are constructed

98 3 Responsivity

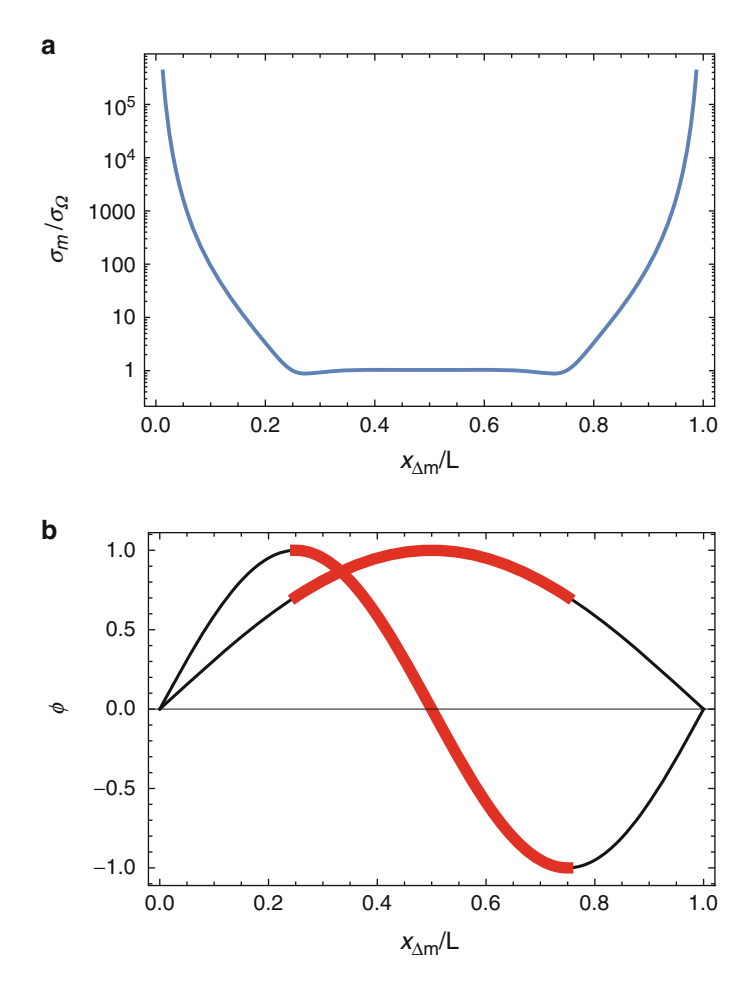


Fig. 3.4 (a) Ratio of mass to frequency uncertainty σ_m/σ_Ω (3.22) as a function of the relative mass position $x_{\Delta m}/L$ along the length L of the resonator. (b) Mode shape plots of the first two modes with the active area available for mass sensing marked red

$$\overline{\phi}(x_{\Delta m}) = \begin{bmatrix} \phi_1^2(x_{\Delta m}) \\ \phi_2^2(x_{\Delta m}) \\ \vdots \\ \phi_n^2(x_{\Delta m}) \end{bmatrix}, \overline{\delta \Omega} = \begin{bmatrix} \frac{\Delta \Omega_1}{\Omega_1} \\ \frac{\Delta \Omega_2}{\Omega_2} \\ \vdots \\ \frac{\Delta \Omega_n}{\Omega_n} \end{bmatrix}. \tag{3.23}$$

The size of the vectors is determined by the number of measured vibrational modes, with a minimum of two modes required to determine the position. Equation (3.14) can now be written as

$$\overline{\delta\Omega} = -\frac{\Delta m}{2m_{\text{eff}}} \, \overline{\phi}(x_{\Delta m}). \tag{3.24}$$

This problem cannot be solved numerically. Therefore first, the particle positions are recovered by creating a term that can be minimized numerically. This is done by creating a normalized scalar product which approaches unity when $\overline{\phi}(x_{\Delta m})$ and $\overline{\delta\Omega}$ become collinear, that is when (3.24) is satisfied.

$$\xi(x_{\Delta m}) = 1 - \frac{\left| \overline{\phi}(x_{\Delta m}) \cdot \overline{\delta \Omega} \right|}{\left\| \overline{\phi}(x_{\Delta m}) \right\| \cdot \left\| \overline{\delta \Omega} \right\|}.$$
 (3.25)

The position $x_{\Delta m}$ can now be found by numerically minimizing ξ . From the computed position the relative mass change induced by the individual particles can then readily be obtained by

$$\Delta m = -2m_{\text{eff}} \frac{\left\| \overline{\delta \Omega} \right\|}{\left\| \overline{\phi}(x_{\Delta m}) \right\|}.$$
 (3.26)

This minimization technique has been extended to detect to multiple masses on a single cantilever by measuring the frequency shifts of multiple resonance modes [6].

A different approach to calculate the mass and position is by mapping the plane of the frequency-shifts to the plane of the mass and position (as plotted for a bridge in Fig. 3.5) via a bivariate transformation by treating the variables as independent probability density functions [3].

The latest development in the field of nanomechanical mass sensing is the detection of the mass density distribution of a point mass, which allows to gather an inertial image with non-diffraction limited resolution [7].

3.1.2 Distributed Mass

A common way of using a nanomechanical resonator as mass sensor, e.g. for gravimetric gas sensing, is, e.g., by coating the top surface of the resonator with a sensitive layer that absorbs the gas to be detected, as schematically depicted in Fig. 3.6. The gas is then absorbed in the sensitive layer which increases the total resonator mass. Under the assumption that the additional mass does not alter the stiffness of the resonator, the absorbed mass can be interpreted as an increase in mass density of the resonator.

In the case of an evenly distributed mass over the sensor surface area, the figure of merit becomes the mass sensitivity per surface area A_S , instead of the total mass

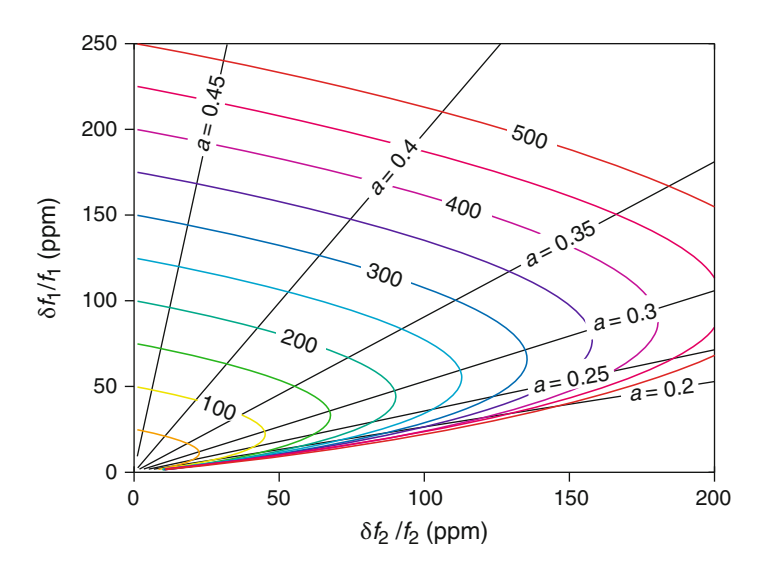
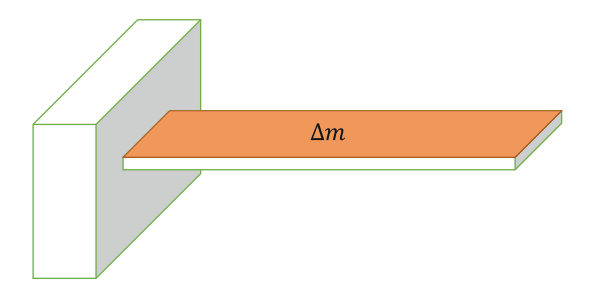


Fig. 3.5 Visualization of the particle location (3.20) and corresponding particle mass (3.19) as a function of the relative frequency shifts of the first and second bending mode of a nanomechanical bridge. The *black straight lines* represent the location $x_{\Delta m} = a$. Colored lines represent the relative mass change $\Delta m/m_{\rm eff}$ in ppm (Reprinted from [3])

Fig. 3.6 Schematic of a cantilever with an additional mass Δm evenly distributed over the entire surface area



sensitivity. The distributed mass sensitivity for a small additional mass can then be approximated by

$$\Delta m_D \approx \frac{\Delta m}{A_s} = \frac{1}{A_s \mathcal{R}} \Delta \omega = \mathcal{R}_D^{-1} \Delta \omega$$
 (3.27)

with the distributed mass responsivity

$$\mathcal{R}_D = A_s \mathcal{R} = -\frac{A_s}{2m_0} \Omega(m_0) \tag{3.28}$$

and the respective relative responsivity

$$\delta \mathcal{R}_D = -\frac{A_s}{2m_0},\tag{3.29}$$

where A_s is the surface area that is homogeneously covered with additional mass.

3.2 Amplitude and Frequency Response to Force

A nanomechanical resonator responds to force in two ways. A force can either directly influence the vibrational amplitude of the resonator, or if the force has a gradient its effect can be measured via a frequency detuning. Both cases are discussed subsequently. It should be noted that the amplitude response discussed in the following subsection constitutes an exception in this chapter in which all other discussed responsivities are based on a change in frequency.

3.2.1 Amplitude Response to a Force

A force F(t) acting on a micro- or nanomechanical resonator, as described by the equation of motion of a damped and driven linear resonator (1.113), directly results in an amplitude response, as discussed in the Sect. 1.2.1. The amplitude response of a lumped-element model resonator is given by (1.124)

$$z = \frac{1/m}{\sqrt{(\Omega^2 - \omega^2)^2 + 4\zeta^2 \Omega^2 \omega^2}} F(t).$$
 (3.30)

The force sensitivity is now given by

$$\Delta F_{\min} = \mathcal{R}^{-1} \Delta z_{\min} \tag{3.31}$$

with the amplitude sensitivity of the readout Δz_{\min} and the amplitude responsivity

$$\mathcal{R} = \frac{\partial z}{\partial F} = \frac{1/m}{\sqrt{(\Omega^2 - \omega^2)^2 + 4\zeta^2 \Omega^2 \omega^2}}.$$
 (3.32)

The readout sensitivity Δz_{min} is discussed in detail in Chap. 5 on page 149.

There are two special situations to be discussed, namely the quasistatic and resonant operation.

3.2.1.1 Quasi-Static Force Sensing ($\omega \ll \Omega$)

In the quasi-static case, the force to be measured has frequency components which are smaller than the eigenfrequency frequency of the resonator ($\omega \ll \Omega$). In this case the amplitude responsivity reduces to the static response

$$\mathcal{R} = \frac{1}{\Omega^2 m} = \frac{1}{k},\tag{3.33}$$

where k is the spring constant of the nanomechanical resonator.

3.2.1.2 Resonant Force Sensing ($\omega = \Omega$)

In the resonant case, the force to be measured has a frequency which matches the eigenfrequency of the resonator ($\omega = \Omega$). In this case the amplitude response reduces to the resonant response

$$\mathcal{R} = \frac{Q}{\Omega^2 m} = \frac{Q}{k} \tag{3.34}$$

is equal to the static response multiplied by the quality factor Q. Apparently, the mechanical quality factor amplifies the force responsivity.

3.2.2 Frequency Response to a Force Gradient

The detection of a force gradient is best known from dynamic atomic force microscopy, where the cantilever-tip interaction with the substrate produces a shift of the cantilever resonance frequency [8]. Assuming a small mechanical vibration z around the equilibrium position of the resonator at z_0 , the force to be measured can be approximated by a first order Taylor series

$$F(z_0 + z) \approx F(z_0) + \frac{\partial F(z_0)}{\partial z} z.$$
 (3.35)

Apparently, if the force has a non-zero gradient component $\partial F(z_0)/\partial z = F'(z_0)$, then the equation of motion of a lumped-element resonator (1.113) becomes

$$m\ddot{z} + c\dot{z} + kz = F(z_0) + F'(z_0) z$$

$$m\ddot{z} + c\dot{z} + (k - F'(z_0)) z = 0.$$
(3.36)

The force gradient is altering the effective spring constant of the mechanical resonator. On the right side of the equation remains a static force $F(z_0)$. This force

pushes the mechanical resonator into a new equilibrium point. Assuming that this force is small, the induced static deflection is negligible for a linear system. The eigenfrequency of the system can then be obtained from the homogenous differential equation (3.36), which readily results in (see Sect. 1.2.1.1 on page 30 for more detail)

$$\Omega = \sqrt{\frac{k - F'(z_0)}{m}} = \Omega_0 \sqrt{1 - \frac{F'(z_0)}{k}}.$$
 (3.37)

Assuming that $F'(z_0)/k \ll 1$, the eigenfrequency can be approximated by the first order Taylor series

$$\Omega \approx \Omega_0 \left(1 - \frac{F'(z_0)}{2k} \right) \tag{3.38}$$

which gives the frequency responsivity

$$\mathcal{R} = \frac{\partial \Omega}{\partial k_F} = -\frac{1}{2k} \Omega_0 \tag{3.39}$$

and the relative frequency responsivity

$$\delta \mathcal{R} = -\frac{1}{2k}.\tag{3.40}$$

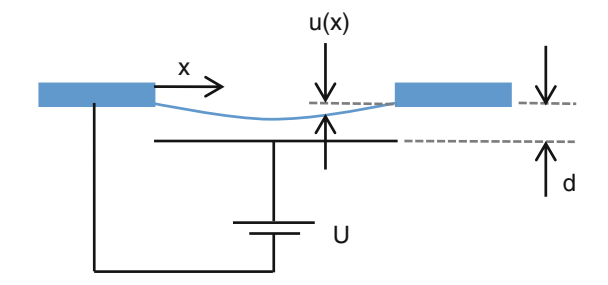
It is noteworthy that the relative frequency responsivity (3.40) is very similar to the amplitude responsivity (3.33). The general rule to obtain a large force or force gradient responsivity is to design a soft nanomechanical resonator with a low spring constant k.

3.2.2.1 Frequency Response to an Electrostatic Potential

Electrostatic forces are a common transduction mechanism to actuate micro and nanomechanical resonators, as it is discussed in more detail in Sect. 4.2.1.1 on page 121. It is possible to tune the resonance frequency by applying a d.c. bias voltage tuning [9, 10]. The same effect can also be used to measure the electrostatic force strength as a function of the applied bias potential [11]. In this subsection, the frequency response of a membrane resonator to a d.c. bias voltage is derived and compared to the response of a lumped-element model resonator (3.38), as derived previously.

Neglecting any electrostatic fringe fields, the electrostatic force between two parallel plates under a potential difference \mathcal{U} , of area A, and separated by a distance ξ is given by

Fig. 3.7 Schematic drawing of a flexural resonator placed in a distance d above a conducting plate. There is an electrostatic potential \mathcal{U} applied between the resonator and the plate



$$F(\xi) = -\varepsilon_0 \varepsilon_r A \frac{1}{\xi^2} \mathcal{U}^2, \tag{3.41}$$

with the permittivity of vacuum ε_0 and the relative permittivity of the surrounding medium ε_r .

A schematic of the membrane resonator is shown in Fig. 3.7. The equilibrium of forces for an infinitesimal piece of membrane with the area $dx \times dy$ and thickness h is then given by

$$\rho h \frac{\partial^2 u}{\partial t^2}(x, y, t) - \sigma h \nabla^2 u(x, y, t) = F(d + u)$$
(3.42)

with the displacement function u(x, y, t), the tensile pre-stress σ , and the mass density ρ . The deflection of a membrane can be described by (1.83)

$$u(x, y, t) = \sum_{n=1}^{\infty} \sum_{j=1}^{\infty} U_{n,j} \phi_{n,j}(x, y) e^{i\omega t}$$
 (3.43)

with the normalized mode shape function

$$\phi_{n,j}(x,y) = \sin \frac{n\pi x}{L_x} \sin \frac{j\pi y}{L_y}.$$
 (3.44)

Considering the first order Taylor approximation of the electrostatic force (3.41), the equation of motion can be written as

$$\rho h \frac{\partial^2 u}{\partial t^2} - \sigma h \nabla^2 u = F(d) + \frac{\partial F(d)}{\partial u} u$$

$$\rho h \frac{\partial^2 u}{\partial t^2} - \sigma h \nabla^2 u = -\frac{\varepsilon_0 \varepsilon_r}{d^2} \mathcal{U}^2 + \frac{2\varepsilon_0 \varepsilon_r}{d^3} \mathcal{U}^2 u$$
(3.45)

In a "linear system," the static force term $\frac{\varepsilon_0\varepsilon_r A}{d^2}\mathcal{U}^2$ causes a static deflection of the membrane. This static deflection does not influence the eigenfrequency and can thus be neglected. Following Galerkin's method, as introduced in Sect. 1.2.1.5 on

page 39, (3.42) can be solved for the fundamental normal mode by multiplying it with $\phi_{1,1}$ and integrating over the entire membrane area $A = L \times L$ with $L = L_x = L_y$. Taking the scalar product of the fundamental mode gives

$$\iint_{A} \left(\rho h \omega^{2} u + \sigma h \nabla^{2} u + \frac{2\varepsilon_{0} \varepsilon_{r}}{d^{3}} \mathcal{U}^{2} u \right) \phi_{1,1} dx dy = 0$$
(3.46)

which with (3.43) can be written as

$$\rho h\omega^2 \iint_A \phi_{1,1}^2 dx dy - 2\frac{\pi^2}{L^2} \sigma h \iint_A \phi_{1,1}^2 dx dy + \frac{2\varepsilon_0 \varepsilon_r}{d^3} \mathcal{U}^2 \iint_A \phi_{1,1}^2 dx dy = 0$$

$$\rho h\omega^2 - 2\frac{\pi^2}{L^2} \sigma h + \frac{2\varepsilon_0 \varepsilon_r}{d^3} \mathcal{U}^2 = 0.$$
(3.47)

The eigenfrequency can now readily be isolated from (3.47)

$$\Omega_{1,1}^2 = \omega^2 = 2\pi^2 \frac{\sigma}{\rho} \frac{1}{L^2} - \frac{2\varepsilon_0 \varepsilon_r}{\rho h d^3} \mathcal{U}^2. \tag{3.48}$$

With the eigenfrequency of a membrane with zero voltage applied $\Omega_{1,1}(\mathcal{U}=0)=\Omega_0$

$$\Omega_0 = \frac{\sqrt{2}\pi}{L} \sqrt{\frac{\sigma}{\rho}} \tag{3.49}$$

the first order Taylor approximation of Ω becomes

$$\Omega \approx \Omega_0 \left(1 - \frac{\varepsilon_0 \varepsilon_r}{d^3 h \rho \Omega_0^2} \mathcal{U}^2 \right). \tag{3.50}$$

From (3.50) it can be seen that an applied bias voltage \mathcal{U} causes a negative frequency detuning.

3.3 Frequency Response to Ambient Temperature and Local Heating

As the quality factor of micro- and nanomechanical resonators is a function of temperature, as introduced in Sect. 2.3.1 on page 69, so is the resonance frequency. The temperature responsivity of the resonance frequency is caused by two main effects: (1) the Young's modulus is a function of temperature E(T), typically a material softens with increasing temperature, and (2) a temperature change ΔT

induces a strain from the thermal expansion of the material $\varepsilon = \alpha \Delta T$. Depending on the configuration, a thermal expansion results in a change of geometry or stress.

For most applications a high frequency stability is required and hence resonators with a small temperature response are sought after. A high temperature responsivity can impede a particular application if a small ambient temperature change, e.g., significantly changes the frequency of a filter or produces a fake sensor signal. Typically, sensors are temperature stabilized either by (1) using a temperature insensitive resonator design, (2) performing a differential measurement between two resonators that both are exposed to the same temperature bath but only one of them is sensing, (3) the measurement signal is temperature corrected by means of an integrated temperature sensor, or (4) the ambient temperature directly is controlled and stabilized. Besides a change in ambient temperature, a significant local heating can also be introduced by the electric or optic transduction of the nanomechanical resonator.

In contrast to the sensor applications mentioned above, a high as possible temperature responsivity is the figure of merit if the resonator is actually used to detect temperature changes. This is the case if micro- and nanomechanical resonators are used as thermometer [12, 13] or to measure the absorption of electromagnetic waves for the application as a bolometer [14] or photothermal absorption spectrometer [15–18]. Another scenario in which a high temperature response is wanted is for thermal frequency tuning [19].

In all cases and for all applications, the understanding of the temperature response of different resonators is crucial. Here, the temperature sensitivity of a few specific structures, such as beams and strings, as they readily allow for the derivation of simple analytical solutions. The temperature response of plates and membranes is more challenging and is best obtained by performing FEM simulations.

3.3.1 Stress Released Resonators

Stress released structures, such as singly clamped beams (cantilevers), as introduced in Sect. 1.1.1, are among the least temperature sensitive resonators. In the first order of approximation, for any cantilever the temperature induced strain can relax, which only results in a slight change of geometry. In this case, it is possible to calculate the eigenfrequency (1.27) after the thermal expansion of the material after a change of temperature $\Delta T = T - T_0$

$$\Omega_n(T) = \lambda_n^2 \sqrt{\frac{E(T) I_y (1 + \alpha \Delta T)^4}{\rho (1 + \alpha \Delta T)^{-3} A (1 + \alpha \Delta T)^2 L^4 (1 + \alpha \Delta T)^4}}$$

$$= \lambda_n^2 \sqrt{\frac{E(T) I_y}{\rho A L^4}} \sqrt{(1 + \alpha \Delta T)} \tag{3.51}$$

with the temperature sensitive Young's modulus with an assumed linear thermal softening coefficient α_E

$$E(T) = E_0(1 + \alpha_E \Delta T). \tag{3.52}$$

The temperature responsivity is then given by

$$\mathscr{R} = \frac{\partial \Omega(T)}{\partial T} \bigg|_{T=T_0} \approx \frac{\alpha + \alpha_E}{2} \Omega_n(T_0)$$
 (3.53)

and the relative responsivity is

$$\delta \mathcal{R} = \frac{\alpha + \alpha_E}{2}.\tag{3.54}$$

Both effects are equally weighted and act on the eigenfrequency proportional to the square root of the specific thermal coefficient. However, as said coefficients are very small, the Taylor expansion can be truncated at the first order obtaining Eq. (3.54). Typically, the temperature induced change in the Young's modulus is dominating over the geometrical effect from the thermal expansion. For example for silicon, the thermal expansion coefficient is $\alpha=2.6$ ppm/K and the thermal softening coefficient is $\alpha=-44$ ppm/K[20]. Hence, the temperature effect on the Young's modulus is roughly one order of magnitude larger than the effect of thermal expansion. The same is true, e.g., for silicon nitride with $\alpha=2.3$ ppm/K and $\alpha_E\approx-87$ ppm/K[21]. The two mechanisms involved are acting in the opposite way. On the one hand, the thermal expansion is causing a frequency increase with increasing temperature, while on the other hand the softening of the Young's modulus is lowering the frequency with increasing temperature.

The analysis, as it is here performed for cantilevers, holds true for all stress released structures as, e.g., one-dimensional bulk vibrations (Sect. 1.1.2), torsional beams vibrations (Sect. 1.1.4), or bending plate vibrations (Sect. 1.1.3).

In some cases, however, it is necessary to look into more detail due to the fact that the stress is never completely released at the clamping. This indeed gives raise to a dependence of the frequency on the stress that might be dominant over the previously analyzed dependencies. In addition, often micro- and nanomechanical structures aren't uniform, but are made from multiple layers of materials with different thermal expansion coefficients. A common design consists, e.g., of a dielectric structural materials, such as SiN or SiC, that is coated with a thin metal layer. In this case, the modelling of the temperature response becomes more difficult, as a temperature change causes a complex stress field and resulting deformation with a hard to predict influence on the eigenfrequency. This effect has, e.g., been observed in 50 nm thick silicon nitride cantilevers coated with a 20 nm thick gold layer. The local heating with a readout laser resulted in a substantial detuning of the resonance frequency [22].

Finally, in the case of doubly clamped beams (bridges), the analysis also holds true for temperature changes that cause only a small stress, where small here is defined as

$$\sigma \ll \frac{E I_{y} n^{2} \pi^{2}}{A L^{2}} \approx \frac{E n^{2} \pi^{2}}{12} \left(\frac{t}{L}\right)^{2}$$

$$\Delta T \ll \frac{I_{y} n^{2} \pi^{2}}{\alpha A L^{2}} \approx \frac{n^{2} \pi^{2}}{12 \alpha} \left(\frac{t}{L}\right)^{2}$$
(3.55)

as can be extracted from (1.48), and by assuming a linear elastic material with a linear thermal expansion $\sigma = E\alpha\Delta T$. As an example, this gives for a silicon bridge with a ratio of length to height of L/h=100 a pretty robust temperature range of roughly $\Delta T\ll 50$ K. But as soon as the length to height ratio becomes larger the temperature induced stress starts to significantly contribute to the eigenfrequency of the resonator, and hence a small temperature change results in a large change of the frequency. Strings and membranes are the extreme cases where the tensile stress is the dominating parameter that defines the eigenfrequency. Hence, strings and membranes are highly responsive to changes of stress and hence to changes of temperature. This case will be discussed in more detail in the following subsection.

3.3.2 Resonators Under Tensile Stress (Strings)

Strings show a particularly strong response to temperature change. The thermal expansion is directly changing the tensile stress, which is the core parameter defining the string's resonance frequency. Here two main scenarios are introduced: (1) the string plus its frame is exposed to a common ambient temperature bath, and (2) the center of the string is heated locally. The first scenario is important when string resonators are used in arbitrary applications that require a good frequency stability, or when the string is employed as ambient temperature sensor. The second scenario plays an important role in many experiments where the string vibration is detected optically, e.g. with an integrated optical ring resonator or a free space laser, as depicted in the schematic in Fig. 3.8. The former configuration is often used in optomechanics [23–25]. Here fluctuations in the laser power could result in frequency noise of the mechanical resonator.

3.3.2.1 Ambient Temperature

The eigenfrequency of a string is given by (1.52) and it is mainly defined by the pre-stress σ . Different thermal expansion of the beam and the supporting chip make the strain of the beam temperature dependent which will result in a temperature dependent tensile stress. A schematic of such a string is shown in Fig. 3.9. The eigenfrequency will therefore also be a function of temperature. If the beam and the frame expands linearly with temperature the temperature dependent strain is given as

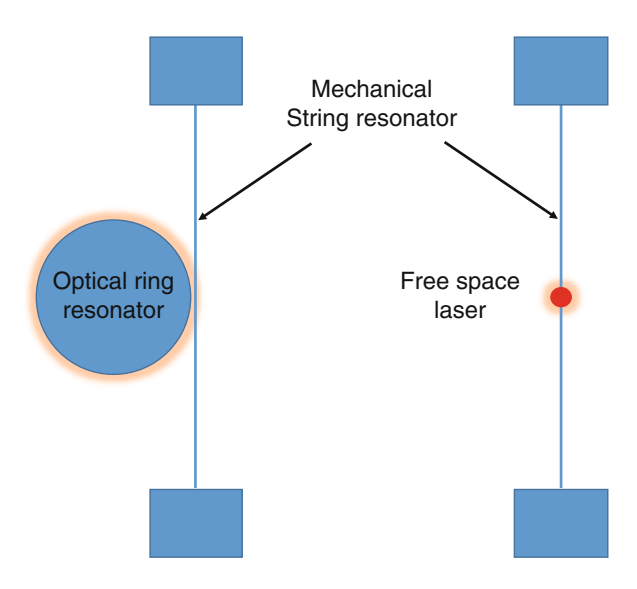


Fig. 3.8 Schematic of two common optical coupling mechanisms with string resonators, both producing a "point"-heating at due to optical absorption in the string center

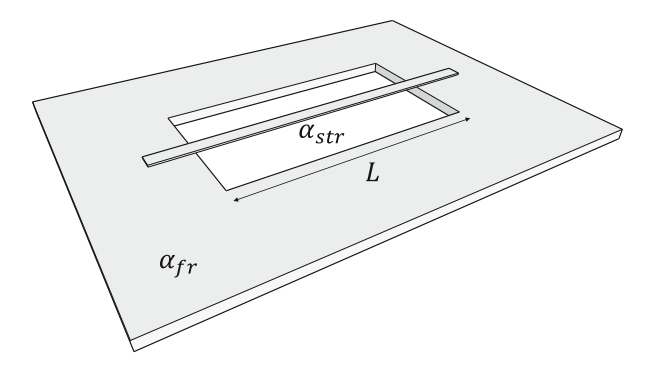


Fig. 3.9 Schematic drawing of a string with length L and a thermal expansion coefficient $\alpha_{\rm str}$ spanned by a frame with a thermal expansion coefficient $\alpha_{\rm fr}$

$$\varepsilon(T) = \varepsilon_0 - (\alpha_{\rm str} - \alpha_{\rm fr})(T - T_0), \tag{3.56}$$

where ε_0 is the strain at temperature T_0 , T the temperature and α_i the coefficient of thermal expansion of the beam and the support. Stress and strain are related to each other via Hook's laws if the beam is made of a linear elastic material and the strain does not exceed the elastic limits. If this is true, the temperature dependent stress can be defined as

$$\sigma(T) = E\varepsilon(T)$$

$$\sigma(T) = E(\varepsilon_0 - (\alpha_{\rm str} - \alpha_{\rm fr})(T - T_0))$$

$$\sigma(T) = \sigma_0 - E(\alpha_{\rm str} - \alpha_{\rm fr})(T - T_0).$$
(3.57)

Inserting the temperature dependent stress into (1.52), the temperature dependent eigenfrequency is given by

$$\Omega_n(T) = \frac{n\pi}{L} \sqrt{\frac{\sigma_0 - E_0(\alpha_{\rm str} - \alpha_{\rm fr})(T - T_0)}{\rho}},$$
(3.58)

which for a small stress change, that is for a small ΔT , can be approximated by the first order Taylor approximation

$$\Omega_n(T) \approx \Omega_n(T_0) \left(1 - \frac{1}{2} \frac{E_0(\alpha_{\text{str}} - \alpha_{\text{fr}})(T - T_0)}{\sigma_0} \right). \tag{3.59}$$

In this approximation temperature induced changes in length, Young's modulus, coefficients of thermal expansion and density have been neglected. For a real beam it can be expected that the length and the coefficients of thermal expansion will be increasing with temperature and that Young's modulus and the density will be decreasing with temperature. Neglecting these changes will introduce a small error when estimating the resonance frequency.

The temperature responsivity of a tensile stressed beam can be written as

$$\mathcal{R} = \frac{\partial \Omega_n}{\partial T} = -\frac{1}{2} \frac{E_0(\alpha_{\text{str}} - \alpha_{\text{fr}})}{\sigma_0} \Omega_n(T_0)$$
 (3.60)

and the relative responsivity

$$\delta \mathcal{R} = -\frac{1}{2} \frac{E_0(\alpha_{\rm str} - \alpha_{\rm fr})}{\sigma_0}.$$
 (3.61)

From this expression it can be seen that the temperature responsivity of a string is increasing with the Young's modulus and a big difference in thermal expansion and for a decreasing pre-stress. The responsivity is negative if the string has a higher coefficient of thermal expansion than the frame and vice versa. Optimizing all parameters, μK resolution can be achieved with nanostring resonators [13].

In the case of string made from multiple layers of different materials, the mass density and the temperature dependent tensile stress can be written in an effective form, which in the particular case of two materials are [26]

$$\rho^* = \frac{h_1 \rho_1 + h_2 \rho_2}{h_1 + h_2} \tag{3.62}$$

and

$$\sigma^*(T) = \frac{h_1 \sigma_1(T) + h_2 \sigma_2(T)}{h_1 + h_2}.$$
(3.63)

Inserting these effective parameters in the eigenfrequency equation for a string (3.57) and substituting the individual tensile stresses σ_i with (3.57) yields the eigenfrequency of a bi-layer string

$$f_n(T) = \frac{n}{2L} \sqrt{\frac{\left(h_1 \left[\sigma_{0,1} - (\alpha_{\text{str},1} - \alpha_{\text{fr}})E_1\right] + h_2 \left[\sigma_{0,2} - (\alpha_{\text{str},2} - \alpha_{\text{fr}})E_2\right]\right) (T - T_0)}{h_1 \rho_1 + h_2 \rho_2}}.$$
(3.64)

The respective responsivity can readily be calculated as done in (3.61).

3.3.2.2 Local Heating at String Center

As mentioned in the introduction to this section, the heating of a string at the center is a common scenario that occurs when an electromagnetic energy is absorbed, e.g., from a readout laser or during a photothermal analysis experiment.

Assuming a stationary situation in which the energy P, absorbed in the string center, is in equilibrium with the heat flow through the strings out into the frame of constant temperature T_0 . In this case the temperature field in the string can be readily described by

$$T(x) = T_0 + 2(T_1 - T_0)\frac{x}{L}$$
 for $0 \le x \le \frac{L}{2}$ (3.65)

as it is depicted in Fig. 3.10.

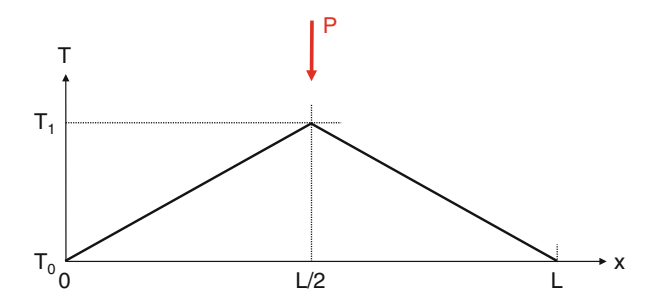


Fig. 3.10 Temperature distribution in a string of length L with a point heat source of power P in the center

The heat flux Q_T through one half of the string (from the string center to the left string end at x = 0) with a cross section A is described by the one-dimensional Fourier's law

$$Q_T = -\kappa A \frac{\partial T}{\partial x} \tag{3.66}$$

with the thermal conductivity κ of the string. The total energy Q flowing from the string center to the frame must be equal to the total power P that is absorbed in the string center $P = 2Q_T$. With (3.65), (3.66) yields the resulting temperature in the string center coming from the absorbed power

$$\Delta T = T_1 - T_0 = \frac{1}{4\kappa} \frac{L}{A} P. \tag{3.67}$$

Knowing the power-dependent temperature field in the string, it is now possible to calculate the temperature induced change of tensile stress. For the given linear temperature field, the average stress change $\langle \Delta \sigma \rangle$ in the string is given by

$$\langle \Delta \sigma \rangle = \alpha E \langle \Delta T \rangle, \qquad (3.68)$$

where the average temperature change for the linear temperature field is given by $\langle \Delta T \rangle = \frac{1}{2} \Delta T$.

For a small stress change, using the first order Taylor approximation, the eigenfrequency of a string (1.52) can be approximated by

$$\Omega_n(P) \approx \Omega_n(0) \left(1 - \frac{1}{2} \frac{\langle \Delta \sigma \rangle}{\sigma} \right)
= \Omega_n(0) \left(1 - \frac{1}{16} \frac{\alpha E}{\kappa \sigma} \frac{L}{A} P \right)$$
(3.69)

which results in the responsivity [17, 18]

$$\mathscr{R} = \frac{\partial \Omega_n(P)}{\partial P} = -\frac{1}{16} \frac{\alpha E}{\kappa \sigma} \frac{L}{A} \Omega_n(0) \tag{3.70}$$

and the relative responsivity

$$\delta \mathcal{R} = -\frac{1}{16} \frac{\alpha E}{\kappa \sigma} \frac{L}{A}.$$
 (3.71)

This formula shows that the responsivity of an absorbed power in the string center is maximal for long and narrow strings with a low tensile stress. Also, a large thermal expansion coefficient and a small thermal conductivity increase the response, which is very intuitive. However, the optimal design is not straightforward, as demonstrated in the case of a SiN string coated with a gold layer with the goal

References 113

to increase the responsivity. On the one hand, gold has a large thermal conductivity, which deteriorates the responsivity. But on the other hand, gold has a larger thermal expansion coefficient than SiN which increases the responsivity. It has been shown that the optimal solution is to remove the gold close to the string ends [17]. In this way the gold layer increases the thermal expansion but the heat flow off the string is minimized.

References

- S. Dohn, R. Sandberg, W. Svendsen, A. Boisen, Enhanced functionality of cantilever based mass sensors using higher modes. Appl. Phys. Lett. 86(23), 233501 (2005)
- S. Dohn, W. Svendsen, A. Boisen, O. Hansen, Mass and position determination of attached particles on cantilever based mass sensors. Rev. Sci. Instrum. 78(10), 103303 (2007)
- M.S. Hanay, S. Kelber, A.K. Naik, D. Chi, S. Hentz, E.C. Bullard, E. Colinet, L. Duraffourg, M.L. Roukes, Single-protein nanomechanical mass spectrometry in real time. Nat. Nanotechnol. 7, 602–608 (2012)
- 4. H. Yu, X. Li, Bianalyte mass detection with a single resonant microcantilever. Appl. Phys. Lett. **94**(1), 173–176 (2009)
- S. Schmid, S. Dohn, A. Boisen, Real-time particle mass spectrometry based on resonant micro strings. Sensors 10(9), 8092–8100 (2010)
- S. Dohn, S. Schmid, F. Amiot, A. Boisen, Position and mass determination of multiple particles using cantilever based mass sensors. Appl. Phys. Lett. 97(4), 044103 (2010)
- M.S. Hanay, S.I. Kelber, C.D. O'Connell, P. Mulvaney, J.E. Sader, M.L. Roukes, Inertial imaging with nanomechanical systems. Nat. Nanotechnol. 10(4), 339–344 (2015)
- 8. B. Voigtlaender, Scanning Probe Microscopy (Springer, New York, 2015)
- I. Kozinsky, H.W.Ch. Postma, I. Bargatin, M.L. Roukes, Tuning nonlinearity, dynamic range, and frequency of nanomechanical resonators. Appl. Phys. Lett. 88(25), 253101 (2006)
- Q.P. Unterreithmeier, E.M. Weig, J.P. Kotthaus, Universal transduction scheme for nanomechanical systems based on dielectric forces. Nature 458(7241), 1001–1004 (2009)
- S. Schmid, T. Bagci, E. Zeuthen, J.M. Taylor, P.K. Herring, M.C. Cassidy, C.M. Marcus, L.G. Villanueva, B. Amato, A. Boisen, Y.C. Shin, J. Kong, A.S. Sørensen, K. Usami, E.S. Polzik, Single-layer graphene on silicon nitride micromembrane resonators. J. Appl. Phys. 115(5), 054513 (2014)
- A.K. Pandey, O. Gottlieb, O. Shtempluck, E. Buks, Performance of an AuPd micromechanical resonator as a temperature sensor. Appl. Phys. Lett. 96, 203105 (2010)
- T. Larsen, S. Schmid, L. Gronberg, A.O. Niskanen, J. Hassel, S. Dohn, A. Boisen, Ultrasensitive string-based temperature sensors. Appl. Phys. Lett. 98, 121901 (2011)
- X..C Zhang, E.B. Myers, J.E. Sader, M.L. Roukes, Nanomechanical torsional resonators for frequency-shift infrared thermal sensing. Nano Lett. 13(4), 1528–34 (2013)
- T. Larsen, S. Schmid, L.G. Villanueva, A. Boisen, Photothermal analysis of individual nanoparticulate samples using micromechanical resonators. ACS Nano 7(7), 6188–6193 (2013)
- T.S. Biswas, N. Miriyala, C. Doolin, X. Liu, T. Thundat, J.P. Davis, Femtogram-scale photothermal spectroscopy of explosive molecules on nanostrings. Anal. Chem. 86, 11368–11372 (2014)
- S. Schmid, K. Wu, P.E. Larsen, T. Rindzevicius, A. Boisen, Low-power photothermal probing of single plasmonic nanostructures with nanomechanical string resonators. Nano Lett. 14, 2318–2321 (2014)
- S. Yamada, S. Schmid, T. Larsen, O. Hansen, A. Boisen, Photothermal infrared spectroscopy of airborne samples with mechanical string resonators. Anal. Chem. 85, 10531–10535 (2013)

19. S.C. Jun, X.M.H. Huang, M. Manolidis, C.A. Zorman, M. Mehregany, J. Hone, Electrothermal tuning of Al–SiC nanomechanical resonators. Nanotechnology **17**(5), 1506–1511 (2006)

- M. Rendón, N. Makarov, Determination of the Si Young's modulus between room and melt temperature using the impulse excitation technique. Phys. Status Solidi C 11(1), 150–155 (2014)
- W.-H. Chuang, T. Luger, R.K. Fettig, R. Ghodssi, Mechanical property characterization of LPCVD silicon nitride thin films at cryogenic temperatures. J. Microelectromech. Syst. 13(5), 870–879 (2004)
- V. Pini, J. Tamayo, E. Gil-Santos, D. Ramos, P. Kosaka, H.-D. Tong, C. van Rijn, M. Calleja, Shedding light on axial stress effect on resonance frequencies of nanocantilevers. ACS Nano 5(6), 4269–4275 (2011)
- G.A. Brawley, M.R. Vanner, P.E. Larsen, S. Schmid, A Boisen, W.P. Bowen, Non-linear optomechanical measurement of mechanical motion (2014). arXiv:1404.5746
- R. Zhang, C. Ti, M.I. Davanço, Y. Ren, V. Aksyuk, Y. Liu, K. Srinivasan, Integrated tuning fork nanocavity optomechanical transducers with high fMQM product and stress-engineered frequency tuning. Appl. Phys. Lett. 107(13), 131110 (2015)
- E. Gavartin, P. Verlot, T.J. Kippenberg, A hybrid on-chip optomechanical transducer for ultrasensitive force measurements. Nat. Nanotechnol. 7, 509–514 (2012)
- S. Bose, S. Schmid, T. Larsen, S.S. Keller, P. Sommer-Larsen, A. Boisen, K. Almdal, Micromechanical string resonators: analytical tool for thermal characterization of polymers. ACS Macro Lett. 3(1), 55–58 (2014)

Chapter 4 Transduction

Abstract The efficient transduction of nanomechanical resonators is quintessential for any practical application. In the context of this book, transduction refers to the translation of mechanical motion to an electrical signal and vice versa for detection and actuation, respectively. In this chapter the most common underlying physical transducing mechanisms are quickly introduced. Most of these mechanisms are of an electrical nature, such as electrodynamic, electrostatic, thermoelastic, piezoresistive, or piezoelectric transduction. Nanomechanical resonators transduced with one of these techniques are therefore known as nanoelectromechanical systems (NEMS). But it is also common practice to transduce nanomechanical resonators by optic means. The full optic transduction and control of nanomechanical resonators is, e.g., employed in the field of cavity optomechanics.

This is an overview of techniques commonly used to transduce (actuate and detect) the mechanical motion of nanomechanical resonators. Every technique is briefly explained and prominent corresponding examples are presented. The reference list is not complete by any means. The idea of this overview is to call the reader's attention to all possible transduction techniques and give him/her an entry point for his/her own thorough literature research.

There are a few techniques that are less common, which in this edition will not be omitted. This, e.g., includes the detection of motion of nanomechanical resonators by tunneling [1], hard contact [2], or field emission [3]. Another technique which will not be discussed in more detail is *magnetostatic transduction*. This includes the transduction of ferromagnetic [4] or paramagnetic [5] mechanical resonators with the help of an external dynamic magnetic field. The increasing inductive reactance of a coil with increasing frequency sets a limit at room temperature of the maximal achievable frequency in the lower kHz range. Hence this technique is rarely used to transduce nanomechanical resonators with frequencies in the MHz range.

The focus of this book is NEMS that is nanomechanical resonators that are transduced by electrical means. Besides electrical transduction, optical detection of nanomechanical motion is commonly used, which can be external or fully integrated. Like many electrical transduction techniques, optical transduction can be used not only to detect but also to actuate a nanomechanical resonator by means of radiation pressure. The full optical transduction and control of nanomechanical

resonators is studied in cavity optomechanics [6, 7]. Cavity optomechanics has developed into a field and its specific transduction methods are not covered in this chapter.

Some transduction techniques allow for both actuation and detection whereas others only work for either detection or actuation. The nature of each technique is assigned in the parentheses behind the title.

4.1 Electrodynamic (Actuation and Detection)

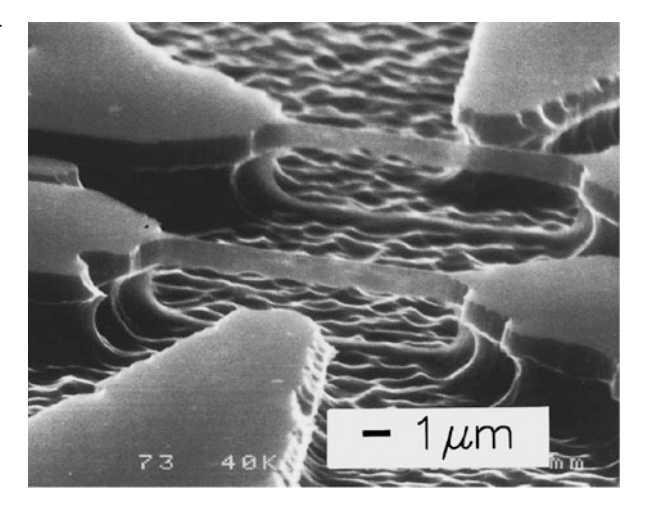
Electrodynamic transduction is based on the *Lorentz force* acting on free charges inside a wire that is located in a uniform magnetic field $\bf B$. The Lorentz force $\bf F$ acting on a single particle with charge q in the absence of an electric field is then given by

$$\mathbf{F_L} = q\mathbf{v} \times \mathbf{B} \tag{4.1}$$

with the velocity vector **v**. From the vector product it is clear that the resulting force is acting in the direction normal to the plane spanned by the magnetic field and velocity vector. The effect of the Lorentz force can be used to actuate and detect the motion of a nanomechanical resonator, as discussed subsequently.

Electrodynamic transduction is relatively easy to implement and allows for an efficient actuation and detection of nanomechanical resonators with frequencies up to the GHz range. It is thus not surprising that electrodynamic transduction had been an enabling technique for the pioneering examples of nanomechanical resonators [8] (see Fig. 4.1).

Fig. 4.1 SEM micrograph of a nanomechanical silicon resonators fully transduced electrodynamically (Reprinted from [8] with the permission of AIP Publishing.)



4.1.1 Lorentz Force on a Straight Wire

A conductive wire carrying an electric current experiences the Lorentz force when it is located inside a uniform magnetic field **B**. Individual electric charges that are traveling with a velocity **v** inside the wire each experience the Lorentz force (4.1). The sum of all the forces acting on all individual charges creates a macroscopic force on the wire. The electric current inside a wire of length L is defined by

$$\mathbf{I} = \frac{nq\mathbf{v}}{L} \tag{4.2}$$

with the total number of charges n. Combining this definition with the Lorentz force law (4.1) yields a term for the total magnetic force acting on the wire as a function of the electric current

$$\mathbf{F} = L\mathbf{I} \times \mathbf{B}.\tag{4.3}$$

The most common ways to implement a Lorentz force actuation creating an outof-plane vibration in singly clamped and doubly clamped nanomechanical beam resonators are shown in Fig. 4.2b. As it is clear from (4.3), the Lorentz force is increasing linearly with the magnetic field strength. At room temperature a strong

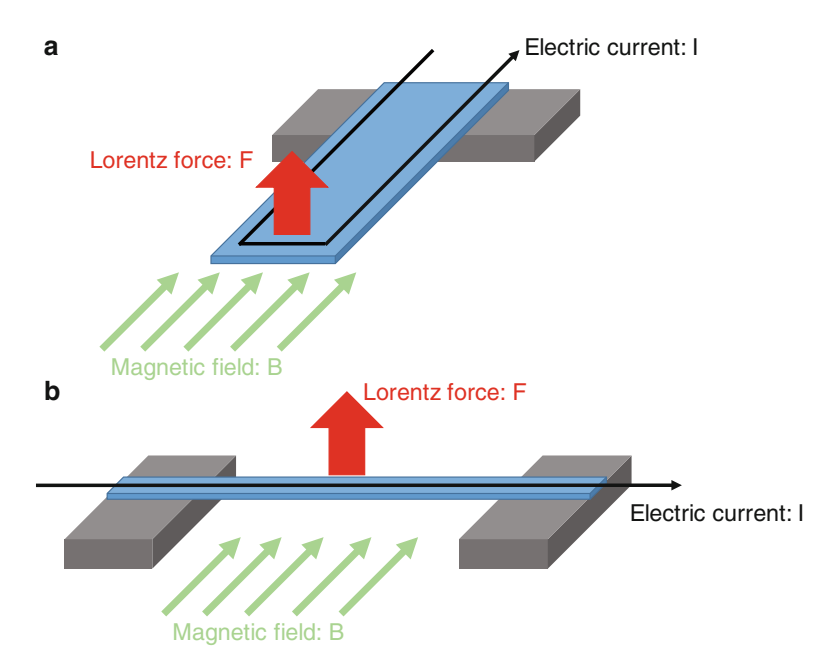


Fig. 4.2 Schematic drawings of two common electrode configuration to actuate (a) singly clamped and (b) doubly clamped beams

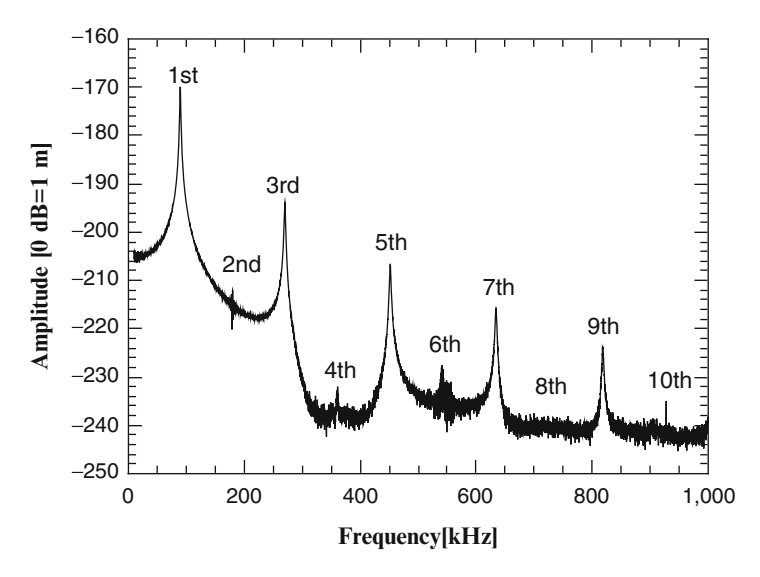


Fig. 4.3 Frequency response of a gold-coated silicon nitride micro string (340 nm) thick and $1000 \,\mu\text{m}$ long) placed in a magnetic Halbach array with a field strength of $0.4 \, \text{T}$ and actuated with an ac voltage of $30 \, \text{mV}$. The resonance was detected with a laser-Doppler vibrometer (MSA-500 from Polytec GmbH) at atmospheric pressure

magnetic field can be achieved with rare earth magnets. When arranging them in a Halbach array magnetic field strengths of up to 2 T can be achieved [9]. At cryogenic temperatures, magnetic fields of up to 7–8 T can be achieved with superconducting coils [8, 10].

Attention has to be paid to the fact that only odd resonant bending modes can be transduced with this technique. In even modes, the induces net force is zero. This effect can be seen in the frequency response of a resonant strings actuated by the Lorentz force shown in Fig. 4.3.

4.1.2 Electrodynamically Induced Voltage (Electromotive Force)

When a wire is moving inside a uniform magnetic field, the individual free charges in the wire experience the Lorentz force (4.1). In the case of the depicted transduction schemes in Fig. 4.2, the magnetic forces are pushing the charges in the direction of the wire. This magnetic force acting on the charges results in a charge separation and hence a potential difference across the length of the wire. In the case of a moving conducting wire this voltage is called the motional *electromotive* force $(U_{\rm EMF})$. This induced voltage is the underlying principle of typical electric generators.

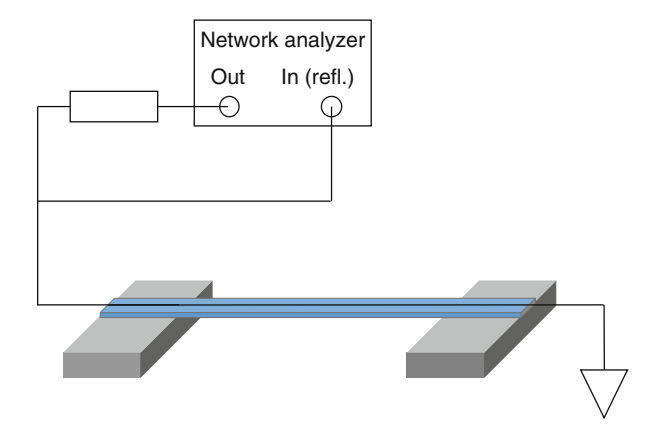


Fig. 4.4 Schematic of simple electrodynamic transduction including actuation by the Lorentz force detection of electromotive current

The potential difference, or voltage, between two points is defined as the work done per unit charge to move the charge from one point to the other. Hence, with the Lorentz force (4.1) acting on a single charge, the EMF between the ends of the wire is given by

$$U_{\rm EMF} = \frac{LF_L}{q} = BLv. \tag{4.4}$$

The detection of this EMF is straightforward and it can directly be picked up, e.g., with a network analyzer [8, 9], as schematically depicted in Fig. 4.4. More complex detection schemes consist of differential setup with a passive reference device for the use in a self-sustaining oscillator circuit [10].

4.2 Electrostatic (Actuation and Detection)

Electrostatic transduction allows for a low-power operation and uncomplicated system integration. Therefore capacitive transduction schemes have become a cornerstone in MicroElectroMechanical Systems (MEMS), where they are very successfully used in devices such as accelerometers, gyroscopes, microphones, pressure sensors, and mirror arrays for projectors, etc. The low power consumption is equally interesting for the use in smaller nanomechanical resonators. However, the smaller size of the moving parts in nano-sized resonators results in smaller electrostatic signals. In this subsection electrostatic transduction techniques are discussed for the application in nanomechanical resonators.

Generally, electrostatic transduction is based on the interaction between quasistatic electric charges. Practically, the electric charge in a nanomechanical resonator

is controlled via conductive electrodes with a defined potential. This scheme of inducing charges by means of a defined potential is the main scope of this subsection. In contrast, electric charges can also locally be trapped, typically at the interface of different materials, in particular on dielectrics. It has, e.g., been shown that local charge separation, resulting in a static dipole moment, can be used to transduce nanomechanical resonators made of GaAs/AlGaAs multilayers [11]. While local charges can be a key part of a transducer design, e.g. in electret microphones, locally trapped charges can hinder an effective electrostatic transduction [12].

4.2.1 Electrostatic Forces

In a lossless system, the force in direction of a specific degree of freedom ξ is given by the change of potential energy W_e of the system in the ξ -direction

$$F = -\frac{\partial W_e(\xi)}{\partial \xi}.$$
 (4.5)

The energy W_e stored in an electrostatic system can be derived by integration of the energy density over the significant system volume v

$$W_e = \int_v \frac{1}{2} \varepsilon_r \varepsilon_0 E^2 \mathrm{d}v, \tag{4.6}$$

where E is the electrostatic field strength, ε_r is the relative dielectric constant, and ε_0 is the permittivity of vacuum. In an electrostatic system with a single electrical terminal pair with a constant potential U, the capacity of the system to store electrostatic energy as a function of the applied potential is typically given as a function of the systems capacitance C, given by

$$W_e = -\frac{1}{2}CU^2. (4.7)$$

Assuming that the system has a single degree of freedom ξ , the electrostatic force in ξ -direction is then, according to (4.5), given by the change of the capacitance in this direction

$$F = \frac{1}{2} \frac{\partial C(\xi)}{\partial \xi} U^2. \tag{4.8}$$

This electrostatic force can be used to drive a nanomechanical resonator. There are two main system configurations, which are discussed subsequently. The first subsection discusses the scenario where the change in capacitance in (4.8) is induced

by the movement of an electrode in the nanoelectromechanial system. The second subsection focuses on the scenario where the system energy (4.6) is altered by the movement of a dielectric material inside the nanoelectromechanical system.

4.2.1.1 Forces Between Electrodes

Electrode pairs with a potential difference U feel the Coulomb force from the net charge difference. This electrostatic force can be exploited to actuate nanomechanical resonators. One way to do so is to use the mechanical resonator as one of the electrodes. That directly implies that the nanomechanical resonator has to be conductive. Either the resonator is made of a conductive material, as, e.g., a carbon nanotube, graphene [14], or aluminium [13, 15, 16]. In case that the mechanical structure is non-conductive, it has to be metallized. Such a examples are shown in Fig. 4.11 of a silicon nitride membrane resonator that is coated with an aluminium thin film or graphene.

Depending on the geometry and arrangement of a specific electrostatic resonator design the appropriate force model has to be used. Here three common models for specific boundary conditions are presented, as schematically depicted in Fig. 4.5.

Normal Force Between Parallel Plates

The probably most commonly found electrode configuration is where a nanome-chanical resonator is arranged in parallel to a surface with a potential difference U in between them. A schematic drawing is shown in Fig. 4.5a. Neglecting fringe fields at the plates' border, the capacitance between two parallel plates of area A = wL and situated in a medium with ε_r is given by

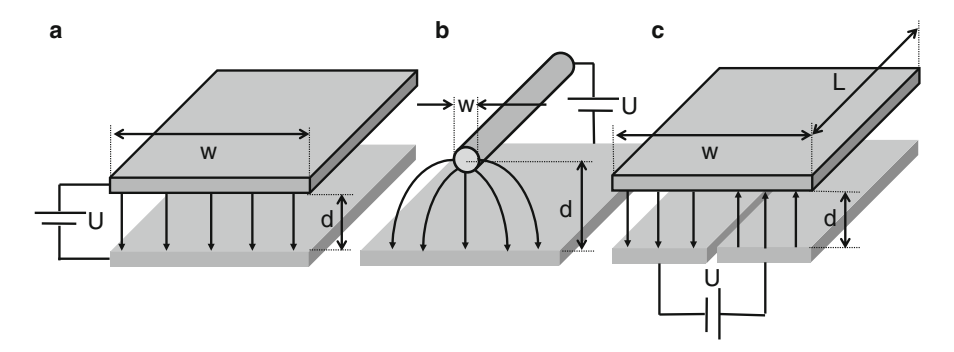


Fig. 4.5 Schematics of three electrode arrangements: (a) parallel plates with potential difference U, (b) wire and parallel surface with potential difference U, and (c) floating potential plate parallel to coplanar electrode pair with potential difference U

$$C = \varepsilon_0 \varepsilon_r \frac{A}{d} \tag{4.9}$$

which with (4.8) yields the force

$$F = -\frac{1}{2}\varepsilon_0\varepsilon_r \frac{A}{d^2}U^2. \tag{4.10}$$

Normal Force Between a Wire Parallel to Substrate

In this scenario, as schematically depicted in Fig. 4.5b, a thin wire with diameter w is placed in a distance $d \gg w$ from a parallel substrate (measured from the center of the wire). Such a situation is typically given for very thin resonators such as carbon nanotubes. In that case the capacitance can be approximated by

$$C = \frac{2\pi\varepsilon_0\varepsilon_r L}{\ln\left(4\frac{d}{w}\right)} \tag{4.11}$$

which with (4.8) yields the electrostatic force normal to the wire's plane

$$F = -\frac{\pi \varepsilon_0 \varepsilon_r L}{d \ln \left(4 \frac{d}{w}\right)^2} U^2. \tag{4.12}$$

In the case of a beam which neither fulfills the non-fringe assumption of the parallel plate model nor the fringe-only assumption of the wire model, the capacitance and the resulting force can be readily approximated by a combination of the two models [17]. For this purpose, the wire diameter is chosen equal to the beam's thickness w = h.

Normal Force Between a Coplanar Electrode Pair and a Floating Electrode

In this configuration, as shown in Fig. 1.10a, a floating electrode of area A is placed in parallel over a coplanar electrode pair with a potential difference U. A schematic drawing is shown in Fig. 4.5c. An equivalent parallel plate capacitor would be half the area with double the distance d, which by neglecting fringe fields results in the capacitance [12]

$$C = \frac{1}{4}\varepsilon_0 \varepsilon_r \frac{A}{d} \tag{4.13}$$

which with (4.8) yields the electrostatic force normal to the plate's plane

$$F = -\frac{1}{8}\varepsilon_0 \varepsilon_r \frac{A}{d^2} U^2. \tag{4.14}$$

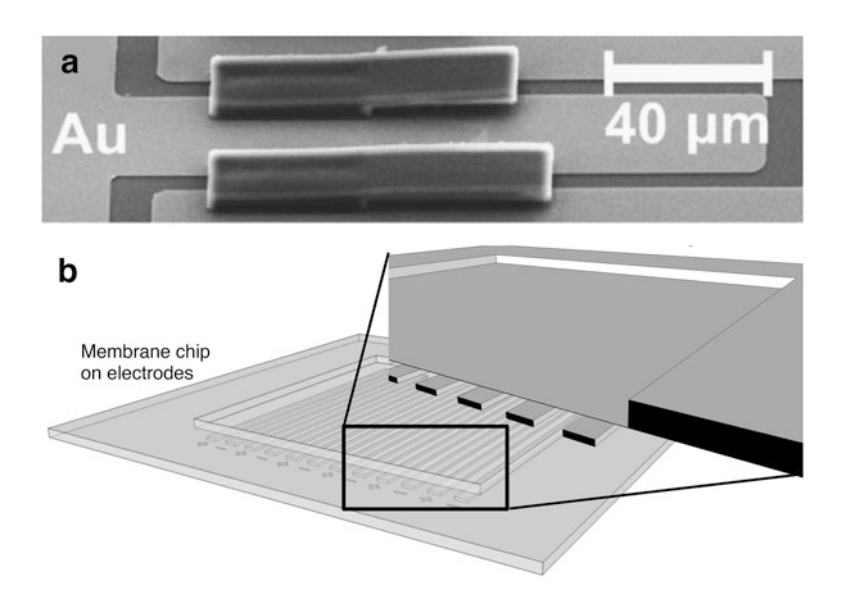


Fig. 4.6 Examples of applications of dielectric polarization forces for transduction of (a) a micromechanical polymeric resonators (Reprinted from [20], with the permission from AIP Publishing), and (b) a silicon nitride membrane resonator (schematic drawing) (Reprinted from [12], with permission from AIP Publishing.)

4.2.1.2 Dielectric Polarization Force

Dielectric polarization force or Kelvin polarization force [18] is the force that is being exerted on a dielectric object located in a nonuniform electric field. A well-known example is the pulling of a dielectric slab into a parallel capacitor by the electric fringe field at the edge of the capacitor, an effect often discussed in standard physics books. The main advantage of the dielectric polarization force over the conventional electrostatic force between electrodes, as discussed in the previous subsection, is the possibility to work with pristine dielectric mechanical structures. The lack of metallization is interesting from many standpoints, as, e.g., minimal mechanical and optical losses. Figure 4.6 shows examples of applications of dielectric polarization forces for the transduction of nanomechanical resonators. Dielectric polarization forces have further been used to transduce silica microtoroids [19] or nanomechanical silicon nitride resonators [21].

The dielectric polarization force acting on a dielectric object can readily be calculated by means of the framework introduced in the beginning of this Sect. 4.2.1 on page 120. Beside the energy approach, it is possible to derive a force term based on a dipole approximation. For this it is assumed that a dipole, that is located in an electric field **E**, does not alter the field. The force acting on a single infinitesimally small dipole is then given by [22]

$$\mathbf{F} = \mathbf{p} \cdot \nabla \mathbf{E},\tag{4.15}$$

where \mathbf{p} is the dipole moment. A dielectric material can be modelled as consisting of an infinity of single noninteracting dipoles, which results in a material dependent macroscopic polarization \mathbf{P} . Replacing the single dipole moment with the macroscopic polarization in (4.15) then yields the *dielectric polarization force density* [18] of a dielectric material

$$\mathbf{f}_{\text{DPF}} = \mathbf{P} \cdot \nabla \mathbf{E}.\tag{4.16}$$

With the polarization of a linear dielectric material with a susceptibility χ_e

$$\mathbf{P} = \varepsilon_0 \chi_e \mathbf{E} = \varepsilon_0 (\varepsilon_r - 1) \mathbf{E} \tag{4.17}$$

the dielectric polarization force density, after some vector algebra, becomes [18]

$$\mathbf{f}_{\text{DPF}} = \frac{1}{2} \varepsilon_0 (\varepsilon_r - 1) \nabla (\mathbf{E} \cdot \mathbf{E}). \tag{4.18}$$

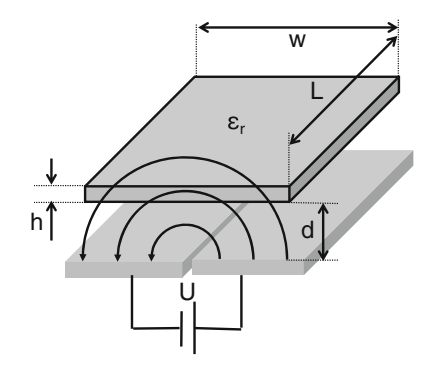
Because the force density is proportional to the gradient of the electric field is squared, the resulting net force always acts towards the electric field intensity maximum.

Coplanar Electrode Design

A typical resonator design based on the dielectric polarization force is based on a coplanar electrode configuration with the dielectric resonator placed on top, as can be seen in the examples in Fig. 4.6a, b. A schematic of this coplanar electrode configuration is schematically depicted in Fig. 4.7. For a relatively small gap between the electrodes and a homogeneous dielectric medium, the electric field lines are concentric circles, given by

$$E_0 = \frac{U}{\pi \sqrt{x^2 + y^2}}. (4.19)$$

Fig. 4.7 Schematic drawing of a coplanar electrode arrangement. The resulting nonuniform electric field exerts a dielectric polarization force on a dielectric beam in the direction of the field intensity maximum which is toward the electrode gap



However, in the here discussed scheme, the concentric field lines get altered by the presence of the nanomechanical dielectric beam. In order to take this field disturbance into account the factor α is introduced. The electric field inside the dielectric beam then is given by

$$E_d = \alpha E_0, \tag{4.20}$$

where α represents the field reduction and field imperfection inside the dielectric material. With (4.18), the Kelvin polarization force density inside the dielectric beam (with ε_r) in the normal direction to the electrodes becomes

$$f_{\text{DPF}} = \frac{1}{2} \varepsilon_0 (\varepsilon_r - 1) \frac{\partial E_d^2}{\partial y}$$

$$= -\varepsilon_0 (\varepsilon_r - 1) \frac{\alpha^2 U^2 y}{\pi^2 (x^2 + y^2)^2}.$$
(4.21)

Assuming that the beam is situated in a medium such as vacuum or air with a relative dielectric constant close to unity, the force acting on the dielectric beam is readily obtained by integration of the force density over the volume of the dielectric beam

$$F_{\text{DPF}} = L \int_{d}^{d+h} \int_{-w/2}^{w/2} f_{\text{DPF}} \, dxdy$$

$$= \frac{1}{\pi^2} \varepsilon_0(\varepsilon_r - 1) \alpha^2 U^2 L \frac{d \arctan \frac{w}{2(d+h)} - (d+h) \arctan \frac{w}{2d}}{d(d+h)}. \tag{4.22}$$

Assuming the beam width to be large compared to its height $(w \gg h)$ and its distance to the electrodes $(w \gg d)$, the force simplifies to

$$F_{\rm DPF} \approx -\frac{1}{2\pi} \varepsilon_0 (\varepsilon_r - 1) \alpha^2 L \frac{h}{d(d+h)} U^2.$$
 (4.23)

The values for the field correction are typically in the range between $0.6 < \alpha < 1$. Numerical α values for dielectric beams with different dielectric constants ε_r and heights h can be calculated from the following heuristic formula

$$\alpha = \frac{8301h^{0.6156}}{8301h^{0.6156} + (\varepsilon_d)^b - 1} \tag{4.24}$$

with

$$b = 0.5887 - \frac{0.003795}{h^{0.3184}},\tag{4.25}$$

which approximates the numerical values with an average relative error of 2.0 %.

When comparing the dielectric polarization force (4.23) acting on a dielectric beam to the electrostatic force acting on a floating conducting beam in vacuum (4.14)

$$F = -\frac{1}{8}\varepsilon_0 L \frac{w}{d^2} U^2 \tag{4.26}$$

it shows that the two force terms are very similar, in particular if the beam thickness is a lot smaller than the distance to the electrodes ($h \ll d$). The main difference is that the force on a dielectric beam is proportional to the beam thickness h while the force on a conducting beam is proportional to the beam width w. For a beam with a height-to-thickness aspect ratio of unity, the forces are of similar order of magnitude. However the width is typically larger than the thickness, this is particularly true for membrane or plate structures. In this case it is possible to design an array of coplanar electrode, which results in an interdigitated electrode design [12]. In such a design the electrode pitch is typically of the order of the distance d. Hence, for a wide membrane or plate structure, the force on a dielectric structure is as a rough approximation a factor h/d smaller.

4.2.2 Capacitively Induced Current

Besides the actuation of a nanomechanical resonator, the capacitive transduction technique can also be used to detect the motion of a vibration. The electric charge Q_e stored in the electrostatic system is given by

$$Q_e = C(\xi)U. \tag{4.27}$$

If the potential U is kept constant, a change of the capacitance causes a change of the amount of stored electric charges in the system. In other words, a mechanical vibration in ξ -direction, which modulates the capacitance, periodically "pumps" electric charges on and off the system. This charge migration can be detected as a small current. According to (4.27), this induced current can readily be increased by increasing the applied potential U, typically called the bias voltage or $U_{\rm DC}$.

In a typical nanomechanical system, the mechanically induced variation of the capacitance $\Delta C \ll C_{\rm ft}$ is a lot smaller than the total systems capacitance, also called feedthrough capacitance $C_{\rm ft}$, which remains constant. The detection of this small relative variation of the system capacitance is a main challenge of the capacitive readout scheme of the vibrational motion of a nanomechanical system. Here, different capacitive readout strategies are discussed briefly.

A common remedy is to perform a differential measurement in which the induced current from a reference capacitance, that is equal to the feedthrough capacitance ($C_{\text{ref}} = C_{\text{ft}}$), is subtracted from the signal obtained from the nanomechanical device. Like that the signal from the feedthrough capacitance disappears. A typical

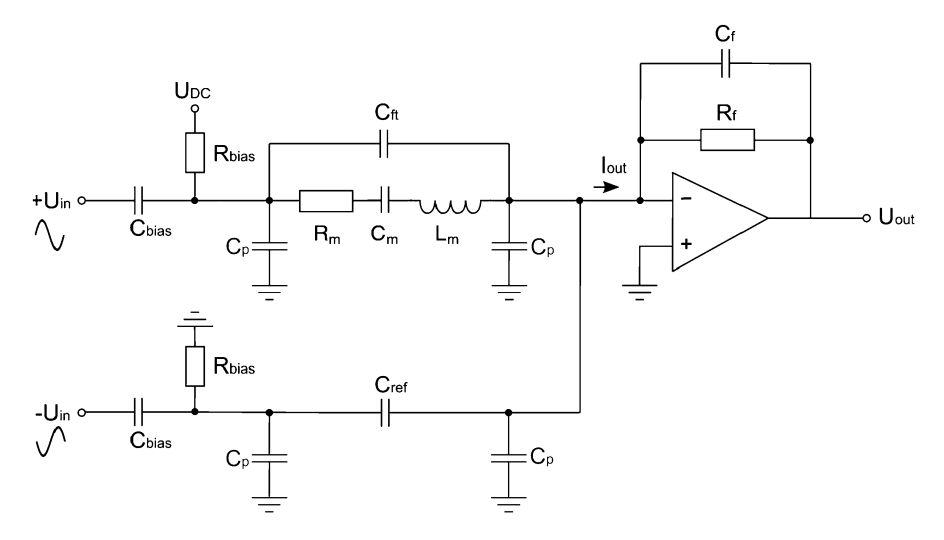


Fig. 4.8 Equivalent circuit diagram of a differential capacitive readout scheme with a transimpedance amplifier [24]

differential circuit is shown in Fig. 4.8. In this readout circuit, the nanomechanical resonator is substituted as an electromechanical LCR (inductor-capacitor-resistor) model.

Assuming the bias voltage $U_{\rm DC}$ to be much larger than the AC excitation voltage $U_{\rm in}$, the equivalent impedance of the nanomechanical resonator can be described by [23]

$$Z_m(s) = R_m + i\omega L_m + \frac{1}{i\omega C_m}$$
(4.28)

and

$$R_{m} = \frac{m_{\text{eff}}\Omega}{U_{\text{DC}}^{2} \left(\frac{\partial C}{\partial \xi}\right)^{2} Q}$$

$$C_{m} = \frac{U_{\text{DC}}^{2} \left(\frac{\partial C}{\partial \xi}\right)^{2}}{\Omega^{2} m_{\text{eff}}}$$

$$L_{m} = \frac{m_{\text{eff}}}{U_{\text{DC}}^{2} \left(\frac{\partial C}{\partial \xi}\right)^{2}}$$
(4.29)

with the eigenfrequency Ω , effective mass $m_{\rm eff}$, quality factor Q, and the capacitance change per unit deflection $\partial C/\partial \xi \approx \partial C_{\rm ft}/\partial \xi$. As depicted in the schematic in Fig. 4.8, it is an option to build a differential scheme with a passive

reference capacitance $C_{\rm ref}$ in parallel to the nanomechanical device. Neglecting parasitic capacitances C_p , the total impedance of the nanomechanical device is the parallel combination of (4.28) and the feedthrough capacitance $C_{\rm ft}$ plus the reference capacitance $C_{\rm ref}$, which then gives the equivalent impedance of

$$Z = \frac{U_{\rm in}}{I_{\rm out}} = \left[\frac{1}{Z_m} + i\omega C_{\rm ft} - i\omega C_{\rm ref}\right]^{-1}.$$
 (4.30)

When measuring I_{out} directly with a device with an input impedance of $Z_f = 50 \Omega$ device, the transfer function H of the nanoelectromechanical system becomes

$$H = \frac{U_{\text{out}}}{U_{\text{in}}} = \frac{Z_f}{Z}.$$
 (4.31)

Example of the transfer function (4.31) for a nanomechanical beam resonator is shown in Fig. 4.9. In the case of an unbalanced transduction scheme with $C_{\text{ref}} = 0$, the nanomechanical vibration induces a small resonance peak plus an anti-peak as a result of the interplay with the feedthrough capacitance C_{ft} . Additionally, the feedthrough capacitance produces a large background signal which overshadows the resonance peak. In the case that the feedthrough capacitance is balanced with an adjusted reference capacitance ($C_{\text{ref}} = C_{\text{ft}}$), the background signal from

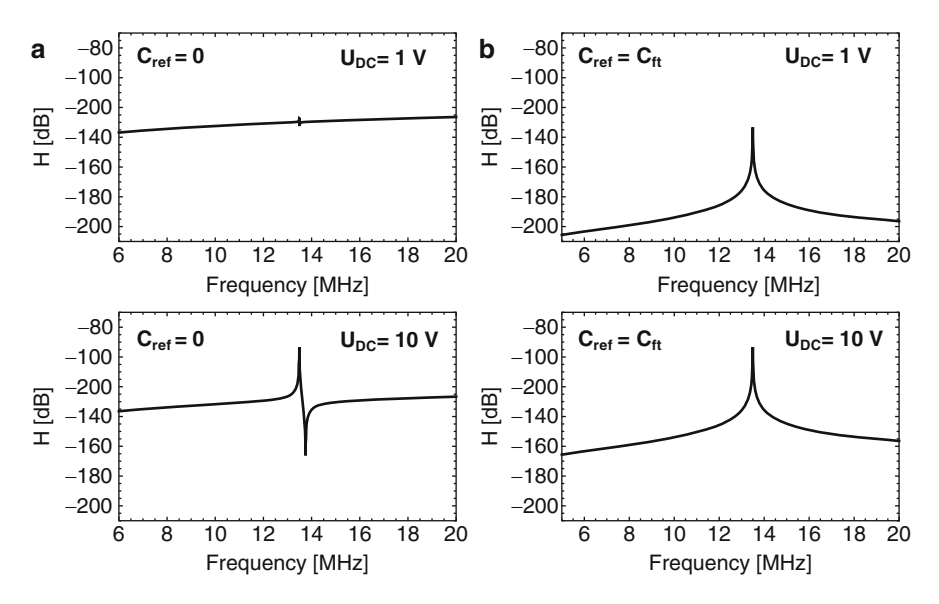


Fig. 4.9 Example of a transfer function (4.31) with unity amplification ($Z_f=1$) of a (a) unbalanced and (b) balanced capacitive detection circuit. The measured resonance peak comes from a doubly clamped silicon nitride beam resonator from [13] with d=130 nm, L=14 μ m, w=200 nm, h=205 nm, $C_{\rm ft}=76$ aF, $\partial C/\partial \xi=0.6$ aF/nm, Q=1800, measured with $U_{\rm DC}=10$ V

the feedthrough capacitance vanishes and only the mechanically induced signal remains. From Fig. 4.9 the importance of the bias voltage $U_{\rm DC}$ becomes eminent. It is therefore advisable to maximize the bias voltage without destroying the nanomechanical device.

From the transfer functions plotted in Fig. 4.9 it can be seen that the obtainable signals are going to be very small. The detection of this faint capacitive current I_{out} is challenging due to impedance mismatches and parasitic capacitances C_p , which were neglected in Fig. 4.9. The root of this challenge lies in the typically ultrahigh impedance of the nanomechanical resonator (4.28). When I_{out} is measured directly with typical $50\,\Omega$ measurement equipment, the corresponding voltage signal gets divided by the large factor $R_m/50$ (this is the value at the resonance peaks in Fig. 4.9) and becomes very difficult to detect. When measuring with equipment with high input impedance the small signal likely gets deteriorated by parasitic capacitances. There are several strategies on how to overcome the challenge of transducing a high impedance nanomechanical resonators. Here two particular impedance mismatch strategies are quickly discussed: the use of a transimpedance amplifier and an LC filter. Similar impedance mismatch issues are also common particularly in piezoresistive (see Sect. 4.4) and piezoelectric (see Sect. 4.5) transduction schemes.

Transimpedance Amplifier

A common practice to overcome the impedance mismatch is to integrate a transimpedance amplifier in close proximity (best on chip) to the nanomechanical resonator (as shown in the schematic in Fig. 4.8) in order to save the signal from draining through the parasitic capacitances [24]. The impedance Z_f of the transimpedance amplifier is given by

$$Z_f = \frac{U_{\text{out}}}{I_{\text{out}}} = \frac{R_f}{1 + i\omega C_f R_f}.$$
 (4.32)

The induced current I_{out} can be amplified by choosing a large resistance R_f .

LC Filter

Another way to solve the impedance mismatch issue is to couple the nanomechanical resonator directly to an LC filter/resonator, as schematically depicted in Fig. 4.10 [13]. The equivalent impedance of this LC impedance matching circuit is given by

$$Z_{\text{LCIM}} = \left[\frac{1}{Z_m} + i\omega C_{\text{ft}} + i\omega C_{\text{LC}}\right]^{-1} + i\omega L_{\text{LC}} + R_{\text{LC}}$$
(4.33)

with the impedances of the LC inductor $Z_L = sL_{LC} + R_{LC}$. The resonance frequency of the LC resonator ($\omega_{LC} = 1/\sqrt{L_{LC}C_{LC}}$) is chosen to match the frequency of the

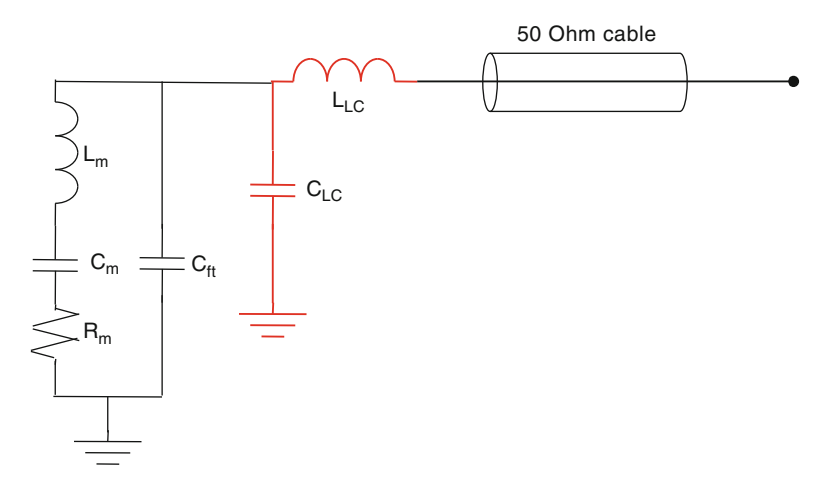


Fig. 4.10 Schematic of an LC impedance matching capacitive detection circuit, according to [13]

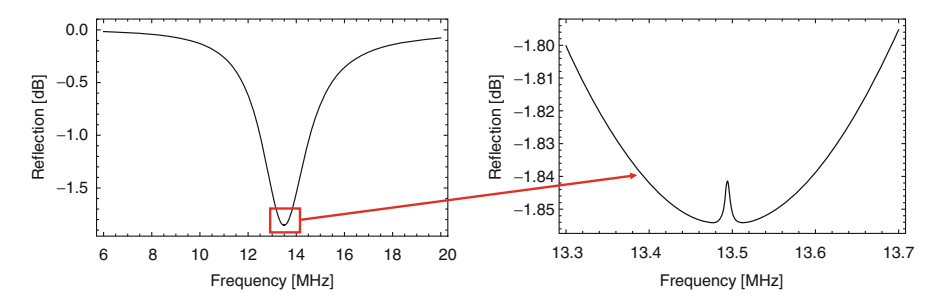


Fig. 4.11 Calculated reflection $(20 \log[(Z_{\rm LCIM}-50)/(Z_{\rm LCIM}+50)])$ of an LC impedance matched capacitive readout circuit (4.33). The measured resonance peak comes from a doubly clamped silicon nitride beam resonator from [13] with d=130 nm, L=14 μm, w=200 nm, h=205 nm, $C_{\rm ft}=76$ aF, $\partial C/\partial \xi=0.6$ aF/nm, Q=1800, measured with $U_{\rm DC}=10$ V, $C_{\rm LC}=4.2$ pF, $L_{\rm LC}=33$ μH, $R_{\rm LC}=470$ Ω

nanomechanical resonator ($\omega_{LC} = \omega_{res}$). At resonance, the total impedance seen from the measurement port is approximately given by $Z_T \approx L_{LC}/(C_{LC}R_m) + R_{LC}$ [13]. The trick is now to adjust the LC components in such a way to match the impedance of the measurement equipment, which typically is 50Ω . However, this can be hindered by the unavoidable losses R_{LC} in the inductor at room temperature. The effect of the LC filter can be seen in the reflectance plots in Fig. 4.11. Off-resonance, the LC filter reflects all energy. On-resonance however energy is absorbed and passed on to the nanomechanical resonator whose reflection peak is visible in the bottom center.

This is a narrow-band technique which requires an adjustment of the LC filter for a particular nanomechanical system. The advantage however lies in its simplicity, low temperature applicability, and possibility of multiplexing, that is to transduce arrays of mechanical resonators via a single channel [13]. The same technique

of on-resonance coupling of a nanomechanical resonator to an LC resonator has also been used inversely, that is to use a nanomechanical resonator for signal detection [15].

4.2.3 Other Capacitive Detection Schemes

Besides the here discussed capacitive detection via the induced current, there exist other capacitive detection schemes, such as coupling of a nanomechanical resonator to a single-electron transistor [25, 26] or a microwave cavity [16, 27]. In the former technique a nanomechanical resonator is vibrating in close proximity to the gate electrode of a transistor. The resonator is capacitively coupled to the transistor and its vibration is detected as a modulation of its conductance. In the latter technique, the displacement of the capacitively coupled nanomechanical resonator changes the resonance frequency of a superconductive microwave cavity. In this optomechanical configuration the mechanical resonance peak appears as a frequency modulation sideband of the cavity.

Carbon nanotube resonators are commonly transduced in semi-capacitive schemes. In these, the carbon nanotubes are spanned in close proximity over a conductive substrate which acts as a gate electrode. The vibration of the semiconductive tubes close to the gate modulates their conductivity. This transistor technique is a widespread technique for the transduction of semiconducting carbon nanotubes [28–33].

4.3 Thermoelastic (Actuation)

A nanomechanical resonator can be actuated by local pulsed heating. The local thermal expansion of the material induces strain fields which can translate into a mechanical motion. This effect is distinct in multi-material structures with variations in the thermal expansion coefficient. In particular in bi-layer beams the heating causes a deflection due to the different thermal expansion of the different layers. In a doubly clamped beam a pulsed heating causes a modulation of the tensile stress resulting in a parametric actuation. But even in a homogeneous material a heating pulse can induce stress gradients which causes a net actuation force. Typically, the thermoelastic effect is maximal when heating the nanomechanical resonator at the anchoring [34]. The local heating can be induced by either local photothermal heating with a pulsed laser or with a resistive heating element, as schematically depicted in Fig. 4.12.

Optical heating is often combined with an external optical readout and allows a fully optical transduction of nanomechanical systems [34]. However, it is important to distinguish this thermoelastic technique from the optic forces used in optomechanics. The thermoelastic technique has several drawbacks, such as the net

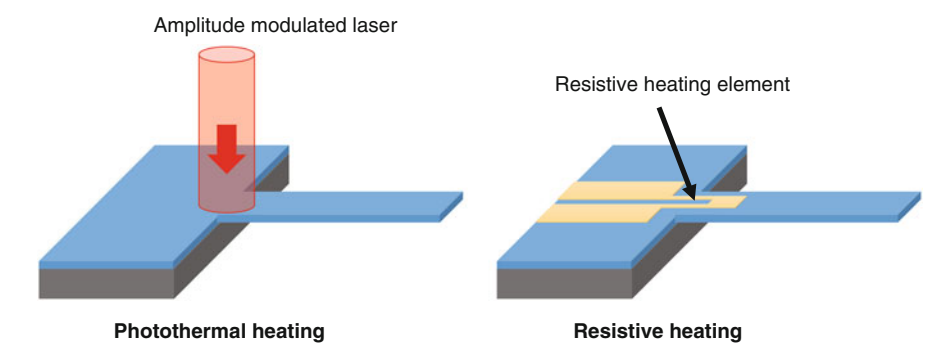


Fig. 4.12 Schematic drawing of thermoelastic actuation by local photothermal heating with an amplitude modulated laser (*left*) or with an integrated resistive element which can be heated by passing an electric current (*right*)

increase in temperature and the thermal relaxation time which limits the frequency bandwidth. The thermoelastic actuation with an integrated ohmic element is a technique that is particularly suitable to be combined with a piezoresistive detection (as discussed in Sect. 4.4) [35]. An example of such a combined transduction of a doubly clamped nanomechanical beam is shown in Fig. 4.13.

4.4 Piezoresistive (Detection)

Piezoresistive detection is based on the strain induced change in resistance of a conductive element, typically called a *strain gauge*. For small elastic strain the piezoresistive effect can be assumed to be linear. In this case the *gauge factor* (GF), is defined as the relative change of the resistance R per strain ε

$$GF = \frac{\Delta R}{R} \frac{1}{\varepsilon}.$$
 (4.34)

The resistance of a longitudinal strain gauge of length L and a rectangular cross section of area A is given by $R = \rho_R L/A$, with the resistivity ρ_R . The change in resistance is given by the sum of the change of each resistance factor

$$\Delta R = \Delta \rho_R \frac{\partial R}{\partial \rho_R} + \Delta L \frac{\partial R}{\partial L} + \Delta A \frac{\partial R}{\partial A}, \tag{4.35}$$

which results in the relative change of resistance

$$\frac{\Delta R}{R} = \frac{\Delta \rho_R}{\rho_R} + \frac{\Delta L}{L} - \frac{\Delta A}{A}.$$
 (4.36)

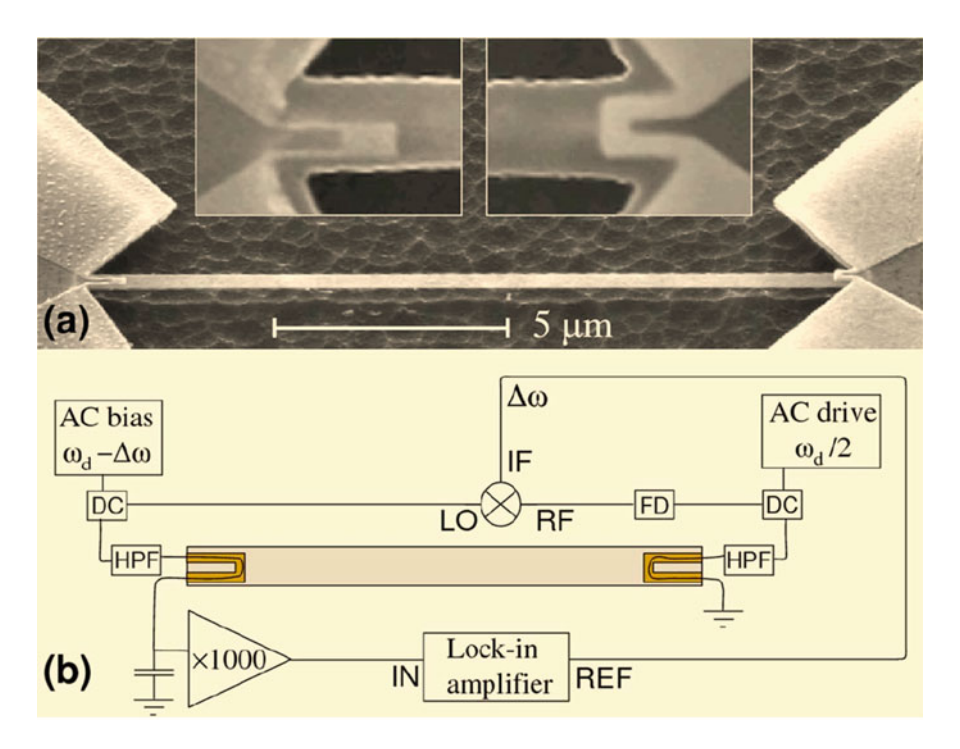


Fig. 4.13 (a) Scanning electron micrograph of one a single-crystal silicon carbon resonator comprising an 80-nm-thick gold thermoelastic bilayer actuator (*right inset*) and a 30-nm-thick piezoresistive loop of a gold palladium alloy (*left inset*). (b) Schematic of the transduction based on a signal downmixing [36]. DC denotes directional coupler, FD frequency doubler, and HPF high-pass filter (Reprinted from [35] with permission from AIP Publishing.)

Substituting the relative changes of geometry with $\Delta L/L = \varepsilon L$ and $\Delta A/A \approx -2\nu\varepsilon$ results in the longitudinal gauge factor according to (4.34) of [37, 38]

$$GF = \frac{\Delta \rho_R}{\rho_R} \frac{1}{\varepsilon} + (1 + 2\nu). \tag{4.37}$$

From the gauge factor in this form two effects contributing to the total piezoresistive behavior in a material can be summed up.

The first term in (4.37) is the *strain coefficient of resistivity*, which comes from the dilation of the material. The resulting change of the inter-atomic distance can alter a material's conductivity mechanism. The second term in (4.37) is a purely geometric effect coming from the elongation and thinning of the material under physical strain.

In bulk metals, typical values for the strain coefficient of resistivity $\frac{\Delta \rho_R}{\rho_R} \frac{1}{\varepsilon}$ range from 0.5 to 3 [39]. The geometric gauge effect typically results in values between 1.6 and 1.9. Combined, this results in typical gauge factors of bulk metals between

2 < GF < 5. There are some exceptions, such as nickel for which large negative gauge factor have been measured (GF = -12) [39]. However, the gauge factor of metals is a function of sheet resistivity which can be controlled by the thickness of a metal thin film [37, 40]. It has been observed that initially *GF* of metal thin films decreases from the initial bulk value when thinned. A minimum of *GF* occurs in most metals at a sheet resistance around $10^3\Omega$ where the gauge factor values are significantly below the bulk values. However, above this sheet resistance the gauge factor has shown to increase steeply for very thin films (<1 nm) with maximal values measured, e.g., for gold of GF = 97 [37].

In semiconductors the strain coefficient of resistivity is particularly distinct and the geometric gauge effect is secondary. Here strain alters the bandgap, which changes the energy barrier an electron has to overcome to raise to the conduction band. Semiconductors, such as silicon, have gauge factors roughly ranging from GF $\approx \pm 30$ for polysilicon [41] to GF $\approx \pm 110$ for single-crystal silicon [42] depending on the doping level, doping type, temperature, and crystal orientation [38]. As in metals, in semiconductors the piezoresistivity is a function of the thickness of the strain gauge. As an example, exceptionally large gauge factors of several thousand have been observed with single-crystal silicon nanowires [43]. Piezoresistive detection is applicable for static as well as dynamic measurements. Typically, a reference and a measuring resonator are connected with two external resistors to form a Wheatstone bridge configuration [44, 45]. In this way an output signal is only recorded when there is a difference in the deflection between the two resonators. Another readout technique is based on signal downmixing [35, 36], as shown in the example in Fig. 4.13.

Instead of striving for maximizing the gauge factor, it has been shown that low-resistance gold metal strain gauges can have significant advantages over high-resistance silicon strain gauges for the transduction of nanomechanical resonators (see Fig. 4.14) [35, 46]. Even though the gauge factor of gold is relatively low compared to silicon, the final frequency resolution is high because of the low electrical noise introduced by the low-resistance gold film. Furthermore, the integrated gold electrode allows a perfect impedance matching with standard electronic equipment with resistances of $50\,\Omega$. This allows the direct pick-up of the piezoresistive signal without the need for a complex signal detection scheme.

4.5 Piezoelectric (Actuation and Detection)

Piezoelectricity is a material property that was first discovered by the Curie brothers circa 1880 [47]. From a physical point of view is the property of a material to generate charges when it is deformed and viceversa, upon the application of an electric field, the material deforms. Mathematically, it can be seen as the coupling between the elastic and electric constitutional equations [48], that can be written down as

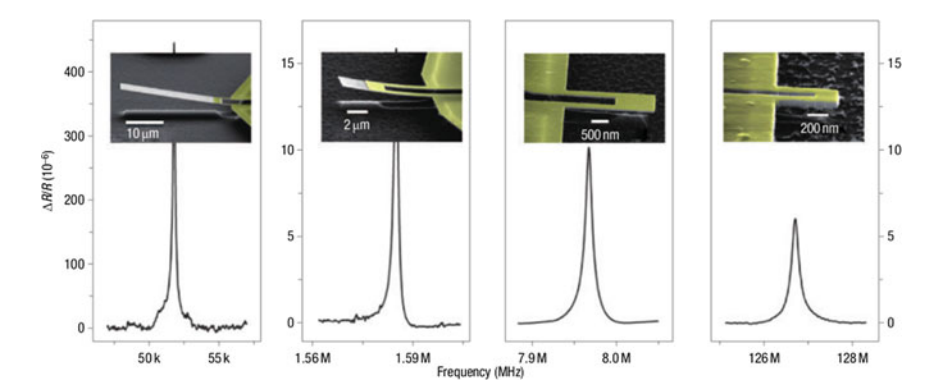


Fig. 4.14 Example of a piezoresistive detection of nanomechanical resonators with gold strain gauges. The SiC nanocantilevers were measured at room temperature in vacuum. The data plots show the fundamental-mode resonance frequencies. The *insets* show SEM micrographs of the specific devices [46]

$$\tilde{\varepsilon}_{ij} = \tilde{C}_{ijkl}\tilde{\sigma}_{kl} + \tilde{d}_{ijk}E_k \to \varepsilon_i = C_{ij}\sigma_j + d_{ij}E_j$$

$$D_i = \epsilon_{ij} E_j + d_{ij}^T\sigma_j,$$
(4.38)

where ε and σ are strain and stress vectors (1x6 vectors) and their counterparts are tensors (3x3 matrices), D and E are the displacement and electric field, C is the compliance matrix (6x6 matrix) and \tilde{C} is the fourth rank compliance tensor, \in is the dielectric permittivity and d is the piezoelectric matrix (3x6 matrix) with \tilde{d} the piezoelectric third rank tensor. In the absence of the latter, both equations in (4.38) remain uncoupled, which is the case for non-piezoelectric materials.

Back at the beginning of the twentieth century much work on the piezoelectric material properties was performed and it ended up with the invention of the piezoelectric oscillator [49], which ended up (and still is) being a fundamental part of the technological development of our society. It took many years till microfabrication processes were able to produce high quality thin layers of piezoelectric materials [50–53]. It is this that has hampered for decades the miniaturization of piezoelectric actuation. As it can be inferred from (4.38), transduction efficiency will be strongly dependent on the magnitude of the piezoelectric tensor, thus the requirement for good materials. Many materials have been used ZnO [54], PZT [51], GaN [55, 56], GaAs [57],... but the preferred material due to its compatibility with standard CMOS post-processing and its overall good material properties has been Aluminum Nitride. The State of the Art of fabrication for this material shows that it can be deposited via sputtering and that layers with a good crystal alignment in the *c-axis* have been obtained even down to 10 nm thick layers [58–60].

The governing equations for both actuation and detection are (4.38). As in any problem of structural mechanics, the actual solution of the kinematic equations, the solution for the deflection/deformation of a structure, will depend on the boundary

136 4 Transduction

conditions. In the case of this book, it will depend on whether the resonator/mode to be studied is flexural, torsional, bulk, 1D, 2D, etc. In each one of those cases the resulting equations will be different. The three more used types of piezoelectric resonators are: flexural beams and cantilevers [58–62], dilational (thickness) bulk acoustic wave mode [52, 55, 63] (Fig. 4.16), and lateral contour mode [64–66].

4.5.1 Piezoelectric Actuation

In this case one should look into the first equation in (4.38). This tells us that we need metal electrodes on top or both sides of the piezoelectric layer in order to create an electric field when applying a voltage. This electric field will modify the generalized Hooke's law [68] and forcing the structure out of the original equilibrium. For bulk mode resonators, the effect is quite direct and one only needs to look into d_{31} and d_{33} coefficients which will directly give the deformation in the case of lateral or thickness modes respectively (assuming that the third axis is defined out of plane and that a symmetry exists where no preferential orientation can be found within the plane). In the case of flexural modes it is a little bit more complicated: the piezoelectric layer that is deformed via the application of voltage must not be centered around the neutral axis of the mechanical structure. Once this condition holds true, the expansion translates into a finite bending moment that, in turn, causes deflection. Equation (4.39) shows the formula for the bending moment of a cantilever (clamped-free) beam of length L and width w (see Fig. 4.15)

$$M(t) = \frac{d_{31}wz_{\text{offset}}}{C_{11}}V(t), \tag{4.39}$$

where z_{offset} is the distance between the center of the piezoelectric layer to the neutral axis of the structure, i.e. if $z_{\text{offset}} = 0$, there is no bending moment and thus no

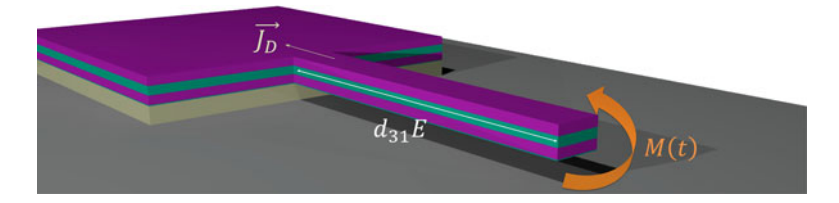


Fig. 4.15 Cartoon of a multi-layer cantilever beam composed by metal and piezoelectric materials. When a voltage is applied between *top* and *bottom* electrodes an electric field E is generated within the piezoelectric layer that is turned into expansion $d_{31}E$. When said layer is not centered around the neutral axis of the structure a bending moment M(t) is created that causes the deflection of the cantilever. This motion creates an alternating strain and stress field that will give rise to a displacement field D. Following Maxwell's equations, an alternating displacement field also creates a displacement current $\overline{J_D}$ which will be collected

deflection. Assuming now that the stiffness of the metal and piezoelectric material are very similar (this is indeed the case when using Mo and AlN), it is possible to write the deflection

$$u_n(\omega) \approx \chi_n^A \frac{d_{31} z_{\text{offset}} L^2}{t_{\text{total}}^3} \frac{V}{1 - \left(\frac{\omega}{\omega_n}\right)^2 + j \frac{\omega}{\omega_n Q}},$$
(4.40)

where the proportionality parameter χ_n^A needs to be calculated for each structure and mode, following

$$\chi_n^A = L \int_0^L \frac{M(x)}{M_{Max}} \phi_n''(x) dx = L \left(\phi_n'(L_{act}) - \phi_n'(0) \right), \tag{4.41}$$

where $L_{\rm act}$ is the length of the actuation electrode. In the case of the first mode of a cantilever with full electrode coverage the coefficient is $\chi^A_{1,\rm cant} \approx 5.34$.

4.5.2 Piezoelectric Detection

In this case one should look into the second equation in (4.38), which tells us that a displacement field will be generated even in the absence of electric field or, rather, that an excess of displacement field will be generated.

As it is very well known from Maxwell's equations, if a displacement field changes over time, that induces a displacement current which for the case represented in Fig. 4.15

$$I_D(t) = \int_{A_{\text{elec}}} \frac{\partial D(t)}{\partial t} dA = j\omega \in \frac{A_{\text{elec}}}{t_{PZE}} V_{\text{in}} + j\omega \chi_n^D \frac{d_{31}}{C_{11}} \frac{w z_{\text{offset}}}{L} u_n(\omega), \tag{4.42}$$

where the term χ_n^D is a proportionality term that is defined as

$$\chi_n^D = L \int_0^{L_{\text{det}}} \phi_n''(x) dx = L \left(\phi_n'(L_{\text{det}}) - \phi_n'(0) \right),$$
 (4.43)

where L_{det} is the length of the actuation electrode. Note that in the case the actuation and detection electrode are the same, then $\chi_n^D = \chi_n^A$.

Combining (4.42) and (4.40) it is possible to reconstruct the full response of the electromechanical system, as done for the electrostatic detection in Sect. 4.2.2 on page 126

138 4 Transduction

$$I_D(t) = \left(j\omega C_0 + j\omega \chi_n^2 \frac{d_{31}^2}{C_{11}} \frac{w L_{\text{coffset}}^2}{t_{\text{total}}^3} \frac{1}{1 - \left(\frac{\omega}{\omega_n}\right)^2 + j\frac{\omega}{\omega_n Q}}\right) V_{\text{in}}, \tag{4.44}$$

where C_0 is the capacitance associated with the electrode. Equation (4.44) shows the different components of the equivalent circuit, as the two terms inside the parenthesis correspond to the feedthrough capacitance and the *LCR* motional term in parallel. In this case it is straightforward to calculate

$$C_{m} = \chi_{n}^{2} \frac{d_{31}^{2}}{C_{11}} \frac{wL_{\text{offset}}^{2}}{t_{\text{total}}^{3}};$$

$$L_{m} = \frac{1}{\omega_{n}^{2} C_{m}};$$

$$R_{m} = \sqrt{\frac{L_{m}}{C_{m}}} \frac{1}{Q}.$$

$$(4.45)$$

4.6 Optic (Actuation and Detection)

Optical transduction methods can either be fully external (off-chip) or integrated (on-chip). External techniques such as interferometry, laser-Doppler vibrometry, optical leverage readout and radiation pressure actuation have the advantage that no physical connection to the NEMS is required with the exception of the access for the laser beam. This facilitates quick and simple testing of NEMS prototypes. In optical waveguide end-coupling, evanescent light coupling and Mach–Zehnder interferometry the optical transduction is fully integrated on-chip. Beside the coupling of an external fiber to the chip, integrated techniques need no alignment of laser beam and nano resonator and compared to the external techniques are not limited by the diffraction of light.

4.6.1 Optical Forces

Photons bare a momentum $p = h/\lambda$, with Planck constant h and wavelength λ , which can be used to actuate nanomechanical resonators. When a photon is reflected in normal direction off a flat mirror it transfers the momentum $\Delta p = 2h/\lambda$ to the mirror called *radiation pressure*. For a photon in the visible range this results in a momentum of the order of $\Delta p \approx 10^{-27} \, \text{kg m/s}$. The resulting force would be even too small to actuate a nanomechanical resonator. However the total momentum can be increased to useful magnitudes by increasing the number of phonons that are

reflected. This can readily be achieved with a high-Q optical resonator, such as a high-finesse optical cavity (the finesse describes the number of reflections a photon undergoes before it escapes the cavity). This interaction of phonons inside an optical cavity with a nanomechanical resonator is the subject of cavity optomechanics [6, 7]. One of the most important features of cavity optomechanics is the possibility to use radiation pressure to counteract the Brownian motion of a nanomechanical resonator by specifically detuning the wavelength of the phonons with respect to the high-finesse cavity. This technique allows the cooling of a nanomechanical resonator to the ground state at which it can exhibit quantum mechanical behavior [69]. Hence, cavity optomechanics is a unique tool to study quantum mechanical theory on macroscopic test objects. The techniques applied in cavity optomechanics have also successfully been applied to electrostatic systems (see Sect. 4.2.1) in the so-called microwave cavity optomechanics [16]. An optical force not only acts if a light beam is reflected off of a reflective nanomechanical structure [70] but also if a nanomechanical waveguide structure is placed in the vicinity of a nonuniform light field (dispersive coupling) [71–73].¹

Light absorbed by the nanomechanical resonator causes a local photothermal heating. Such a heating can induce a thermoelastic response which can be used for actuation. This thermoelastic technique is discussed in Sect. 4.3 on page 131.

4.6.2 Interferometric Detection

Interferometric detection of nanomechanical motion is among the most precise detection techniques available. The principle lies in the superposition of two optical waves of the same frequency. A phase difference in one wave, induced by the interaction with a nanomechanical resonator, causes an interference pattern in the combined wave. There are several interferometric detection schemes, such as the Fabry–Pérot cavity, or Mach–Zehnder interferometer Michelson interferometer, which are commonly used to detect the motion of nanomechanical resonators in a myriad of different configurations.

A *Fabry–Pérot cavity* is the most basic interferometer consisting of one semi-transparent and one reflective plate (see schematic in Fig. 4.16a). In its most simple form it can be formed between a suspended nanomechanical resonator and the underlying reflective substrate. The movement of the suspended structure is detected by shining a coherent light on it and detecting the change in intensity of the reflected light [74]. This method works well for micro-sized structures. Even though

¹There is an interesting analogy to electrostatic to be made. The optical radiation pressure observed in optical cavity transduction schemes has an electrostatic analog in the force between two electrodes or capacitor plates (see Sect. 4.2.1.1 on page 121). And the dispersive optical force experienced by a nanomechanical waveguide in a nonuniform optical field has an analog in the force acting on a dielectric nanomechanical structure that is placed in a nonuniform electric field (see Sect. 4.2.1.2 on page 123).

140 4 Transduction

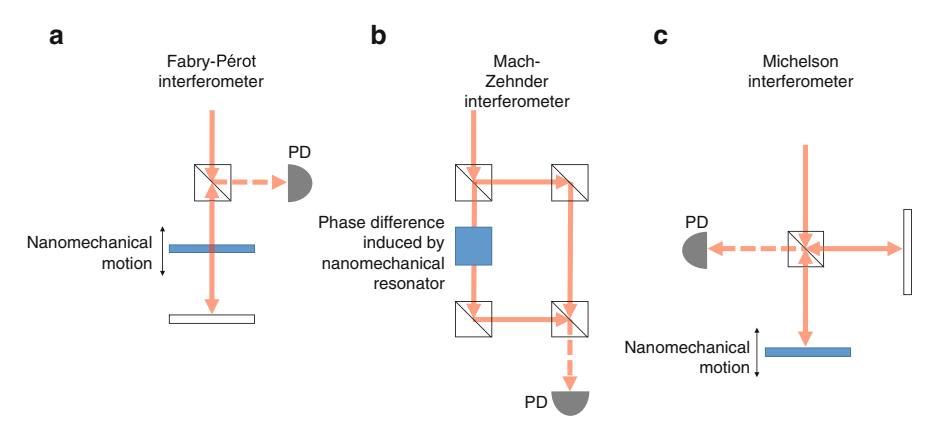


Fig. 4.16 Schematic drawings of the different types of interferometers commonly used for the detection of nanomechanical motion. (a) Fabry–Pérot interferometer, (b) Mach–Zehnder interferometer, (c) Michelson interferometer

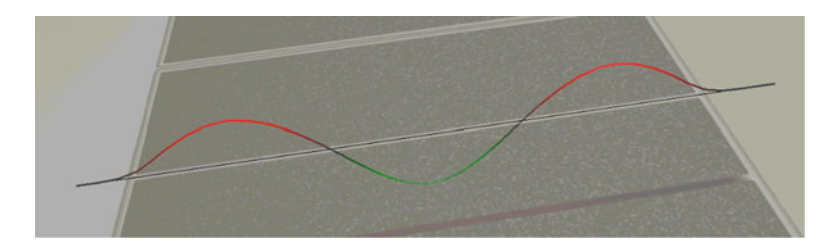


Fig. 4.17 Scan of the 3rd bending mode of a $200\,\mu m$ and $103\,nm$ thick silicon nitride micro string measured with MSA-500 from Polytec GbmH

it is limited by the diffraction of light it has been successfully used to detect the vibration of nanowires [75]. More advanced Fabry–Pérot cavities with high finesses are typically used in optomechanics [70, 73, 76].

In a *Mach–Zehnder interferometer* (see schematic in Fig. 4.16b) the light from a single source is split into two paths which are recombined afterwards. In one of the two path branches a phase difference is induced by a nanomechanical resonator, which after recombination results in an interference [71, 72, 77].

In a *Michelson interferometer* (see schematic in Fig. 4.16c) the light from a single source is split and recombined after the probe light beam reflected off a nanomechanical resonator and the reference beam reflected off a mirror. Microscope based interferometers based on a Michelson interferometer are commercially available with frequency bandwidths up to 1.2 GHz with scanning capability.² Figure 4.17 shows a scan of a transparent silicon nitride micro string measured with an MSA-400 system from Polytec.

²UHF-120 Ultra High Frequency Vibrometer from Polytec GmbH Waldbronn Germany.

4.6.3 Beam Deflection Detection

The vibrational motion of nanomechanical resonators can be detected by the deflection of a probing light beam by the resonator. Two common techniques are schematically depicted in Fig. 4.18 and briefly explained in the following paragraphs.

4.6.3.1 Optical Leverage

Optical leverage is a commonly used detection technique known from atomic force microscopy and is often used for static and dynamic detection of micro cantilevers. A schematic of the technique is depicted in Fig. 4.18a. A laser is focused on the back of a cantilever. The reflected light is then detected by a position sensitive photo-detector. However this method is rarely used for nanomechanical resonator. The method requires a resonator end-point deflection and thus works best with cantilevers whereas in NEMS doubly clamped beams are prevalent. Another drawback is the difficult alignment of the laser such that it hits the photo-detector after having been reflected on the nanomechanical resonator. Furthermore, the resonator typically requires a reflective coating in order to reflect enough light into the position sensing photodetector.

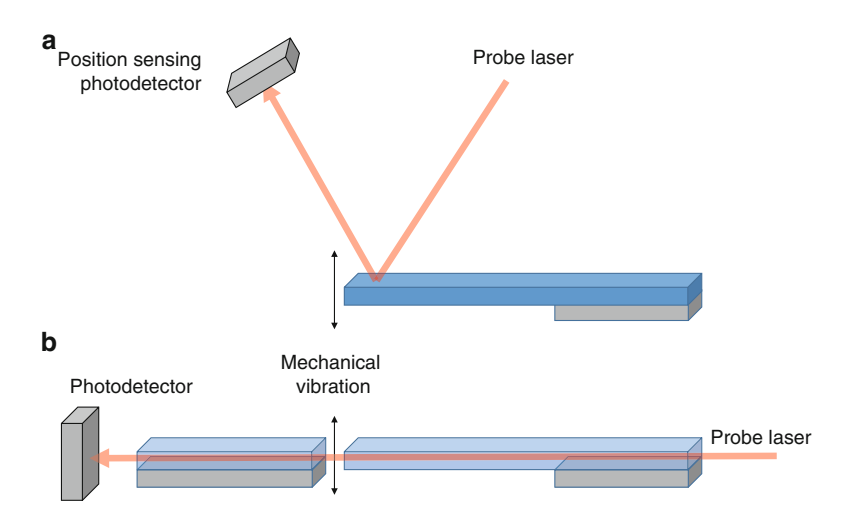


Fig. 4.18 Schematic drawings of the (a) optical leverage detection and the (b) end-coupled optical waveguide detection

142 4 Transduction

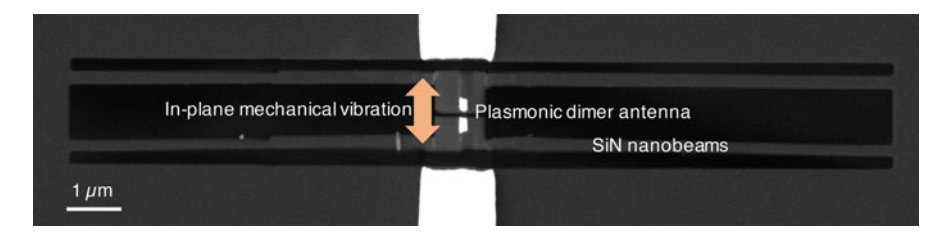


Fig. 4.19 An example of a pair of silicon nitride (SiN) nanomechanical resonator with integrated nanoplasmonic dimer antenna for plasmomechanical readout

4.6.3.2 End-Coupled Optical Waveguide

In this detection method, the nanomechanical resonator acts as a waveguide that couples at its end to another waveguide (see Fig. 4.18b). When the waveguide-cantilever is vibrating, it changes the coupling efficiency (transmission) which results in an optical amplitude modulation [78, 79]. This method enables the multiplexing of an array of resonators with a single probing laser. In order to obtain a maximal response, it is favorable if the coupled waveguides are a bit misaligned to each other. This detection method does not require a coherent light source as interferometric methods do. It is also not limited by the diffraction of light, which is a problem of the optical leverage technique.

4.6.4 Plasmonic Detection

Plasmonic resonances correspond to the resonant oscillation of the polarized electron cloud of metallic nanostructures. These resonance frequencies are typically located at the frequency of light in the visible to near infrared regime. In between two such plasmonic nanostructures that are in close proximity, a strong and very localized electromagnetic field enhancement can be observed, which is often referred to as a "hotspot." These hotspots are famously used in surface enhanced Raman spectroscopy (SERS) to "focus" the probing light below the diffraction limit. It is possible to couple plasmonic resonances to the mechanical motion of nanomechanical motion (Fig. 4.19). The plasmonic resonance can either be a surface plasmon resonance, supported by the surface of a gold coated resonator [80, 81], or a localized surface plasmon resonance, supported by metallic nanoparticles [82]. The plasmonic readout scheme is schematically explained in Fig. 4.20 for the case of a plasmonic dimer antenna (two metallic nanoparticles). An increase of the particle distance causes a blue shift of the plasmonic resonance peak. This shift modulates a probing laser with a wavelength located at the slope of the plasmonic resonance peak.

References 143

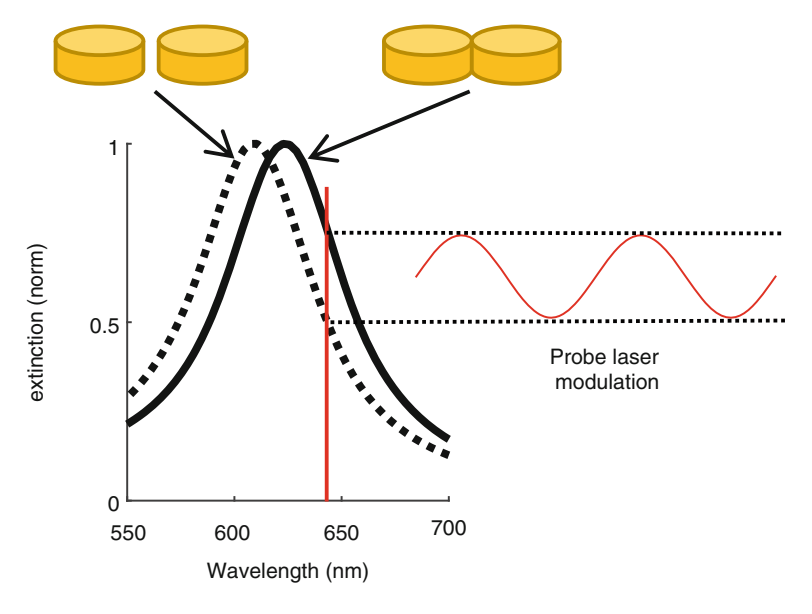


Fig. 4.20 Schematic of the readout with a plasmonic dimer antenna. An increasing gap distance causes a *blue* shift of the optic extinction peak, which can be detected with a probing laser

References

- D.V. Scheible, A. Erbe, R.H. Blick, Dynamic control and modal analysis of coupled nanomechanical resonators. Appl. Phys. Lett. 82, 3333 (2003)
- S. Dohn, O. Hansen, A. Boisen, Measurement of the resonant frequency of nano-scale cantilevers by hard contact readout. Microelectron. Eng. 85(5–6), 1390–1394 (2008)
- 3. K. Jensen, J. Weldon, H. Garcia, A. Zettl, Nanotube radio. Nano Lett. 7(11), 3508–3511 (2007)
- O. Cakmak, E. Ermek, N. Kilinc, S. Bulut, I. Baris, I.H. Kavakli, G.G. Yaralioglu, H. Urey, A cartridge based sensor array platform for multiple coagulation measurements from plasma. Lab Chip 15(1), 113–120 (2015)
- M. Suter, O. Ergeneman, J. Zürcher, S. Schmid, A. Camenzind, B.J. Nelson, C. Hierold, Superparamagnetic photocurable nanocomposite for the fabrication of microcantilevers. J. Micromech. Microeng. 21(2), 025023 (2011)
- T.J. Kippenberg, K.J. Vahala, Cavity optomechanics: back-action at the mesoscale. Science 321(5893), 1172–1176 (2008)
- M. Aspelmeyer, T.J. Kippenberg, F. Marquard, Cavity optomechanics. Rev. Mod. Phys. 86(4), 1391–1452 (2014)
- 8. A.N. Cleland, M.L. Roukes, Fabrication of high frequency nanometer scale mechanical resonators from bulk Si crystals. Appl. Phys. Lett. **69**, 2653 (1996)
- W.J. Venstra, H.J.R. Westra, K.B. Gavan, H.S.J. der Zant, Magnetomotive drive and detection of clamped-clamped mechanical resonators in water. Appl. Phys. Lett. 95(26), 263103 (2009)
- X.L. Feng, C.J. White, A. Hajimiri, M.L. Roukes, A self-sustaining ultrahigh-frequency nanoelectromechanical oscillator. Nat. Nanotechnol. 3(6), 342–346 (2008)
- H.X. Tang, X.M.H. Huang, M.L. Roukes, M. Bichler, W. Wegscheider, Two-dimensional electron-gas actuation and transduction for GaAs nanoelectromechanical systems. Appl. Phys. Lett. 81(20), 3879–3881 (2002)

144 4 Transduction

S. Schmid, T. Bagci, E. Zeuthen, J.M. Taylor, P.K. Herring, M.C. Cassidy, C.M. Marcus, L.G. Villanueva, B. Amato, A. Boisen, Y.C. Shin, J. Kong, A.S. Sørensen, K. Usami, E.S. Polzik, Single-layer graphene on silicon nitride micromembrane resonators. J. Appl. Phys. 115(5), 054513 (2014)

- P.A. Truitt, J.B. Hertzberg, C.C. Huang, K.L. Ekinci, K.C. Schwab, Efficient and sensitive capacitive readout of nanomechanical resonator arrays. Nano Lett. 7(1), 120–126 (2007)
- P. Weber, J. Güttinger, I. Tsioutsios, D.E. Chang, A. Bachtold, Coupling graphene mechanical resonators to superconducting microwave cavities. Nano Lett. 14(5), 2854–2860 (2014)
- T. Bagci, A. Simonsen, S. Schmid, L.G. Villanueva, E. Zeuthen, J. Appel, J.M. Taylor, A. Sørensen, K. Usami, A. Schliesser, E.S. Polzik, Optical detection of radio waves through a nanomechanical transducer. Nature 507(7490), 81–85 (2014)
- J.D. Teufel, D. Li, M.S. Allman, K. Cicak, A.J. Sirois, J.D. Whittaker, R.W. Simmonds, Circuit cavity electromechanics in the strong-coupling regime. Nature 471(7337), 204–208 (2011)
- C.P. Yuan, T.N. Trick, A simple formula for the estimation of the capacitance of twodimensional interconnects in VLSI circuits. IEEE Electron Device Lett. 3(12), 391–393 (1982)
- H.A. Haus, J.R. Melcher, *Electromagnetic Fields and Energy* (Prentice Hall, Englewood Cliffs, NJ, 1989)
- T. McRae, K. Lee, G. Harris, J. Knittel, W. Bowen, Cavity optoelectromechanical system combining strong electrical actuation with ultrasensitive transduction. Phys. Rev. A 82(2), 1–7 (2010)
- S. Schmid, M. Wendlandt, D. Junker, C. Hierold, Nonconductive polymer microresonators actuated by the Kelvin polarization force. Appl. Phys. Lett. 89(16), 163506 (2006)
- Q.P. Unterreithmeier, E.M. Weig, J.P. Kotthaus, Universal transduction scheme for nanomechanical systems based on dielectric forces. Nature 458(7241), 1001–1004 (2009)
- 22. T.B. Jones, Electromechanics of Particles (Cambridge University Press, Cambridge, 1995)
- C.T.-C. Nguyen, R.T. Howe, An integrated CMOS micromechanical resonator high-Q oscillator. IEEE J. Solid State Circuits 34(4), 440–455 (1999)
- S. Schmid, Electrostatically actuated all-polymer microbeam resonators. In: Characterization and Application. Scientific Reports on Micro and Nanosystems, vol. 6 (Der Andere, Uelvesbüll, 2009)
- R.G. Knobel, A.N. Cleland, Nanometre-scale displacement sensing using a single electron transistor. Nature 424(6946), 291–293 (2003)
- M.D. LaHaye, O. Buu, B. Camarota, K.C. Schwab, Approaching the quantum limit of a nanomechanical resonator. Science 304(5667), 74 (2004)
- C.A. Regal, J.D. Teufel, K.W. Lehnert, Measuring nanomechanical motion with a microwave cavity interferometer. Nat. Phys. 4(7), 555–560 (2008)
- 28. B. Witkamp, M. Poot, H.S.J. Van Der Zant, Bending-mode vibration of a suspended nanotube resonator. Nano Lett. 6(12), 2904–2908 (2006)
- 29. V. Sazonova, Y. Yaish, H. Üstünel, D. Roundy, T.A. Arias, P.L. McEuen, A tunable carbon nanotube electromechanical oscillator. Nature **431**(7006), 284–287 (2004)
- B. Lassagne, D. Garcia-Sanchez, A. Aguasca, A. Bachtold, Ultrasensitive mass sensing with a nanotube electromechanical resonator. Nano Lett. 8(11), 3735–3738 (2008)
- 31. V. Gouttenoire, T. Barois, S. Perisanu, J.L. Leclercq, S.T. Purcell, P. Vincent, A. Ayari, Digital and FM demodulation of a doubly clamped single-walled carbon-nanotube oscillator: towards a nanotube cell phone. Small **6**(9), 1060–1065 (2010)
- 32. J. Chaste, A. Eichler, J. Moser, G. Ceballos, R. Rurali, A. Bachtold, A nanomechanical mass sensor with yoctogram resolution. Nat. Nanotechnol. 7(5), 301–304 (2012)
- J. Moser, J. Güttinger, A. Eichler, M.J. Esplandiu, D.E. Liu, M.I. Dykman, A. Bachtold, Ultrasensitive force detection with a nanotube mechanical resonator. Nat. Nanotechnol. 8(7), 493–496 (2013)
- B. Ilic, S. Krylov, K. Aubin, R. Reichenbach, H.G. Craighead, Optical excitation of nanoelectromechanical oscillators. Appl. Phys. Lett. 86, 193114 (2005)

References 145

 I. Bargatin, I. Kozinsky, M.L. Roukes, Efficient electrothermal actuation of multiple modes of high-frequency nanoelectromechanical resonators. Appl. Phys. Lett. 90(9), 093116 (2007)

- I. Bargatin, E.B. Myers, J. Arlett, B. Gudlewski, M.L. Roukes, Sensitive detection of nanomechanical motion using piezoresistive signal downmixing. Appl. Phys. Lett. 86(13), 1–3 (2005)
- R.L. Parker, A. Krinsky, Electrical resistance-strain characteristics of thin evaporated metal films. J. Appl. Phys. 34(9), 2700–2708 (1963)
- 38. Y. Kanda, A graphical representation of the piezoresistance coefficients in silicon. IEEE Trans. Electron Devices **29**(1), 64–70 (1982)
- G.C. Kuczynski, Effect of elastic strain on the electrical resistance of metals. Phys. Rev. 94(1), 61–64 (1954)
- 40. S.U. Jen, C.C. Yu, C.H. Liu, G.Y. Lee, Piezoresistance and electrical resistivity of Pd, Au, and Cu films. Thin Solid Films **434**(1–2), 316–322 (2003)
- 41. P.J. French, A.G.R. Evans, Piezoresistance in polysilicon and its applications to strain gauges. Solid State Electron. **32**(1), 1–10 (1989)
- 42. C.S. Smith, Piezoresistance effect in germanium and silicon. Phys. Rev. **94**(1), 42–49 (1954)
- 43. R. He, P. Yang, Giant piezoresistance effect in silicon nanowires. Nat. Nanotechnol. 1(1), 42–46 (2006)
- 44. X. Yu, J. Thaysen, O. Hansen, A. Boisen, Optimization of sensitivity and noise in piezoresistive cantilevers. J. Appl. Phys. **92**(10), 6296–6301 (2002)
- 45. A. Boisen, J. Thaysen, H. Jensenius, O. Hansen, Environmental sensors based on micromachined cantilevers with integrated read-out. Ultramicroscopy **82**(1–4), 11–16 (2000)
- M. Li, H.X. Tang, M.L. Roukes, Ultra-sensitive NEMS-based cantilevers for sensing, scanned probe and very high-frequency applications. Nat. Nanotechnol. 2(2), 114–120 (2007)
- 47. J. Curie, P. Curie, Development by pressure of polar electricity in hemihedral crystals with inclined faces. Bull. Soc. Min. de France 3, 90 (1880)
- 48. W.G. Cady, Piezoelectricity; An Introduction to the Theory and Applications of Electromechanical Phenomena in Crystals, New revised edition (Dover, New York, 1964)
- 49. W.G. Cady, The piezo-electric resonator. Proc. Inst. Radio Eng. 10(2), 83–114 (1922)
- G.A. Racine, P. Muralt, M.A. Dubois, Flexural-standing-wave elastic force motor using ZnO and PZT thin film on micromachined silicon membranes for wristwatch applications. Smart Mater. Struct. 7(3), 404–416 (1998)
- 51. M.A. Dubois, P. Muralt, Pzt thin film actuated elastic fin micromotor. IEEE Trans. Ultrason. Ferroelectr. Freq. Control **45**(5), 1169–1177 (1998)
- 52. M.A. Dubois, P. Muralt, L. Sagalowicz, Aluminum nitride thin films for high frequency applications. Ferroelectrics **224**(1–4), 671–678 (1999)
- 53. F. Martin, P. Muralt, M.A. Dubois, A. Pezous, Thickness dependence of the properties of highly c-axis textured ALN thin films. J. Vac. Sci. Technol. A 22(2), 361–365 (2004)
- 54. T. Itoh, T. Suga, Development of a force sensor for atomic force microscopy using piezoelectric thin films. Nanotechnology **4**, 218 (1993)
- 55. A. Ansari, M. Rais-Zadeh, A thickness-mode algan/gan resonant body high electron mobility transistor. IEEE Trans. Electron Devices **61**(4), 1006–1013 (2014)
- A. Ansari, C.Y. Liu, C.C. Lin, H.C. Kuo, P.C. Ku, M. Rais-Zadeh, Gan micromechanical resonators with meshed metal bottom electrode. Materials 8(3), 1204–1212 (2015)
- S.C. Masmanidis, R.B. Karabalin, I. De Vlaminck, G. Borghs, M.R. Freeman, M.L. Roukes, Multifunctional nanomechanical systems via tunably coupled piezoelectric actuation. Science 317(5839), 780–783 (2007)
- R.B. Karabalin, M.H. Matheny, X.L. Feng, E. Defay, G. Le Rhun, C. Marcoux, S. Hentz, P. Andreucci, M.L. Roukes, Piezoelectric nanoelectromechanical resonators based on aluminum nitride thin films. Appl. Phys. Lett. 95(10), 103111 (2009)
- N. Sinha, G.E. Wabiszewski, R. Mahameed, V.V. Felmetsger, S.M. Tanner, R.W. Carpick, G. Piazza, Piezoelectric aluminum nitride nanoelectromechanical actuators. Appl. Phys. Lett. 95(5), 053106 (2009)

146 4 Transduction

 U. Zaghloul, G. Piazza, Synthesis and characterization of 10nm thick piezoelectric ALN films with high c-axis orientation for miniaturized nanoelectromechanical devices. Appl. Phys. Lett. 104(25), 253101 (2014)

- 61. P. Ivaldi, J. Abergel, M.H. Matheny, L.G. Villanueva, R.B. Karabalin, M.L. Roukes, P. Andreucci, S. Hentz, E. Defay, 50 nm thick ALN film-based piezoelectric cantilevers for gravimetric detection. J. Micromech. Microeng. 21(8), 085023 (2011)
- R.B. Karabalin, L.G. Villanueva, M.H. Matheny, J.E. Sader, M.L. Roukes, Stress-induced variations in the stiffness of micro- and nanocantilever beams. Phys. Rev. Lett. 108(23), 236101 (2012)
- A.D. O'Connell, M. Hofheinz, M. Ansmann, R.C. Bialczak, M. Lenander, E. Lucero, M. Neeley, D. Sank, H. Wang, M. Weides, J. Wenner, J.M. Martinis, A.N. Cleland, Quantum ground state and single-phonon control of a mechanical resonator. Nature 464(7289), 697–703 (2010)
- 64. G. Piazza, P.J. Stephanou, A.P. Pisano, Piezoelectric aluminum nitride vibrating contour-mode MEMS resonators. J. Microelectromech. Syst. **15**(6), 1406–1418 (2006)
- G. Piazza, P.J. Stephanou, A.P. Pisano, Single-chip multiple-frequency ALN MEMS filters based on contour-mode piezoelectric resonators. J. Microelectromech. Syst. 16(2), 319–328 (2007)
- 66. G. Piazza, P.J. Stephanou, A.P. Pisano, One and two port piezoelectric higher order contour-mode MEMS resonators for mechanical signal processing. Solid State Electron. 51(11–12), 1596–1608 (2007)
- 67. A. Cho, The first quantum machine. Science **330**(6011), 1604 (2010)
- J.M. Gere, B.J. Goodno, Mechanics of Materials, 8th edn. (Cengage Learning, Stamford, CT, 2013)
- J. Chan, T.P.M. Alegre, A.H. Safavi-Naeini, J.T. Hill, A. Krause, S. Gröblacher, M. Aspelmeyer, O. Painter, Laser cooling of a nanomechanical oscillator into its quantum ground state. Nature 478(7367), 89–92 (2011)
- S. Gröblacher, K. Hammerer, M.R. Vanner, M. Aspelmeyer, Observation of strong coupling between a micromechanical resonator and an optical cavity field. Nature 460(7256), 724–727 (2009)
- 71. M. Li, W.H.P. Pernice, C. Xiong, T. Baehr-Jones, M. Hochberg, H.X. Tang, Harnessing optical forces in integrated photonic circuits. Nature **456**(7221), 480–484 (2008)
- G. Anetsberger, O. Arcizet, E. Gavartin, Q.P. Unterreithmeier, E.M. Weig, J.P. Kotthaus, T.J. Kippenberg, Near-field cavity optomechanics with nanomechanical oscillators. In: 2010 Conference on Lasers and Electro-Optics (CLEO) and Quantum Electronics and Laser Science Conference (QELS), vol. 5(12), pp. 1–9 (2010)
- 73. J.D. Thompson, B.M. Zwickl, A.M. Jayich, F. Marquardt, S.M. Girvin, J.G.E. Harris, Strong dispersive coupling of a high-finesse cavity to a micromechanical membrane. Nature **452**(7183), 72–75 (2008)
- D.W. Carr, L. Sekaric, H.G. Craighead, Measurement of nanomechanical resonant structures in single-crystal silicon. J. Vac. Sci. Technol. B: Microelectron. Nanometer Struct. 16(6), 3821–3824 (1998)
- M. Belov, N.J. Quitoriano, S. Sharma, W.K. Hiebert, T.I. Kamins, S. Evoy, Mechanical resonance of clamped silicon nanowires measured by optical interferometry. J. Appl. Phys. 103, 74304 (2008)
- R.W. Andrews, R.W. Peterson, T.P. Purdy, K. Cicak, R.W. Simmonds, C.A. Regal, K.W. Lehnert, Bidirectional and efficient conversion between microwave and optical light. Nat. Phys. 10, 321–326 (2014)
- 77. E. Verhagen, S. Deléglise, S. Weis, A. Schliesser, T.J. Kippenberg, Quantum-coherent coupling of a mechanical oscillator to an optical cavity mode. Nature **482**(7383), 63–67 (2012)
- 78. M. Li, W.H.P. Pernice, H.X. Tang, Broadband all-photonic transduction of nanocantilevers. Nat. Nanotechnol. **4**(6), 377–382 (2009)
- M. Nordström, D.A. Zauner, M. Calleja, J. Hübner, A. Boisen, Integrated optical readout for miniaturization of cantilever-based sensor system. Appl. Phys. Lett. 91, 103512 (2007)

References 147

 R. Thijssen, E. Verhagen, T.J. Kippenberg, A. Polman, Plasmon nanomechanical coupling for nanoscale transduction. Nano Lett. 13, 3293–3297 (2013)

- 81. J.-Y. Ou, E. Plum, J. Zhang, N.I. Zheludev, An electromechanically reconfigurable plasmonic metamaterial operating in the near-infrared. Nat. Nanotechnol. 8(4), 252–255 (2013)
- 82. R. Thijssen, T.J. Kippenberg, A. Polman, E. Verhagen, Plasmomechanical resonators based on dimer nanoantennas. Nano Lett. **15**(6), 3971–3976 (2015)

Chapter 5 Measurement and Noise

Abstract Max Planck used to say that the only things that exist are those that can be measured. In this chapter a general vision of the issues faced while performing measurements of nanomechanical resonators is presented. Different noise sources are analyzed: thermomechanical noise, electrical noise (Johnson, 1/f, shot noise), and amplifier noise; to later define the Allan variance and how it relates to frequency noise. This chapter will provide the reader with the necessary information and tools to understand the basics of measurements and to maybe motivate further reading beyond these pages.

The potential impact of nanomechanical resonators in the field of sensing has been delineated in the previous chapter. However, the outstanding responsivity that is associated with their small sizes is not enough to make a good sensor. Indeed, it is typically the sensitivity that contains information about the sensor performance, as it determines the minimum detectable amount of the target magnitude. As a consequence, it is of the utmost importance to analyze the different noise sources that enter these systems so that a full picture can be formed upon their usability in actual applications. In this chapter, different noise sources are analyzed, starting by a study of noise affecting the motion of the device (thermomechanical noise) or the conversion of this motion into an electrically readable signal (transduction related noise). Following the transduction chain, amplifier noise is then studied. This is shown schematically in Fig. 5.1. Finally, the implications of these noise sources into the determination of the device's frequency are taken into consideration, as well as other noise sources directly affecting the frequency.

5.1 Amplitude Noise

This section describes the different noise sources that affect the determination of the amplitude of motion, both in magnitude and phase. It can also be referred to as "open loop" as a contrast to the next section where the effect of the different noise sources in the determination of frequency is going to be described.

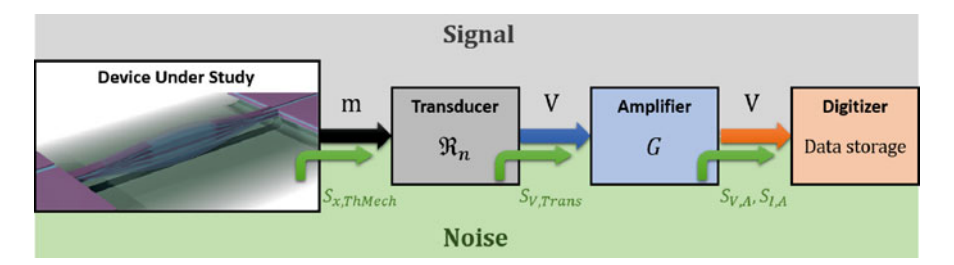


Fig. 5.1 Schematic showing the different noise sources along the different transduction stages. Within the resonator itself, still in the mechanical domain thermomechanical noise enters the system. Within the transduction to electrical signal, different noises may enter the system, e.g. Johnson–Nyquist, Hooge, and Shot noise. Finally the amplifying stage of the system will insert the input noise of the amplifier(s), dominated by current and voltage noise of the first amplifier

5.1.1 Fundamentals

Before starting the description of the different types of noise that can enter into NEMS resonators, it is interesting to first take a look into two basic and fundamental concepts: Transduction chain noise transfer and *noise referred to input* (RTI).

5.1.1.1 Transduction Chain Noise Transfer

It can be deduced from Fig. 5.1 that the final noise in the measurement (digital data) will have contributions from the different noises in the transduction chain. But such contributions have different influence on the final noise. Using the notation in the figure, one can write that the total noise of the signal arriving at the digitizer is

$$S_{V,\text{total}} = G_V^2 \left(S_{V,A} + S_{V,\text{Trans}} + \mathfrak{R}_n^2 \left(S_{x,\text{ThMech}} \right) \right), \tag{5.1}$$

with the mode specific transducer responsivity \mathfrak{R}_n , amplifier voltage gain G_V , thermomechanical noise $S_{X,\text{ThMech}}$, transduction noise $S_{V,\text{Trans}}$, and amplifier noise $S_{V,A}$. (5.1) can be generalized to any transduction chain. For example, if a second amplifier was to be used, the final noise would be given by

$$S_{V,\text{total}} = G_2^2 \left(S_{V,A2} + G_1^2 \left(S_{V,A1} + S_{V,\text{Trans}} + \mathfrak{R}_n^2 \left(S_{x,\text{ThMech}} \right) \right) \right)$$
 (5.2)

where it becomes clear that the noise in the first amplifier is the most important one within the amplifying chain.

5.1.1.2 Noise Referred to Input (RTI)

A direct consequence from the equations in the previous paragraph is that the final noise $S_{V,\text{total}}$ depends directly on the transduction chain. This is the reason why, in

order to compare transduction chains from a noise perspective, the magnitude that is taken to perform such comparison is the RTI. By comparing two different noise RTIs one can see which transduction chain "adds" more noise to the signal.

The concept of noise RTI is easy to understand and calculate. It is first important to substitute the transduction gain (with multiple stages) by a single stage with an *equivalent* gain and an *equivalent* noise at the input of said single stage. Like that, the system shown in Fig. 5.1 has an equivalent gain of: $G_{\text{equiv}} = G_1 \Re_n$ and a noise RTI given by

$$S_{\text{RTI}} = \frac{S_{V,\text{total}}}{G_{\text{equiv}}^2} = \frac{S_{V,A} + S_{V,\text{Trans}}}{\Re_n^2} + S_{x,\text{ThMech}}.$$
 (5.3)

Or in the case that two amplifiers were to be used, the noise RTI becomes

$$S_{\text{RTI}} = \frac{S_{V,\text{total}}}{G_2^2 G_1^2 \mathfrak{R}_n^2} = \frac{S_{V,A2}}{G_1^2 \mathfrak{R}_n^2} + \frac{S_{V,A1} + S_{V,\text{Trans}}}{\mathfrak{R}_n^2} + S_{x,\text{ThMech}}.$$
 (5.4)

As it can be seen in both (5.3) and (5.4), the contribution of each stage in the amplifying chain will be divided by the overall gain just until that stage, which makes the stages closest to the sensor/device the most important ones in terms of noise.

5.1.2 Thermomechanical Fluctuations

Any system that has a dissipation is subjected to damping, as is shown in Chap. 2. In the particular case of mechanical resonators, this dissipation can be seen as the coupling (interaction) between a cavity and a thermal reservoir full of randomly distributed phonons. This coupling, due to the randomness of the phonons in the reservoir, causes a noisy force that is applied to the mechanical resonator itself, as it is explained by the *fluctuation dissipation theorem* (FDT) [1, 2]. This can be easily written in equation form using the equation of motion that is analyzed in Chap. 1. Here, (1.181) is simplified to not include axial tension, nonlinearity nor external force

$$\rho A \frac{\partial^2 u(x,t)}{\partial t^2} + c \frac{\partial u(x,t)}{\partial t} + E I_z \frac{\partial^4 u(x,t)}{\partial x^4} = \bar{\xi}(x,t). \tag{5.5}$$

If now a single mode motion is considered, it is possible to use the same approach that is introduced in Chap. 1 in order to obtain a lump model of the noisy equation. This implies multiplying by the mode shape and integrate along the length of the mechanical structure

$$m_{\text{eff},n}\ddot{u}_n(t) + \Gamma_{\text{eff},n}\dot{u}_n(t) + k_{\text{eff},n}u_n(t) = \int_0^L \bar{\xi}(x,t)\phi_n(t)dt \equiv \xi_n(t). \tag{5.6}$$

It is important to remember that the magnitude denoting the amplitude of vibration $u_n(t)$ in this case is noise, meaning that the average over a long period of time is going to be zero. Indeed this is a direct cause of the contact with the thermal reservoir which causes the noisy force $\xi(t)$ to be white noise, i.e.

$$\langle \xi_n(t)\xi_n(t')\rangle \equiv \lim_{T \to \infty} \frac{1}{T} \int_t^{t+T} \xi_n(t)\xi_n(t') dt' = 2I_{\text{ThMech},n}\delta(t-t')$$
 (5.7)

where $I_{\text{ThMech},n}$ is the intensity of the noise for the *n*th mode and $\delta(t-t')$ is the delta function. The latter (5.7) can be written also in the frequency domain by taking the Fourier transform and using (5.7) itself

$$\langle \Xi_{n}(\omega)\Xi_{n}^{*}(\omega')\rangle = \int_{-\infty}^{\infty} \int_{-\infty}^{\infty} \langle \xi_{n}(t)\xi_{n}(t')\rangle e^{j\omega t} e^{-j\omega't'} dt dt'$$

$$= \int_{-\infty}^{\infty} 2I_{\text{ThMech},n} e^{j(\omega-\omega')t} dt$$

$$= 4\pi I_{\text{ThMech},n} \delta(\omega-\omega')$$
(5.8)

where $\Xi_n(t)$ is defined as

$$\Xi_n(\omega) = \int_{-\infty}^{\infty} \xi_n(t) e^{j\omega t} dt.$$
 (5.9)

If now (5.6) is transformed into the frequency domain, it can be obtained that

$$u_n(\omega) = \frac{\frac{\mathcal{E}_n(\omega)}{m_{\text{eff},n}}}{(\omega_n^2 - \omega^2) + j \frac{\Gamma_{\text{eff},n}}{m_{\text{off},n}} \omega}$$
(5.10)

and now taking the ensemble average of this magnitude

$$\langle u_{n}(\omega)u_{n}^{*}(\omega')\rangle = \frac{1}{m_{\text{eff},n}^{2}} \frac{\langle \Xi_{n}(\omega)\Xi_{n}^{*}(\omega')\rangle}{\left(\omega_{n}^{2} - \omega^{2} + j\frac{\Gamma_{\text{eff},n}}{m_{\text{eff},n}}\omega\right)\left(\omega_{n}^{2} - \omega'^{2} - j\frac{\Gamma_{\text{eff},n}}{m_{\text{eff},n}}\omega'\right)}$$

$$= \frac{1}{m_{\text{eff},n}^{2}} \frac{4\pi I_{\text{ThMech},n}}{(\omega_{n}^{2} - \omega^{2})^{2} + \left(\frac{\Gamma_{\text{eff},n}}{m_{\text{eff},n}}\omega\right)^{2}}\delta(\omega - \omega')$$
(5.11)

(5.11) can be used now to calculate the expected value of $u_n(t)$

$$\langle u_{n}(t)u_{n}(t)\rangle = \frac{1}{4\pi^{2}} \int_{-\infty}^{\infty} \int_{-\infty}^{\infty} \langle u_{n}(\omega)u_{n}^{*}(\omega')\rangle e^{j\omega t} e^{-j\omega' t} d\omega d\omega'$$

$$= \frac{1}{\pi} \int_{-\infty}^{\infty} \frac{1}{m_{\text{eff},n}^{2}} \frac{I_{\text{ThMech},n}}{(\omega_{n}^{2} - \omega^{2})^{2} + \left(\frac{\Gamma_{\text{eff},n}}{m_{\text{eff},n}}\omega\right)^{2}} d\omega$$

$$\approx \frac{I_{\text{ThMech},n}}{2\pi m_{\text{eff},n}^{2}\omega_{n}^{2}} \int_{-\infty}^{\infty} \frac{1}{(\omega_{n} - \omega)^{2} + \left(\frac{\Gamma_{\text{eff},n}}{2m_{\text{eff},n}}\right)^{2}} d\omega$$

$$= \frac{I_{\text{ThMech},n}}{m_{\text{eff},n}\Gamma_{\text{eff},n}\omega_{n}^{2}}$$
(5.12)

Equation (5.12) is fundamental in the study of noisy systems as it provides an expression that can be used within the equipartition of energy

$$k_{\text{eff},n}\langle u_n^2(t)\rangle = m_{\text{eff},n}\omega_n^2\langle u_n^2(t)\rangle = k_B T \to I_{\text{ThMech},n} = k_B T \Gamma_{\text{eff},n},$$
 (5.13)

which can be used to calculate the magnitude of the noise that is being inserted into the system, i.e.

$$\langle \xi_n(t)\xi_n(t')\rangle = 2k_B T \Gamma_{\text{eff},n}\delta(t-t'). \tag{5.14}$$

Equations (5.13) and (5.14) show how the noise intensity directly depends on the temperature and the damping rate or, in other words, it depends on the phonon population within the thermal reservoir and the level of interaction that is allowed between the bath and the resonator.

When performing noise measurements, the magnitude that is typically measured is the *power spectral density* (PSD). In order to obtain an expression for this magnitude, it is possible to make use of the definition of the PSD given by

$$\langle u_n^2(t)\rangle \equiv \int_{-\infty}^{\infty} S_{xx}(f) \mathrm{d}f,$$
 (5.15)

which combined with (5.12) provides a formula for the PSD for systems with low dissipation

$$S_{xx}(f) = \frac{k_B T \Gamma_{\text{eff},n}}{m_{\text{eff},n}^2 \omega_n^2} \frac{1}{(\omega_n - 2\pi f)^2 + \left(\frac{\Gamma_{\text{eff},n}}{2m_{\text{eff},n}}\right)^2}.$$
 (5.16)

This equation manifests that even though the input noise *in force* is white (5.7), the resulting noise in motion is *colored* as it has a Lorentzian shape. From (5.15) it is also possible to extract the noise magnitude at the peak of the Lorentzian

$$S_{xx}(f_n) = \frac{k_B T}{2\pi^2 \Gamma_{\text{eff},n} f_n^2} = \frac{k_B T Q_n}{4\pi^3 m_{\text{eff},n} f_n^3}.$$
 (5.17)

It is worth noting that, even though the maximum value of $S_{xx}(f)$ is linearly proportional to the quality factor of the resonator Q_n , the overall noise $\langle x^2(t) \rangle$ is inversely proportional to Q_n . In other words, for a given resonator, high Q_n means less noise overall but a higher (and narrower) noise peak.

5.1.2.1 Amplitude Calibration

Before continuing to the next section, it is also interesting to mention the utility of thermomechanical noise to calibrate the responsivity of the transduction mechanism selected to detect the motion of the resonator. No matter the transduction mechanism, the magnitude that is actually measured in the lab is electrical power coming into the analyzer (e.g., spectrum, network, or lock-in amplifier). Thus, displacement (in meters) is transduced into an electrical signal (volts) and it is necessary to find an experimental way to estimate this transduction coefficient, which can be called responsivity and in general is different for each resonator mode

$$\mathfrak{R}_n = \frac{\partial V_n}{\partial u_n}. (5.18)$$

One of the typical ways of estimating \Re_n is to use thermomechanical noise, and the fact that the frequency dependence (5.16) and the overall integral along the frequency spectrum (5.15) of such noise are both known. The procedure starts by measuring the noise of the system under study around the resonance frequency with a spectrum analyzer. The result should always be in units of noise (e.g., $\frac{V^2}{Hz}$) so that the size of the resolution bandwidth does not modify the final result. Once this measurement has been performed, it is necessary to fit the data to a Lorentzian function (5.16) with a background that accounts for other noise sources that are analyzed later in this chapter. This background can typically be considered as white noise (flat in the frequency domain), assuming that the measurement is narrow-range around the resonant frequency of the device. The results for the fitting parameters can be equated to the expected value(s) from (5.16), and like that one can obtain the value for the transduction responsivity, \Re_n (Fig. 5.2).

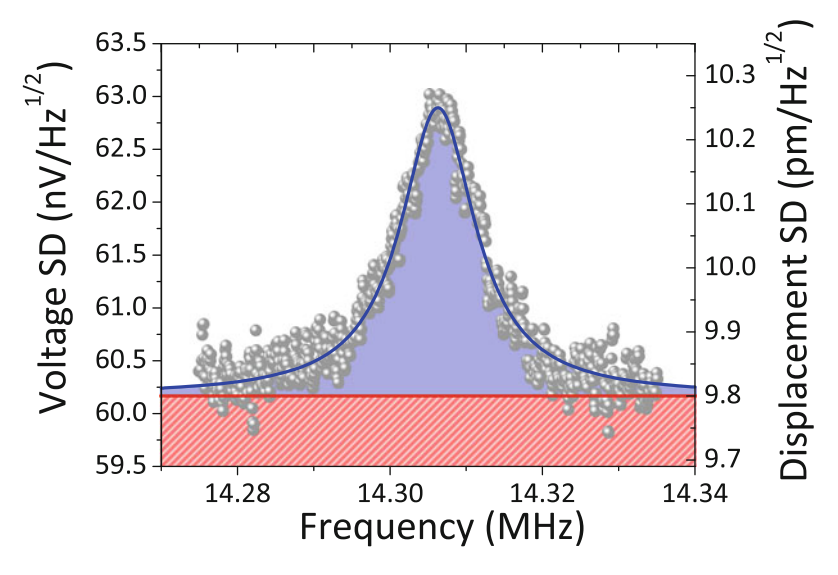


Fig. 5.2 Example of a thermomechanical noise measurement (scattered data). The fitting to a Lorentzian function (*purple line*) with background (*red line*) provides us information about the different noise sources in the measurement: system noise (including transduction and amplifier noise) for the flat background and thermomechanical noise for the peak. Even though the measurement is performed in volts (*left axis*), using the procedure described above it is possible to calibrate the transduction back into meters (*right axis*)

5.1.3 Transduction Related Noise

As it is shown in Chap. 4, there are many different ways to detect the motion of a mechanical device and transduce it into electrical energy. This of course affects the value of the first responsivity \mathfrak{R}_n that is shown in Fig. 5.1, but it also determines the transduction noise, $S_{V,\text{Trans}}$ or $S_{I,\text{Trans}}$, which is the noise in the electrical domain that is inserted in the system due to the transduction technique being used. This noise S_{Trans} might have itself several possible origins. Johnson–Nyquist thermal noise, Hooge 1/f noise, and Shot noise are generally the main contributions which will be analyzed in the following paragraphs.

5.1.3.1 Johnson-Nyquist Thermal Noise

Electrical thermal noise is caused by the random thermally excited vibration of the charge carriers in a conductor. This is, in some way, similar to the Brownian motion of particles or the previously described thermomechanical motion of the resonator.

Thermal noise was first observed by J.B. Johnson and contemporaneously explained by Nyquist [2]. It can be thus generalized via the FDT [1, 2], because a conductor has a dissipative part, i.e. the real part of the impedance or Re(Z). The noise is white up to a high frequency limit, where a roll-off occurs, allowing for the *overall* noise level to remain finite. The noise magnitude, already estimated by Johnson [3], in units of PSD is

$$S_{V_{\text{th}}} = 4k_B T R \left[\frac{V^2}{\text{Hz}} \right]$$

$$S_{I_{\text{th}}} = \frac{4k_B T}{R} \left[\frac{A^2}{\text{Hz}} \right]$$
(5.19)

depending whether the noise is modelled as a current source in parallel to a noiseless resistance or a voltage source in series with a noiseless resistance. In (5.19), k_B is the Boltzmann's constant, T is the temperature of the resistor in Kelvin, and R is the value of the resistance or, in the more general case, the value for the real part of the impedance. In reality, as said above, the noise is not completely white as (5.19) shows, but presents a cutoff frequency beyond which the noise relaxes down, as shown in Fig. 5.3. This cutoff is fundamentally determined via the thermal occupancy of states or by the fastest time scale on which electrons are typically scattered. A more *mundane* reason for the roll-off is the parasitic capacitance that

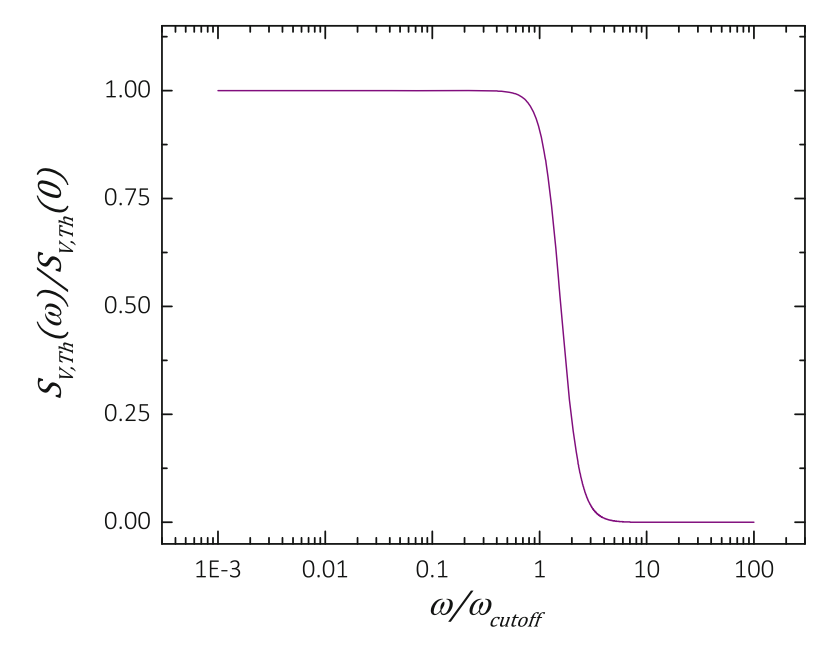


Fig. 5.3 Scaled thermal noise power spectral density versus scaled frequency. The noise is white, i.e. constant, all the way until the cutoff frequency where it drops down to zero

is always present in parallel to a resistor, thus limiting the amount of noise that is transferred to other parts of the circuit.

As for any type of noise, in order to calculate the actual voltage or current noise in the measurement one needs to integrate the PSD over the bandwidth, which will be defined in particular for said experiment. The bandwidth of a measurement establishes which part of the frequency spectrum is allowed to enter the detector. A very large bandwidth will thus mean a larger noise but, at the same time, a shorter integration time. On the other hand, having a small bandwidth will imply much smaller noise but a larger integration time, which it can lead (but not necessarily) to a slower response time.

The overall noise formula is given by

$$V_{\text{th}} = \sqrt{\int_{f_0}^{f_1} 4k_B T R \, df} = \sqrt{4k_B T R \, BW}$$

$$I_{\text{th}} = \sqrt{\int_{f_0}^{f_1} \frac{4k_B T}{R} \, df} = \sqrt{\frac{4k_B T}{R} \, BW}$$
(5.20)

where BW = $f_1 - f_0$ is the bandwidth of the measurement and it is assumed that the cutoff frequency described in Fig. 5.3 is much larger than f_1 , which is typically the case.

To finalize this section it is necessary to highlight that this analysis presented here is *strictly* only valid when the resistor is not biased. In other words, it only works when the electrons are, in average, not moving. In the biased case, there can be a departure from the predicted values of (5.20), see [4] for more details. In addition, as soon as the resistors are biased, two more noises enter to play: shot noise and Hooge (1/f) noise.

5.1.3.2 Shot Noise

Current flowing is not smooth nor continuous. In the end, due to the fact that charge is quantized, one can consider current as the succession of discontinuous pulses, one for each arriving carrier. A useful analogy can be the raindrops of a heavy rain falling on a tin roof.

Shot noise is the most fundamental model of discontinuous noise in physical systems. It is not restricted to electrical systems but can be also found in any system with quantized carriers like optical systems (photons), communication systems (packets), acoustic systems (phonons), etc.

Shot noise was first described by Campbell [5, 6], followed by many studies [7], out of which the experiments done by Schottky in 1918 represent an important milestone [8]. It is associated with partitioned systems, like when current flows across a potential barrier, e.g. in diodes, transistors, vacuum tubes, etc. The spectrum is white and the intensity is given by

$$S_{I_{\text{shot}}} = 2e\zeta I_{\text{bias}} \left[\frac{A^2}{\text{Hz}} \right]$$

 $S_{V_{\text{shot}}} = 2e\zeta I_{\text{bias}} R^2 \left[\frac{V^2}{\text{Hz}} \right],$ (5.21)

where e is the unitary electron charge, I_{bias} is the current that passes through the noisy part of resistance R, and ζ is the Fano or correlation factor, which is a proportionality factor that ranges from 0 when the material is a perfect conductor to 1 for systems with full partition, e.g. for tunnel junctions, semiconductor fully depleted regions, etc. For the rest of cases, $0 < \zeta < 1$. In the particular case of disordered conductors, it is possible to prove that $\zeta \to \frac{1}{3}$ [9].

From (5.21) it is possible to calculate the actual value of the noise by following the same procedure shown in (5.20)

$$I_{\text{shot}} = \sqrt{\int_{f_0}^{f_1} 2e\zeta I_{\text{bias}} \, \mathrm{d}f} = \sqrt{2e\zeta I_{\text{bias}} \, \mathrm{BW}}$$

$$V_{\text{shot}} = \sqrt{\int_{f_0}^{f_1} 2e\zeta I_{\text{bias}} R^2 \, \mathrm{d}f} = \sqrt{2e\zeta I_{\text{bias}} R^2 \, \mathrm{BW}}, \tag{5.22}$$

where once again BW is the bandwidth of the measurement. It is interesting to note the dependence of the noise intensity with the square root of the current itself, meaning that the larger the current the larger the noise (remember the analogy with the heavy rain on the rooftop, where more rain would imply more noise).

5.1.3.3 Hooge (1/f) "Flicker" Noise

Up to now, the three noises that have been analyzed in this chapter have been white (thermomechanical noise is white in force, Johnson and shot noise are white in current). On the other hand, 1/f noise has a PSD that increases, in principle without limit, as frequency decreases. The first observations of this noise were done on vacuum tubes and they caused flickering in the plate current, hence the name "flicker" noise.

This noise has several unique properties and it is quite ubiquitous, not only in electronic systems (in particular in disordered conductors), but more generally in most physical systems there is always an increase in the noise at low frequencies. Even though it generally is called 1/f this is an abuse of language. As it has been widely reported [10, 11], the reality is that the noise has a power dependence of the type $1/f^{\alpha}$ where $\alpha=1$ is the most common value. In electronic circuits, the exponent is generally found within a range, typically $0.8 < \alpha < 1.3$. But there are many other systems that show mechanisms with larger values of α , e.g. fluctuations of the Earth's rotation frequency have $\alpha=2$, and galactic radiation noise has $\alpha=2.7$. From now on, for simplicity, the most common value for the exponent will be taken.

The origin of this type of noise in electronic components seems to stem from fluctuations of the conductance/resistance of the devices. Hooge [12] built a semi-empirical law to model this noise, which is given by

$$S_{V_{1/f}} = \frac{\gamma}{N_c} \frac{V_{\text{bias}}^2}{f} \left[\frac{V^2}{\text{Hz}} \right]$$

$$S_{I_{1/f}} = \frac{\gamma}{N_c} \frac{V_{\text{bias}}^2}{R^2 f} \left[\frac{A^2}{\text{Hz}} \right], \qquad (5.23)$$

where γ is a proportionality constant to be empirically estimated for a given device, N_c is the number of carriers in the device, and V_{bias} is the bias voltage applied to the noisy part of resistance R. Equation (5.23) hints the important temperature dependence that this noise has, as the number of carriers (N_c) depends strongly on temperature, plus the proportionality constant has also been observed to depend on temperature. This, in turn, makes this type of noise extremely dependent on the device and operating conditions that are being used for an experiment.

To estimate the actual noise contribution of this type, it is necessary to integrate the power spectrum density over the bandwidth

$$V_{1/f} = \sqrt{\int_{f_0}^{f_1} \frac{\gamma}{N_c} \frac{V_{\text{bias}}^2}{f} \, df} = V_{\text{bias}} \sqrt{\frac{\gamma}{N_c} \ln\left(\frac{f_1}{f_0}\right)}$$

$$I_{1/f} = \sqrt{\int_{f_0}^{f_1} \frac{\gamma}{N_c} \frac{V_{\text{bias}}^2}{R^2 f} \, df} = \frac{V_{\text{bias}}}{R} \sqrt{\frac{\gamma}{N_c} \ln\left(\frac{f_1}{f_0}\right)}.$$
(5.24)

A theoretical derivation for this noise can be found in the literature [13] and is based on the superposition of multiple relaxation processes, each of them with a Lorentzian-like power spectrum but different relaxation rates. After averaging, the characteristic power law 1/f is recovered.

5.1.3.4 Noise Equivalent Circuit

Before moving on to the amplifier noise, it is interesting to show how the noise sources that have just been analyzed look like when a circuit needs to be considered, how to place them so that one can perform a proper noise analysis and translate such noise to other places in the circuit. The two basic schematics that can be used are either the Thevenin or the Norton equivalent circuit, as it is shown in Fig. 5.4.

5.1.4 Amplifier Noise

As illustrated in Fig. 5.1, after the transduction of the motion into an electrical signal, an amplifying stage is typically used to bring the signal to a level that can be

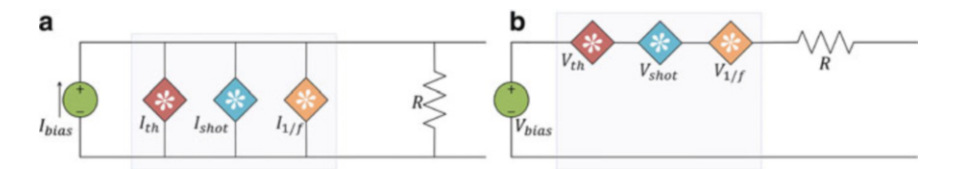


Fig. 5.4 Noise equivalent circuits for a biased resistive element. Either option, Norton (a) or Thevenin (b), can be used to calculate the overall noise and to estimate how much this noise affects the next stage in the system

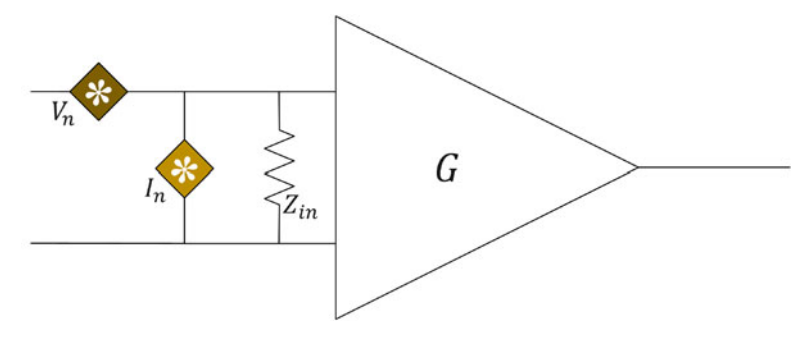


Fig. 5.5 Noise equivalent circuit to describe the ensemble of effects that are present internally in any amplifier. V_n and I_n are, respectively, the voltage and current noise of the amplifier, G is its gain and $Z_{\rm in}$ is its input impedance which in general can take complex values. The amplifier in the model maintains the same gain as the original one, but in this case it is an *ideal* amplifier, which means that is noiseless and with an infinite input resistance

detected or digitized by other equipments in the lab. Amplifiers are very complex devices that contain many components, which makes it virtually impossible to perform a thorough and detailed analysis of how each of these components affects the overall noise within the amplifier. A noise model is helpful to simplify noise analysis at the circuit/system level, i.e. how much the *noise referred to input* is. The most extended noise model for amplifiers, which is also the simplest that allows a full analysis, is the one that includes voltage and current noise in the input of a noiseless amplifier (see Fig. 5.5 for a schematic of the equivalent circuit).

Once the schematic for the amplifier noise model is set, it is possible to calculate the noise referred to input for this amplifier when other parts are connected to it. As a simple example, let's consider the circuit presented in Fig. 5.6, where an input signal $V_{\rm in}$ is sent to an amplifier through a resistive line of value R, which has an associated noise $V_{n,R}$. The actual gain of the whole (total) system, which can be defined as $G_t = \frac{V_{\rm out}}{V_{\rm in}}$, is different than the gain of the ideal amplifier present in the schematic. It is rather straightforward to obtain that

$$V_{\text{out}} = G \frac{Z_{\text{in}}}{R + Z_{\text{in}}} V_{\text{in}} \rightarrow G_t = G \frac{Z_{\text{in}}}{R + Z_{\text{in}}}.$$
 (5.25)

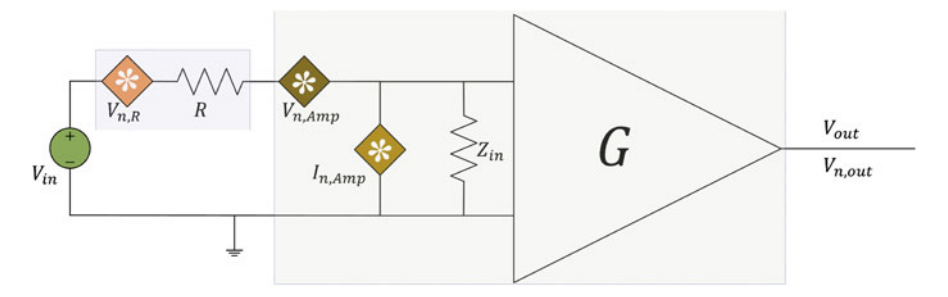


Fig. 5.6 Noise equivalent circuit for an amplifier connected to a source and a resistive element. The amplifier model is the one present in Fig. 5.5

In order to estimate the noise referred to input it is necessary to consider independently every noise source present in the schematic of Fig. 5.6. To do this, one needs to "null" (short-circuiting voltage sources and leaving current sources open) all sources in the system except for one and calculate the noise contribution and add these contributions squared. Following this approach it is easy to obtain the noise in the output of the amplifier

$$V_{n,\text{out}}^2 = \left(V_{n,R}^2 + V_{n,A}^2\right) G^2 \left(\frac{Z_{\text{in}}}{R + Z_{\text{in}}}\right)^2 + I_{n,A}^2 G^2 \left(\frac{R Z_{\text{in}}}{R + Z_{\text{in}}}\right)^2.$$
 (5.26)

Combining (5.26) and (5.25), one can obtain the noise referred to input of the whole system

$$V_{n,\text{RTI}} = \sqrt{\left(V_{n,R}^2 + V_{n,A}^2\right) + I_{n,A}^2 R^2}.$$
 (5.27)

It needs to be pointed out here that all the previous equations are strictly valid only if there is no correlation between voltage and current noise. In reality, it is possible to find some correlation between the two of them, which complicates the analysis requiring an extra term with the cross product of voltage and current noise [14].

Following with the system schematized in Fig. 5.6, one can now post the question about how does the signal to noise ratio (SNR) evolves from before and after the amplifier. The SNR is a dimensionless figure of merit that allows to estimate the quality (cleanliness) of your measurement technique, being better the larger the SNR. The power SNR before and after the amplifier is, respectively, given by

$$\left(\frac{S}{N}\right)_{\rm in} = \left(\frac{V_{\rm in}}{V_{n,R}}\right)^2 \tag{5.28}$$

and

162

$$\left(\frac{S}{N}\right)_{\text{out}} = \left(\frac{V_{\text{out}}}{V_{n,\text{out}}}\right)^{2}$$

$$= \frac{G^{2}\left(\frac{Z_{\text{in}}}{R+Z_{\text{in}}}\right)^{2}V_{\text{in}}^{2}}{\left(V_{n,R}^{2} + V_{n,A}^{2}\right)G^{2}\left(\frac{Z_{\text{in}}}{R+Z_{\text{in}}}\right)^{2} + I_{n,A}^{2}G^{2}\left(\frac{RZ_{\text{in}}}{R+Z_{\text{in}}}\right)^{2}}$$

$$= \frac{V_{\text{in}}^{2}}{V_{n,R}^{2} + V_{n,A}^{2} + I_{n,A}^{2}R^{2}}$$

$$= \frac{V_{\text{in}}^{2}}{V_{n,R}^{2}}.$$
(5.29)

The ratio between these two SNR defines the *noise factor*, *F* of the amplifier, which is given by

$$F = \frac{\left(\frac{S}{N}\right)_{\text{in}}}{\left(\frac{S}{N}\right)_{\text{out}}} = \frac{V_{n,R}^2 + V_{n,A}^2 + I_{n,A}^2 R^2}{V_{n,R}^2} = 1 + \frac{V_{n,A}^2 + I_{n,A}^2 R^2}{V_{n,R}^2}$$
(5.30)

where $F \ge 1$, and that it is equal to 1 when the amplifier does not add any noise to the measurement, the *ideal* case. One could argue that this implies that the amplifier only makes the measurement *worse*, as the SNR is smaller after the amplifier than before. But when considering the final stage of the measurement chain, e.g. a digitizer or an analog acquisition device, there are parts which will be noisier than the noise coming from the transduction (in the example $V_{n,R}$) and also noisier than the amplifier. Thus, the selection of a good amplifier for the first step in the amplifying stage is critical.

5.1.4.1 Noise Figure and Noise Temperature

As it has been shown in previous paragraphs, the noise factor determines how good or bad an amplifier is. There are two other parameters that are often used to describe this point: noise figure (NF) and noise temperature ($T_{\rm Amp}$) which are defined as follows

$$NF = 10 \log_{10}(F) \tag{5.31}$$

and

$$T_{\rm Amp} = T_0 (F - 1),$$
 (5.32)

where T_0 is typically taken to be 290 K. The noise figure is a positive magnitude that in the case of the ideal amplifier tends to zero, and is expressed in dB. Noise temperature is a useful magnitude that uses the concept of noise being proportional to temperature (in power), as it has been shown in the case of thermomechanical and Johnson noise. It gives an idea of how much "hotter" the system is after the amplifier.

An important point to address is that with neither of these parameters: noise factor (F), noise figure (NF), or noise temperature $(T_{\rm Amp})$; it is not possible to have a direct estimation of the amplifier noise, but only a ratio to $V_{n,R}$. However, the latter noise is typically considered to be Johnson noise of a 50 Ω resistor at 290 K (unless specified otherwise), which is the most common impedance value for transmission lines. Still, this does not allow to distinguish between current and voltage noise in the amplifier, but only gives a concrete value for $V_{n,A}^2 + I_{n,A}^2 R^2$. It should also be noted that (5.30) and subsequent expressions are written as a function of noise, not PSD. However, one can consider the noise contributions from the amplifier as white within the measurement bandwidth. Thus, (5.30) becomes

$$F = 1 + \frac{S_{V,A} + S_{I,A}R^2}{S_R}. (5.33)$$

5.2 Frequency Noise

In the previous section of the chapter, the noise in the determination of the amplitude of motion has been analyzed. Recalling from Chap. 3, most of the applications that use a NEMS as sensor involve the measurement of the resonant frequency rather than the amplitude. Hence, it is very important to study how to determine the noise in the frequency measurement. Let us make clear from the beginning that the somewhat extended version of the frequency detection, which is illustrated in Fig. 5.7, and that involves the acquisition of successive amplitude vs. frequency curves is not the typical (nor optimal) way of performing this detection. In this case, the time between two consecutive experimental data points, i.e. two consecutive determinations of a device's natural frequency take very long, as many points need to be acquired to be able to fit each curve and extract the frequency.

In practice, the usual way of proceeding is to generate a *closed loop system* that allows for a direct estimation of the resonant frequency of the device. There are two main ways of generating said closed loop, either by means of a *phase-locked loop* (PLL) or via a *self-sustained oscillator*.

5.2.1 Phase-Locked Loop

A PLL, in its broadest definition, is a control system that balances its operating point as a function of the difference between the phase of the output signal and its comparison with a given set-point.

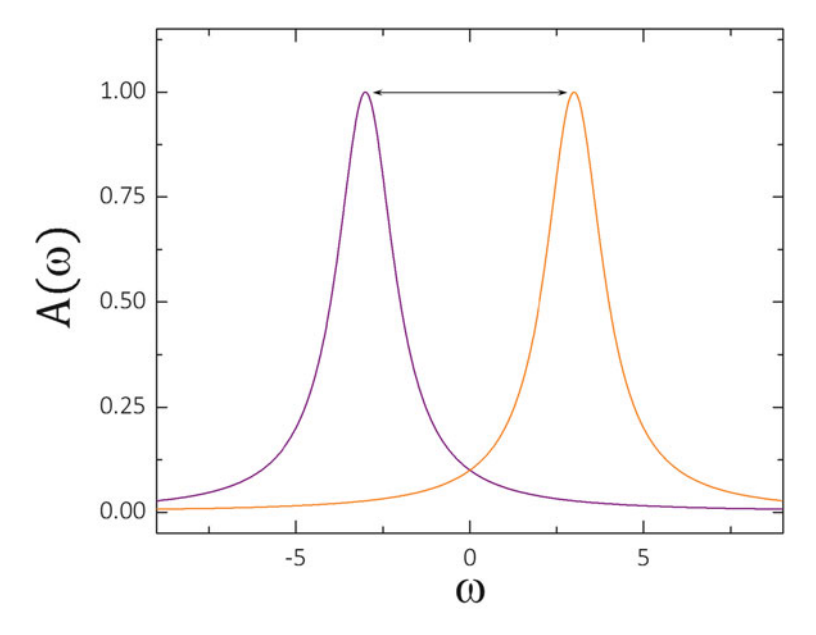


Fig. 5.7 Two adjacent amplitude vs. frequency responses for an imaginary device: before and after an event. The frequency shift can be related to the magnitude of said event. However, this way of operation is not ideal nor recommended as it takes much longer than required to perform the measurement, reducing the bandwidth of the measurement

PLLs are widely used, e.g., in telecommunications, radio, computers. They can be used to recover a signal from a noisy communication channel, demodulate a signal, synthesize harmonic signals at multiples of an input frequency, etc.

In particular for the case of resonant NEMS sensors, the typical configuration is schematized in Fig. 5.8, and it has been used by many different groups in different variations [15–18]. A given frequency generator outputs a signal that splits into two branches: the reference arm and the measurement arm. While the measurement arm passes through the device under study (DUT) and hence observing a phase shift, the reference arm passes through a phase shifter that sets the phase to a given set point. Later the phases in both signals are compared and the difference is used as an input to the loop gain element, also called filter, which will calculate the shift in the frequency output by the original generator. This gain function can be proportional to the phase difference $\delta \phi$ but it can also depend on the time derivative or the integral of said phase difference (P-I-D control).

So in essence the PLL needs a very accurate determination of the phase, otherwise the noise in the frequency will increase. If, for the sake of simplicity, a proportional gain is considered in the PLL, it is rather straightforward that noise in the phase determination will be proportional to noise in the frequency, and this proportionality is given by the quality factor

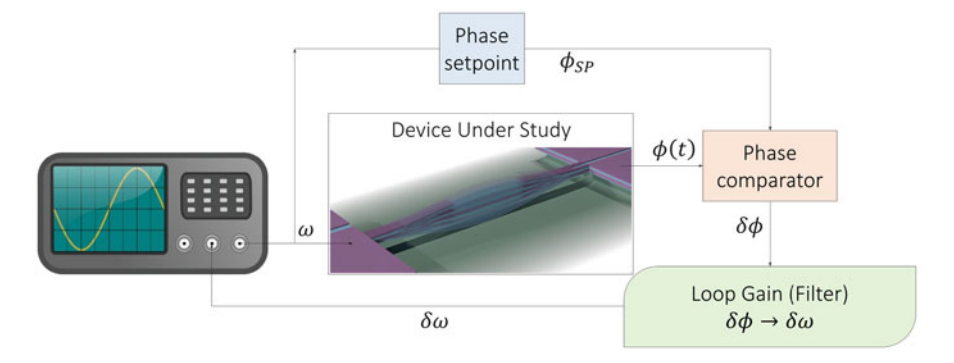


Fig. 5.8 Typical schematic of a PLL for NEMS. A signal source generates on the resonator a force at a frequency ω . At the output of the resonator its phase difference with respect to the reference signal is calculated and input to the loop gain (or filter) that takes care of translating said phase difference $\delta \phi$ into a jump in the frequency output from the signal generator, which in turn causes the phase difference to reduce and eventually be cancelled. By monitoring the frequency output of the source one can directly know the frequency of the device

$$\frac{\delta\omega}{\omega_n} = \frac{2}{\pi Q} \delta\psi. \tag{5.34}$$

Figure 5.9a shows the phase response vs. frequency of a resonator with noise. An accurate determination of said phase will directly impact the frequency stability of the PLL. A visual interpretation of this noise in the phase determination can be seen in Fig. 5.9b that shows a resonator in its rotatory (stroboscopic) frame of reference. Due to the noise in the determination of the resonator state a cloud is generated around the noiseless case. The angle sustained by such cloud represents the noise in the determination of the phase. Needless to say that, provided the noise is white, averaging for longer reduces the angle $\delta \psi$ and thus the frequency noise $\delta \omega$.

5.2.2 Self-Sustained Oscillator

In the previous section the concept of PLL is introduced and specifically how it can be used to monitor the frequency. Using a PLL has certain limitations regarding the speed of the measurement. Even though much faster than performing successive frequency sweeps to determine the amplitude peaks, it still involves a feedback loop that might be slow in some cases, e.g. if the processing box is inside a computer.

An alternative, in some sense one could consider this as a form of an analog PLL, is to send back to the resonator the amplitude signal after amplification and proper phase shift. This is typically called the *oscillator* or the *positive feedback* technique. This has been tried by many different groups in different types of implementations[19–30].

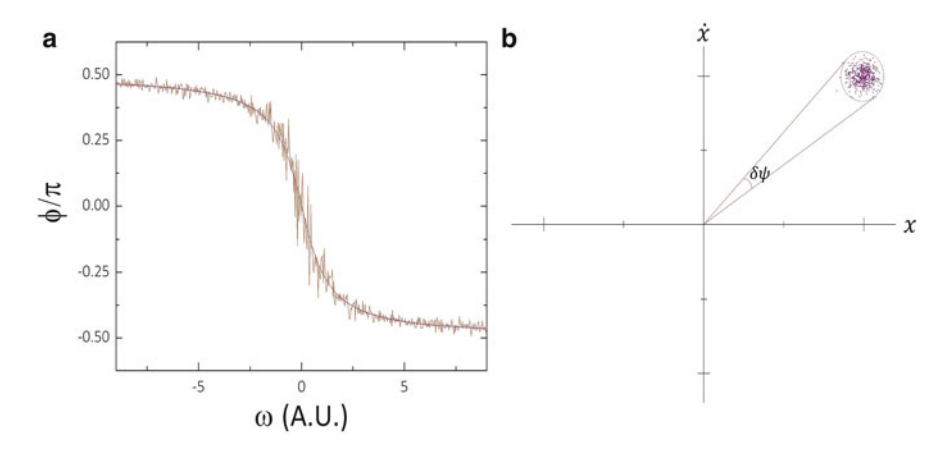


Fig. 5.9 (a) Phase vs. frequency response of a resonator, including the noise in the measurement. The noise magnitude is scaled to make it visible. Said noise is shown larger close to the resonant frequency because it is assumed that thermomechanical noise dominates over the other sources of noise. (b) Schematic representation of the resonator state in the rotatory (stroboscopic) frame. The cloud of points represent the different states after each cycle, taking into account the noise in the system. The angle $\delta\psi$ can be considered as the magnitude of the noise in the determination of the phase

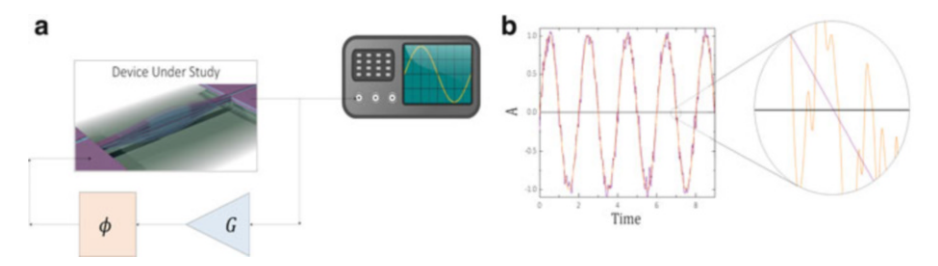


Fig. 5.10 (a) Schematic of a self-sustained oscillator system. The amplitude of motion of the device is transduced to the electrical domain to be amplified and phase corrected to eventually be sent as a feedback force to the device. The gain in the amplifier must be large enough as to compensate the losses that are generated within the resonator and the electromechanical transduction associated losses. To measure the frequency, the signal is taken out of the loop and sent to a frequency counter. (b) Noisy harmonic signal to show the effect of such noise in the determination of the frequency. Each time that the signal crosses through zero, there is noise caused in the frequency determination. In addition to this *direct* or *residual* noise, the noisy signal is being feedback to the device as a force

Figure 5.10a shows a schematic for this technique. The gain in the amplifier (G) needs to be large enough as to compensate the losses within the resonator and transduction efficiency whereas the phase shift (ϕ) needs to be adjusted so that the feedback signal is in phase with the velocity $(\pi/2)$ out-of-phase with respect to the amplitude.

The equation governing the motion of a particular mode within a resonator is given by (5.35), which is very similar to (5.6) but with a feedback term

$$m_{\text{eff},n}\ddot{u}_n(t) + \Gamma_{\text{eff},n}\dot{u}_n(t) + k_{\text{eff},n}u_n(t) = G_m\dot{u}_n(t) + \xi_n(t), \tag{5.35}$$

where the transduction efficiency is hidden in the effective mechanical gain G_m , which is the gain in the amplifier of Fig. 5.10a only with the transduction efficiency (both actuation and detection) embedded within. (5.35) can be rewritten so that the conditions mentioned above become clearer

$$m_{\text{eff},n}\ddot{u}_n(t) + (\Gamma_{\text{eff},n} - G_m)\dot{u}_n(t) + k_{\text{eff},n}u_n(t) = \xi_n(t),$$
 (5.36)

where it is now evident that when the condition $G_m > \Gamma_{\text{eff},n}$ is held, the system becomes unstable, a self-sustained oscillation starts and higher nonlinear terms need to be considered to actually saturate the motion. These two conditions are typically known as the *Barkhausen criterium* for oscillation, i.e. the gain in the feedback compensates the losses in the resonator and the phase is matched to the velocity.

Once the system is operating, one needs to measure the frequency in this case a frequency counter is typically used. This is a device that counts how many times a signal passes through zero within a certain time and calculates the frequency using that number and the measurement time. This now poses the question of what is the type of noise that affects now this determination of the frequency. Within Fig. 5.10b it is shown an example of a noisy harmonic signal. The inset shows the zone close to one of the crossings around zero and that is the critical part where noise in the amplitude directly affects the determination of the frequency. This is the direct contribution, sometimes also called residual noise. There is another contribution to the noise which happens within the feedback itself. In this case, the force driving the resonator is not coming from an external device, i.e. being clean, but is defined by the transduced amplitude of motion, which means that said driving force will be noisy. This second contribution is in the loop, meaning that the noisy force causes a noisier amplitude which in turn causes a noisier force and so on and so forth.

One can now analyze the differences between the PLL solution and the self-sustained oscillator solution. The latter, as already advanced, is typically faster as the feedback is purely analog, as opposed to the PLL solution where already the lag caused by the external frequency source is larger. This difference is even more pronounced when the PLL needs of a computer to perform the loop gain calculation, in which case the delay might reach fractions of a second or even more. On the other hand, in the case of a PLL the feedback force sent to the device will be cleaner than in the case of the self-sustained oscillator. In the end, the most appropriate method will be determined by every particular application, its requirements and limitations.

5.2.3 Allan Variance

To finalize this chapter it is important to talk about the magnitude that is typically used as a metric for the frequency noise of the sensors. This is the so-called *Allan variance*, named after its inventor Allan et al. [31, 32]. In principle this can be applied to any magnitude as it is defined very generally

$$\sigma_y^2(\tau) = \frac{1}{2} \langle (\Delta y)^2 \rangle = \frac{1}{2(N+1)} \sum_{i=1}^{N} (y_{i+1,\tau} - y_{i,\tau})^2,$$
 (5.37)

where y_i is the *i*th measurement of the magnitude y which is taken during an average time τ , i.e.

$$y_{i,\tau} = \frac{1}{\tau} \int_{(i-1)\tau}^{i\tau} y(t) dt.$$
 (5.38)

The final result as a function of the integration time τ provides a magnitude that, in presence of white noise, reduces when τ increases. Indeed this shows the major advantage of this variance over the classical variance. The Allan variance converges for most of the commonly encountered kinds of noise, whereas the classical variance does not always converge to a finite value. As an example, 1/f noise has a classical variance which does not converge, and it is commonly occurring in nature and, in particular, clock-like systems (like oscillators or PLLs).

Equations (5.37) and (5.38) are very general as they can be applied to any dimensionless variable y. In the particular case of resonance-based sensors y is chosen to be

$$y(t) = \frac{\omega(t) - \omega_n}{\omega_n},\tag{5.39}$$

which is the normalized instantaneous frequency difference to the natural frequency of the resonator.

The Allan variance is the best known of the time-domain magnitudes to characterize frequency inaccuracy. To know more about the other variances, the reader is directed to follow the Appendixes in Ref. [33] and the references therein. It is important to address the fact that in addition to these time-domain magnitudes there exist their frequency-domain counterparts, which can be defined as

$$\sigma_{y}^{2}(\tau) = 2 \int_{0}^{f_{h}} S_{y}(f) \frac{\sin^{4}(\pi f \tau)}{(\pi f \tau)^{2}} df, \qquad (5.40)$$

where f_h is the cutoff frequency associated with the measurement system.

Depending on the application domain, time-domain or frequency-domain magnitudes are preferred. In the sensors community, it is rather the Allan variance, in the

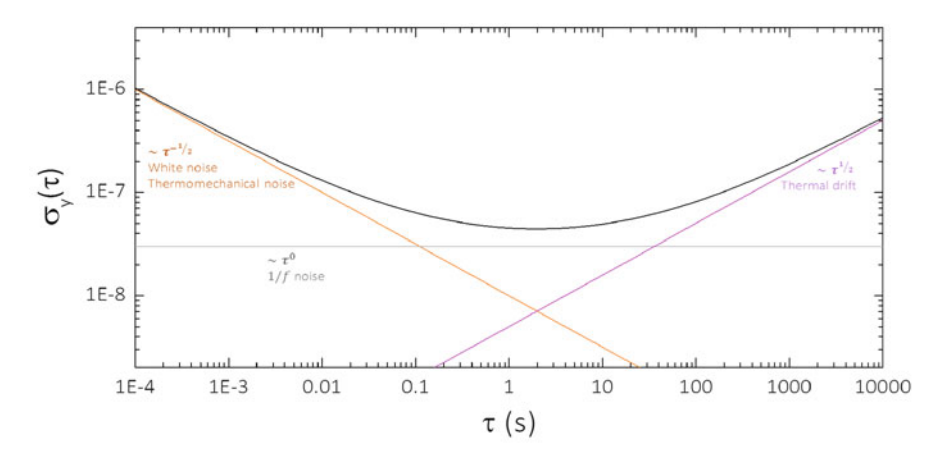


Fig. 5.11 Typical Allan deviation plot as a function of the integration time τ . The *black line* shows the overall Allan deviation which is composed by three different contributions (in this particular example): the white noise and thermomechanical noise, which are inversely proportional to $\sqrt{\tau}$ and follow the *orange line*; the 1/f noise that gives a flat contribution across the integration time (*grey line*); and the drift or random walk that will increase proportional to τ or $\tau^{0.5}$, as it is marked by the *pink line*. The minimum noise can be found in this case for $\tau \approx 2$ s, but that does not necessarily mean that this will be the most appropriate operation point. It might be that one needs to compromise resolution in favor of speed in the measurement

time domain, what is used so that one can directly estimate the noise in the system for a given integration time.

In previous sections the noise that needs to be accounted for in the PLL and oscillator has been explained. The consequence of these types of noise in the Allan variance (or rather Allan deviation) can be seen graphically in Fig. 5.11. White noise in the amplitude determination and thermomechanical noise are translated into a σ_y that decreases proportionally to the square root of the integration time. 1/f noise shows as a flat region, i.e. with such noise source it is not possible to improve your measurement by averaging longer. Finally, when drift exists in the system σ_y will increase proportional to $\tau^{0.5}$ or τ . Theoretically it is typically easy to access the measurement of the white noise, so that part of the graph can be estimated. This can be done following the *Robbin's formula*

$$\sigma_y^2(\tau) = \frac{2}{\pi^2 Q^2} \left\langle \left(\frac{\delta u_n}{u_n} \right)^2 \right\rangle \to \sigma_y(\tau) = \frac{\sqrt{2}}{\pi Q} \frac{1}{\text{SNR}} = \frac{\sqrt{2}}{\pi Q} \frac{S_x^{1/2}}{\langle x \rangle} \sqrt{\text{BW}}, \quad (5.41)$$

which indeed shows the time dependence that can be seen in Fig. 5.11.

However, the actual limitation for the detection cannot be estimated that easily as it normally comes from either of the other contributions. Therefore, in order to actually determine a system's limits, the Allan deviation must be measured experimentally. Once that is done, one can easily locate which is the most effective point for operation. This might coincide with the minimum, but it can also happen

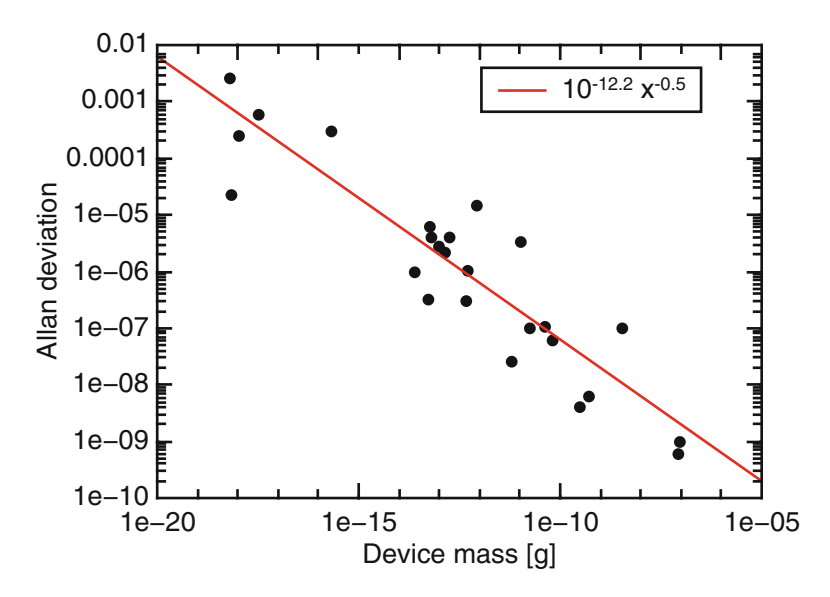


Fig. 5.12 The frequency stability of micro- and nanomechanical resonators at room temperature as a function of their mass, extracted from literature. The data is taken from [34]

that the application requires faster response time (smaller integration time τ) and thus resolution is compromised in favor of a faster measurement.

It has been shown recently that the theoretical calculation of the frequency noise is resulting in σ values that are roughly two order of magnitude lower than experimentally observed values [34]. However, the Allan deviation was found to correlate with the resonator's mass (see Fig. 5.12). Hence, the fit to the experimental data can be used as a heuristic predictor for the achievable frequency noise of a nanomechanical system of a given total mass m and is given by

$$\sigma \approx 10^{-12.2} \frac{1}{\sqrt{m}}.\tag{5.42}$$

References

- 1. H.B. Callen, T.A. Welton, Irreversibility and generalized noise. Phys. Rev. **83**(1), 34–40 (1951)
- H. Nyquist, Thermal agitation of electric charge in conductors. Phys. Rev. 32(1), 110–113 (1928)
- 3. J.B. Johnson, Thermal agitation of electricity in conductors. Nature 119, 50–51 (1927)
- 4. M.L. Roukes, M.R. Freeman, R.S. Germain, R.C. Richardson, M.B. Ketchen, Hot-electrons and energy-transport in metals at millikelvin temperatures. Phys. Rev. Lett. **55**(4), 422–425 (1985)
- 5. N. Campbell, The study of discontinuous phenomena. Proc. Camb. Philos. Soc. 15, 117–136 (1910)

References 171

- 6. N. Campbell, Discontinuities in light emission. Proc. Camb. Philos. Soc. 15, 310–328 (1910)
- E. Mathieson, Derivation of noise formulas using Campbells theorem. Am. J. Phys. 45(12), 1184–1186 (1977)
- 8. W. Schottky, Regarding spontaneous current fluctuation in different electricity conductors. Ann. Phys. **57**(23), 541–567 (1918)
- 9. C. Beenakker, C. Schonenberger, Quantum shot noise. Phys. Today **56**(5), 37–42 (2003)
- D. Halford, A general mechanical model of random perturbations which generate a noise spectral density law lflalpha with reference to flicker noise law 1/lfl. IEEE Trans. Instrum. Meas. 15(4), 404–411 (1966)
- 11. M.S. Keshner, 1/f noise. Proc. IEEE **70**(3), 212–218 (1982)
- 12. F.N. Hooge, 1/f noise. Phys. B & C 83(1), 14-23 (1976)
- 13. E. Milotti, Linear processes that produce 1/f or flicker noise. Phys. Rev. E 51, 3087 (1995)
- C.D. Motchenbacher, J.A. Connelly, C.D. Motchenbacher, Low-Noise Electronic System Design (Wiley, New York, 1993)
- A.K. Naik, M.S. Hanay, W.K. Hiebert, X.L. Feng, M.L. Roukes, Towards single-molecule nanomechanical mass spectrometry. Nat. Nanotechnol. 4(7), 445–450 (2009)
- Y.T. Yang, C. Callegari, X.L. Feng, K.L. Ekinci, M.L. Roukes, Zeptogram-scale nanomechanical mass sensing. Nano Lett. 6(4), 583–586 (2006)
- 17. Y.T. Yang, C. Callegari, X.L. Feng, M.L. Roukes, Surface adsorbate fluctuations and noise in nanoelectromechanical systems. Nano Lett. **11**(4), 1753–1759 (2011)
- 18. J. Chaste, A. Eichler, J. Moser, G. Ceballos, R. Rurali, A. Bachtold, A nanomechanical mass sensor with yoctogram resolution. Nat. Nanotechnol. **7**(5), 300–303 (2012)
- S. Schmid, P. Senn, C. Hierold, Electrostatically actuated nonconductive polymer microresonators in gaseous and aqueous environment. Sensors Actuators A Phys. 145–146, 442–448 (2008)
- X.L. Feng, C.J. White, A. Hajimiri, M.L. Roukes, A self-sustaining ultrahigh-frequency nanoelectromechanical oscillator. Nat. Nanotechnol. 3(6), 342–346 (2008)
- A. Ayari, P. Vincent, S. Perisanu, M. Choueib, V. Gouttenoire, M. Bechelany, D. Cornu, S.T. Purcell, Self-oscillations in field emission nanowire mechanical resonators: a nanometric dc-ac conversion. Nano Lett. 7(8), 2252–2257 (2007)
- P. Vincent, S. Perisanu, A. Ayari, M. Choueib, V. Gouttenoire, M. Bechelany, A. Brioude, D. Cornu, S.T. Purcell, Driving self-sustained vibrations of nanowires with a constant electron beam. Phys. Rev. B 76(8), 085435 (2007)
- S. Schmid, P. Senn, C. Hierold, Electrostatically actuated nonconductive polymer microresonators in gaseous and aqueous environment. Sensors Actuators A Phys. 145, 442–448 (2008)
- L.G. Villanueva, R.B. Karabalin, M.H. Matheny, E. Kenig, M.C. Cross, M.L. Roukes, A nanoscale parametric feedback oscillator. Nano Lett. 11(11), 5054–5059 (2011)
- L.G. Villanueva, E. Kenig, R.B. Karabalin, M.H. Matheny, R. Lifshitz, M.C. Cross, M.L. Roukes, Surpassing fundamental limits of oscillators using nonlinear resonators. Phys. Rev. Lett. 110(17), 177208 (2013)
- E. Kenig, M.C. Cross, L.G. Villanueva, R.B. Karabalin, M.H. Matheny, R. Lifshitz, M.L. Roukes, Optimal operating points of oscillators using nonlinear resonators. Phys. Rev. E 86(5), 056207 (2012)
- C.Y. Chen, S. Lee, V.V. Deshpande, G.H. Lee, M. Lekas, K. Shepard, J. Hone, Graphene mechanical oscillators with tunable frequency. Nat. Nanotechnol. 8(12), 923–927 (2013)
- C.J. Zuo, J. Van der Spiegel, G. Piazza, Dual-mode resonator and switchless reconfigurable oscillator based on piezoelectric ALN MEMS technology. IEEE Trans. Electron Devices 58(10), 3599–3603 (2011)
- C.J. Zuo, J. Van der Spiegel, G. Piazza, 1.05-GHz CMOS oscillator based on lateral-field-excited piezoelectric ALN contour-mode MEMS resonators. IEEE Trans. Ultrason. Ferroelectr. Freq. Control 57(1), 82–87 (2010)
- Y. Hui, T.X. Nan, N.X. Sun, M. Rinaldi, High resolution magnetometer based on a high frequency magnetoelectric MEMS-CMOS oscillator. J. Microelectromech. Syst. 24(1), 134–143 (2015)

- D.W. Allan, H.E. Machlan, J.E. Gray, National bureau of standards atomic time scales generation, dissemination, stability, and accuracy. IEEE Trans. Instrum. Meas. 21(4), 388–391 (1972)
- 32. F.L. Walls, D.W. Allan, Measurements of frequency stability. Proc. IEEE **74**(1), 162–168 (1986)
- 33. D.A. Allan, N Ashby, C.C. Hodge, The science of timekeeping. Report, Hewlett Packard (1997)
- M. Sansa, E. Sage, E.C. Bullard, M. Gély, T. Alava, E. Colinet, A.K. Naik, L.G. Villanueva, L. Duraffourg, M.L. Roukes, G. Jourdan, S. Hentz, Frequency fluctuations in silicon nanoresonators (2015). arXiv:1506.08135 [cond-mat]

Index

Symbols	D
-3dB bandwidth method, 36	Damped linear resonator, 29
1/f noise, 158	Damped nonlinear resonators, 45
	Damping dilution factor, 82
	Damping dilution in strings & membranes, 81
A	Damping ratio, 31
Actuation nonlinearity, 48	Debye equations, 73
Akhiezer damping, 79	Debye peak, 74
Akhiezer effect, 79	Detection nonlinearity, 49
Allan deviation, 167	Dielectric polarization force, 123
Allan variance, 167	Dielectric polarization force density, 124
Amplifier noise, 159	Dispersion relationship, 8
Amplitude calibration, 154	Dispersive coupling, 139
Amplitude noise, 149	Distributed mass responsivity, 100
Amplitude response to a force, 101	Drag-force damping, 62
Anelasticity, 70	Driven damped vibration, 32
Arrhenius' law, 75	Duffing resonator, 52
В	E
B Barkhausen criterium, 167	E Effective parameters 38
Barkhausen criterium, 167	Effective parameters, 38
Barkhausen criterium, 167 Beam deflection detection, 141	Effective parameters, 38 Eigenfrequenchy of rectangular plate
Barkhausen criterium, 167 Beam deflection detection, 141 Boundary liquid, 59	Effective parameters, 38 Eigenfrequenchy of rectangular plate (clamped), 23
Barkhausen criterium, 167 Beam deflection detection, 141	Effective parameters, 38 Eigenfrequenchy of rectangular plate (clamped), 23 Eigenfrequency, 1
Barkhausen criterium, 167 Beam deflection detection, 141 Boundary liquid, 59	Effective parameters, 38 Eigenfrequenchy of rectangular plate (clamped), 23 Eigenfrequency, 1 Eigenfrequency of a string, 15
Barkhausen criterium, 167 Beam deflection detection, 141 Boundary liquid, 59	Effective parameters, 38 Eigenfrequenchy of rectangular plate (clamped), 23 Eigenfrequency, 1
Barkhausen criterium, 167 Beam deflection detection, 141 Boundary liquid, 59 Bridge, 11 C	Effective parameters, 38 Eigenfrequenchy of rectangular plate (clamped), 23 Eigenfrequency, 1 Eigenfrequency of a string, 15 Eigenfrequency of beam under tensile stress, 14
Barkhausen criterium, 167 Beam deflection detection, 141 Boundary liquid, 59 Bridge, 11 C Cantilever, 9	Effective parameters, 38 Eigenfrequenchy of rectangular plate (clamped), 23 Eigenfrequency, 1 Eigenfrequency of a string, 15 Eigenfrequency of beam under tensile stress, 14 Eigenfrequency of circular membrane, 27
Barkhausen criterium, 167 Beam deflection detection, 141 Boundary liquid, 59 Bridge, 11 C	Effective parameters, 38 Eigenfrequenchy of rectangular plate (clamped), 23 Eigenfrequency, 1 Eigenfrequency of a string, 15 Eigenfrequency of beam under tensile stress, 14
Barkhausen criterium, 167 Beam deflection detection, 141 Boundary liquid, 59 Bridge, 11 C Cantilever, 9 Capacitively induced current, 126 Circular membranes, 26	Effective parameters, 38 Eigenfrequenchy of rectangular plate (clamped), 23 Eigenfrequency, 1 Eigenfrequency of a string, 15 Eigenfrequency of beam under tensile stress, 14 Eigenfrequency of circular membrane, 27 Eigenfrequency of longitudinal vibration of a beam, 19
Barkhausen criterium, 167 Beam deflection detection, 141 Boundary liquid, 59 Bridge, 11 C Cantilever, 9 Capacitively induced current, 126	Effective parameters, 38 Eigenfrequenchy of rectangular plate (clamped), 23 Eigenfrequency, 1 Eigenfrequency of a string, 15 Eigenfrequency of beam under tensile stress, 14 Eigenfrequency of circular membrane, 27 Eigenfrequency of longitudinal vibration of a
Barkhausen criterium, 167 Beam deflection detection, 141 Boundary liquid, 59 Bridge, 11 C Cantilever, 9 Capacitively induced current, 126 Circular membranes, 26 Circular plates, 24	Effective parameters, 38 Eigenfrequenchy of rectangular plate
Barkhausen criterium, 167 Beam deflection detection, 141 Boundary liquid, 59 Bridge, 11 C Cantilever, 9 Capacitively induced current, 126 Circular membranes, 26 Circular plates, 24 Clamping loss, 66	Effective parameters, 38 Eigenfrequenchy of rectangular plate
Barkhausen criterium, 167 Beam deflection detection, 141 Boundary liquid, 59 Bridge, 11 C Cantilever, 9 Capacitively induced current, 126 Circular membranes, 26 Circular plates, 24 Clamping loss, 66 Closed-loop noise, 163	Effective parameters, 38 Eigenfrequenchy of rectangular plate

174 Index

Electrical charge damping, 58 Electrodyamic transduction, 116 Electromotive force, 118 Electrostatic forces, 120 End-coupled optical waveguide, 142 Euler-Bernoulli beam theory, 7	Localized surface plasmon, 142 Lorentz force, 116 Lorentz force on a straight wire, 117 Lorentzian, 36, 37 Loss modulus, 71 Loss tangent, 72 Lumped-element model, 29
F	
Fabry-Pérot interferometer, 139	M
Field emission transduction, 115	Mach-Zehnder interferometer, 140
Forces between electrodes, 121	Magnetomotiv damping, 58
Free bending vibration of membranes, 25	Magnetostatic transduction, 115
Free bending vibration of plates, 21	Material nonlinearity, 46
Free damped vibration, 31	Mean free path length, 62
Free undamped vibration, 30	Medium interaction losses, 58
Frequency equation of cantilever, 10	Membrane, 25
Frequency noise, 163	Michelson interferometer, 140
Frequency response to a force gradient, 102	Mode shape function of a string, 15
Frequency response to an electrostatic	Modeshape of a beam, 13
potential, 103	Modeshape of a cantilever, 10
Frequency response to mass, 92	Modeshape of a string, 17
Friction losses, 70	Modeshape of longitudinal vibration in a
Full width at half maximum, 37	bream, 19
G	N
Gas damping, 61	Natural frequency, 32
Gauge factor, 132	Noise, 149
Geometric nonlinearity, 47	Noise equivalent circuit, 159
	Noise Figure, 162
	Noise Referred to Input, 150
H	Noise Temperature, 162
Hard contact transduction, 115	Nonlinear damping, 49
	Normal coordinate, 44
I	Normal mode splitting, 45
Impedance mismatch strategies, 129	Normal modes, 45
Interferometric detection, 139	
Intrinsic damping, 69	
Intrinsic damping mechanisms, 69	0
manusic damping meetamisms, 0)	Open loop noise, 149
	Optical forces, 138
J	Optical leverage, 141
Johnson-Nyquist Thermal noise, 155	Optical transduction, 138
	Oscillator, 165
K K L :	P
Kelvin polarization force, 123	_
Knudsen number, 62	Phase-locked loop, 163
	Phonon-phonon interaction loss, 79 Piezoelectric actuation, 136
L	Piezoelectric actuation, 136 Piezoelectric detection, 137
LC filter impedance mismatch, 129	Piezoelectric detection, 137 Piezoelectric transduction, 134
Liquid damping, 58	Piezoresistive detection, 132
1 dmP2, 00	1 1020100101110 0010011011, 132

Index 175

Plasmonic detection, 142	Strong coupling, 45
Plate, 21	Surface friction, 77
PLL, 163	Surface plasmon resonance, 142
Point mass responsivity, 95	Suspended microchannel resonators, 60
Positive feedback, 165	_
Power spectral density, 153	
1	T
Q	Temperatur responsivity of stress released resonators, 106
Quality factor, 35	Temperature response of string to local heating,
R Radiation pressure, 138 Rayleigh method, 2, 22 Rayleigh-Ritz method, 5 Rectangular membrane, 25 Rectangular membranes, 25 Rectangular Plates, 21 Relative responsivity, 92 Relaxed Young's modulus, 74 Resonance, 1	Thermoelastic actuation, 131 Thermoelastic damping, 78 Thermomechanical noise, 151 Time temperature equivalence, 75 Torsional paddle resonator, 40 Torsional vibration of thin beams, 27 Transduction chain noise transfer, 150 Transimpedance amplifier, 129 Tunneling transduction, 115 Two level system, 75
Resonance frequency, 1, 34 Responsivity, 91 Reynold's number, 60 Ring down method, 37 Ritz method, 5 Robbin's formula, 169	U U-tube resonators, 60 Unrelaxed Young's modulus, 74
Roots of frequency equation of bridge, 12	v
Roots of frequency equation of cantilever, 10	Viscoelasticity, 70
s	viscoeiasticity, /0
Shot noise, 157	\mathbf{W}
Squeeze-film damping, 62	Wave velocity inside a material, 18
Standard linear sold, 70	Wave velocity inside a string or membrane, 15
Storage modulus, 71	Wavenumber, 7
Storage Young's modulus, 71	White noise, 152
Strain coefficient of resistivity, 133	
Strain gauge, 132	
String responsivity to ambient temperature,	\mathbf{Z}
108	Zener model, 70